New Developments in Early Diagenetic Modeling:
pH Distributions, Calcite Dissolution and Compaction

Parisa Jourabchi

New Developments in Early Diagenetic Modeling: pH Distributions, Calcite Dissolution and Compaction

Nieuwe ontwikkelingen in het simuleren van vroege diagenetische
processen: pH profielen, het oplossen van calciet en compactie

(met een samenvatting in het Nederlands)

PROEFSCHRIFT

ter verkrijging van de graad van doctor aan de Universiteit Utrecht op
gezag van de rector magnificus, prof. dr. J.C. Stoof, ingevolge het
besluit van het college voor promoties in het openbaar te verdedigen
op maandag 15 oktober 2007 des middags te 12.45 uur

door

Parisa Jourabchi

geboren op 2 september 1972 te Tehran, Iran

Promotor: prof. dr. P. Van Cappellen

Contents

Summary

Early diagenetic models encompass the mathematical formulation and numerical solution of complex biogeochemical reaction systems, and thus contribute to and profit from the advances made in the broader field of reaction transport models (RTMs). Biogeochemical reactions common to many natural systems (e.g. redox reactions, mineral dissolution/precipitation processes, and acid/base equilibria) have been extensively studied in laboratory and field studies, leading to a wealth of knowledge on the mechanisms and (empirical) rate expressions plus related parameters governing these reaction processes.

Based on the concept of a Knowledge Base (KB), the available information on individual reaction processes is systematically compiled, in order to facilitate the assemblage of RTMs. In chapter 2, the KB is interfaced with one-dimensional transport descriptions relevant to many compartments of the Earth system (rivers, estuaries, groundwater or sediments) to yield a unified simulation environment. The flexibility of this reactive transport modeling framework, which is based on symbolic programming and automatic code generation, is illustrated in two model applications dealing with redox and coupled acid-base chemistry in sediments and groundwater environments. Using a new method developed in chapter 3 for the calculation of proton production/consumption rates, the trends in pH distributions in these two, redox-dominated environmental systems are explored.

The distribution of pore water pH in aquatic sediments is investigated in greater detail in chapter 3. The quantitative prediction of pH profiles requires a rigorous mathematical treatment of the coupling of acid-base equilibria, irreversible kinetic reactions and transport processes. In the proposed approach, the chemical species participating in equilibrium reactions appear explicitly in the kinetic reaction stoichiometries. As the stoichiometric coefficients of these species are treated as unknowns in the model, the kinetic reaction stoichiometries are allowed to vary with time and depth in the sediment.

The general theory for deriving the stoichiometric coefficients is presented for a batch reactor seawater system, taking into account the acid-base equilibria of the dissolved inorganic carbon, sulfide, and borate systems. The variable stoichiometric coefficients are expressed in terms of the stoichiometric coefficient of the proton, for which an explicit expression is derived. This method, which can be generalized to include other equilibrium reactions, yields the proton production and consumption rates due to each kinetic reaction process.

Summary

Calculation of the reaction-specific proton production and consumption rates provides a mechanistic and quantitative interpretation of pH distributions in aquatic sediments. The model is applied by simulating the coupled early diagenetic processes in a sediment representative of the continental shelf. The computed pH profiles exhibit features commonly observed in measured profiles. In particular, the occurrence of a pH minimum and maximum is explained in terms of the depth distributions of proton production and consumption by the various biogeochemical reactions. The proposed approach also provides a means to interpret the saturation state of pore waters with respect to mineral phases (carbonates, sulfides, oxides), since they are intimately linked to variations in pH. In this respect, the role of microbial sulfate reduction in controlling the calcite saturation state is investigated, by explicitly computing the rate at which carbonate ions are produced or consumed by sulfate respiration. In contrast to the commonly held view, the results demonstrate that under certain depositional conditions sulfate reduction may increase the degree of pore water undersaturation with respect to calcite. Model simulations are also used to determine the response of pH to variations in calcite dissolution kinetics and irrigation intensity.

The model developed in chapter 3 is then applied to the joint interpretation of pore water oxygen and pH microprofiles measured in 13 deep-sea sediments (chapter 4). The statistical analysis of the model simulation results shows that two sedimentary pools of organic matter with distinct reactivities are necessary to reproduce the oxygen profiles at the majority of the sites considered (11 out of 13). Estimation of only three parameters (the input fluxes of the two organic matter fractions, plus the degradation rate constant of the more reactive pool) is sufficient to successfully simulate the observed oxygen profiles at all the sites. The model results further indicate that, although oxic respiration is the dominant pathway of degradation of organic matter, suboxic degradation plays a non-negligible role in most of the deep-sea sediments considered.

In contrast to oxygen, the successful simulation of the pore water pH profiles is less straightforward, due to the larger number of processes that affect the proton balance, as well as the uncertainties associated with the calcite dissolution kinetics. Hence, only 9 out of the 13 pH microprofiles are satisfactorily reproduced. In addition, while fitting the O_2 pore water concentrations yields estimates of the deposition flux of degradable organic matter, it is not possible to constrain the deposition flux of $CaCO_3$ from the pH data. This is because organic matter is unstable in early diagenetic environments, while pore waters reach equilibrium with respect to calcite. As a consequence, the depth-integrated calcite dissolution rate, rather than the corresponding deposition flux, is obtained from the best-fit pH profiles. As expected, the

CaCO$_3$ dissolution rates reflect both the (model-derived) benthic O$_2$ uptake rate and the (imposed) saturation state of the overlying bottom water.

The model results highlight the major role of calcite dissolution in buffering pore water pH in marine sediments. Furthermore, dissolution rate expressions including nonlinear dependencies on the degree of undersaturation yield the best agreement between modeled and measured pH profiles. Nonetheless, the model-derived profiles overpredict the amplitude of pH variations observed at a number of the sites, even when CaCO$_3$ dissolution is included. Additional proton exchange processes, involving functional groups of mineral surfaces and sedimentary organic matter, may therefore also contribute to pore water buffering.

Chapter 5 presents a one-dimensional, steady state model of physical and chemical compaction, which is coupled to a reaction-transport model for the interpretation of porosity profiles in aquatic sediments. The model is based on a more general continuum theory that considers the conservation of mass and momentum. Most importantly, the model can be used to separate the effects of mechanical compaction from mineral dissolution or precipitation reactions on porosity. Thus, the application of the model to available porosity data may yield information about the rates of important mineral reactions.

Parameters defining the hydraulic conductivity and elastic response of a set of deep-sea sediments are estimated through an inverse modeling approach, as these parameter values are not readily available for these natural porous media. Preliminary model results indicate an inverse relationship between the elastic response coefficient and the lithogenic content of the sediment. This points to the possibility of linking the compaction behavior of unconsolidated surficial sediments to their composition, based on an extended data analysis encompassing a larger range of depositional settings.

An iterative approach is used to couple the reaction-transport model (developed in chapter 3) to the sediment compaction model. The coupled model is used to investigate the calcite dissolution rate order. The simulation results for three different rate orders ($n = 1, 2,$ and 4.5) indicate a slightly improved porosity fit to available data when using the nonlinear rate laws, though application to more data sets of porosity and sediment composition will be needed to draw any definitive conclusions. The results obtained so far, however, show that treating porosity as an unknown represents a potentially useful addition to current early diagenetic reactive transport modeling efforts.

The rigorous combination of pore water data with reactive transport modeling extends our understanding of early diagenetic processes and benthic-pelagic coupling beyond the temporal and spatial scales accessible to direct measurements. This understanding is

necessary when embedding benthic exchanges into regional or global ocean models, in particular in the context of climate simulations that extend back over glacial-interglacial timescales. The work presented in this thesis not only illustrates the success in quantifying benthic O_2 dynamics, but also identifies remaining limitations in representing pore water acid-base chemistry and early diagenetic $CaCO_3$ dynamics. The latter has significant implications for the long-term interpretation of paleo-proxies linked to calcite composition and preservation, and highlights the need for further quantitative studies.

Samenvatting

Vroeg diagenetische modellen beschrijven de complexe biogeochemische reactie systemen in sedimenten op basis van wiskundige formuleringen en numerieke oplossingen. Op die manier dragen ze bij tot, en profiteren ze van, de vooruitgangen op het gebied van reactief transport modellen (RTM). Biogeochemische reacties die voorkomen in veel natuurlijke systemen (bv. redox reacties, oplossing-neerslag van mineralen, zuur-base evenwichten) zijn uitgebreid bestudeerd in laboratorium en veldstudies en hebben geleid tot een rijkdom van kennis wat betreft de mechanismen, de (empirische) snelheids uitdrukkingen en de parameters die bij deze processen betrokken zijn.

Gebaseerd op het concept van een 'Kennis Basis (KB)' wordt de beschikbare informatie over individuele reactie processen systematisch samengesteld en opgeslagen, met als doel het vergemakkelijken van het samenstellen van een RTM. In hoofdstuk 2 wordt de KB gekoppeld aan ééndimensionale advectief-diffusief transport beschrijvingen die relevant zijn in aardse compartimenten (rivieren, estuaria, grondwater of sediment), met als doel een uniforme simulatie omgeving te creëren.

De flexibiliteit van deze reactief transport model benadering is gebaseerd op symbolische programmering. De automatische generatie van computer codes wordt geïllustreerd aan de hand van twee model toepassingen op het gebied van de redox en gekoppelde zuur-base chemie in sedimenten en grondwater systemen. De pH trends in deze twee redox gedomineerde systemen wordt onderzocht met een in hoofdstuk 3 ontwikkelde nieuwe methode die proton consumptie en productie berekend.

In hoofdstuk 3 worden diepte profielen van pH in poriewater in detail onderzocht. De kwantitatieve voorspelling van pH profielen vereist een rigoureuze mathematische aanpak van gekoppelde zuur-base evenwichten, irreversibele biogeochemische reacties en transport processen. In de voorgestelde aanpak verschijnen de chemische verbindingen die deel uitmaken van evenwichtsreacties expliciet in de stoichiometrie van een kinetische reactie. Aangezien de stoichiometrische coëfficiënten van de chemische verbindingen in het model worden behandeld als onbekenden kan de sociometrie van een bepaalde kinetische reactie in het sediment variëren in de tijd en met de diepte. De algemene theorie voor het afleiden van stoichimetrische coëfficiënten wordt geillustreerd voor een 'batch reactor' zeewater systeem, waarbij rekening gehouden werd met zuur-base evenwichten van opgelost anorganisch koolstof, sulfide en boraat. De variabele stoichiometrische coefficienten worden uitgedrukt in termen van de stoichiometrische coëfficiënt van het proton (H^+) waarvoor een expliciete

uitdrukking wordt afgeleid. Deze methode, die gegeneraliseerd kan worden door het toevoegen van andere evenwichtsreacties levert de proton productie en consumptie snelheden van elk kinetisch reactie proces op.

Het berekenen van proton productie en consumptie snelheden door de verschillende biogeochemische reactie processen levert een mechanistisch en kwantitatieve interpretatie op van pH profielen in aquatische sedimenten. Het model is vervolgens toegepast door het simuleren van gekoppelde vroeg diagenetische processen in een sediment dat representatief is voor het continentaal plat. De berekende pH profielen vertonen kenmerken die ook gevonden worden in gemeten profielen. Zo kan het vaak voorkomen van een pH minimum en maximum bijvoorbeeld verklaard worden door de onderlinge verdeling over de diepte van proton producerende en consumerende biogeochemische reacties.

De voorgestelde aanpak voorziet ook in een manier om de verzadiginggraden van het poriewater met betrekking tot reactieve minerale fasen (carbonaten, sulfides, oxides) te interpreteren omdat deze sterk gerelateerd zijn aan variaties in pH. Vanuit dit oogpunt wordt de rol van microbiële sulfaat reductie in het reguleren van de verzadigingsgraad van poriewater met betrekking tot calciet onderzocht. Hierbij wordt expliciet de snelheid waarmee carbonaat ionen geproduceerd of geconsumeerd worden door sulfaat respiratie berekend. In tegenstelling tot de algemeen aangenomen opvatting laten de resultaten zien dat onder bepaalde omstandigheden sulfaat reductie de mate van onderverzadiging van poriewater met betrekking tot calciet kan verhogen. Model simulaties worden ook gebruikt om de afhankelijkheid van pH profielen op de irrigatie intensiteit en de kinetiek van calciet oplosbaarheid te onderzoeken.

Het model dat ontwikkelt is in hoofdstuk 3 wordt vervolgens toegepast door simultaan de poriewater zuurstof en pH microprofielen in 13 diepzee sedimenten te simuleren (hoofdstuk 4). Statistische analyse van de model resultaten laat zien dat om de zuurstof profielen op de meerderheid van de locaties (11 uit 13) te kunnen reproduceren het afbreekbaar organisch materiaal in het sediment uit ten minste 2 verschillende fracties met 2 verschillende reactiviteiten moet bestaan. Een schatting van slechts 3 parameters (de aanbreng van de 2 organische fracties, en de reactie constante voor de afbraak van de meest reactieve fractie) is genoeg om de geobserveerde zuurstof profielen succesvol te reproduceren. De model resultaten laten verder zien dat, ondanks het feit dat aёrobe respiratie de dominante afbraakroute van organisch materiaal is, suboxische afbraak een niet verwaarloosbare rol speelt in de meeste diepzee sedimenten.

In tegenstelling tot zuurstof ligt het simuleren van pH profielen minder voor de hand, mede vanwege het grote aantal processen dat de proton balans van poriewater beïnvloedt, en de onzekerheden die verbonden zijn aan de kinetiek van de calciet oplossing reactie. Daarbij komt dat terwijl het 'fitten' van zuurstof poriewater profielen de aanbreng uit de waterkolom van afbreekbaar organisch materiaal oplevert, het niet mogelijk blijkt de aanbreng van CaCO₃ van pH gegevens af te leiden. De oorzaak hiervan is dat het organisch materiaal niet stabiel is in vroeg diagenetische omgevingen, terwijl thermodynamisch evenwicht tussen het poriewater en calciet wel kan worden bereikt. Het gevolg is dat het passen van het model aan de gemeten pH profielen de met de diepte geïntegreerde calciet oplosbaarheids snelheid oplevert en niet de aanbreng uit de water kolom (de zgn. deposition flux). Zoals verwacht weerspiegelt de hoeveelheid CaCO₃ dat oplost zowel de zuurstof opname door het sediment als de verzadigingsgraad van het overliggende bodemwater.

De model resultaten benadrukken de belangrijke rol van calciet oplossing in het bufferen van de pH van poriewater in mariene sedimenten. Ze tonen ook aan dat niet-lineaire snelheidsvergelijkingen voor calciet oplossing de beste overeenkomst tussen gemeten en gemodelleerde pH profielen opleveren. Toch zijn de door het model afgeleide variaties in pH hoger dan deze geobserveerd op een aantal locaties, zelfs nadat CaCO₃ oplossing in rekening is gebracht. Andere proton uitwisseling processen, bijvoorbeeld aan functionele groepen van minerale oppervlaktes en organisch materiaal, blijken ook bij te dragen aan de buffering van poriewater.

In hoofdstuk 5 wordt een eendimensionaal, stationair model van chemische en fysische compactie gepresenteerd, die gekoppeld is aan een RTM om profielen van de porositeit in aquatische sedimenten te interpreteren. Het model is gebaseerd op een meer algemene theorie die rekening houdt met behoud van massa en van moment. Belangrijk is dat het model gebruikt kan worden om effecten van fysische en chemische compactie van elkaar te scheiden. Chemische compactie is het gevolg van oplossing- en neerslagreacties van mineralen op de porositeit. Toepassing van het model op beschikbare porositeit gegevens kan op deze manier informatie opleveren met betrekking tot belangrijke reacties die mineralen ondergaan. Parameters die de hydraulische conductiviteit en elastische respons in een serie diepzee sedimenten definiëren worden geschat door een inverse modeleer aanpak aangezien parameter waarden niet beschikbaar zijn voor marine sedimenten. Model resultaten tonen een omgekeerde relatie tussen de elastische response coëfficiënt en de lithogene inhoud van het sediment. Dit duidt op de mogelijkheid om het compactie gedrag van losse oppervlakte

sedimenten te voorspellen op basis van hun samenstelling. Hiervoor is echter een meer uitgebreide data analyse over meer sedimentaire systemen noodzakelijk.

Een iteratieve aanpak wordt gebruikt om het RTM ontwikkelt in hoodfdstuk 3 aan het sediment compactie model te koppelen. Het gekoppelde model wordt gebruikt om de kwantitatieve beschrijving van calciet oplosbaarheid in sedimenten te onderzoeken. De simulatie resultaten voor de verschillende reactie orders in the snelheidsvergelijking (n = 1, 2, en 4.5) duiden op een lichtelijk betere prestatie van niet-lineaire vergelijkingen ($n \neq 1$). Om definitieve conclusies te trekken zal het model op meer data sets toegepast moeten worden. Vooralsnog tonen de resultaten van het onderzoek het belang aan van het behandelen van de porositeit als een onafhankelijke variabele in vroeg diagenetische reactief transport modellen.

De systematische interpretatie van poriewater gegevens door middel van reactief transport modelleren breidt ons begrip van vroeg diagenetische processen en de 'benthisch-pelagische' koppeling uit, in het bijzonder op temporele en spatiele schalen die niet toegankelijk zijn voor directe metingen en experimenten. Dit is van belang wanneer we de wisselwerkingen tussen de oceanen en de onderliggende sedimenten willen voorstellen in regionale of globale oceaan modellen, bijvoorbeeld in de context van klimaatsimulaties over glaciaal – interglaciale tijdschalen. Het werk wat gepresenteerd wordt in dit proefschrift laat zien dat de zuurstof dynamiek in marine sedimenten met succes kan worden gekwantificeerd. Het toont ook de overblijvende beperkingen in het modelleren van poriewater zuur-base chemie en vroeg diagenetische $CaCO_3$ dynamiek. Het laatste heeft belangrijke implicaties voor lange termijn interpretaties van paleoproxies die gerelateerd zijn aan de chemische samenstelling van biogeen calciet en laat zien dat verder kwantitatief onderzoek in de toekomst van groot belang is.

Chapter 1

1. Introduction

Biogeochemical transformations of organic and inorganic particulate matter deposited at the seafloor result from a complex interaction of physical, chemical and biological processes which, together, constitute the early diagenesis of marine sediments. These transformations not only alter the sedimentary record, but also induce chemical mass transfers across the sediment-water interface and determine the ultimate burial fluxes of biogenic constituents (Van Cappellen and Gaillard, 1996). Of particular importance is the preservation or dissolution of calcium carbonate in marine sediments, which alters the carbonate chemistry of the overlying seawater and, hence, influences the atmospheric pCO_2 (Broecker and Peng, 1987; Archer and Meier-Reimer, 1994). A major objective of the current research on the fate of carbon in marine sediments is to develop a more quantitative basis for the assessment of calcite diagenesis in surficial sediments (Metz et al., 2005; Kleypas et al., 2006).

The dissolution of calcite mainly depends on the saturation state of the sediment pore water, which in turn is closely linked to pore water pH. As most biogeochemical processes in sediments affect the proton balance of the pore water, an accurate description of the pH distribution requires an integrative and quantitative representation of all the relevant biochemical reactions coupled to the transport of solids and solutes (Luff et al., 2001). At the same time, pH can be measured accurately and with high vertical resolution (e.g., Cai and Reimers, 1993). Thus, available measurements combined with early diagenetic modeling should make the pore water pH distribution an excellent diagnostic indicator of the biogeochemical processes occurring in marine sediments.

The goal of this thesis is to advance the field of early diagenetic modeling, through the quantitative interpretation of pH distributions within the framework of a reaction-transport model, or RTM. Particular attention is given to calcite dissolution, as well as sediment compaction. The introduction is divided into five sections and begins with a background on RTMs and their role in early diagenetic modeling (section 1.1). The next three sections (1.2-1.4) give an overview on the main aspects of the thesis: pH distributions, calcite dissolution, and sediment compaction. The last section (1.5) introduces the outline of this thesis with an overview of chapters 2-5.

1.1. Reaction-Transport Models

In the natural sciences, reaction-transport models (RTMs) account for the coupling of chemical, physical, and biological interactions, ranging in spatial scales from that of a single living cell (Sayyed-Ahmad et al., 2003) to those of a groundwater system or a macrotidal estuary (Mayer et al., 2002; Arndt et al., 2007). One of the early theoretical formulations and applications of RTMs has been the study of the redox zonation characterizing marine sediments (Berner, 1980). Many recent advances, however, have focused on groundwater and contaminant transport (Steefel et al., 2005).

Fundamental to all RTMs for porous media is the conservation of mass, expressed mathematically in terms of concentrations of chemical (or biological) species that are averaged over a representative elemental volume (REV). In early diagenetic RTMs, sediment properties such as concentrations are averaged over an REV before the mass balance equations are written. Alternatively, hydrologists and engineers assert that mass balance equations apply within a single phase and at a microscopic scale, requiring the averaging of the equations over the REV (e.g., Hassanizadeh, 1986; Plumb and Whitaker, 1990; Gray et al., 1993). Boudreau (1997) reconciles these two approaches through the reduction in molecular diffusion resulting from the fine scale structure of the porous medium. In this thesis, the early diagenetic modeling approach of averaging sediment properties is adopted.

Despite the wide range of temporal and spatial scales of the environmental compartments to which RTMs are applied, there are a number of biogeochemical reactions common to many natural systems (e.g., redox reactions, mineral dissolution/precipitation, and acid/base reactions). Laboratory and field studies have advanced the process-based studies of these reactions, leading to a wealth of knowledge on the mechanisms and (empirical) rate expressions and related parameters governing these processes. Thus, efforts have been made to create databases of thermodynamic and kinetic information for relevant biogeochemical reactions (Katsev et al., 2004).

Flexible modeling environments that allow one to adapt and modify reaction and transport processes to specific environmental settings have also been developed. These include reaction-transport codes such as MEDIA (Meysman et al., 2003) for early diagenesis and MIN3P (Mayer et al., 2002) for groundwater systems. A more general approach is demonstrated by the computer program CRUNCH (Steefel, 2001) for multicomponent reactive transport in porous media, with example applications in the vadose zone (Saripalli et al., 2006) and marine sediments (Maher et al., 2006).

On the basis of a generalized continuum representation of the mass-balance equations, Regnier et al. (2002 and 2003) developed a flexible modeling framework that can couple various transport regimes of the hydrosphere to extensive biogeochemical reaction networks. The approach is based on a knowledge base (KB) of processes interfaced to a numerical engine through an automatic code generator. **Chapter 2** describes the development of a web-distributed KB system and its application to redox dynamics in two contrasting environments: a continental shelf sediment and a groundwater aquifer contaminated by a landfill plume.

1.2. Process Identification and pH Typology

The buffering of pH in the pore waters of marine sediments has been of interest for over three decades. Ben-Yaakov (1973) examined the pH change due to sulfate reduction in a closed system and noted that this process will increase pH only if all the sulfides produced are removed (e.g., as a result of transport in an open system or precipitation of sulfides). Fisher and Matisoff (1981), among the first ones to use a micro-pH electrode in estuarine and lake sediments, observed that chemical reactions affect pH on vertical scales much smaller than 1 cm, that is, at a smaller scale than can be resolved using the traditional pore water sampling methods. Using a pH microelectrode, they observed a local pH minimum immediately below the oxidized zone in all sediments examined.

Open-system models, which account for the transport of chemical species in the sediment, were subsequently developed to calculate the pH depth profiles (Emerson and Bender, 1981; Boudreau, 1987). These models made a quantitative link between the degradation of organic carbon in oxic sediments and the undersaturation of pore waters with respect to calcite, and its resulting dissolution. The simulated pH profiles of pore waters collected from the sediments of Guatemala Basin also showed a local pH minimum (Boudreau, 1987).

At the same time, Murray et al. (1980) showed the effect of pressure on alkalinity, and hence pH, in interstitial waters from the Guatemala Basin sediments through the comparison of in-situ and shipboard sampling methods. The combination of in-situ measurements and microelectrode technology resulted in the availability of accurate and high-resolution pH profiles. This led to the application of a diffusion-reaction model to in-situ microelectrode data for the estimation of calcite dissolution in sediments deposited above and below the calcite saturation horizon in the equatorial Atlantic (Archer et al., 1989).

Recognizing the complex interplay of processes shaping pH distributions in sediments and its effect on the saturation state of pore waters with respect to minerals, a number of studies focused on the application of RTMs to simulate pH dynamics. Boudreau (1987)

simulated pH variations in the pore waters of oxic and suboxic sediments, while Boudreau and Canfield (1988) constructed a model to simulate pH in anoxic pore waters. In a subsequent study, Boudreau (1991) successfully reproduced the effect of sulfide oxygenation on the pH gradient at the sediment-water interface of a microbial mat. Additionally, in a comparison study of open and closed-system models, Boudreau and Canfield (1993) illustrated the significance of the oxidation of reduced species (e.g., NH_4^+, H_2S, and HS^-) on the pH distribution at the base of the oxic layer.

Further field studies showed typical trends in pH microprofiles from pore waters of sediments underlying oxic waters and supersaturated with respect to calcite. From coastal to deep-sea sediments, a sharp decrease below the sediment-water interface and a local pH minimum near the oxygen penetration depth are typically observed (e.g., Cai et al., 2000; Wenzhöfer et al., 2001; Pfeifer et al., 2002). With the application of RTMs to pH data from coastal and deep-sea environments, a number of studies interpreted the local pH minimum near the aerobic–anaerobic boundary as the transition from oxic degradation of organic carbon and the reoxidation of reduced species, to the redox cycling of Fe and Mn (Van Cappellen and Wang, 1996; Wenzhöfer et al., 2001).

To illustrate the influence of redox processes on the proton balance and the buffering effect of calcite dissolution induced by redox chemistry, the model described in **Chapter 2** is run to steady state for conditions representative of the deep sea. Figures 1 and 2 (**Chapter 1**) show examples of simulated pH profiles and their response to depositional fluxes of organic carbon and calcite, respectively. Parameters and boundary conditions are mostly from Van Cappellen and Wang (1995) with a flux of calcite from Tsunogai and Noriki (1991).

The results in figure 1 imply that a minimum deposition flux of degradable organic carbon is needed to induce redox cycling of Mn and Fe, which leads to an increase in pH with depth. Once a pH minimum is established, the addition of calcite buffers the drop in pH, but does not alter the location of the pH minimum (figure 2). The buffering provided by the deposition and dissolution of calcite is, however, limited once the pore waters approach equilibrium with respect to calcite. Consistent with observations, figure 3 shows a near-linear correlation between the oxygen penetration depth and the depth of the pH minimum in marine sediments. Figures 1-3 examplify the use of RTMs for the potential application of pH profiles as a diagnostic indicator of processes occurring in marine sediments.
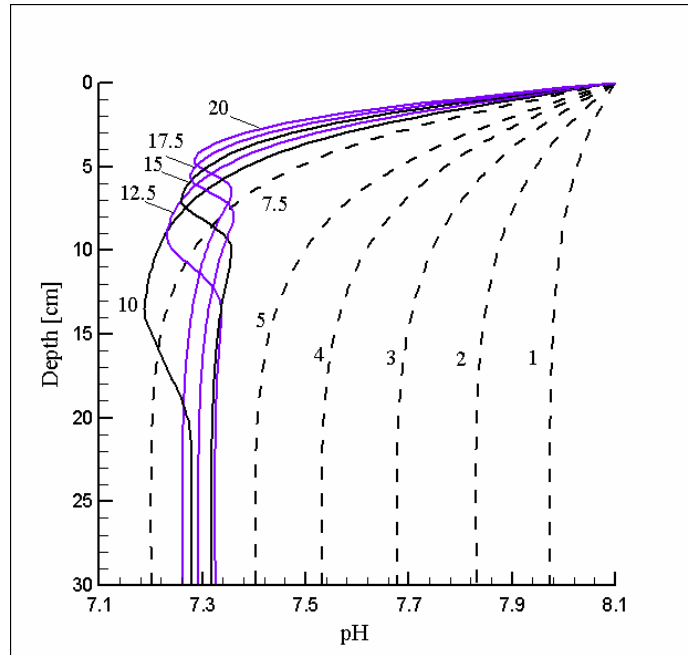
Figure 1: Example simulations of deep-sea pore water pH profiles with varying flux of organic carbon reaching the sediment. The vertical axis corresponds to depth below the water-sediment interface. The imposed organic carbon fluxes range from 1 to 20 μmol/cm^2/a, with the values indicated next to each profile. The flux of calcite is kept constant at 0. Note that for organic carbon deposition fluxes $\geq$ 10 μmol/cm^2/a, the pH depth profile exhibits a characteristic minimum.
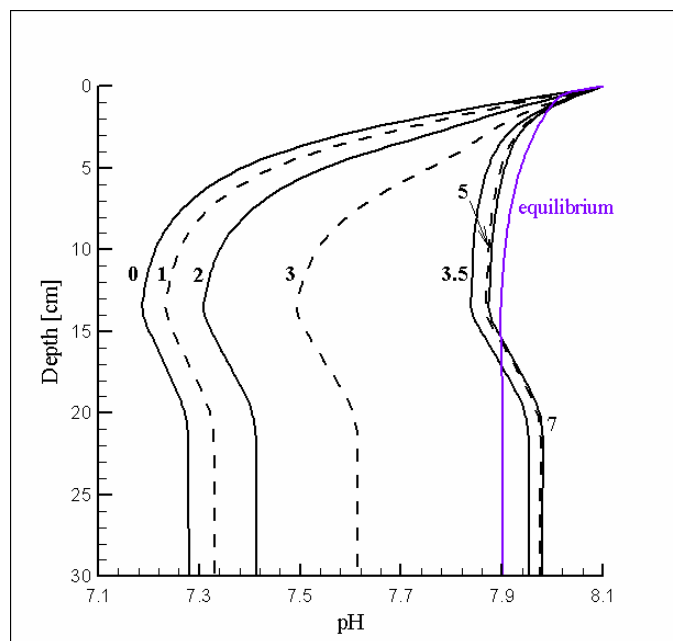
Figure 2: Example simulations of deep-sea pore water pH profiles with varying flux of calcite reaching the sediment. The calcite fluxes range from 0 to 7 μmol/cm^2/a, with the values indicated next to each profile. Also shown is the simulation result when the pore waters are assumed to be in equilibrium with respect to calcite. The deposition flux of organic carbon is kept constant at 10 μmol/cm^2/a. The results illustrate the large buffering of pore water pH by calcite dissolution.

Figure 3: Comparison of oxygen penetration depths and pH minimum depths in deep-sea sediments. The dashed line indicates a 1:1 relationship.

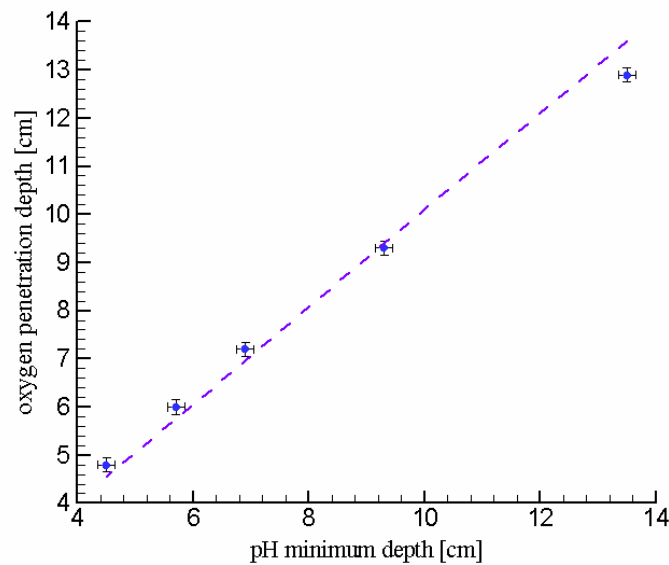In **Chapter 3**, new model developments lead to the calculation of proton production or consumption rates by individual kinetic reactions. This method allows for the quantitative interpretation of commonly observed features of measured pH profiles. The proposed approach also provides a means to interpret the saturation state of pore waters with respect to mineral phases (carbonates, sulfides, oxides), as they are intimately linked to variations in pH.

1.3. Modeling Calcite Dissolution Kinetics

In a modeling study of the global ocean calcite lysocline, Archer (1996) predicts that only 20-30% of the global flux of $CaCO_3$ to the seafloor escapes dissolution, of which roughly half is estimated to occur in the deep sea. Calcite dissolution has long been considered one of the major early diagenetic processes in pelagic sediments (Berner, 1980), whose intensity is greatly influenced by the degradation of organic carbon (e.g., Emerson and Bender, 1981; Jahnke et al., 1994; Wenzhöfer et al., 2001). As suggested by Boudreau and Canfield (1993), the treatment of calcite dissolution/precipitation as an equilibrium process in early diagenetic models leads to the overestimation of the amount of dissolution in undersaturated pore waters. They conclude that accurate modeling of calcite dissolution and its effect on pH requires a kinetic treatment.

Rate expressions for calcite dissolution are generally assumed to be proportional to the degree of undersaturation raised to a power n (Wollast,1990)

$$R = k(1 - \Omega)^n ,$$

where Ω is the saturation state of the aqueous solution with respect to calcite. The constant of proportionality (k) and the reaction rate order (n), however, are not well constrained (Jansen et al., 2002; Hales, 2003). Laboratory studies of dissolution in seawater using biogenic calcites from marine sediments suggest nonlinear rate laws, with $n > 1$ (Keir, 1980; Walter and Morse, 1985; Gehlen et al., 2005). On the other hand, rate orders ranging from 1 to 4.5 have been used in early diagenetic models of calcite dissolution (Cai et al., 1995; Hales and Emerson, 1997; Jahnke et al., 1997).

Rate constants determined for specific sites through parameter fitting range from 0.2%/day to 1000%/day for $n = 4.5$, and from 4×10^{-4}%/day to 0.01%/day for $n = 1$. In several modeling studies, a linear rate law ($n = 1$) results in less variability in the dissolution rate constant, k, when comparing pore water data from multiple locations characterized by variable saturation states of the bottom water (Gehlen et al., 1999; Hales and Emerson, 1997; Mekik et al, 2002). The majority of modeling studies use a rate order of either 1 or 4.5 with the latter being most dominant.

The pH profiles for deep-sea sediments in figures 1 and 2, and for a continental shelf setting in **Chapter 3** are simulated by a dissolution rate law with $n = 4.5$ and $k = 5$%/day. **Chapter 3** considers the effect of two additional scenarios (increasing k to 1000%/day, and assuming a linear rate law with $k = 0.01$%/day) on the resulting pH profile. In **Chapter 4**, the dissolution rate constants are determined by fitting to measured pH profiles using four different values of n (0.5, 1, 2, and 4.5). **Chapter 5** investigates the effect of reaction order through a coupled reaction-transport and compaction model applied to available pH and porosity data.

1.4. Sediment Compaction

Several early diagenetic models have successfully depicted and interpreted biogeochemical processes in marine sediments with the simplifying assumption of constant porosity with depth (Jahnke et al., 1982; Boudreau, 1987; Van Cappellen and Wang, 1996). Yet, a decrease of porosity with depth is an ubiquitous observation in sediments. The observed decrease can often be described by an exponential decay as a function of depth (Van Cappellen and Gaillard, 1996). Rabouille and Gaillard (1991) assessed the effect of near surface compaction on model-calculated organic carbon preservation efficiencies and the depth of oxygen penetration. Their simulation results showed that using a decreasing porosity profile as a forcing variable in the model, instead of constant porosity, leads to higher carbon preservation and a decrease in the oxygen penetration depth. Therefore, more recent RTMs

typically impose an exponentially decaying porosity profile (e.g., Soetaert et al., 1996; Hensen et al., 1997; Wijsman et al., 2002; Canavan et al., 2006).

Although the significance of calcite dissolution in pelagic sediments and its potential effect on sediment compaction have been discussed by Berner (1980), most early diagenetic models do not explicitly account for the distinct effects of physical and chemical compaction on porosity profiles. In a recent study of the effect of compaction and bioturbation on solid tracer profiles, Meysman et al. (2005) postulated that a more general continuum theory, which considers the conservation of mass and momentum, is needed to broaden the currently mass balance-only approach in early diagenetic theory.

Equally important is the development of models that can quantitatively separate the effects of mechanical compaction from mineral dissolution/precipitation on porosity. Combined with the widely available porosity database for sediments, such a model could be used to investigate the rates of mineral reactions that cannot be directly measured. Another potential application of a compaction model is the determination of hydraulic conductivity and elastic response properties of sediments, which can be important from both engineering and ecological perspectives (Dorgan et al. 2005; Dorgan et al., 2006).

In **Chapter 5**, the model of physical and chemical compaction used to compute the porosity and advection velocities of solids and solutes in one dimension is presented. The stand-alone compaction model is used to estimate parameters defining the hydraulic conductivity and elastic response of the sediments through inverse modeling (figure 4). Moreover, an iterative approach is adopted in order to couple a reaction-transport model to the compaction model. The coupled model is then applied to pH and porosity data in order to constrain the calcite dissolution rate order, whose value is a subject of debate (see above; Hales, 2003; Gehlen et al., 2005).
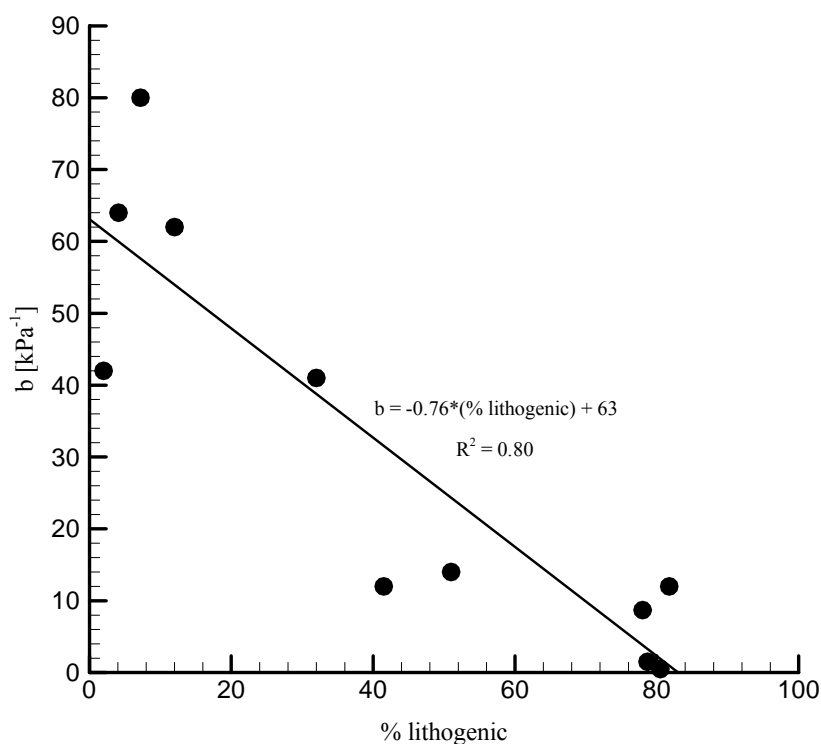
Figure 4: Model estimates of elastic response coefficients determined by fitting to measured porosity profiles from 11 deep-sea sediments vs. the fraction of lithogenic content of the sediments. The results imply lower elastic response coefficients for sediments with higher lithogenic content.

1.5. Thesis Outline

The general aim of this thesis is to advance the modeling of biogeochemical processes during early diagenesis in marine sediments. The first part of the thesis discusses new developments in reaction transport models and presents theoretical tools for the quantitative interpretation of pH distributions (**Chapters 2 and 3**). The second part focuses on the application of RTMs to measured data sets from deep-sea sediments (**Chapters 4 and 5**). The dynamics of calcite dissolution is a common theme throughout the thesis. The last chapter presents a new model of sediment compaction, which is coupled to a RTM. This section provides a more detailed overview of the topics covered in this thesis.

Chapter 2 presents the development and implementation of the Web-distributed Knowledge Base. Starting from the commonality of biogeochemical reaction networks relevant to various Earth surface environments, this flexible modeling framework is applied to systems with contrasting transport regimes. Through transient simulations of a contaminant plume in a groundwater aquifer and early diagenesis in continental shelf sediments, trends in pH in these two redox dominated systems are explored.

The early diagenetic example illustrates an implementation of a model that considers the mechanistic description of organic carbon degradation, including primary and secondary redox reactions, acid/base equilibria, and mineral dissolution/precipitation processes. It provides a basis for the transient simulations of early diagenetic scenarios in which species-specific transport of solutes is included. The pH distributions for both the groundwater and early diagenetic simulations are explained by the proton production and consumption rates, using the method described in **Chapter 3**.

Apart from an accurate determination of pH distributions, efficiency in computational time is a key aspect of early diagenetic models. Efficiency is important not only for coupling to other ocean process models for global studies, but also for parameter estimation routines in quantitative interpretation of data, both of which require numerous simulations with differing reaction parameters and boundary conditions. To this end, we developed a direct steady state solver and used it to simulate pore water pH distributions (**Chapter 3**).

In **Chapter 3**, a new approach to defining kinetic reactions with unknown stoichiometric coefficients leads to a quantitative interpretation of the impact of individual processes shaping the pH distribution at steady state. The rates of proton production and consumption due to individual kinetic reactions are used to study their relative contribution to simulated pH profiles for depositional conditions representative of those encountered on the continental shelf. The role of sulfate reduction in controlling the calcite saturation state is investigated, by explicitly computing the rate at which carbonate ions are produced or consumed by sulfate reduction. Model simulations are also used to determine the response of pH to variations in calcite dissolution kinetics and irrigation intensities.

The RTM developed in **Chapter 3** is applied to 13 data sets of oxygen and pH microelectrode profiles measured in deep-sea sediments (**Chapter 4**). In a systematic and data-driven approach, the model is fitted to the measured profiles in order to quantify organic matter loading and reactivity, as well as the role of calcite dissolution on pore water pH. Four different rate laws for calcite dissolution are considered, and the simulation results are used to explore the relationship between the integrated rate of calcite dissolution and the benthic oxygen uptake flux.

Mineral dissolution and precipitation reactions, and in particular calcite dissolution, can induce porosity changes or chemical compaction in deep-sea sediments. Available porosity data can therefore yield additional information on the extent of mineral reaction processes, provided that the effects of physical compaction are accounted for. To assess the relative

roles of mechanical compaction and mineral reactions, a steady state compaction model based on the conservation of mass and momentum is developed (**Chapter 5**). The developed model accounts for the effect of mineral dissolution and precipitation reactions on changes in the pore volume, and is parameterized by the elastic response and hydraulic conductivity properties of the sediment.

First, the compaction model is used to examine the relationship between the physical properties and sediment composition (figure 4). Next, the effect of chemistry at three sites with available mineral dissolution rates (calcite and silica) are evaluated. The compaction model is then coupled to the RTM described in **Chapters 3 and 4** for the parallel simulation of pH and porosity. The coupled model is applied to a set of pH and porosity data to further constrain the most appropriate form of the calcite dissolution rate law.

References

Archer D., Emerson S., and Reimers C. (1989) Dissolution of calcite in deep-sea sediments: pH and O_2 microelectrode results. *Geochimica et Cosmochimica Acta* **53**, 2831-2845.

Archer D. and Maier-Reimer E. (1994) Effect of deep-sea sedimentary calcite preservation on atmospheric CO_2 concentration. *Nature* **367**, 260-263.

Archer D. E. (1996) An atlas of the distribution of calcium carbonate in sediments of the deep sea. *Global Biogeochemical Cycles* **10**, 159-174.

Arndt S., Vanderborght J.-P., and Regnier P. (2007) Diatom growth response to physical forcing in a macrotidal estuary: Coupling hydrodynamics, sediment transport, and biogeochemistry. *Journal of Geophysical Research* **112**, C05045, doi:10.1029/2006JC003581.

Ben-Yaakov S. (1973) pH buffering of pore water of recent anoxic marine sedimnets. *Limnology and Oceanography* **18**, 86-94.

Berner R. A. (1980) Early diagenesis: a theoretical approach, 250 pp., Princeton University Press, Princeton.

Boudreau B. P. (1987) A steady-state diagenetic model for dissolved carbonate species and pH in the porewaters of oxic and suboxic sediments. *Geochimica et Cosmochimica Acta* **51**, 1985-1996.

Boudreau B. P. and Canfield D. E. (1988) A provisional diagenetic model for pH in anoxic porewaters: Application to the FOAM site. *Journal of Marine Research* **46**, 429-455.

Boudreau B. P. (1991) Modelling the sulfide-oxygen reaction and associated pH gradients in porewaters. *Geochimica et Cosmochimica Acta* **55**, 145-159.

Boudreau B. P. and Canfield D. E. (1993) A comparison of closed- and open-system models for porewater pH and calcite-saturation state. *Geochimica et Cosmochimica Acta* **57**, 317-334.

Boudreau B. P. (1997) *Diagenetic models and their implementation: modelling transport and reactions in aquatic sediments*. 414 pp., Springer-Verlag, Berlin.

Broecker W. S. and Peng T. H. (1987) The role of $CaCO_3$ compensation in the glacial to interglacial atmospheric CO_2 change. *Global Biogeochemical Cycles* **1**, 15-29.

Cai W.-J. and Reimers C. E. (1993) The development of pH and P_{CO2} microelectrodes for studying the carbonate chemistry of pore waters near the sediment-water interface. *Limnology and Oceanography* **38**, 1762-1773.

Cai W.-J., Reimers C. E., and Shaw T. (1995) Microelectrode studies of organic carbon degradation and calcite dissolution at a California Continental rise site. *Geochimica et Cosmochimica Acta* **59**, 497-511.

Cai W.-J., Zhao P., and Wang Y. (2000) pH and pCO$_2$ microelectrode measurements and the diffusive behavior of carbon dioxid species in coastal marine sediments. *Marine Chemistry* **70**, 133-148.

Canavan R. W., Slomp C. P., Jourabchi P., Van Cappellen P., Laverman A. M., and van den Berg G. A. (2006) Organic matter mineralization in sediment of a coastal freshwater lake and response to salinization. *Geochimica et Cosmochimica Acta* **70**, 2836-2855.

Dorgan K. M., Jumars P. A., Johnson B., Boudreau B. P., and Landis E. (2005) Burrow extension by crack propagation. *Nature* **433**, 475.

Dorgan K. M., Jumars P. A., Johnson B. D., and Boudreau B. P. (2006) Macrofaunal burrowing: the medium is the message. *Oceanography and Marine Biology: An Annual Review* **44**, 85-121.

Emerson S. and Bender M. (1981) Carbon fluxes at the sediment-water interface of the deep sea: calcium carbonate preservation. *Journal of Marine Research* **39**, 139-162.

Fisher J. B. and Matisoff G. (1981) High resolution vertical profiles of pH in recent sediments. *Hydrobiologia* **79**, 277-284.

Gehlen M., Mucci A., and Boudreau B. (1999) Modelling the distribution of stable carbon isotopes in porewaters of deep-sea sediments. *Geochimica et Cosmochimica Acta* **63**, 2763-2773.

Gehlen M., Bassinot F. C., Chou L., and McCorkle D. (2005) Reassessing the dissolution of marine carbonates: II. Reaction kinetics. *Deep-Sea Research I* **52**, 1461-1476.

Gray W. G., Leijnse A., Kolar R. L., and Blain C. A. (1993) *Mathematical tools for changing spatial scales in the analysis of physical systems*. 256 pp., CRC Press, London.

Hales B. and Emerson S. (1997) Evidence in support of first-order dissolution kinetics of calcite in seawater. *Earth and Planetary Science Letters* **148**, 317-327.

Hales B. (2003) Respiration, dissolution, and the lysocline. *Paleooceanography* **18**, doi:10.1029/2003PA000915.

Hassanizadeh S. M. (1986) Derivation of basic equations of mass transport in porous media; Part I. Macroscopic balance laws. *Advances in Water Resources* **9**, 196-206.

Hensen C., Landenberger H., Zabel M., Gundersen J. K., Glud R. N., and Schulz H. D. (1997) Simulation of early diagenetic processes in continental slope sediments off southwest Africa: the computer model CoTAM tested. *Marine Geology* **144**, 191-210.

Jahnke R. A., Emerson S. R., and Murray J. W. (1982) A model of oxygen reduction, denitrification, and organic matter mineralization in marine sediments. *Limnology and Oceanography* **27**(4), 610-623.

Jahnke R. A., Craven D. B., and Gaillard J.-F. (1994) The influence of organic matter diagenesis on $CaCO_3$ dissolution at the deep-sea floor. *Geochimica et Cosmochimica Acta* **58**, 2799-2809.

Jahnke R. A., Craven D. B., McCorkle D. C., and Reimers C. E. (1997) $CaCO_3$ dissolution in California continental margin sediments: The influence of organic matter remineralization. *Geochimica et Cosmochimica Acta* **61**, 3587-3604.

Jansen H., Zeebe R. E., and Wolf-Gladrow D. A. (2002) Modeling the dissolution of settling $CaCO_3$ in the ocean. *Global Biogeochemical Cycles* **16**, doi: 10.1029/2000GB001279.

Katsev S., Rancourt D. G., and L'Heureux I. (2004) dSED: a database tool for modeling sediment early diagenesis. *Computers & Geosciences* **30**, 959-967.

Keir R. S. (1980) The dissolution kinetics of biogenic calcium carbonates in seawater. *Geochimica et Cosmochimica Acta* **44**, 241-252.

Kleypas J. A., Feely R. A., Fabry V. J., Langdon C., Sabine C. L., and Robbins L. L. (2006) Impacts of ocean acidification on coral reefs and other marine calcifiers: A guide for

future research. In *report of a workshop held 18-20 April 2005*, 88 pp.. NSF, NOAA, and the U. S. Geological Survey.

Luff R., Haeckel M., and Wallmann K. (2001) Robust and fast FORTRAN and MATLAB® libraries to calculate pH distributions in marine systems. *Computers & Geosciences* **27**, 157-169.

Maher K., Steefel C. I., DePaolo D. J., and Viani B. E. (2006) The mineral dissolution rate conundrum: Insights from reactive transport modeling of U isotopes and pore fluid chemistry in marine sediments. *Geochimica et Cosmochimica Acta* **70**, 337-363.

Mayer K. U., Frind E. O., and Blowes D. W. (2002) Multicomponent reactive transport modeling in variably saturated porous media using a generalized formulation for kinetically controlled reactions. *Water Resources Research* **38**, doi:10.1029/2001WR000862.

Mekik F. A., Loubere P. W., and Archer D. E. (2002) Organic carbon flux and organic carbon to calcite flux ratio recorded in deep-sea carbonates: Demonstration and a new proxy. *Global Biogeochemical Cycles* **16**, 1052.

Metz B., Davidson O., Coninck H. d., Loos M., and Meyer L. (2005) *IPCC special report on carbon dioxide capture and storage*. 440 pp., Cambridge University Press, Working Group III, New York.

Meysman F. J. R., Middelburg J. J., Herman P. M. J., and Heip C. H. R. (2003) Reactive transport in surface sediments. II. Media: an object-oriented problem-solving environment for early diagenesis. *Computers & Geosciences* **29**, 301-318.

Meysman F. J. R., Boudreau B. P., and Middelburg J. J. (2005) Modeling reactive transport in sediments subject to bioturbation and compaction. *Geochimica et Cosmochimica Acta* **69**, 3601-3617.

Murray J. W., Emerson S., and Jahnke R. (1980) Carbonate saturation and the effect of pressure on the alkalinity of interstitial waters from the Guatemala Basin. *Geochimica et Cosmochimica Acta* **44**, 963-972.

Pfeifer k., Hensen C., Adler M., Wenzhöfer F., Weber B., and Schulz H. D. (2002) Modeling of subsurface calcite dissolution, including the respiration and reoxidation processes of marine sediments in the region of equatorial upwelling off Gabon. *Geochimica et Cosmochimica Acta* **66**, 4247-4259.

Plumb O. A. and Whitaker S. (1990) Diffusion, adsorption and dispersion in porous media: small-scale averaging and local volume averaging. In *Dynamics of fluids in hierarchical porous media* (ed. J. H. Cushman), 97-148. Academic Press, San Diego, Ca.

Rabouille C. and Gaillard J.-F. (1991) A Coupled Model Representing the Deep Sea Organic Carbon Mineralization and Oxygen Consumption in Surficial Sediments. *Journal of Geophysical Research* **96**, 2761-2776.

Regnier P., O'Kane J. P., Steefel C. I., and Vanderborght J. P. (2002) Modelling complex multi-component reactive-transport systems: towards a simulation environment based on the concept of a Knowledge Base. *Applied Mathematical Modelling* **26**, 913-927.

Regnier P., Jourabchi P., and Slomp C. P. (2003) Reactive-Transport modeling as a technique for understanding coupled biogeochemical processes in surface and subsurface environments. *Netherlands Journal of Geosciences* **82**, 5-18.

Saripalli K. P., Freedman V. L., McGrail B. P., and Meyer P. D. (2006) Characterization of the specific solid-water interfacial area-water saturation relationship and its import to reactive transport. *Vadose Zone Journal* **5**, 777-783.

Sayyed-Ahmad A., Tuncay K., and Ortoleva P. J. (2003) Toward automated cell model development through information theory. *Journal of Physical Chemistry A* **107**, 10554-10565.

Soetaert K., Herman P. M. J., and Middelburg J. J. (1996) Dynamic response of deep-sea sediments to seasonal variations: a model. *Limnology and Oceanography* **41**, 1651-1668.

Steefel C. I. (2001) Software for modeling multicomponent, multidimensional reactive transport. Lawrence Livermore National Laboratory, Livermore, Ca. UCRL-MA-143182.

Steefel C. I., DePaolo D. J., and Lichtner P. C. (2005) Reactive transport modeling: An essential tool and a new research approach for the Earth sciences. *Earth and Planetary Science Letters* **240**, 539-558.

Tsunogai S. and Noriki S. (1991) Particulate fluxes of carbonate and organic carbon in the ocean. Is the marine biological activity working as a sink of the atmospheric carbon? *Tellus* **43B**, 256-266.

Van Cappellen P. and Wang Y. (1995) Metal cycling in surface sediments: modelling the interplay of transport and reaction. In *Metal Contaminated Sediments* (ed. H. E. Allen), 21-62. Ann Arbor Press, Chelsea, MI.

Van Cappellen P. and Gaillard J.-F. (1996) Biogeochemical dynamics in aquatic sediments. In *Reactive transport in porous media*, (ed. P. C. Lichtner, C. I. Steefel, and E. H. Oelkers) pp. 335-376, Reviews in Mineralogy, volume 34, Mineralogical Society of America, Washington DC.

Van Cappellen P. and Wang Y. (1996) Cycling of iron and manganese in surface sediments: a general theory for the coupled transport and reaction of carbon, oxygen, nitrogen, sulfur, iron, and manganese. *American Journal of Science* **296**, 197-243.

Walter L. M. and Morse J. W. (1985) The dissolution kinetics of shallow marine carbonates in seawater: A laboratory study. *Geochimica et Cosmochimica Acta* **49**, 1503-1513.

Wijsman J. W. M., Herman P. M. J., Middelburg J. J., and Soetaert K. (2002) A model for early diagenetic processes in sediments of the continental shelf of the Black Sea. *Estuarine, Coastal and Shelf Science* **54**, 403-421.

Wenzhöfer F., Adler M., Kohls O., Hensen C., Strotmann B., Boehme S., and Schulz H. D. (2001) Calcite dissolution driven by benthic mineralization in the deep sea: In situ measurements of Ca^{2+}, pH, pCO_2, and O_2. *Geochimica et Cosmochimica Acta* **65**, 2677-2690.

Wollast R. (1990) Rate and mechanism of dissolution of carbonates in the system $CaCO_3$-$MgCO_3$. In *Aquatic chemical kinetics: reaction rates of processes in natural waters* (ed. W. Stumm), 431-445. Wiley, New York.

Chapter 2

A knowledge-based reactive transport approach for the simulation of biogeochemical dynamics in Earth systems

Abstract

A Knowledge-Based Reactive Transport Model (KB-RTM) for simulation of coupled transport and biogeochemical transformations in surface and subsurface flow environments is presented (http://www.geo.uu.nl/kbrtm). The scalable Web-distributed Knowledge Base (KB), which combines Information Technology (IT), an automatic code generator, and database management, facilitates the automated construction of complex reaction networks from comprehensive information stored at the level of biogeochemical processes. The reaction-centric approach of the KB-RTM system offers full flexibility in the choice of model components and biogeochemical reactions. The procedure coupling the reaction networks to a generalized transport module into RTMs is also presented. The workings of our KB-RTM simulation environment are illustrated by means of two examples of redox and acid-base chemistry in a typical shelf sediment and an aquifer contaminated by landfill plumes.

1. Introduction

Reactive transport models (RTMs) are powerful tools for capturing the dynamic interplay between fluid flow, constituent transport, and biogeochemical transformations [Steefel and Van Cappellen, 1998]. They have been used to simulate, among others, rock weathering and soil formation [e.g., Ayora et al., 1998; Soler and Lasaga, 1998; Steefel and Lichtner, 1998a, 1998b; Thyne et al., 2001; Soler, 2003; De Windt et al., 2004], nutrient dynamics in river drainage basins and estuaries [e.g., Soetaert and Herman, 1995; Billen et al., 1994; Regnier et al., 1997; Regnier and Steefel, 1999; Vanderborght et al., 2002], reactive transport in groundwater, like contamination of aquifers [e.g., Engesgaard and Traberg,1996; Brown et al., 1998; Hunter et al., 1998; Xu et al.,1999; Murphy and Ginn, 2000; Barry et al., 2002; Brun and Engesgaard, 2002; Thullner et al., 2004; van Breukelen et al., 2004], early diagenetic transformations in sediments [e.g., Soetaert et al., 1996; Boudreau, 1996; Van Cappellen and Wang, 1996; Dhakar and Burdige, 1996; Berg et al., 2003; Jourabchi et al., 2005], benthic-pelagic coupling in ocean systems [e.g., Soetaert et al., 2000; Archer et al., 2002; Lee et al., 2002] and hydrocarbon migration and maturation in sedimentary basins [e.g., Person and Garven, 1994]. By integrating experimental, observational and theoretical knowledge about geochemical, biological and transport processes into mathematical formulations, RTMs provide the grounds for prognosis, while diagnostic comparison between model simulations and measurements can help identify gaps in the conceptual understanding

of a specific system or uncertainties in proper parameterization of biogeochemical processes [Berg et al., 2003; Jourabchi et al., 2005].

RTMs have traditionally been developed and used to investigate the fate and transport of a selected set of chemical constituents within a given compartment of the Earth system (e.g., the early diagenetic models by Soetaert et al. [1996], Boudreau [1996], Van Cappellen and Wang [1996], Dhakar and Burdige [1996], and references cited above). As a result, they have tended to be environment and application specific with regards to the flow regime and the biogeochemical reaction network.

Although the first attempts to develop interactive software systems for automatic solution of models based on ordinary and partial differential equations date back to the creation of digital computers [e.g., Young and Juncosa, 1959; Lawrence and Groner, 1973; Mikhailov and Aladjem, 1981, and references therein], such developments have so far received little attention in the field of reactive-transport modeling. Literature review shows that RTM codes allowing for more flexible definition of state variables and processes without requiring in-depth knowledge of programming or numerical solution techniques have been developed over the last decade [e.g., Reichert, 1994; Chilakapati, 1995; Regnier et al., 1997; Chilakapati et al., 2000; MacQuarrie et al., 2001; Meysman et al., 2003a, 2003b; Van der Lee et al., 2003]. Database tools, such as that developed by Katsev et al. [2004], have also been presented recently to the reactive transport community. Model flexibility is a critical feature since a major challenge in the field of reactive transport modeling is the realistic representation of the highly complex reaction networks (RN) that characterize the biogeochemical dynamics of natural environments [e.g., Mayer et al., 2002; Berg et al., 2003; Quezada et al., 2004]. At the same time, many field-and laboratory-based experiments are also being conducted to identify novel reaction pathways, quantify reaction rates and microbial activity levels, describe ecological community structures, and elucidate interactions between biotic and abiotic processes. This rapidly growing knowledge about biogeochemical transformation processes creates a need for efficient means of transferring new experimental findings into RTMs.

Here, a unified modeling approach for implementing complex reaction networks in RTMs is presented. Our simulation environment is based on a modular approach to facilitate incorporation of new theoretical and experimental information on the rates and pathways of biogeochemical reactions. The key novel feature of the modeling environment is a Web-distributed Knowledge Base (KB) of biogeochemical processes, which acts as the evolving repository of up-to-date information gained in the field of geochemistry. The implementation

of such a library within a simulation environment is a major step toward the model's flexibility, because it is at the level of an easily accessible open resource, the KB, that process-based theoretical and experimental advances are incorporated in the modeling process. Model generation is conducted via a graphical user interface (GUI) on a Web-based ''runtime'' server, which allows for the development of biogeochemical reaction network modules. That is, information stored at the level of individual biogeochemical processes can be combined into mathematical expressions defining completely the (bio)chemical dynamics of the system. Since the reaction network is assembled from information stored at the process level, almost any conceivable combination of mixed kinetic and equilibrium reactions can be implemented in our model architecture. The selected RN can easily be merged with existing transport models, hence creating a flexible framework in which to assemble RTMs. The proposed approach allows the RTM community to test and compare, in close collaboration with experimentalists, alternative mathematical descriptions of coupled biogeochemical reaction networks. For example, increasingly detailed representations of biogeochemical processes can be incorporated in the Knowledge Base. Reaction network modules of increasing complexity may then be assembled and coupled to surface or subsurface flow models, in order to determine which level of biogeochemical complexity is adequate to simulate chemical system dynamics at variable spatial and temporal resolutions. By taking a ''reaction-centric'' approach which utilizes the unifying conceptual and mathematical principles underlying all RTMs, one-dimensional (1D) transport descriptions relevant to many compartments of the Earth system (rivers, estuaries, groundwater or sediments) can be incorporated in our simulation environment. The proposed approach should thus help overcome traditional disciplinary barriers between the different subfields of RTMs.

The paper is structured as follows: First, the mass conservation equation describing 1D coupled transport and reaction is briefly presented. A generalized continuum representation is proposed, which allows for the simulation of reactive-transport problems characterized by different flow regimes and dispersion intensities. A brief description on how an existing Automatic Code Generator (ACG) based on symbolic programming [Regnier et al., 2002] can be used to create the model specific source code necessary to the numerical solution of the governing equations is then given. We demonstrate how our Web-distributed Knowledge Base concept, which combines Information Technology with symbolic computing techniques, directs the mathematical formulation of the biogeochemical reaction network and leads to a modeling environment offering full flexibility. Finally, the workings of our KB-

RTM are illustrated with two contrasting examples of complex redox and acid-base geochemistry in an aquatic sediment and an aquifer, respectively.

2. Mathematical Representation of Reactive-Transport Equations

A one-dimensional continuum representation of coupled mass transport and chemical reactions in Earth systems can be described mathematically by a set of partial differential equations (PDEs) in time and space of the form

$$\xi \frac{\partial C_j}{\partial t} = \underbrace{\left[\frac{\partial}{\partial x}\left(D \cdot \xi \cdot \frac{\partial C_j}{\partial x} \right) - \frac{\partial}{\partial x}\left(v \cdot \xi \cdot C_j \right) \right]_j}_{T} + \underbrace{\sum_{k=1}^{N_r} \lambda_{k,j} \cdot \sigma_k}_{R}; \quad j = 1,...,m, \tag{1}$$

where t is time and x denotes the position along the 1D spatial domain. Particular solutions of equation (1) require specification of initial and boundary conditions. Further discussion about the generalized continuum representation of the advection-dispersion-reaction (ADR) equation is given by Regnier et al. [2002] and Meile [2003]. The first two terms on the right hand side, in square brackets, compose the transport operator (T); the last one (R) represents the sum of transformation processes (e.g., reactions) affecting a species j of concentration C_j. Table 1 shows that ξ, D and v are generic variables which take different meanings depending on the environment considered. σ_k represents, for kinetic reactions, the rate of the k-th reaction and $\lambda_{k,j}$ is the stoichiometric coefficient of species j in that reaction. Currently, it is assumed that the reaction processes (R) have no effect on the physical or transport (T) properties of the system (i.e., ξ, D and v are unaffected by reactions). The rate σ_k is of arbitrary form, even nonlinear, and can be a function of several concentrations of the system. Through this coupling by the reaction terms, most multicomponent problems result in a set of coupled nonlinear partial differential equations (PDEs) of size m, number of species of the reaction network. In the event that some of the reactions considered are assumed to be at equilibrium, algebraic expressions based on mass action laws are introduced into the system of equations to be solved [Regnier et al., 2002]. By replacing one or more of the m differential equations associated with reactions with algebraic relations based on a mass action expression in the local equilibrium case, the set of ODEs is transformed into a set of differential-algebraic equations (DAEs) [Chilakapati, 1995; Hindmarsh and Petzold, 1995a, 1995b; Brenan et al., 1989]. This transformation leads to a system of m equations to solve, including m_k equations associated with kinetic reactions, and m_e algebraic equations based on mass action expressions.

Table 1. Meaning of the Generalized Variables ξ, D, and v for Different Environments[a]

	Surface Flow	Aquatic Sediment		Groundwater Flow Path	
	Solutes or Suspended Solids	Solids	Solutes	Solids	Solutes
ξ	A	$1-\phi$	ϕ	$1-\phi$	ϕ
v	V_{flow}	ω	$\omega + v_{flow}$	0	V_{flow}
D	K_{turb}	D_b	$D_b + D_{sed}$	0	D_{disp}

[a] From *Meile* [2003]. In porous media flow, distinction between an aqueous and a solid phase must be considered, and C is either a concentration of solute or solid. $A[\mathrm{L}^2]$, cross-section area of the surface flow channel; ϕ [−], porosity; $V_{flow}[\mathrm{LT}^{-1}]$, externally imposed flow velocity; $\omega[\mathrm{LT}^{-1}]$, burial velocity defined with respect to the sediment-water interface (SWI); $v_{flow}[\mathrm{LT}^{-1}]$, flow velocity acting only on solutes externally imposed or from porosity change; usually defined with respect to the SWI [e.g., *Boudreau*, 1997]; $K_{turb}[\mathrm{L}^2\mathrm{T}^{-1}]$, longitudinal turbulent dispersion coefficient; $D_b[\mathrm{L}^2\mathrm{T}^{-1}]$, bioturbation coefficient; $D_{sed}[\mathrm{L}^2\mathrm{T}^{-1}] = D_{mol}/(1 - \ln(\phi^2))$, tortuosity corrected molecular diffusion coefficient for solutes at in situ temperature and salinity [*Boudreau*, 1997]; $D_{disp}[\mathrm{L}^2\mathrm{T}^{-1}] = \alpha_L \cdot |V_{flow}|$, longitudinal dispersion, where α_L [L] is the longitudinal dispersivity [*Freeze and Cherry*, 1979].

The numerical solution of the set of discretized PDEs and DAEs ($\partial t \rightarrow \Delta t, \partial x \rightarrow \Delta x$) commonly requires the use of implicit methods in order to be computationally efficient [Steefel and MacQuarrie, 1996]. We currently make use of the time splitting technique, which consists of solving first the transport and then the reaction terms in sequence for a single time step. This method is referred to as the sequential noniterative approach (SNIA). When solving the reaction part an iterative method is required to numerically find the roots of the function residuals, f_j, which correspond to mass balance equations and, if equilibrium reactions are included, mass action equations. This is because the reaction terms can be nonlinear functions of the species concentrations. By far the most common approach for finding the root of nonlinear sets of equations is the Newton-Raphson method [Press et al., 1992]. This method involves the use of a first degree Taylor series expansion to linearize the problem for every single iteration step. The function residuals, f_j, representing the reaction network (RN), and the Jacobian matrix, which contains the partial derivatives of the function residuals with respect to the unknown concentrations, are the most important pieces of information required to implement the Newton-Raphson algorithm [e.g., Dennis and Schnabel, 1996]. Once linearized, the resulting problem is solved using linear algebra

methods, such as the LU decomposition [e.g., Strang, 1988]. A precise definition of the function residuals and the Jacobian matrix is given by Regnier et al. [2002].

3. Reactive Transport Modeling With the Knowledge Base

Inspection of the transport and reaction operators T and R in equation (1) shows that the following information is required to define a specific reaction transport application:

1. Domain definition: spatiotemporal size and resolution (x_{tot}, Δx, t_{tot}, Δt), where x_{tot} and t_{tot} stand for the total domain length and simulation time, respectively, and Δx and Δt are the space and time step used for numerical integration, respectively.

2. Transport coefficients ξ, v and D (Table 1).

3. Reaction Network (RN): processes; rate parameters and equilibrium constants; species involved and stoichiometry.

4. Boundary (BC) and initial (IC) conditions for every species of the RN.

In a modeling environment offering full flexibility, this information is specific to each RTM application and needs to be automatically translated into source code. This task is relatively easy for the physical domain definition, transport parameters, BC and IC. However, if flexibility in choosing process formulations is also important, then the stiff system of differential equations using a linearization method (such as the above-cited Newton-Raphson algorithm) necessitate automatic differentiation schemes for the calculation of the terms in the Jacobian matrix. Automatic symbolic differentiation offers the advantage of producing derivatives of potentially complicated functions which are accurate up to the precision of the programming language used (e.g., FORTRAN), plus the convenience of updating the derivatives easily if the original functions are changed [Steefel and MacQuarrie, 1996]. Automated differentiation for stiff sets of differential equations is one of the key features of our Automatic Code Generation (ACG) procedure [Regnier et al., 2002].

The simultaneous implementation of a library of biogeochemical processes into a Knowledge Base (KB) is an additional crucial component of the proposed simulation environment. The KB makes it possible to take full advantage of the ACG. The integration of these two components within a Web system shows how the combination of Information Technology with advanced symbolic programming allows the use of the Internet as a software provider in the area of Reactive-Transport modeling (Figure 1).

3.1. The Internet as a Software Provider

An Internet system developed in PHP language (http://www.php.net) provides the adaptive JavaScript and HTML code for the Graphical User Interface (GUI), as well as the Web-based ''runtime'' server to our modeling environment. It is accessible at http://www.geo.uu.nl/kbrtm. The GUI is of evolutionary nature, that is, it dynamically adapts to changes in structure and content of the KB system as well as to the selections made by the user.

Initially, the user accesses an interface for the KB system in the style of a Web form for selection of desired biogeochemical processes (Figure 1, step 1; further detailed in Figure 2). Species-independent physical parameters (definition of spatiotemporal domain and most transport coefficients in Table 1) are also defined at this stage.
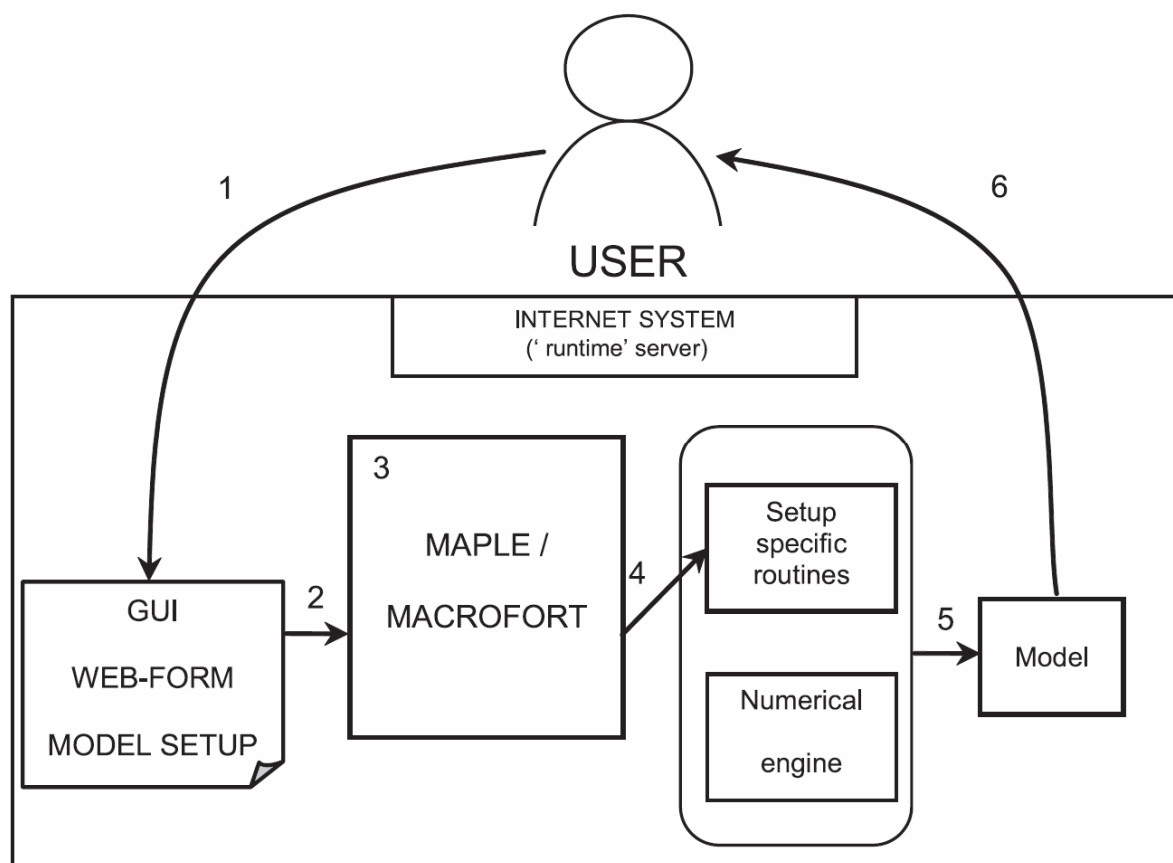

Figure 1. Structure of the Knowledge-Based (KB) Reactive Transport Model (RTM) environment which uses the Web as a software provider: 1, form submission; 2, parsing of the ASCII files into MAPLE; 3, MAPLE/MACROFORT symbolic computing; 4, translation of MAPLE results into FORTRAN; 5, linking and compilation of the FORTRAN code; 6, transfer of the executable file to the user via e-mail.

Figure 2 gives a detailed description of the model design procedure. The KB system consists of a set of biogeochemical processes, containing default formulations for reactions, which are available to all users of the system (common KB) and which cannot be modified.

However, these common processes can be edited if desired, or new processes created using a standard template, and stored in a ''private'' KB library which is inaccessible to other users. To facilitate model development, processes can be grouped in different subsets, for instance, in terms of reaction types (see below).
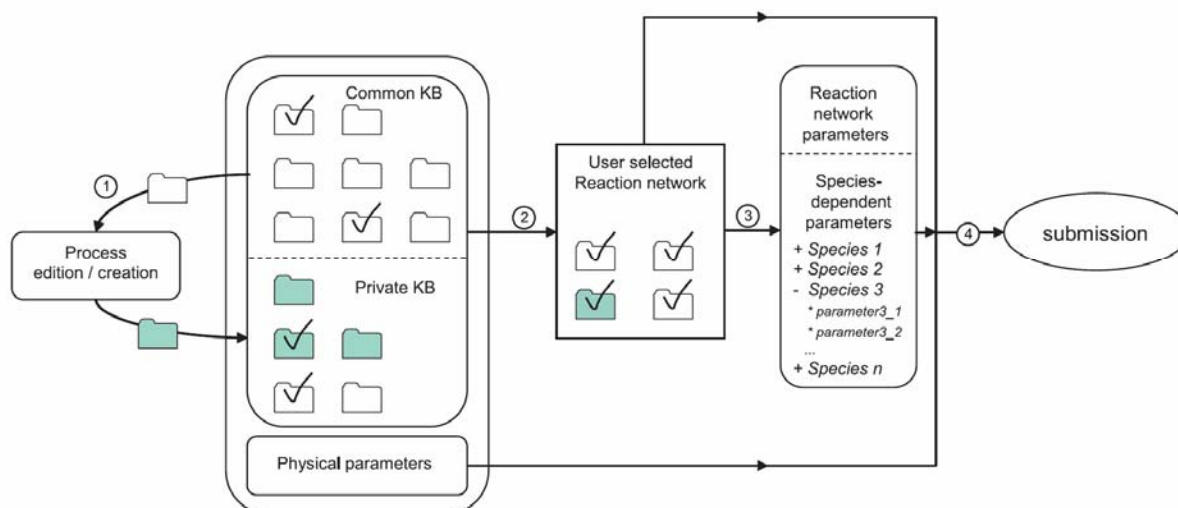

Figure 2. KB-Internet model design process (detailed description of step 1 in Figure 1): (1) Process edition or creation. Templates can be used to speed up the implementation of new processes. Modified or new process files are stored in a ''private'' KB which is accessible only to a single user. (2) Process selection from the common and private KB process pools, and specification of the physical support. (3) Analysis of the selection and creation of a dynamically adaptive Web form to input reaction network dependent parameters. (4) Submission of complete model information (processes selected, physical parameters, and species-dependent parameters) to the ACG via our Web server.

The selected processes specify the user-defined reaction network. The latter is then analyzed to determine the list of chemical species involved in the RN. A second Web submission form is subsequently created to specify all species-dependent parameters (such as molecular diffusion coefficients, initial and boundary conditions). At this stage, default parameter values for reaction dynamics expressions can also be modified. All model settings can be stored on the server and used again or modified in future modeling sessions.

3.2. Knowledge Base (KB)

The common KB (Figure 2) contains subsets of biogeochemical process libraries and parameter values, including default formulations for biogeochemical reaction rates and equilibria. The design provides an expandable structure permitting the easy addition of new elements (processes, variables, parameters) into a ''private'' KB library. Several formulations can be implemented for the same biogeochemical process, simply by naming the respective process files differently. This permits a ready-made set of specialized process descriptions for

a number of different scenarios, and therefore the formulation that best fits the simulation requirements can be selected.

The biogeochemical processes currently implemented are distributed among the following classes, which form the architecture of our KB: primary redox reactions (PRR) involving organic matter oxidation pathways, secondary redox processes (SRR, biotic and abiotic redox reactions), aqueous complex formation (ACF), homogeneous acid-base equilibrium reactions (ABE), nonredox mineral precipitation and dissolution (MPD), adsorption and ion exchange (AIE) and gas-water reactions (GWR). These classes represent only one of the many possible categorizations. In fact, model specific categories can be added to the system. According to different criteria, one process could be assigned not solely to one, but potentially to several classes.

The file structure for each process consists of the set of species (dissolved or solid) involved in the specific process, the definition of the reaction type (kinetic or equilibrium) and the stoichiometry. The corresponding rate or mass action law and default parameter values are also specified. Fields of informative nature (e.g., reaction class, keywords for searching, documentation, units for parameters and concentrations) complete the process file description. As an example, Figure 3 shows the process file for aerobic degradation of organic matter as an example. Finally, the set of variables and parameters for the entire selection of process files, along with the respective functions characterizing kinetic or equilibrium processes and their corresponding stoichiometries, fully determine the RN.
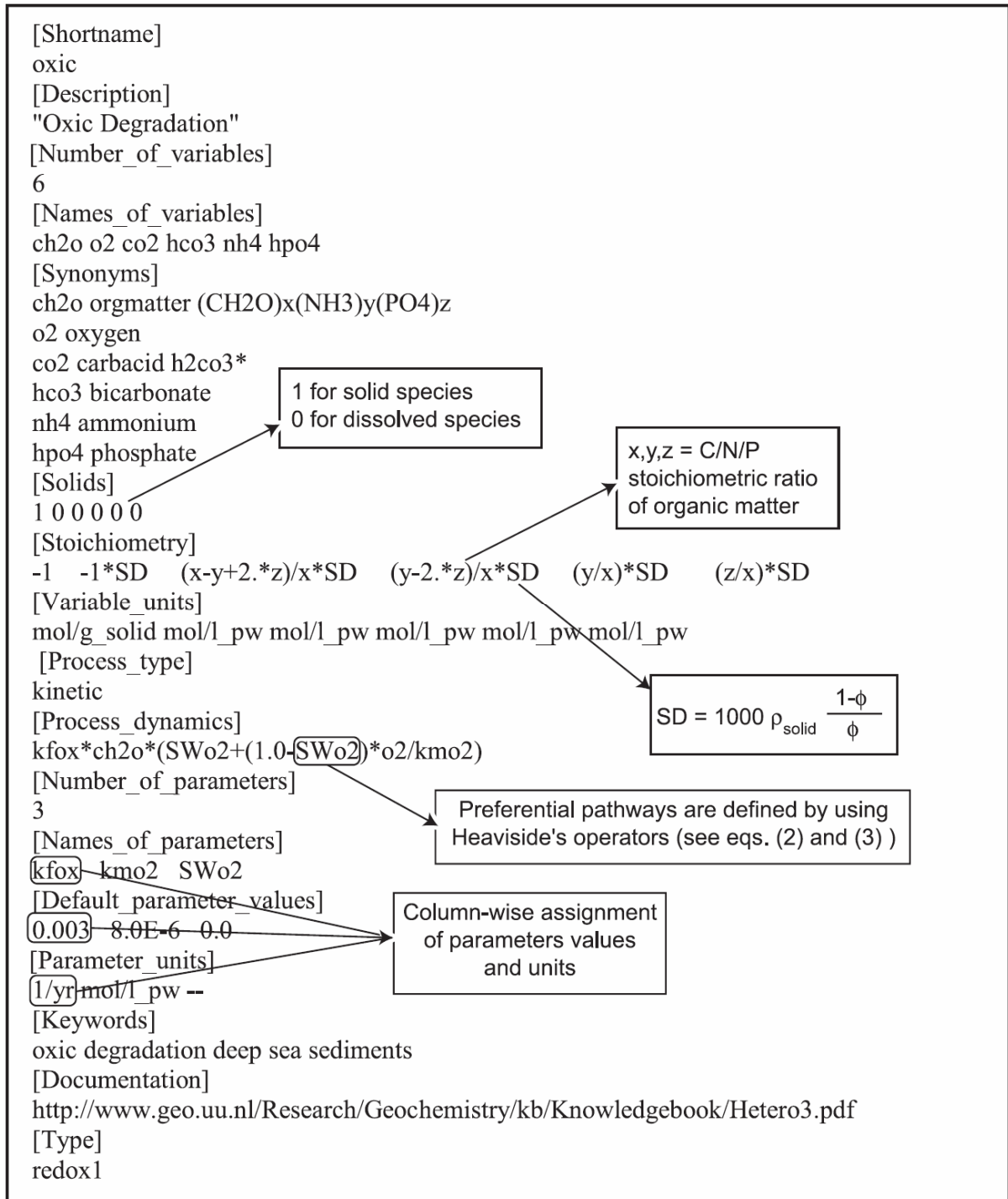
```
[Shortname]
oxic
[Description]
"Oxic Degradation"
[Number_of_variables]
6
[Names_of_variables]
ch2o o2 co2 hco3 nh4 hpo4
[Synonyms]
ch2o orgmatter (CH2O)x(NH3)y(PO4)z
o2 oxygen
co2 carbacid h2co3*
hco3 bicarbonate           1 for solid species
nh4 ammonium               0 for dissolved species
hpo4 phosphate
[Solids]
1 0 0 0 0 0
[Stoichiometry]                              x,y,z = C/N/P
-1  -1*SD   (x-y+2.*z)/x*SD   (y-2.*z)/x*SD  stoichiometric ratio
                                             of organic matter
[Variable_units]                (y/x)*SD    (z/x)*SD
mol/g_solid mol/l_pw mol/l_pw mol/l_pw mol/l_pw mol/l_pw
 [Process_type]
kinetic
[Process_dynamics]                    SD = 1000 ρ_solid (1-φ)/φ
kfox*ch2o*(SWo2+(1.0-SWo2)*o2/kmo2)
[Number_of_parameters]
3                          Preferential pathways are defined by using
[Names_of_parameters]      Heaviside's operators (see eqs. (2) and (3) )
kfox  kmo2  SWo2
[Default_parameter_values]  Column-wise assignment
0.003  8.0E-6  0.0          of parameters values
[Parameter_units]                and units
1/yr mol/l_pw --
[Keywords]
oxic degradation deep sea sediments
[Documentation]
http://www.geo.uu.nl/Research/Geochemistry/kb/Knowledgebook/Hetero3.pdf
[Type]
redox1
```

Figure 3. Example of the process file for oxic degradation of organic matter: ''oxic.txt.'' The reaction expression described by the process file, with the corresponding stoichiometric coefficients (underlined), is $\underline{1}$ch2o + $\underline{SD}$ o2 $\rightarrow$ $\underline{\dfrac{(x-y+2z)\cdot SD}{x}}$ co2 + $\underline{\dfrac{(y-2z)\cdot SD}{x}}$ hco3 + $\underline{\dfrac{y\cdot SD}{x}}$ nh4. The values for the entries [Solids], [Stoichiometry], and [Variable_units], on the one hand, and [Default_parameter_values] and [Parameter_units], on the other hand, follow the column-wise order of the entries for [Names_of_variables] and [Names_of_parameters], respectively.

3.3. Parsing Procedure and Automatic Code Generation

After the reactions of interest have been selected and their list submitted in addition to the remaining application-specific data (step 1 in Figure 1), an automated procedure is launched that parses all this information into ASCII files. This completes the model setup procedure carried out by the user on the GUI of the Web-distributed KB. It is illustrated in detail by means of examples in the next section.

The parsing procedure involves reading information from files directly generated by the Internet system (e.g., definition of the physical domain) and from files originated by the KB system (reaction network). The former can easily be processed by the Automatic Code Generator (ACG), whereas the information contained in the KB files must first be concatenated in the appropriate format. The main features of the parsing involves extracting and assembling, from the set of selected processes, a number of lists containing all the species involved in the RN, along with appropriate initial and boundary conditions, the complete set of kinetic expressions and equilibrium constraints necessary to define the function residuals f_j, and all the parameters appearing in f_j, including their associated numerical values. Stoichiometric coefficients, which relate the changes in species concentrations to the progress in any individual reaction, is another crucial component extracted from the KB process files. A check for unit consistency for both species concentrations and parameters values is carried out at this stage.

Once parsing is completed, the following operations are performed in background on our Web-based ''runtime'' server (Figure 1, steps 2–5). First, the information from the ASCII-files is used to assemble the stoichiometric matrix, that is, the mathematical representation of the user-defined reaction network (Figure 1, step 2). Second, a set of symbolic programming operations is performed (Figure 1, step 3) using the MAPLE software environment [Chilakapati, 1995; Regnier et al., 1997; Amberg et al., 1999; Regnier et al., 2002]. The most important one involves the construction of the Jacobian matrix from the series of function residuals. Third, the function residuals, the Jacobian matrix, plus all user-dependent information are translated into fully structured FORTRAN code (Figure 1, step 4) using the MACROFORT package [Gómez, 1990] combined with our own library of MAPLE procedure (ACGLIB©). The resulting routines are then linked with our numerical engine, which contains standard routines for solving transport equations and a linear algebra solver for the sets of linearized process equations generated by the preprocessor (Figure 1, step 5).

Finally, upon completion of the automated generation procedure, the ''runtime'' server compiles and sends the resulting model executable to the user via e-mail (Figure 1, step 6).

The accuracy of the numerical engine and the ACG (referred to as Biogeochemical Reaction Network Simulator (BRNS) by Regnier et al. [2003]) has recently been evaluated by Thullner et al. [2005], from a comparison between their model results with those obtained with two well established RTMs for porous media flow applications (e.g., STEADYSED [Van Cappellen and Wang, 1996; Hunter et al., 1998] and TBC [Schäfer et al., 1998a, 1998b]). Comparison with field data from Skagerrak sediments [Canfield et al., 1993] and a sand column experiment [von Gunten and Zobrist, 1993] was also performed by these authors. Here, the performance of the KB-RTM is evaluated further by means of two contrasting scenarios. However, the focus is mainly on the Web-distributed KB system and how this concept facilitates the incorporation and modification of complex biogeochemical reaction networks into RTM applications.

4. Applications

4.1. Introduction

Two applications of redox dynamics in porous media are presented: an early diagenetic (ED) model (saved in our server system as ''EDscenario'') of shelf sediments and two simulations of a groundwater aquifer (GWA) contaminated by a landfill plume (saved respectively as ''GWscenario1'' and ''GWscenario2''). All model applications can be found on our Web-based ''runtime'' server as part of the KB, at http://www.geo.uu.nl/kbrtm. In what follows, the discussion addresses only the major features, that is, similarities and differences between the applications. The user is referred to the Web site for exact parameterization.

In short, the focus is on redox processes, acid-base chemistry and carbonate/sulfide mineral phases precipitation-dissolution. Since the interplay of these processes determines the pH in both systems, which itself is sensitive to relative imbalances in reaction rates [Jourabchi et al., 2005, and references therein], computation of realistic pH profiles with mechanistic process models represents a challenging and important test application.

The structure of the reaction network (RN) is similar for the sediments and groundwater applications, with organic matter serving as the primary electron donor. The RN combines 23 species and 24 reactions for the ED scenario, and 25 species and 36 reactions for the GWA application. This includes kinetic transformations (all primary and secondary redox reactions and nonredox mineral precipitation-dissolution processes) and equilibrium acid-base

reactions (see below). Almost 50 parameters are used in the definitions of rates and equilibrium constraints. Even though the set of reactions is similar in both applications, reaction parameter values may contrast. For example, the quality of the organic matter may differ, leading to faster degradation rates near the contaminant site, or differences in ionic strengths affect the apparent solubility constant in the marine setting. Note also that different units are used in both applications, with solute and solid concentration respectively expressed in mol/$L_{pore\ water}$ and mol/g_{solid} in the ED application, and concentrations in moles/$L_{pore\ water}$ for the solutes, and moles/$L_{total\ volume}$ for the solids in the GWA examples. We will adopt the units used in the ED simulation in what follows. The reader should refer to the GWA scenario files in our server (http://www.geo.uu.nl/kbrtm) for more details about the unit system selected. The respective RNs are complex and involve many parameters and rate formulations, yet they can be easily assembled through the KB and the Web interface. The system of DAEs is stiff in both environments, which presents a rigorous test for the proposed modeling approach.

Time and space scales of the ED and GWA simulations are fundamentally different (dm and millennia versus km and decades, respectively; Table 2). In addition, the mechanisms and relative intensities of transport processes are not the same, with dominant diffusional transport by bioturbation and molecular diffusion in the ED and dominant advective transport in the GWA. Another major difference between the two applications is the treatment of solid species in the model: in the GWA, a moving fluid percolates through a fixed solid matrix, while in the ED, solids are mixed by bioturbation.

Table 2. Web Submission Form I (Physical Parameters): Definition of the Physical Domain, Major Transport Coefficients and Forcing Functions as Well as Global Output Parameters for the Early Diagenetic and Groundwater Aquifer Applications, Respectively[a]

	ED	GWA
Total time	1500 yr	22 yr
Time step	1.0×10^{-4} yr	5.0×10^{-4} yr
Total length	40 cm	40000 cm
Number of nodes	401	101
Porosity	0.85	0.25
Cross section	1.0 cm^2	1.0 cm^2
Flow velocity	0.0 cm/yr	250.0 cm/yr
Burial velocity	0.04 cm/yr	0.0 cm/yr
Bioturbation coefficient	3.0 cm^2/yr	0.0 cm^2/yr
Longitudinal dispersivity	0.0 cm	400 cm
Temperature	10°C	15°C
Salinity	35.0 PSU	0.1 PSU
First output time	1.0 yr	1.0 yr
Output interval period	2.0 yr	1.0 yr

[a] ED, early diagenetic; GWA, groundwater aquifer. All entries are species independent and hence are not influenced by the selected RN. For each selected kinetic process, the Web interface prompts the user whether a spatial distribution of rates should be generated at output times.

4.1.1. Groundwater Aquifer

In the GWA application, the focus is on the biogeochemical evolution of the major constituents in a landfill leachate plume infiltrating an initially oxic, pristine aquifer of low porosity ($\phi = 0.25$). Simulations are carried out over a 400 m flow path which is infiltrated at the upstream boundary by the anoxic landfill-leachate recharge. In this case, the model setup (see the scenario files in our Web system) is based on Hunter et al. [1998] and Van Cappellen and Wang [1996]. On the inflow side of the domain ($x = 0$ cm), a specified concentration (i.e., Dirichlet boundary condition) is applied for all solute species. The chemical composition of the leachate is characterized by a high dissolved organic carbon (DOC) loading represented by two fractions of different reactivity. At the outflow ($x_{tot} = 4 \cdot 10^4$ cm), a concentration gradient (i.e., Neumann boundary condition) is specified for all dissolved chemical species. Solids are considered immobile and therefore are only affected by local biogeochemical transformations. Solutes are transported by fluid flow motion (250 cm·yr^{-1}) and macroscopic dispersion (dispersion coefficient $D = 4 \cdot 10^5$ cm^2 yr^{-1} or dispersivity $\alpha_L = 400$ cm). The overall redox dynamics and the resulting effect on pH evolution are investigated

along a flow line after a transient simulation period of 22 years. Table 2 presents the values of the coefficients implemented to define the GWA physical framework via the Web submission form I.

4.1.2. Shelf Sediment

In the ED simulation, transient depth distributions of redox sensitive species and rates are computed for the case of a typical shelf sediment (total depth: 40 cm, T: 10°C, S: 35‰) of high porosity (ϕ = 85%). The simulation period is 1500 years, starting from constant concentration profiles. The model setup is a slightly modified version of the shelf case presented by Van Cappellen and Wang [1996]. The exact definition can be found in our Web system (http://www.geo.uu.nl/kbrtm). The primary driving force for biogeochemical transformation is the solid flux of organic matter (32 μmol cm^{-2} yr^{-1}) depositing at the sediment-water interface, assumed to be constant in time. The length scale of the simulation (x_{tot} = 40 cm) is chosen such that at $x = x_{tot}$, all rates are very close to zero, a condition which allows the specification of a Neumann boundary condition. At the sediment-water interface (x = 0 cm), a flux boundary condition is assigned for all solids, while typical bottom-water concentrations (Dirichlet condition) provide the upper boundary condition for solutes. Externally impressed flow is neglected here, and hence the advective velocity (0.04 cm/yr) is solely due to the burial rate. All chemical species are subject to bioturbation, and solutes are further transported by molecular diffusion. Table 2 presents the values of the coefficients implemented to define the ED physical framework via the Web submission form I.

4.2. Reaction Network

The reaction network, which is common to the two simulations, consists of the six major metabolic pathways for organic matter degradation (aerobic degradation, denitrification, Mn and Fe reduction, sulfate reduction and methanogenesis), and a set of 10 secondary reoxidation reactions (Table 3a). In addition to the microbial and chemical reduction of Mn and Fe oxides, precipitation/dissolution of $MnCO_3$, $FeCO_3$ and FeS mineral phases are also included, which have an effect on redox and acid-base chemistry. Over 45 parameters (such as k_{PRR}, K_{EA}, k_{SRR}, k_d, k_p, SSA, K_{sp}, and K_{eq}, see below) are extracted from the KB for these simulations.

Table 3a. Web Submission Form I (Reaction Network): List of Processes Incorporated Into the Reaction Network, Following the "Taxonomy" Proposed in Our Knowledge Base System[a]

Group of Processes	Reaction
Acid-base reactions (ABE) ($\leftrightarrow$)	1) Carbonate 2) Bicarbonate 3) Sulfide 4) Borate[b]
Primary redox (PRR) ($\rightarrow$)	5) degradation 6) Denitrification 7) Mn(IV) reduction 8) Fe(III) reduction 9) Sulfate reduction 10) Methanogenesis
Secondary redox (SRR) ($\rightarrow$)	11) Nitrification 12) Mn^{2+} reoxidation by O_2 13) Fe^{2+} reoxidation by O_2 14) Fe^{2+} reoxidation by MnO_2 15) Sulfide reoxidation by O_2 16) Sulfide reoxidation by MnO_2 17) Sulfide reoxidation by $Fe(OH)_3$ 18) Methane reoxidation by O_2 19) Methane reoxidation by SO_4^{2-} 20) FeS reoxidation by O_2
Precipitation-dissolution (MPD) ($\rightarrow$)	21) FeS dissolution[c]/precipitation 22) $MnCO_3$ dissolution[c]/precipitation 23) $FeCO_3$ dissolution[c]/precipitation 24) $CaCO_3$ dissolution/precipitation[c]
Adsorption-Ion exchange	25) Ammonium adsorption[c]

[a] Information similar to the one shown in Figure 3 is parsed into the ACG for each of the selected processes. For each selected kinetic process, the Web interface prompts the user whether or not a space distribution of kinetic rates should be generated at output times (see Table 2). In the GWA case, two fractions of organic matter with different reactivities have been taken into consideration, which therefore have separate respective primary redox reactions.

[b] Specific to ED.

[c] Specific to the GWA.

The shelf sediment application is also forced by a constant flux of calcite (8 μmol cm^{-2} yr^{-1}). Calcium carbonate buffering is ignored in the groundwater application, as it is assumed that the landfill plume percolates through a noncalcareous groundwater aquifer. Larger pH changes are thus expected in this case. Finally, the acid-base chemistry of the ED application includes the dissociation of carbonic, sulfidic and boric acids. Since total boron is negligible in freshwater environments, the dissociation of the latter weak acid is ignored in the GWA simulation.

According to the mathematical functional expressions and the ''taxonomy'' proposed in our KB, four types of chemical processes are included in our RN (Table 3a). For primary redox reactions (PRR), the rates of the respective metabolic pathway (PRR$_i$) are given by [e.g., Van Cappellen and Gaillard, 1996]

$$\begin{cases} \text{if } [EA_{i-1}] > K_{EA,i-1} & \text{then PRR}_i = 0 \\ \\ \text{if } [EA_{i-1}] \leq K_{EA,i-1} \quad \text{then} \begin{cases} \text{if } [EA_i] > K_{EA,i} & \text{then PRR}_i = k_{PRR}.[CH_2O].f_i \\ \text{if } [EA_i] \leq K_{EA,i} & \text{then PRR}_i = k_{PRR}.[CH_2O].f_i.\dfrac{[EA_i]}{K_{EA,i}} \end{cases} \end{cases} \tag{2}$$

where k_{PRR}[yr^{-1}] is the rate constant, CH_2O represents the electron donor (complex macromolecular organic matter) and EA_i is the electron acceptor of the ith metabolic pathway, and

$$f_i = \left(1 - \sum_{j=1}^{i-1} \frac{\left[EA_j \right]}{\left[K_{EA,j} \right]} \right) \tag{3}$$

The proposed rate law assumes first-order dependency with respect to the electron donor and a pseudo Michaelis-Menten type relationship with respect to the EA. Equation (2) indicates that a specific metabolic pathway is inhibited if a more favorable EA is present in the system at sufficiently high concentrations, that is, if a reaction yielding more free energy takes place [e.g., Van Cappellen and Wang, 1996; Berg et al., 2003].

Rates of secondary redox reaction (SRR) are currently implemented as bimolecular rate laws with a first-order dependency with respect to each of the reactants [e.g., Van Cappellen and Wang, 1996]:

$$\text{SRR} = k_{SRR} \cdot [EDO] \cdot [EA], \tag{4}$$

where EDO is an inorganic electron donor (e.g., Fe^{+2}, Mn^{+2}, H_2S, ...) and k_{SRR} is the rate constant with units of $L_{pore\ water} \cdot mol^{-1}\ yr^{-1}$ if all reactants are solutes, or $g_{solid} \cdot mol^{-1}\ yr^{-1}$ if a solid species is involved in the SRR (e.g., MnO_2 or $Fe(OH)_3$).

Nonredox Mineral Precipitation/Dissolution (MPD) rate laws are given by [e.g., Appelo and Postma, 1999]

$$MPD = k_d \cdot [MIN] \cdot \left(1 - IAP/K_{sp}\right)^n \quad \text{if } IAP < K_{sp}$$

$$MPD = k_p \cdot \left(1 - IAP/K_{sp}\right)^n \qquad \text{if } IAP > K_{sp}$$

(5)

where k_d [yr^{-1}] and k_p [$mol \cdot g^{-1}_{solid} \cdot yr^{-1}$] are the rate constants for dissolution and precipitation, respectively, [MIN] denotes the concentration of the dissolving mineral [mol/g_{solid}], IAP is the Ion Activity Product, K_{sp} the equilibrium constant (or solubility product), and n the order of the reaction. In the groundwater scenario, equilibrium constants corrected for the in-situ temperature (15°C) are used, while in the early diagenetic simulations, apparent equilibrium constants which incorporate both temperature (10°C) and electrolyte effects of marine solutions have been applied [Boudreau, 1997].

Acid-base equilibriums (ABE) are constrained according to [e.g., Van Cappellen and Wang, 1996]

$$ABE \equiv k_{eq} \cdot \left[H_m A^{n-}\right] - \left[H^+\right] \cdot \left[H_{m-1} A^{(n+1)-}\right] = 0,$$

(6)

where A stands for the fully dissociated form of the protolytic species (e.g., CO_3^{2-}, S^{2-} or BO_3^{2-}), m is the number of protons (e.g., $m = 2$ in H_2CO_3), n is the negative charge of the dissociating species (e.g., $n = 0$ for H_2CO_3, $n = 1$ for HS^-), and K_{eq} is the equilibrium constant for a specific acid-base reaction. Corrections for in-situ conditions are performed identically than for solubility products.

Adsorption-desorption reactions (ADS) are currently implemented as equilibrium-type processes [e.g., Langmuir, 1997], using a classical distribution coefficient (K_d):

$$ADS \equiv k_d \cdot \left[X_{aq}\right] - \left[X_{ads}\right] = 0,$$

7

Where X_{aq} and X_{ads} denote the dissolved and adsorbed species, respectively.

Table 3b gives the complete list of variables which is automatically concatenated from the selected RN. Since in the convention used in the ED application, solid and solute concentrations are expressed in $moles/g_{solid}$ and $moles/L_{pore\ water}$, respectively, a conversion factor has to be applied to the stoichiometric coefficients of solutes, if a rate is expressed in moles of solid transformed per unit time and vice-versa. This conversion factor, SD, is given by

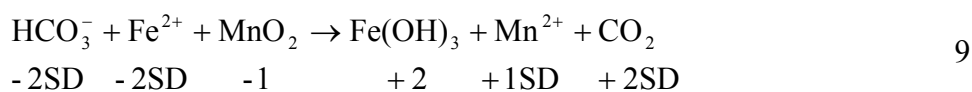$$SD = \rho \cdot \left(\frac{1-\phi}{\phi} \right) \cdot 1000,$$

8

where ρ [g/cm^3$_{solid}$] is the density of the bulk solid phase and ϕ[--] the porosity. Note that such coefficient is not needed for the GWA application, since, in this case, the convention used for concentrations is moles/L$_{pore\ water}$ for the solutes, and moles/L$_{total\ volume}$ for the solids.

Table 3b. Complete List of Variables Automatically Associated With the Selected Reaction Network[a]

Common				Specific GWA	ED
H^+ (d)	Mn^{2+} (d)	CO_3^{2-} (d)	$Fe(OH)_3$ (s)	$(CH_2O)_{lab}$ (d)	CH_2O (s)
Ca^{2+} (d)	MnO_2 (s)	H_2CO_3 (d)	$MnCO_3$ (s)	$(CH_2O)_{ref}$ (d)	$B(OH)_3$ (d)
$CaCO_3$ (s)	O_2 (d)	CH_4 (d)	HS^- (d)	$NH_{4(ads)}^+$ (s)	$B(OH)_4^-$ (d)
NH_4^+ (d)	NO_3^- (d)	H_2S (d)	FeS (s)		
SO_4^{2-} (d)	HCO_3^- (d)	Fe^{2+} (d)	$FeCO_3$ (s)		
HPO_4^{2-} (d)					

[a] Variables are either solids (s) or dissolved (d) chemical species. Note that the GWA application includes organic matter as both labile (lab) and refractory (ref) fraction. CH_2O denotes complex macromolecular organic matter characterized by the formula $(CH_2O)_x(NH_3)_y(H_3PO_4)_z$, where x:y:z is the stoichiometric C:N:P ratio.

For instance, the rate of reoxidation of Fe^{2+} by MnO_2 (reaction 14 in Table 3a) is given by $R_{14} = d[MnO_2]/dt = k_{SRR,14}[Fe^{2+}] \cdot [MnO_2]$. Since the rate law is given in moles of MnO_2 reduced per unit time per unit gram of solid (i.e., k_{SRR} has units of L/(mol$_{Fe2+}$ yr)), the appropriate stoichiometric coefficients for each species are

$$\begin{array}{ccccccc} HCO_3^- & + Fe^{2+} & + MnO_2 & \rightarrow Fe(OH)_3 & + Mn^{2+} & + CO_2 \\ -2SD & -2SD & -1 & +2 & +1SD & +2SD \end{array}$$

9

As explained in the previous section, the concatenated list of variables (Table 3b) is used to generate a new Web submission form in which all variable-specific parameters are constrained. The information to be provided is identical for every variable of the RN. As an example, Table 4 shows such parameterization for O_2 in the case of the ED application.

The information provided in Tables 2, 3a, 3b, and 4 completely specifies the problem at hand. This information is then parsed in the ACG for creation of the model executable via our Web-based runtime server. Examples of model results are succinctly discussed below.

Table 4. Web Submission Form II: Species-Dependent Parameters Associated With Oxygen for the ED Application[a]

Parameter Group	Field	Assignment
Molecular diffusion coefficient	value at 0°C	380.45
	temperature dependency α	0.06
Upper boundary condition	type	fixed concentration
	value	250.0e-6
Lower boundary condition	type	fixed gradient
	value	0.0
Output file	generate	yes
	name	o2.dat

[a] Similar information must be provided for every chemical species of the RN (Table 3b).

4.3. Results and Discussion

4.3.1. Groundwater Simulation

A stepwise approach is used here to investigate redox and acid-base chemistry. In the first simulation (scenario 1, Figures 4 and 5), only the primary redox reactions and acid-base equilibria are considered (reactions 1–10, Table 3a). In a second scenario (Figures 6 and 7), reoxidation reactions of the reduced products of organic matter degradation and precipitation/dissolution of carbonate and sulfide minerals are added to the reaction network.

4.3.1.1. Scenario 1

In this first simulation, only the six primary biodegradation reactions as well as the carbonate and sulfide dissociation reactions are considered (reactions 1, 3 and 5–10, Table 3a). The location and magnitude of the overall rate of organic matter oxidation are subject to the value of the rate constant selected for each of the two CH_2O fractions. The highly reactive pool (CH_2O_{lab}, k_{PRR} = 30 yr^{-1}) is rapidly depleted within the first 12 m downstream of the recharge point (not shown) while the more refractory fraction (CH_2O_{ref}, k_{PRR} =0.3 yr^{-1}) disappears after 300 m (Figure 4). There, it is clearly shown a general inverted sequence of degradation pathways, starting with sulfate reduction and methanogenesis at the leachate

source, followed by an extensive zone with coexisting Fe(III) and Mn(IV) reduction, denitrification and, finally, a plume front dominated by oxic respiration. Such a reversed pattern in the order of primary redox reactions is frequently observed in groundwater systems contaminated with high loads of organic carbon [Chapelle, 2001].
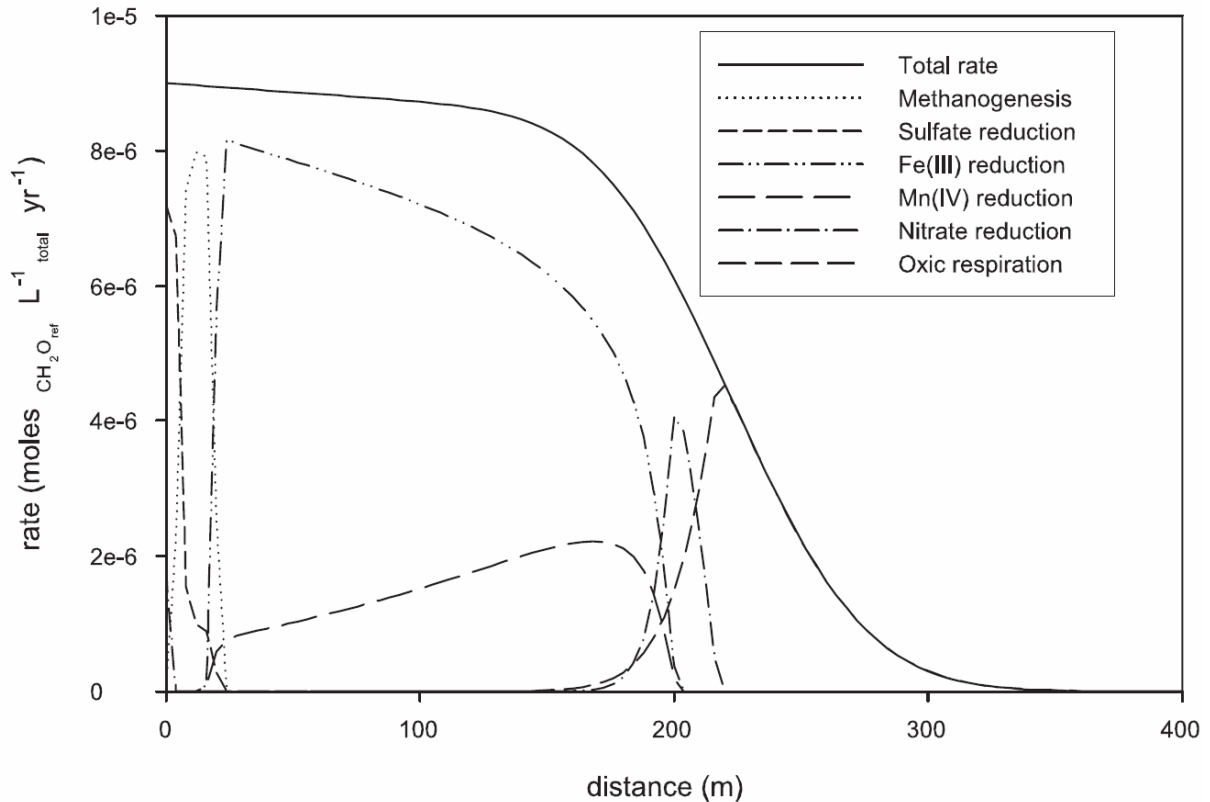

Figure 4: Pathways of CH_2O_{ref} degradation obtained in the GWA application for scenario 1 after a transient simulation time of 22 years.
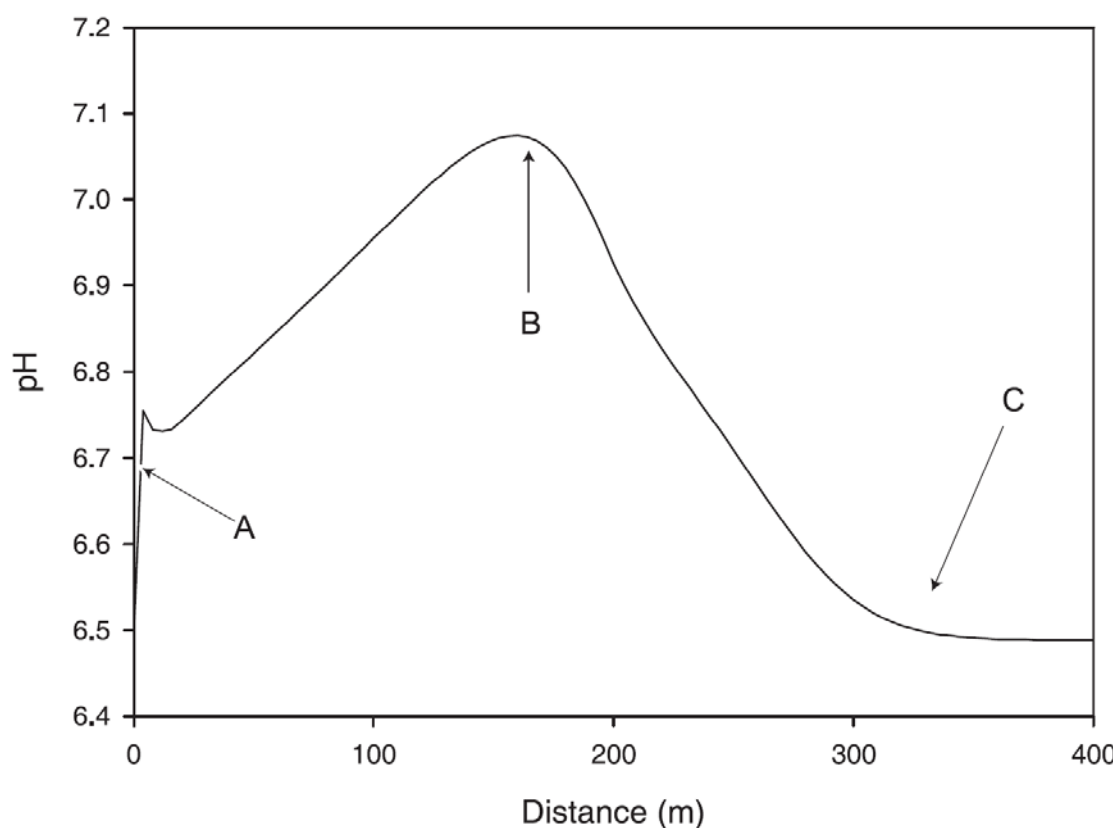
Figure 5: The pH distribution along the flow path in the GWA application for scenario 1 after a transient simulation time of 22 years.

The individual effect of each of the PRR on the proton balance can be estimated from the modeled process rates (Figure 4), taking into account appropriate stoichiometric coefficients of protons produced or consumed per mole of metabolized organic matter. The stoichiometric coefficients have been calculated from the charge balance constraint, using the proper speciation of the aqueous carbonate and sulfur species at the in situ (computed) pH (not shown). For a detailed methodology, see Jourabchi et al. [2005]. A positive value for proton production rates leads to a decrease in pH and vice-versa. The pH distribution resulting from the effect of redox kinetic processes, combined with the buffering capacity of the carbonate-sulfur system, is shown in Figure 5. The profile is characterized by three distinct areas: In region A, a sharp increase in pH close to the point of recharge is predicted, which is caused by sulfate reduction of the CH_2O_{lab} pool. The steady increase in the middle of the profile up to point B corresponds to a region where organic carbon degradation of CH_2O_{ref} is dominated by Fe(III) and Mn(IV) reduction processes, both of which cause a net proton consumption. The subsequent decrease in pH from B to C results from aerobic degradation, which is the major respiratory pathway between 200 and 300 m downstream of the recharge (Figure 4).

<u>4.3.1.2. Scenario 2</u>

In scenario 1, the reduced end-products of organic carbon degradation ($NH4^+$, Mn^{2+}, Fe^{2+}, H_2S and CH_4) were accumulating along the flow path without possibility of further reoxidation. In scenario 2, secondary redox reactions are considered. Figure 6 shows that these reactions significantly influence the relative contributions and spatial distribution of the various organic carbon mineralization pathways. Although sulfate reduction and methanogenesis still predominate at the leachate source, the Mn reduction zone between 10–200 m is no longer observed in Figure 6. MnO_2 is instead reduced by the chemical reoxidation of Fe^{2+} (Table 3a, reaction 14) produced by the Fe(III) reduction process. When compared to the previous simulation, the latter process dominates the other organic matter degradation pathways between 20–225 m. This trend can be explained from the fact that the rate by which $Fe(OH)_3$ is being produced through Fe^{2+} reoxidation by O_2/ MnO_2 (Table 3a, reactions 13 and 14) is faster than the $Fe(OH)_3$ consumption rate by total sulfide (TS) oxidation (Table 3a, reaction 17).
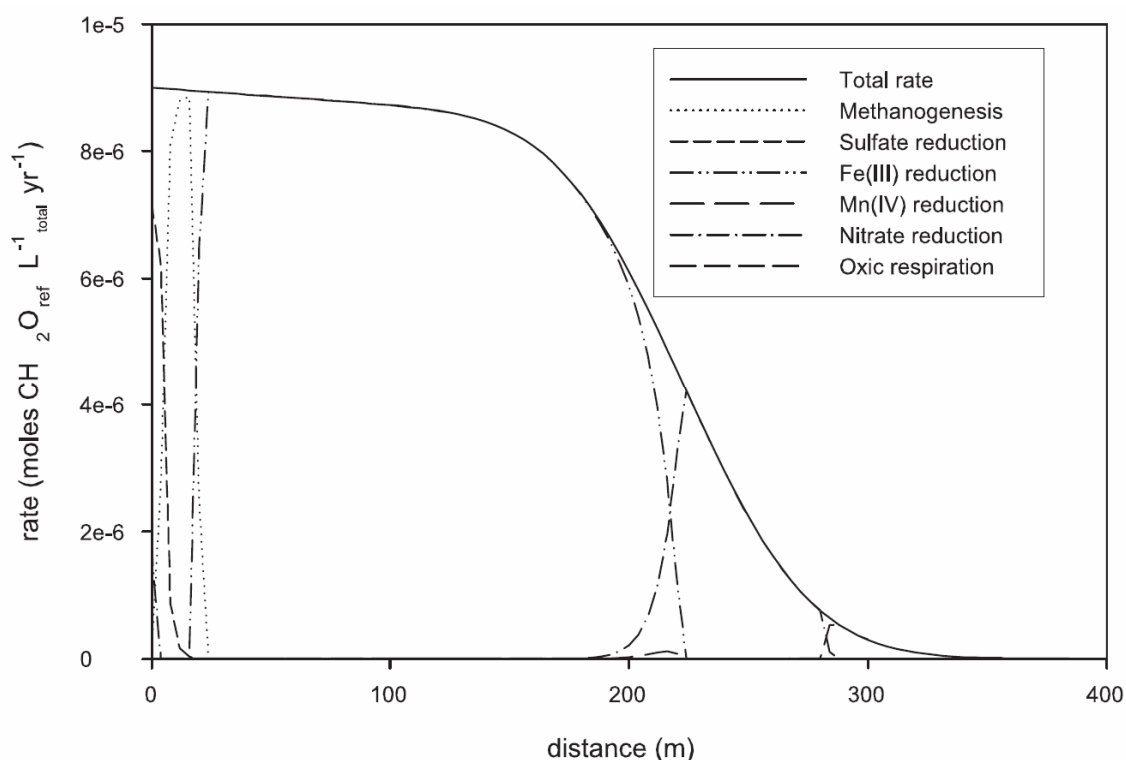

Figure 6. Pathways of CH_2O_{ref} degradation obtained in the GWA application for scenario 2 after a transient simulation time of 22 years.

Another significant difference between the two scenarios is the increased relative importance of denitrification at the downstream edge of the moving CH_2O_{ref} front when secondary redox reactions are incorporated in the RN. The additional source of NO_3^- is the

nitrification process (reaction 11, Table 3a), which consumes O_2 and hence increases the relative contribution of denitrification at the expense of aerobic respiration. The contribution of O_2 as an oxidant for organic carbon (OC) degradation is further reduced by the other secondary redox reactions (Mn^{2+}, Fe^{2+} and TS oxidation by O_2) which operate right at the edge of the CH_2O_{ref} front (approximately 300 m).

The resulting pH distribution obtained for scenario 2 is shown in Figure 7. Precipitation of FeS and $FeCO_3$ at the leachate source leads to a considerable pH drop from the boundary value of 6.5 down to 5.6 (region A). The sharp increase in pH in region B is predominantly due to the combined effect of TS reoxidation reactions by $Fe(OH)_3$ and MnO_2, both of which are localized at a distance of around 280 m. The slight pH drop (about 0.1 unit) in area C results from the reoxidation of Fe^{2+} by O_2 (Table 3a, reaction 13) and MnO_2 (Table 3a, reaction 14), respectively. Further downstream of area C, the results are still dependent on the initial conditions since the CH_2O_{ref} front has not yet propagated into this area.
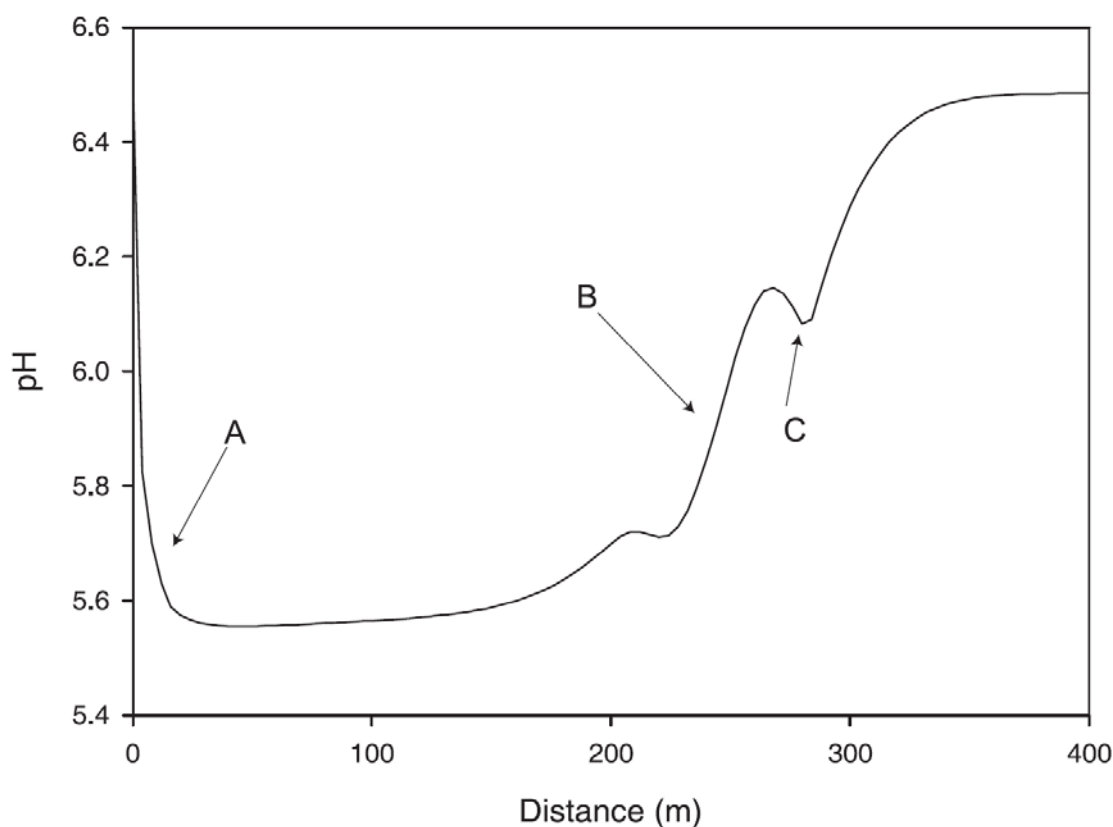

Figure 7. The pH distribution along the flow path in the GWA application for scenario 2 after a transient simulation time of 22 years.

4.3.2. Early Diagenetic Simulation

Figure 8 shows a classical redox sequence of organic matter degradation pathways which develops over the first 15 cm of the sediment column. Since sulfate is present in excess, all

metabolic pathways except methanogenesis are active in the system. Integration of the rates indicates the predominance of sulfate reduction, followed by oxic degradation, denitrification, iron reduction and finally manganese reduction in the overall rate of organic matter degradation. These calculations take into account the contributions of the various reoxidation reactions in the carbon balance. The latter have a predominant influence on the depth distribution of pH (Figure 9). Indeed, except for iron reduction, which is an important proton consumption reaction in the system, the major processes controlling the H^+ balance are nitrification, oxygenation of TS and Mn^{2+}, reoxidation of Fe^{2+} by MnO_2 as well as reoxidation of TS by $Fe(OH)_3$ (Table 3a). The former four reactions produce protons while the latter is a proton-consuming process. Two zones in the sediment profile can thus be distinguished: a zone of pH decrease (0– 2 cm) dominated by the aerobic oxidation of Mn^{2+} and TS, and a zone of pH increase (2–4 cm) dominated by Fe(III) reduction and reoxidation of TS by iron oxides. Note that the proton production by secondary redox reactions in the uppermost layer leads to a significant dissolution of calcite which is buffering the pH drop. Further analysis of the complex interplay between redox, pH dynamics and carbonate precipitation/dissolution is provided by Jourabchi et al. [2005].
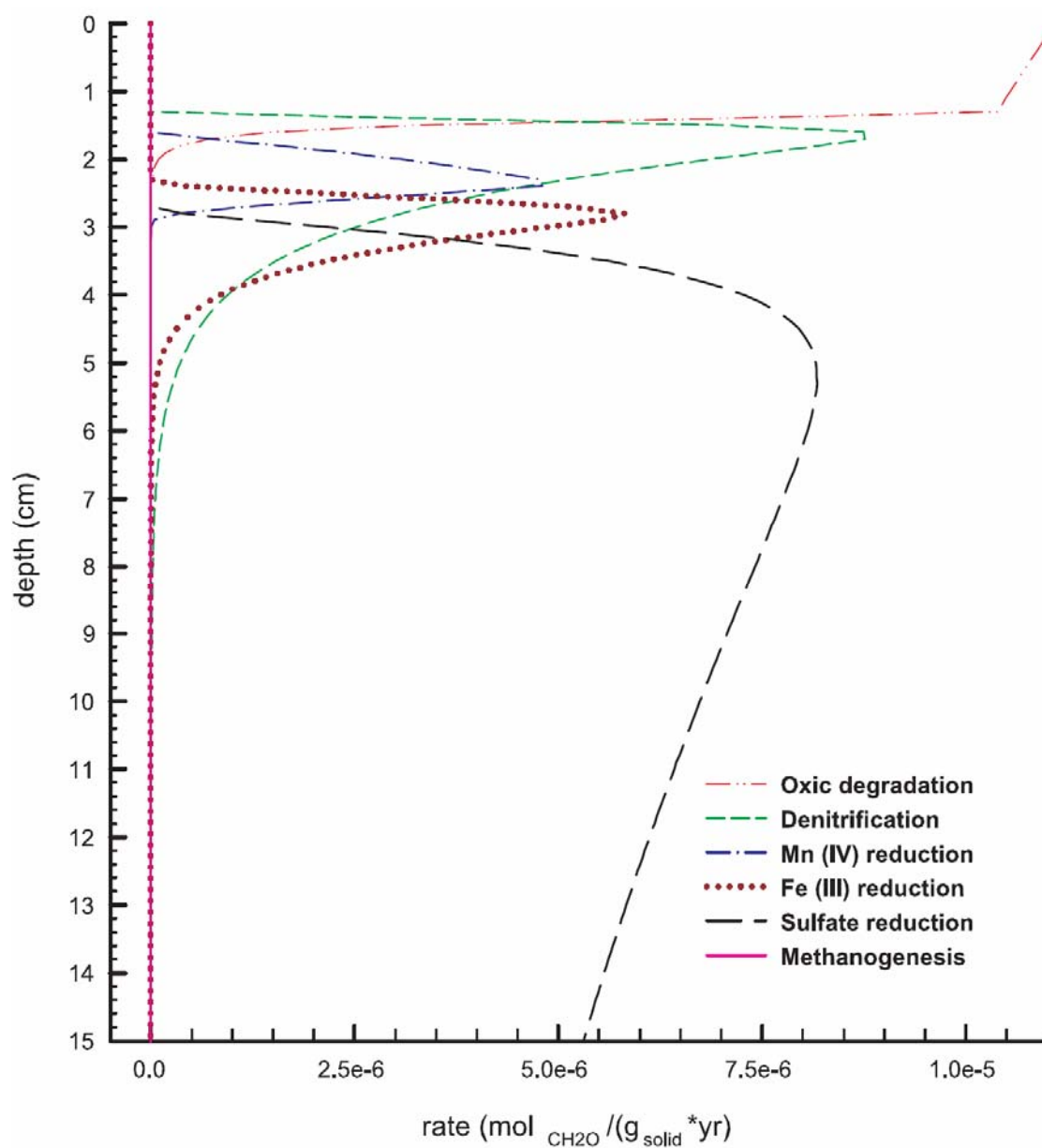
Figure 8. Redox sequence of organic matter degradation pathways which develops for the ED application over the first 15 cm of the sediment column.
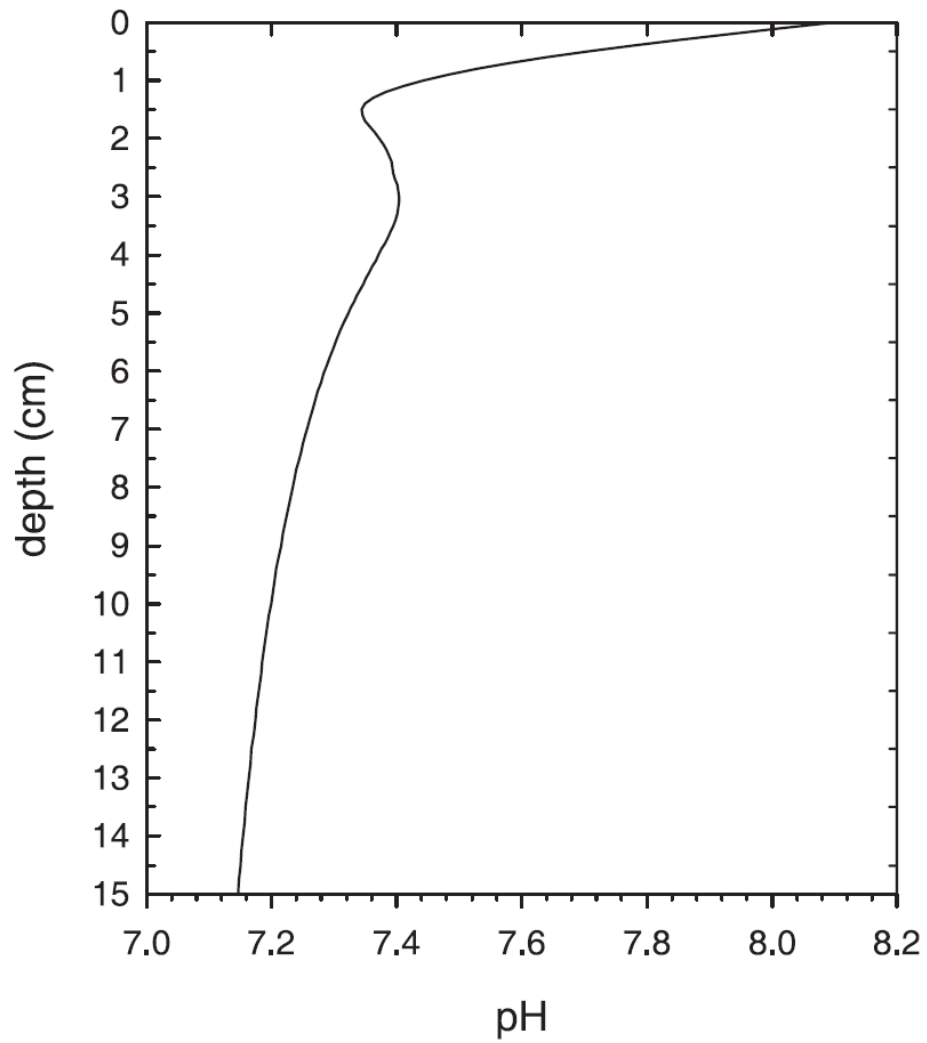
Figure 9. The pH distribution for the ED application over the first 15 cm of the sediment column after 1500 years.

5. Conclusions

This paper presents a simulation environment for one-dimensional reactive transport applications that addresses the major hurdles for the common use of complex reactive transport models. In particular, the KB-RTM approach provides complete flexibility in the choice of model components (chemical species) and the description of the interaction between them (reactions) by using a generic form of the advection-dispersion equation and by taking a ''reaction-centric'' approach which utilizes the unifying conceptual and mathematical principles underlying all RTMs. Thus 1-D transport descriptions relevant to many compartments of the Earth system (rivers, estuaries, groundwater or sediments) can be incorporated in our simulation environment. The proposed approach should thus help overcome traditional disciplinary barriers between the different subfields of RTM. In addition, the use of symbolic programming and automatic code generation allows testing and comparison of alternative process formulations. As a result, it facilitates the evaluation of the effect of competing model structures on predictions and uncertainties.

The shear volume of ever growing knowledge on process dynamics in the natural environment can also impede its timely incorporation into RTMs. We argue that the Knowledge Base (KB) is a particularly efficient approach for constructing reactive-transport applications of increasing complexity, as well as testing and comparing alternative process formulations. The KB system allows expertise to be stored in a dynamically evolving, Web-distributed Knowledge Base and provides a platform where both modelers and experimentalists can share expertise. The KB-RTM is available via our Web server at http://www.geo.uu.nl/kbrtm.

Further development and maintenance of the simulation environment will involve the progressive implementation of a larger number of processes, and a continuing effort to keep the content of the KB up-to-date with new results from the scientific community. A Web-based Knowledge Book, consisting of documentation material for every process implemented in the KB, will also be implemented with complete reference to the source material, following the strategy already used for the CONTRASTE model [Regnier et al., 2002]. The Web-based system further offers the prospect for use as a forum for discussion, open to user feedback and contribution.

Here, we have illustrated the workings of our simulation environment using two model applications dealing with redox and coupled acid-base chemistry in sediments and

groundwater environments. Our examples demonstrate the flexibility and potential of the proposed simulator.

Our objectives have been achieved by adhering to a modular structure, where information assemblage precedes symbolic process formulation, followed by automatic code generation and combination with numerical algorithms for solution. Finally, accessibility through the Internet is a key feature for such dissemination and combination of expert knowledge on modeling and process description. To our knowledge, this is the first attempt to use a Web-distributed flexible system to provide dynamically adaptive reactive transport models in the field of geosciences.

References

Amberg, G., R. Tonhard, and C. Winkler (1999), Finite element simulations using symbolic computing, Math. Comput. Simul., 49, 257–274.

Appelo, C.A.J., and D. Postma (1999), Geochemistry, Groundwater and Pollution, 536 pp., A. A. Balkema, Brookfield, Vt.

Archer, D. E., J. L. Morford, and S. R. Emerson (2002), A model of suboxic sedimentary diagenesis suitable for automatic tuning and gridded global domains, Global Biogeochem. Cycles, 16(1), 1017, doi:10.1029/2000GB001288.

Ayora, C., C. Tabernera, M. W. Saaltink, and J. Carrera (1998), The genesis of dedolomites: A discussion based on reactive transport modeling, J. Hydrol., 209, 346–365.

Barry, D. A., H. Prommer, C. T. Miller, P. Engesgaard, A. Brun, and C. Zheng (2002), Modelling the fate of oxidisable organic contaminants in groundwater, Adv. Water Resour., 25, 945–983.

Berg, P., S. Rysgaard, and B. Thamdrup (2003), Dynamic modeling of early diagenesis and nutrient cycling: A case study in an arctic marine sediment, Am. J. Sci., 303, 905 – 955.

Billen, G., J. Garnier, and P. Hanset (1994), Modelling phytoplankton development in whole drainage networks: The RIVERSTRAHLER Model applied to the Seine river system, Hydrobiologia, 289, 119–137.

Boudreau, B. P. (1997), Diagenetic Models and Their Implementation: Modeling Transport and Reactions in Aquatic Sediments, 414 pp., Springer, New York.

Boudreau, R. A. (1996), A method-of-lines code for carbon and nutrient diagenesis in aquatic sediments, Comput. Geosci., 22, 479 –496.

Brenan, K. E., S. L. Campbell, and L. R. Petzold (1989), Numerical Solution of Initial-Value Problems in Differential-Algebraic Systems, Elsevier, New York.

Brown, J. G., R. L. Bassett, and P. D. Glynn (1998), Analysis and simulation of reactive transport of metal contaminants in ground water in Pinal Creek Basin, Arizona, J. Hydrol., 209, 225–250.

Brun, A., and P. Engesgaard (2002), Modelling of transport and biogeochemical processes in pollution plumes: Literature review and model development, J. Hydrol., 256, 211-227.

Canfield, D. E., B. Thamdrup, and J. W. Hansen (1993), The anaerobic degradation of organic matter in Danish coastal sediments: Iron reduction, manganese reduction, and sulphate reduction, Geochim. Cosmochim. Acta, 57, 3867-3883.

Chapelle, F. H. (2001), Ground-Water Microbiology and Geochemistry, 477 pp., John Wiley, Hoboken, N. J.

Chilakapati, A. (1995), RAFT: A simulator for reactive flow and transport of groundwater contaminants, Internal Rep. 10636, Pac. Northwest Lab., Richland, Wash.

Chilakapati, A., S. B. Yabusaki, J. Szecsody, and W. MacEvoy (2000), Groundwater flow, multicomponent transport and biogeochemistry: Development and application of a coupled process model, J. Contam. Hydrol., 43, 303 –325.

De Windt, L., D. Pellegrini, and J. van der Lee (2004), Coupled modeling of cement/claystone interactions and radionuclide migration, J. Contam. Hydrol., 68(3 –4), 165–182.

Dennis, J. E., Jr., and R. B. Schnabel (1996), Numerical Methods for Unconstrained Optimization and Nonlinear Equations, Classics Appl. Math., vol. 16, pp. 86 –91, SIAM, Philadelphia, Pa.

Dhakar, S. P., and D. J. Burdige (1996), A coupled, non-linear, steady state model for early diagenetic processes in pelagic sediments, Am. J. Sci., 296, 296–330.

Engesgaard, P., and R. Traberg (1996), Contaminant transport at a waste residue deposit: 2. Geochemical transport modeling, Water Resour. Res., 32(4), 939–952.

Freeze, R. A., and J. A. Cherry (1979), Groundwater, 604 pp., Prentice-Hall, Englewood Cliffs, N. J.

Gómez, C. (1990), MACROFORT: A FORTRAN code generator in MAPLE, Rapp. Tech. 119, Inst. Natl. de Rech. en Inf. et en Autom., Le Chesnay, France.

Hindmarsh, A. C., and L. R. Petzold (1995a), Algorithms and software for ordinary differential equations and differential/algebraic equations, Part 1: Euler methods and error estimation, Comput. Phys., 9, 34–41.

Hindmarsh, A. C., and L. R. Petzold (1995b), Algorithms and software for ordinary differential equations and differential/algebraic equations, Part 2: Higher-order methods and software packages, Comput. Phys., 9, 148–155.

Hunter, K. S., Y. Wang, and P. Van Cappellen (1998), Kinetic modeling of microbially-driven redox chemistry of subsurface environments: Coupling transport, microbial metabolism and geochemistry, J. Hydrol., 209, 53–80.

Jourabchi, P., P. Van Cappellen, and P. Regnier (2005), Quantitative interpretation of pH distributions in aquatic sediments: A reaction-transport modeling approach, Am. J. Sci., 305, 919-956.

Katsev, S., D. G. Rancourt, and I. L'Heureux (2004), dSED: A database tool for modeling sediment early diagenesis, Comput. Geosci., 30, 959 –967.

Langmuir, D. (1997), Aqueous Environmental Geochemistry, 600 pp., Prentice-Hall, Upper Saddle River, N. J.

Lawrence, C. R., and G. F. Groner (1973), CHEMCSMP: A CSMP/360 precomplier for kinetic chemical equations, Rep. P-4812, 27 pp., Rand, Santa Monica, Calif.

Lee, J.-Y., P. Tett, K. Jones, S. Jones, P. Luyten, C. Smith, and K. Wild-Allen (2002), The PROWQM physical-biological model with benthic-pelagic coupling applied to the northern North Sea, J. Sea Res., 48, 287–331.

MacQuarrie, K. T. B., E. A. Sudicky, and W. D. Robertson (2001), Multicomponent simulation of wastewater-derived nitrogen and carbon in shallow unconfined aquifers II. Model application to a field site, J. Contam. Hydrol., 47, 85 –104.

Mayer, K. U., E. O. Frind, and D. W. Blowes (2002), Multicomponent reactive transport modeling in variably saturated porous media using a generalized formulation for kinetically controlled reactions, Water Resour. Res., 38(9), 1174, doi:10.1029/2001WR000862.

Meile, C. (2003), Heterogeneity, uncertainty and process identification in early diagenesis: New model developments with applications to biological mixing, Geol. Ultraiectina, 231, 135 pp.

Meysman, F., J. J. Middelburg, P. Herman, and C. Heip (2003a), Reactive transport in surface sediments. I. Model complexity and software quality, Comput. Geosci., 29, 291-300.

Meysman, F., J. J. Middelburg, P. Herman, and C. Heip (2003b), Reactive transport in surface sediments. II. Media: An object-oriented problem-solving environment for early diagenesis, Comput. Geosci., 29, 301–318.

Mikhailov, M. D., and M. A. Aladjem (1981), Automatic solution of thermal problems, in Numerical Methods in Heat Transfer, edited by R. W. Lewis, K. Morgan, and O. C. Zienkiewicz, pp. 27–49, John Wiley, Hoboken, N. J.

Murphy, E. M., and T. R. Ginn (2000), Modeling microbial processes in porous media, Hydrogeol. J., 8, 142–158.

Person, M., and G. Garven (1994), A sensitivity study for the driving forces on fluid-flow during continental-drift basin evolution, Geol. Soc. Am. Bull., 106(4), 461–475.

Press, W. H., B. P. Flannery, S. A. Teukolsky, and W.T. Vetterling (1992), Numerical Recipes (Fortran Version), Cambridge Univ. Press, New York.

Quezada, C. R., T. P. Clement, and K.-K. Lee (2004), Generalized solution to multi-dimensional multi-species transport equations coupled with a first-order reaction network involving distinct retardation factors, Adv. Water Resour., 27, 507–520.

Regnier, P., and C. I. Steefel (1999), A high resolution estimate of the inorganic nitrogen flux from the Scheldt estuary to the coastal North Sea during a nitrogen-limited algal bloom, spring 1995, Geochim. Cosmochim. Acta, 63, 1359–1374.

Regnier, P., R. Wallast, and C. I. Steefel (1997), Long-term fluxes of reactive species in macrotidal estuaries: Estimates from a fully transient, multicomponent reaction-transport model, Mar. Chem., 58, 127–145.

Regnier, P., J. P. O'Kane, C. I. Steefel, and J. P. Vanderborght (2002), Modeling complex multi-component reactive-transport systems: Towards a simulation environment based on the concept of a Knowledge Base, Appl. Math. Modeling, 26, 913–927.

Regnier, P., P. Jourabchi, and C. P. Slomp (2003), Reactive-transport modeling as a technique for understanding coupled biogeochemical processes in surface and subsurface environments, Netherlands J. Geosci., 82(1), 5–18.

Reichert, P. (1994), Aquasim—A tool for simulation and data analysis of aquatic systems, Water Sci. Technol., 30, 21–30.

Schäfer, D., W. Schäfer, and W. Kinzelbach (1998a), Simulation of reactive processes related to biodegradation in aquifers: 1. Structure of the three-dimensional reactive transport model, J. Contam. Hydrol., 31, 167–186.

Schäfer, D., W. Schäfer, and W. Kinzelbach (1998b), Simulation of reactive processes related to biodegradation in aquifers: 2. Model application to a column study on organic carbon degradation, J. Contam. Hydrol., 31, 187– 209.

Soetaert, K., and P. M. J. Herman (1995), Nitrogen dynamics in the Westerschelde estuary (SW Netherlands) estimated by means of the ecosystem model MOSES, Hydrobiologia, 311, 225–246.

Soetaert, K., P. M. J. Herman, and J. J. Middelburg (1996), A model of early diagenetic processes from the shelf to abyssal depths, Geochim. Cosmochim. Acta, 60(6), 1019–1040.

Soetaert, K., J. J. Middelburg, P. M. J. Herman, and K. Buis (2000), On the coupling of benthic and pelagic biogeochemical models, Earth Sci. Rev., 51, 173–201.

Soler, J. M. (2003), Reactive transport modeling of the interaction between a high pH plume and a fractured marl: The case of Wellenberg, Appl. Geochem., 18, 1555 –1571.

Soler, J. M., and A. C. Lasaga (1998), An advection-dispersion-reaction model of bauxite formation, J. Hydrol., 209, 311–330.

Steefel, C. I., and P. C. Lichtner (1998a), Multicomponent reactive transport in discrete fractures: I. Controls on reaction front geometry, J. Hydrol., 209, 186–199.

Steefel, C. I., and P. C. Lichtner (1998b), Multicomponent reactive transport in discrete fractures: II: Infiltration of hyperalkaline groundwater at Maqarin, Jordan, a natural analogue site, J. Hydrol., 209, 200–224.

Steefel, C. I., and K. T. B. MacQuarrie (1996), Approaches to modeling of reactive transport in porous media, in Reactive Transport in Porous Media: General Principles and Application to Geochemical Processes, Rev. Mineral., vol. 34, edited by P. C. Lichtner, C. I. Steefel, and E. H. Oelkers, pp. 83–130, Mineral. Soc. of Am., Washington, D. C.

Steefel, C. I., and P. Van Cappellen (1998), Reactive transport modeling of natural systems, J. Hydrol., 209, 1–7.

Strang, G. (1988), Linear Algebra and Its Applications, pp. 32–39, W. B. Saunders, Philadelphia, Pa.

Thullner, M., M. H. Schroth, J. Zeyer, and W. Kinzelbach (2004), Modeling of a microbial growth experiment with bioclogging in a two-dimensional saturated porous media flow field, J. Contam. Hydrol., 70, 37–62.

Thullner, M., P. Van Cappellen, and P. Regnier (2005), Modeling the impact of microbial activity on redox dynamics in porous media, Geochim. Cosmochim. Acta, 69, 5005-5019.

Thyne, G., B. P. Boudreau, M. Ramm, and R. E. Midtbo (2001), Simulation of potassium feldspar dissolution and illitization in the Statfjord Formation, North Sea, AAPG Bull., 85(4), 621–635.

van Breukelen, B. M., J. Griffioen, W. F. M. Röling, and H. W. van Versefeld (2004), Reactive transport modelling of biogeochemical processes and carbon isotope geochemistry inside a landfill leachate plume, J. Contam. Hydrol., 70, 249–269.

Van Cappellen, P., and J.-F. Gaillard (1996), Biogeochemical dynamics in aquatic sediments, in Reactive Transport in Porous Media: General Principles and Application to Geochemical Processes, Rev. Mineral., vol. 34, edited by P. C. Lichtner, C. I. Steefel, and E. H. Oelkers, pp. 335 –376, Mineral. Soc. of Am., Washington, D. C.

Van Cappellen, P., and Y. Wang (1996), Cycling of iron and manganese in surface sediments: A general theory for the coupled transport and reaction of carbon, oxygen, nitrogen, sulfur, iron and manganese, Am. J. Sci., 296, 197–243.

Van der Lee, J., L. D. Windt, V. Lagneau, and P. Goblet (2003), Module-oriented modeling of reactive transport with HYTEC, Comput. Geosci., 29, 265–275.

Vanderborght, J. P., R. Wollast, M. Loijens, and P. Regnier (2002), Application of a transport-reaction model to the estimation of biogas fluxes in the Scheldt estuary, Biogeochemistry, 59(1–2), 207–237.

von Gunten, U., and J. Zobrist (1993), Biogeochemical changes in groundwater-infiltrations systems: Column studies, Geochim. Cosmochim. Acta, 57, 3895–3906.

Xu, T., J. Samper, C. Ayora, M. Manzano, and E. Custodio (1999), Modeling of non-isothermal multi-component reactive transport in field scale porous media flow systems, J. Hydrol., 214, 144–164.

Young, D. M., and M. D. Juncosa (1959), SPADE—A set of subroutines for solving elliptic and parabolic partial differential equations, Report P-1709, Rand, Santa Monica, Calif.

Quantitative interpretation of pH distributions in aquatic sediments: a reaction-transport modeling approach

Abstract

Despite its status of master variable, there have been relatively few attempts to quantitatively predict the distributions of pH in biogeochemical reactive transport systems. Here, we propose a theoretical approach for calculating the vertical pore water profiles of pH and the rates of proton production and consumption in aquatic sediments. In this approach, the stoichiometric coefficients of species that participate in acid-base equilibrium reactions are treated as unknown variables in the biogeochemical reaction network. The mixed kinetic-equilibrium reaction system results in a set of coupled differential and algebraic equations and is solved using a new numerical solver. The diagnostic capabilities of the model are illustrated for depositional conditions representative of those encountered on the continental shelf. The early diagenetic reaction network includes the major microbial degradation pathways of organic matter and associated secondary redox reactions, mineral precipitation and dissolution processes, and homogeneous acid-base reactions. The resulting pH profile in this baseline simulation exhibits a sharp decrease below the sediment-water interface, followed by an increase with depth and again a decrease. The features of the pH profile are explained in terms of the production and consumption of protons by the various biogeochemical processes. Secondary oxygenation reactions are the principal proton producers within the oxic zone, while reduction of iron and manganese oxyhydroxides are primarily responsible for the reversal in the pH gradient in the suboxic zone. Proton production in the zone of sulfate reduction outweighs alkalinity production, maintaining the undersaturation of the pore waters with respect to calcite. Integrated over the entire depth of early diagenesis, dissolution of $CaCO_3$ is the main sink for protons. Variations in the reaction rate order and rate constant for $CaCO_3$ dissolution do not fundamentally alter the shape of the pH profile. An entirely different shape is obtained, however, when the pore waters are assumed to remain in thermodynamic equilibrium with calcite at all depths. Pore water (bio)irrigation decreases the amplitude of pH changes in the sediment and may modify the shape of the pH profile.

1. Introduction

The dissolved hydrogen ion concentration is considered a master variable in aquatic (bio)geochemistry (Stumm and Morgan, 1996). The pH of the aqueous medium influences the occurrence and biochemical activity of organisms, the saturation state with respect to most reactive mineral phases, and the adsorption of soluble species. In turn, the spatial and temporal distribution of pH in a given environment may provide information on the biogeochemical reactivity and buffering capacity of the system.

The unique status of the aqueous hydrogen ion, H^+(aq), in the biogeochemistry of aquatic sediments has been reviewed in detail by Boudreau and canfield (1993). Measured pore water pH profiles exhibit distinct features, which can be related to bottom water chemistry, solid sediment composition, and redox reactions associated with the degradation of organic matter. In the majority of studies, however, pH profiles are only used as qualitative support for the interpretation of early diagenetic data sets, or they are imposed *a priori* when performing saturation state calculations (Hales and others, 1994; Cai and others, 1995; Reimers and others, 1996; Carman & Rahm, 1997; Hales and Emerson, 1997a; Hensen and others, 1997; Luff and others, 2000; Thamdrup and others, 2000; Adler and others, 2001; Wijsman and others, 2002; Müller and others, 2003; Forja and others, 2004).

The lack of systematic quantitative treatment of pH distributions in early diagenetic studies partially reflects the highly complex reaction network controlling the acid-base properties of pore waters (for example, Boudreau and Canfield, 1988). With the exception of water, H^+ (and OH^-) ions participate in more chemical reactions than any other species. Even in a closed-system, the calculation of pH due to biogeochemical reactions is not a simple task (Ben-Yaakov, 1973). The difficulty is compounded, by the coupling of reaction and transport processes in sediments. Kulik and others (2000) and Wijsman and others (2002) have reviewed the challenges of accurate and efficient computation of pH distributions in reactive transport models, while Luff and others (2001) provide a detailed comparison of three methods for their calculation: alkalinity conservation, charge balance, and the "advancement approach".

A limited number of early diagenetic reactive transport codes include an explicit calculation of pore water pH (see table 1, for a summary). In some models, a linear combination of a subset of dissolved species such as alkalinity or total dissolved inorganic carbon are transported as components, to which weighted average transport properties are assigned (for example, STEADYSED and CANDI, table 1). In other models (for example,

C. CANDI, MEDIA, and BRNS, table 1), transport fluxes are calculated for all individual species (for example, HCO_3^-, CO_3^{2-} and $CO_2 \equiv CO_2 + H_2CO_3$). Using a simple example, Luff and others (2001) demonstrate that transporting individual protolytic species participating in equilibrium reactions, rather than transporting components, can lead to non-negligible differences in species distributions among reactive transport models, unless the system is strongly dominated by calcium carbonate dissolution. Even in the latter case, the authors show that there can be significant differences in the calculated solute fluxes across the sediment water interface.

Because pH distributions are intimately linked to all major biogeochemical reaction processes in sediments, and because they can be measured accurately and with high vertical resolution (for example: Fisher and Matisoff, 1981; Archer and others, 1989; Cai and Reimers, 1993; Cai and others, 1995; Hales and Emerson, 1996; Reimers and others, 1996; Komada and others, 1998; Wenzhöfer and others, 2001), they possess unequalled diagnostic capabilities. To unlock these capabilities, however, it is necessary to combine measured pH profiles with a quantitative description of the production and consumption of H^+(aq) in sediments. In this paper, we address the theoretical challenges of modeling reactive transport in mixed kinetic-equilibrium reaction systems dominated by molecular diffusion of the solutes, and propose a general approach to include H^+(aq) in multi-species early diagenetic models. The added value of a process-based interpretation of pore water pH profiles is illustrated by performing steady state simulations of a representative continental shelf sediment.

Table 1

Comparison of existing reactive transport models (RTMs) of early diagenesis that consider both kinetic and equilibrium reactions.

Study/model	Numerical scheme	Steady state solution	Transport
This study/ BRNS-global	global	direct	species
Katsev and others (unpublished data) /LSSE	global	TD	species
Hales (2003)	OS	direct	species
Luff and others (2003) /C.CANDI	global	TD	species & components
Meysman and others (2003) /MEDIA	global	TD	species
Archer and others (2002) /Muds	global	direct	components
Regnier and others (2002) /BRNS-OS	OS	TD	species
Adler and others (2001) /CoTReM	OS	TD	species
Hensen and others (1997) /CoTAM	OS	TD	species
Jahnke and others (1997)	global	TD	species
Boudreau (1996) /CANDI	global	TD	components
Van Cappellen and Wang (1995) /SteadySed	global	direct	components
Archer and others (1989)	global	TD (solids) direct (solutes)	species

The numerical scheme is noted as either global or operator splitting (OS). In the first case, at every time step or iteration, the concentrations of all species are solved for simultaneously at all spatial nodes. In the second case, at every time step or iteration, transport (of every species or component) and reaction (at every spatial node) calculations are performed in sequence.

The method of obtaining steady state solutions is divided into two categories. In the time-dependent (TD) approach the transient solution is allowed to evolve until it meets a pre-defined criterion indicating no further change in the species concentrations with time. In the direct solution the net rate of change of each species concentrations is set to zero, and the set of coupled ordinary differential equations representing mass conservation are solved directly.

The RTMs may be based on mass balance equations written either for individual chemical species, or for components (linear combinations of subsets of chemical species), thereby reducing the number of state variables. In the latter approach, the transport properties of each component are calculated as the weighted average of the properties of individual species comprising the component. Three models (Hales and others, 2003; LSSE; MEDIA) use components for mass balance equations, yet compute the concentration and gradient of individual species in calculating the mass flux of the component.

2. Theory

2.1. Mass Conservation

Reactive transport in sediments is described by the general diagenetic equation for mass conservation of solid and dissolved species (Berner, 1980). Using C_k to represent the concentration of a solid or dissolved species, this equation can be written as:

$$\frac{\partial(\xi_k C_k)}{\partial t} = -\nabla \cdot F_k + \sum_i s_k^i R^i + \alpha_k \xi_k (C_{k0} - C_k),$$ (1)

where t is time, F_k is the sum of all advective and diffusive fluxes of the kth species, s_k^i is the stoichiometric coefficient of species k in the kinetically controlled reaction i, with rate R^i (expressed per unit of total volume of sediment), and ξ_k is the volume fraction in which the concentration of species k is defined. For example, in a two phase (solid/solute) system, the concentration of a dissolved species is usually given in units of mass per unit volume of pore water, hence, ξ_k = porosity (ϕ). Likewise, for a solid species, whose concentration is expressed per unit volume of solid sediment, $\xi_k = (1 - \phi)$. Pore water irrigation is included in the mass conservation equation as a source or sink function analogous to a kinetic rate. It is calculated as the product of the irrigation intensity, α_k ($\alpha_k = 0$ for all solids) and the difference in concentration of species k relative to the concentration at the sediment-water interface (SWI), C_{k0}.

In the absence of externally impressed flow, the advective and diffusive fluxes in equation (1) arise from sediment burial (rate = ω_k), biodiffusional mixing or bioturbation (coefficient = D_b), and molecular diffusion (coefficient = D_k). While we assume that D_b is the same for all species, the burial rate of solids may differ from that of the dissolved species, for instance due to sediment compaction. By expanding the flux term in equation (1) in one-dimension, we obtain

$$\frac{\partial(\xi_k C_k)}{\partial t} = -\frac{\partial(\xi_k \omega_k C_k)}{\partial x}$$
$$+ \frac{\partial}{\partial x}\left(D_b \varphi \frac{\partial(\xi_k C_k)}{\partial x} + D_b(1-\varphi)\xi_k \frac{\partial C_k}{\partial x} + D_k \xi_k \frac{\partial C_k}{\partial x} \right) + \sum_i s_k^i R^i + \alpha_k (C_{k0} - C_k),$$ (2)

where x is depth into the sediment ($x = 0$ at the SWI) and $D_k = 0$ for all solid species. Equation (2) is based on the general diagenetic equation presented by Berner (1980), where the parameter, φ, defines the mixing model used in describing bioturbation ($0 < \varphi < 1$). The end member mixing models are (1) interphase mixing with $\varphi = 1$, in which the solids and pore waters are assumed to intermix in the bioturbation process, hence altering the depth

dependence of porosity, and (2) intraphase mixing with $\varphi = 0$, in which sediment porosity is assumed to be unaffected (Boudreau, 1986; Mulsow and others, 1998). In this paper, the intraphase mixing model is used.

In general, the rate of a kinetically controlled reaction (or 'slow' reaction) is a function of a subset of the species concentrations. The full mathematical description of the reactive transport system thus requires the solution of a set of coupled partial differential equations in the form of equation (2). In the absence of fast reversible reactions, and when the stoichiometric coefficients, s_k^i, and transport properties of each species are well defined, the number of unknown state variables (C_k) is equal to the number of partial differential equations. The latter can be solved numerically with appropriately specified initial and boundary conditions.

However, due to 'fast' reversible reactions, which algebraically relate some of the species concentrations through mass action laws, it is not possible to uniquely specify, *a priori*, the stoichiometric coefficients of these species involved in the kinetic reactions, at all points in time and space. To illustrate with a simple example, consider the bacterially mediated oxidation of organic matter (represented by the simplified formula CH_2O) by O_2 in pure water with no gas exchange. The state variables are CH_2O, O_2, the three carbonate species (CO_2, HCO_3^-, and CO_3^{2-}), protons (H^+), hydroxyls (OH^-), and H_2O (table 2). Although the stoichiometric coefficient of total dissolved inorganic carbon, *DIC* can be defined exactly,

$$CH_2O + O_2 \rightarrow DIC + s_6^1 H^+ + s_7^1 OH^- + s_8^1 H_2O , \qquad\qquad R^1 \qquad\qquad (3a)$$
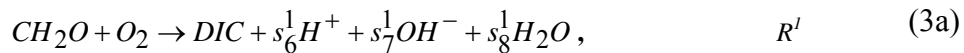
those of the protons, hydroxyls, individual carbonate species, and H_2O depend upon the speciation of *DIC* and water as governed by the equilibria

$$CO_2 \leftrightarrow H^+ + HCO_3^-$$
$$HCO_3^- \leftrightarrow H^+ + CO_3^{2-} , \qquad\qquad (3b)$$
$$H_2O \leftrightarrow H^+ + OH^-$$
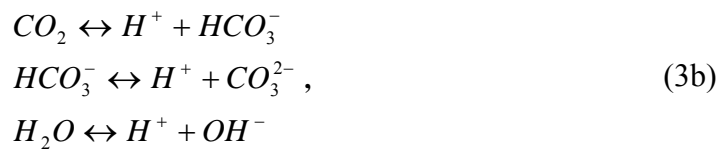
and their corresponding mass action laws,

$$K_1^* = \frac{[H^+][HCO_3^-]}{[CO_2]} = \frac{C_6 C_4}{C_3}$$

$$K_2^* = \frac{[H^+][CO_3^{2-}]}{[HCO_3^-]} = \frac{C_6 C_5}{C_4} \quad .$$

$$K_3^* = \frac{[H^+][OH^-]}{[H_2O]} = \frac{C_6 C_7}{C_8}$$

(4)

The dissociation constants K_1^*, K_2^*, and K_3^* of carbonic acid, bicarbonate, and water, used in the mass action laws (eqs 4) correspond to apparent (or otherwise referred to as stoichiometric) constants based on a total concentration scale (Pilson, 1998). They may therefore vary with temperature, pressure, ionic strength and relative composition of the solution.

Table 2

Species and stoichiometric coefficients in a
simple system involving only oxic respiration of
organic matter (CH_2O) as kinetic reaction process.

Species # k	Species	s_k^1
1	CH_2O	-1
2	O_2	-1
3	CO_2	Variable
4	HCO_3^-	Variable
5	CO_3^{2-}	Variable
6	H^+	Variable
7	OH^-	Variable
8	H_2O	Variable

Taking into account all possible species, reaction (3a) can now be rewritten as

$$s_1^1 CH_2O + s_2^1 O_2 \rightarrow s_3^1 CO_2 + s_4^1 HCO_3^- + s_5^1 CO_3^{2-} + s_6^1 H^+ + s_7^1 OH^- + s_8^1 H_2O,$$ (5)

where the stoichiometric coefficients of 6 of the 8 species are additional unknowns in the system (table 2). Omitting the concentration of H_2O as an explicit state variable (Morel & Hering, 1993), the solution of the system of 7 partial differential equations expressing mass conservation of the 7 unknown concentrations, $C_1 - C_7$, requires prior knowledge of s_3^1, s_4^1, s_5^1, s_6^1 and s_7^1. However, fulfilling the equilibrium conditions gives rise to three additional constraints through the mass action laws (eqs 4), which together with conservation of total dissolved inorganic carbon and charge balance, close the full mathematical description of the

system of 12 unknowns (7 species and 5 stoichiometric coefficients) and 12 linearly independent equations (7 partial differential and 5 algebraic equations).

2.2. Stoichiometric Coefficients

The following is a derivation of expressions for the stoichiometic coefficients of protolytic species in an example seawater system, considering the acid-base equilibria for borates, sulfides, and carbonates. It should be noted that the approach based on stoichiometric coefficients can, in principle, be extended to other equilibrium reactions, including heterogeneous reactions such as adsorption or mineral solubility reactions. The common variable in all equilibrium conditions considered here is the total proton concentration $[H^+]$, which includes not only the proton or hydronium ion concentration, but also the concentrations of HSO_4^- and HF in solution, in accordance with the seawater scale for pH (Pilson, 1998).

To calculate the rate of production or consumption of protons by a given kinetically controlled reaction i, with rate R^i, we define the stoichiometric coefficients of total dissolved inorganic carbon (T_C), total dissolved sulfide (T_S), total dissolved borate (T_B), and total alkalinity (T_A) to be t_c^i, t_s^i, t_b^i, and t_a^i, respectively, such that

$$\left.\frac{dT_C}{dt}\right|_i = t_c^i R^i$$

$$\left.\frac{dT_S}{dt}\right|_i = t_s^i R^i$$

$$\left.\frac{dT_B}{dt}\right|_i = t_b^i R^i \qquad (6)$$

$$\left.\frac{dT_A}{dt}\right|_i = t_a^i R^i$$

These stoichiometric coefficients (t_c^i, t_s^i, t_b^i, and t_a^i) are uniquely defined for each kinetic reaction, i, and remain constant at all points in time and space. It is important to note that the time derivatives in equation (6) refer only to rates of change due to kinetic reactions. In the following, we assume that there are no reactions affecting the concentration of total borates and, thus, $t_b^i = 0$ for all i.

Using the total proton concentration as the master variable, each equilibrium species concentration can be written as a fraction of the total component concentration

$$[HCO_3^-] = \chi_1 T_C$$
$$[CO_3^{2-}] = \chi_2 T_C$$
$$[CO_2] = \chi_3 T_C$$
$$[HS^-] = \sigma_1 T_S \qquad ,$$
$$[H_2S] = \sigma_2 T_S$$
$$[B(OH)_4^-] = \beta_1 T_B$$
$$[B(OH)_3] = \beta_2 T_B$$

(7)

where the fractions are

$$\chi_1 \equiv \frac{K_1^*[H^+]}{[H^+]^2 + K_1^*[H^+] + K_1^* K_2^*}$$

$$\chi_2 \equiv \chi_1 \frac{K_2^*}{[H^+]}$$

$$\chi_3 \equiv 1 - \chi_1 - \chi_2$$

$$\sigma_1 \equiv \frac{K_4^*}{K_4^* + [H^+]}$$

(8)

$$\sigma_2 \equiv 1 - \sigma_1$$

$$\beta_1 \equiv \frac{K_5^*}{K_5^* + [H^+]}$$

$$\beta_2 \equiv 1 - \beta_1$$

In the above equations, we use the apparent dissociation constants, K_4^* and K_5^*, for the dissociation of H₂S and B(OH)₃, respectively. As with K_1^*, K_2^*, and K_3^*, these parameters depend on the pressure, temperature, ionic strength and relative composition of the solution.

From the definition of total alkalinity in our system,

$$T_A = T_C(\chi_1 + 2\chi_2) + T_S \sigma_1 + T_B \beta_1 + \frac{K_3^*}{[H^+]} - [H^+],$$

(9)

the rate of alkalinity production by a given kinetic reaction i is derived as

$$\left.\frac{dT_A}{dt}\right|_i = \left.\frac{dT_C}{dt}\right|_i (\chi_1 + 2\chi_2) + T_C \frac{\partial(\chi_1 + 2\chi_2)}{\partial[H^+]} \left.\frac{d[H^+]}{dt}\right|_i + \left.\frac{dT_S}{dt}\right|_i \sigma_1 + T_S \frac{\partial\sigma_1}{\partial[H^+]} \left.\frac{d[H^+]}{dt}\right|_i$$

$$+ \left.\frac{dT_B}{dt}\right|_i \beta_1 + T_B \frac{\partial\beta_1}{\partial[H^+]} \left.\frac{d[H^+]}{dt}\right|_i - \frac{K_3^*}{[H^+]^2} \left.\frac{d[H^+]}{dt}\right|_i - \left.\frac{d[H^+]}{dt}\right|_i + \sum_{m=1}^{N_{eq}} \eta_m \left.\frac{dK_m^*}{dt}\right|_i,$$

(10)

which can also be expressed in terms of the instantaneous rates of T_A, T_C, and T_S production (eq 6)

$$\left(t_a^i - t_c^i(\chi_1 + 2\chi_2) - t_s^i\sigma_1\right)R^i =$$
$$\left(T_C \frac{\partial(\chi_1 + 2\chi_2)}{\partial[H^+]} + T_S \frac{\partial\sigma_1}{\partial[H^+]} + T_B \frac{\partial\beta_1}{\partial[H^+]} - \frac{K_3^*}{[H^+]^2} - 1\right)\frac{d[H^+]}{dt}\bigg|_i + \sum_{m=1}^{N_{eq}} \eta_m \frac{dK_m^*}{dt}\bigg|_i \cdot \qquad (11)$$

The last term on the right hand side (RHS) of equations (10) and (11) represents the rate of change of each of the N_{eq} apparent equilibrium constants, K_m^*, due to changes in the activity coefficients of the solute species (Appendix I).

In systems where the apparent dissociation constants are assumed to be invariant with respect to time and space, the instantaneous rate of proton production/consumption can be solved for explicitly. This assumption allows us to express the instantaneous rate of proton production or consumption due to each kinetically controlled reaction *i,* as

$$\frac{d[H^+]}{dt}\bigg|_i = \frac{t_a^i - (\chi_1 + 2\chi_2)t_c^i - t_s^i\sigma_1}{A_1}R^i . \qquad (12)$$

where A_1 is defined by

$$A_1 \equiv T_C \frac{\partial\chi_1}{\partial[H^+]} + 2T_C \frac{\partial\chi_2}{\partial[H^+]} + T_S \frac{\partial\sigma_1}{\partial[H^+]} + T_B \frac{\partial\beta_1}{\partial[H^+]} - \frac{K_3}{[H^+]^2} - 1. \qquad (13)$$

Thus, the stoichiometric coefficient of protons for each reaction *i* is

$$s_{H^+}^i = \frac{t_a^i - (\chi_1 + 2\chi_2)t_c^i - t_s^i\sigma_1}{A_1}, \qquad (14)$$

which depends on the proton concentration and can be used in conjunction with equations (7) and (8) in order to calculate the stoichiometric coefficients of the remaining protolytic species. The explicit calculation of proton production or consumption rates (eq 12) provides the basis for the quantitative interpretation of the pore water pH distribution in terms of individual reactions.

2.3. Numerical Solution

A method for the numerical solution of the Differential-Algebraic Equation (DAE) system is presented in two parts. In the first part, we describe the spatially discretized mass conservation equation for a single species. This equation is then used in the second part to derive a global implicit equation for all species at all nodes in the model domain. A summary of the symbols used in this section is provided in table 3.

Table 3

Description of symbols used in the proposed numerical solution (*section 2.3*).
Arrows and bold font are used to indicate vectors and matrices, respectively.
The dimension of all vectors and matrices are provided in square brackets.

x	depth into the sediment ($x = 0$ at the SWI)
t	time
N_x	number of spatial nodes in the model domain
N_s	number of species
$C_{\ell/k}^{j}$	species ℓ/k concentration at node j
$R^{i,j}$	rate of reaction i at node j
α_k^{j}	irrigation intensity of species k at node j
$s_k^{i,j}$	stoichiometric coefficient of species k in reaction i at node j
R_k^{j}	total rate (source and sink) of species k at node j
$\vec{C}_k$	concentration vector of species k for all nodes $[N_x]$
$\vec{\mathsf{R}}_k$	total rate vector of species k for all nodes $[N_x]$
$\boldsymbol{T}_k$	tri-diagonal transport matrix for species k $[N_x, N_x]$
$\boldsymbol{\xi}_k$	diagonal volume fraction matrix for species k $[N_x, N_x]$
Δt	time step
N	number of species times the number of nodes ($N_s N_x$)
$\boldsymbol{J}^{j}$	jacobian matrix of total rates with respect to species at node j $[N_s, N_s]$
$\vec{C}$	concentration vector for all species at all nodes $[N]$
$\vec{\mathsf{R}}$	total rates vector for all species at all nodes $[N]$
$\boldsymbol{T}$	(diagonal-)block tri-diagonal transport matrix $[N, N]$
$\boldsymbol{\xi}$	diagonal volume fraction matrix $[N, N]$
$\boldsymbol{J}$	block diagonal jacobian matrix $[N, N]$
$\vec{C}\big|_{eq}$	equilibrium concentration vector of all species at all nodes (see text) $[N]$
$\boldsymbol{\beta}^{j}$	diagonal Lagrange multiplier matrix at node j $[N_s, N_s]$
$\boldsymbol{\beta}$	Diagonal Lagrange multiplier matrix at all nodes $[N, N]$
$\boldsymbol{G}$	block tri-diagonal matrix (see fig. 1) $[N, N]$
$\vec{d}$	vector on the RHS of equation in the global approach (see fig. 1) $[N]$
$\boldsymbol{G}^{j}$	diagonal block j of $\boldsymbol{G}$ $[N_s, N_s]$

2.3.1. Discretized equation for a single species.

For each of the N_s chemical species in the mixed kinetic-equilibrium reaction system, the mass conservation equation (2) is spatially discretized as

$$\frac{\partial(\boldsymbol{\xi}_k \vec{C}_k)}{\partial t} = \boldsymbol{T}_k \vec{C}_k + \vec{\mathsf{R}}_k , \qquad (15)$$

in which $\boldsymbol{T}_k$ is the N_x by N_x tri-diagonal matrix containing the transport terms and boundary conditions of species k, N_x denoting the number of spatial nodes in the model domain. The vectors $\vec{C}_k$ and $\vec{R}_k$ are each of length N_x. Their respective elements are the concentration of species k and the sum of all sources and sinks affecting species k, respectively, at every node in the model domain. The volume fractions at each node are represented by the diagonal matrix, $\boldsymbol{\xi}_k$, of dimension N_x by N_x. In $\boldsymbol{\xi}_k$, every diagonal entry represents the volume fraction at a specific node in the domain for species k.

The sources and sinks are defined by all the kinetic reaction rates and irrigation intensities, and their corresponding stoichiometric coefficients, affecting species, k, at every node, j, such that every element in vector $\vec{R}_k$ can be represented by

$$R_k^j \equiv \sum_i s_k^{i,j} R^{i,j} + \alpha_k^j \xi_k^j \left(C_{k0} - C_k^j\right), \tag{16}$$

where $R^{i,j}$ is the rate of reaction i, as defined in *section 2.1*, at node j and $s_k^{i,j}$ is the stoichiometric coefficient of the kth species in the ith reaction at node j.

2.3.2. Discretized equation for all species: global implicit scheme.

The spatially discretized reaction-transport equations for all species k result in a set of N_s non-linear equations, each of which has a unique transport matrix $\boldsymbol{T}_k$. The reaction terms couple the set of equations at each node, j, as the rates may depend on more than one species concentration. The set of equations are solved iteratively by using implicit numerical schemes for the transport and reaction terms. The latter is approximated by a first-order Taylor series expansion with respect to each of the species concentrations. Note that $\boldsymbol{T}_k$ may depend on the species concentration through composition-dependent diffusion coefficients (Van Cappellen & Gaillard, 1996).

The Taylor expansion of the total rate terms and the temporal discretization of equation (15) is detailed in Appendix II. The discretized mass conservation equation (II-4) can be recast as

$$\left(\boldsymbol{\xi} - \Delta t \boldsymbol{T} - \Delta t \boldsymbol{J}\big|_{old}^{t_{m+1}}\right)\vec{C}\big|_{new}^{t_{m+1}} = \boldsymbol{\xi}\vec{C}\big|^{t_m} - \Delta t \boldsymbol{J}\big|_{old}^{t_{m+1}}\vec{C}\big|_{old}^{t_{m+1}} + \Delta t \vec{R}\big|_{old}^{t_{m+1}}, \tag{17}$$

and solved iteratively for the transient solution. In order to obtain the steady state solution, the rate of change of species concentrations on the left hand side of equation (II-4) is set to zero, and an initial guess for $\vec{C}\big|_{old}$ is used to calculate $\vec{C}\big|_{new}$:

$$\left(\boldsymbol{T} + \boldsymbol{J}\big|_{old}\right)\vec{C}\big|_{new} = \boldsymbol{J}\big|_{old}\,\vec{C}\big|_{old} - \vec{\mathrm{R}}\big|_{old}\,.\tag{18}$$

2.3.3. Incorporation of equilibrium constraints.

As discussed in *section 2.1*, solution of equation (17) or (18) requires values for the stoichiometric coefficients, s_k^i, of the species involved in the fast acid-base reactions. Some reactive transport models decouple the computations involving the algebraic equations for the equilibrium constraints, from those involving the differential equations arising from the mass balance of components (for example, Marzal and others, 1994; Van Cappellen and Wang, 1995). In these models, the operator-splitting of the equilibrium and kinetic calculations is combined with a sequential iterative approach to reach convergence of the species concentrations. Here, we have directly implemented the equilibrium constraints in the discretized mass balance equations (that is, equation 17 or 18 for transient or steady state conditions) through the use of stoichiometric coefficients s_k^i.

Prior to each iteration step, the concentration values $\vec{C}\big|_{old}$ are used to define the conserved quantities corresponding to the equilibrium reactions. In the example described in *section 2.2*, these quantities are T_C, T_S, T_B and T_A. At this point, if necessary, the ionic strength of the solution, the activity coefficients, ionic diffusion coefficients, and the apparent equilibrium constants can be updated using appropriate models (for example, non-ideal effects can be accounted for by ion pairing calculations or Pitzer's equations). An equilibrium speciation module then calculates the corresponding equilibrium concentrations for the subset of species involved in the equilibrium reactions, $\vec{C}\big|_{eq}$, from which the unknown stoichiometric coefficients, s_{eq}^i to be used in the kinetic reactions are derived.

In the approach outlined above, the stoichiometric coefficient of protons (as defined, for example, by equation (14) in the example of *section 2.2*) and the proton concentration are defined independently of the stoichiometric coefficients of the other equilibrium acid-base species. That is, the mathematical system of algebraic-differential equations is over-determined and one of the equations must be omitted. A natural choice is to eliminate the mass balance equation of the proton itself. The proton (or pH) distribution can then be viewed as the necessary condition for closure of the mixed kinetic-equilibrium reactive transport system. An important advantage of this choice is that it eliminates the uncertainties

associated with the deviating diffusion behavior of protons in aqueous solution (for example, Cussler, 1984).

In our global approach, the equilibrium constraints are coupled to the transport and kinetic reactions calculations by introducing a Lagrange multiplier term,

$$\boldsymbol{\beta}\left(\left.\vec{C}\right|_{new} - \left.\vec{C}\right|_{eq} \right),$$ (19)

in equation (17) or (18). For every node in the model domain, the Lagrange multiplier β^{j}, is set to the largest transport coefficient in the corresponding diagonal block of matrix $\boldsymbol{T}$. For consistency, $\left.\vec{C}\right|_{eq}$ is defined as a vector of length $N_s N_x$, where the entries corresponding to species not involved in the equilibrium reactions are simply assigned their $\left.\vec{C}\right|_{old}$ values. Following this strategy, $\boldsymbol{\beta}$ is thus defined as a diagonal matrix of the same shape and dimension as $\boldsymbol{\xi}$. This approach is preferred, because it ensures a fast and robust convergence to the solution.

The final equations obtained for the iterative solutions of the transient and steady state cases are then, respectively

$$\left(\boldsymbol{\xi} - \Delta t\boldsymbol{T} - \Delta t\boldsymbol{J}\big|_{old}^{t_{m+1}} + \Delta t\boldsymbol{\beta} \right)\vec{C}\Big|_{new}^{t_{m+1}} = \boldsymbol{\xi}\,\vec{C}\Big|^{t_m} - \Delta t\boldsymbol{J}\big|_{old}^{t_{m+1}}\,\vec{C}\Big|_{old}^{t_{m+1}} + \Delta t\vec{R}\big|_{old}^{t_{m+1}} + \Delta t\boldsymbol{\beta}\vec{C}\Big|_{eq},$$ (20)

and

$$\left(\boldsymbol{T} + \boldsymbol{J}\big|_{old} + \boldsymbol{\beta} \right)\vec{C}\Big|_{new} = \boldsymbol{J}\big|_{old}\,\vec{C}\big|_{old} - \vec{R}\big|_{old} + \boldsymbol{\beta}\vec{C}\big|_{eq}.$$ (21)

2.3.4. Numerical implementation

For both transient and steady state solutions, the numerical equation to be solved at each iteration step, assumes the general form

$$\boldsymbol{G}\vec{C}\Big|_{new} = \vec{d},$$ (22)

with $\boldsymbol{G}$ as a sparse, N by N, block tri-diagonal matrix,

$$
\boldsymbol{G} = \begin{bmatrix} \begin{bmatrix} \boldsymbol{G}^1 \\ & \ddots \end{bmatrix} & \begin{bmatrix} \ddots \\ \boldsymbol{G}^2 \end{bmatrix} & \ddots & & \\ & \ddots & \ddots & \ddots & \\ & & \ddots & \begin{bmatrix} \boldsymbol{G}^{N_x-1} \end{bmatrix} & \begin{bmatrix} \ddots \end{bmatrix} \\ & & & \begin{bmatrix} \ddots \end{bmatrix} & \begin{bmatrix} \boldsymbol{G}^{N_x} \end{bmatrix} \end{bmatrix},
\tag{23}
$$

and $\bar{d}$ is a vector of length N. The block matrices, $\boldsymbol{G}^j$ ($j = 1$ to N_x), are each of dimension N_s by N_s. The proposed iterative procedure for the numerical solution of transient and steady state simulations is summarized in figure 1.
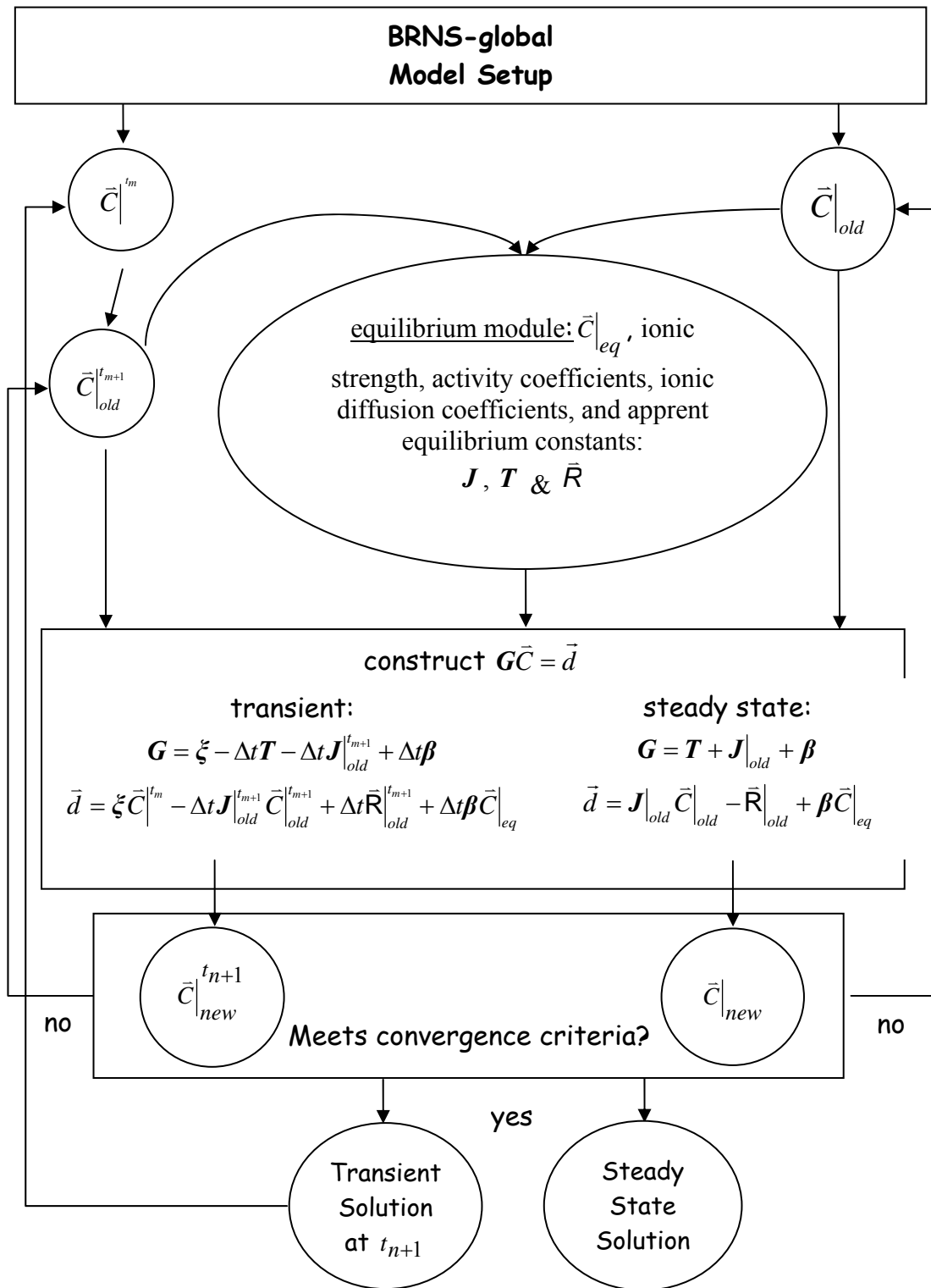
Fig. 1: Schematic flow chart of the global implicit solver.

The reaction network is implemented in the Biogeochemical Reaction Network Simulator (BRNS©), a flexible simulation environment for multicomponent reaction transport calculations (Regnier and others, 2002; Aguilera and others, 2005; see also

www.geo.uu.nl/~kbrtm).   All the reactions, transport processes, parameter values, boundary conditions and physical domain characteristics are defined by the user via a Maple$^{©}$ interface worksheet.   An automatic code generator (ACG) then produces and compiles the corresponding FORTRAN code, providing the user with the corresponding model executable. In particular, for any reactive transport application, the ACG automatically constructs the elements of the Jacobian matrix plus enables the construction of $\mathbf{G}$ and $\bar{d}$. It is a modified version of the ACG presented in Aguilera and others, 2005, where further details about the methodology are provided. As the proposed approach facilitates modification and expansion of the reaction network, the BRNS is a particularly flexible tool for the reactive transport simulation of complex biogeochemical problems.

3. Application

The proposed modeling approach is used to compute the vertical distributions of pH and proton production/consumption rates in a model sediment representative of depositional environments encountered on the continental shelves. A major goal of the application is to illustrate how pH depth profiles can be interpreted in terms of proton production or consumption by the various biogeochemical processes in the sediment. Sediment properties, the reaction network, and reaction plus transport parameters are taken from Van Cappellen & Wang (1995). The main differences with the simulations presented by these authors are the inclusion of calcite dissolution and boric acid dissociation in the reaction network.

First, results of a baseline simulation are shown in which pore water irrigation is omitted ($\alpha = 0$, *section 3.1*). Second, the proton production and consumption rates (as described in *section 2.2*, equation 12) are used in the interpretation of the model predicted pH profile (*section 3.2*). *Section 3.3* presents an analysis of the effects of sulfate reduction and sulfur cycling on pH and calcite saturation. Finally, in *sections 3.4* and *3.5*, the effects of calcite dissolution and pore water irrigation on the pH distribution are further explored.

For simplicity, we limit ourselves to steady state simulations. Due to the high ionic strength and uniform electrolyte composition of seawater, which mask changes of the pore water ionic medium due to early diagenetic reactions, we further assume that the apparent acid dissociation constants do not vary with depth. This assumption may no longer be valid in nearshore settings where variations in sulfate concentration may significantly change the ionic composition, and thereby affect the total hydrogen ion concentration (Gaillard and others, 1989; see also *section 3.3*). The contribution of protons and hydroxyl ions to total alkalinity are assumed to be negligible. The resulting pH and alkalinity profiles provide *a posteriori* validation of this assumption for all the simulation results presented.

The use of mass conservation equation (1) requires a consistent set of units for the specification of mass, length, and time. In the definition of model parameters and presentation of the simulation results, we use units of years for time, g for mass, and moles in specifying the concentration units. Whereas the length units of cm are commonly used in the specification of the physical parameters (e.g. sedimentation rate, diffusion coefficient), the more convenient unit of dm^3 (that is, L) is used in specifying the solute concentrations. Furthermore, the unit of moles per gram of solid sediment (rather than per cm^3) is used to define the concentrations of the solid species, by assuming a constant density for the solid

sediment (ρ_s). As such, the mass balance equations are further scaled by $1/\rho_s$ for the solids and $\frac{1000 cm^3}{1L}$ for the solutes.

3.1. Baseline Model Setup and Simulation Results

Most chemical and biological transformations occuring in marine sediments are linked to the oxidation of deposited organic matter (Berner, 1980). The pathways of organic carbon oxidation are therefore referred to as the primary redox reactions (Van Cappellen and Gaillard, 1996). These reactions proceed in the order of decreasing free energy yield and result in the production of reduced chemical species, for example, NH_4^+, Mn^{2+}, Fe^{2+}, HS^-, and CH_4. The upward migration of the reduced species into more oxidizing sediment layers causes their re-oxidation via a set of secondary redox reactions, which sustain a continuous, early diagenetic cycle of redox-sensitive elements such as N, S, Fe and Mn. Especially for iron, manganese and sulfur, the redox cycles involve the dissolution and precipitation of mineral phases.

An important mineral dissolution/precipitation system is that of calcium carbonate. While, strictly speaking, the dissolution and precipitation reactions of $CaCO_3$ are not redox-dependent, variations in the saturation state of pore waters with respect to calcite are intimately linked to the network of primary and secondary redox reactions through their effects on T_A and T_C (Hales, 2003). In the simulations performed here, calcite dissolution is included as a possible reaction pathway, with a rate that depends on the degree of pore water undersaturation. It is assumed that the sediments are deposited in bottom waters that are moderately supersaturated with respect to calcite.

The reaction network of primary and secondary redox processes, non-redox mineral precipitation or dissolution reactions, plus the acid-base equilibria of the carbonate, sulfide, and boric acid systems, considered in the baseline scenario is summarized in table 4. It contains a total of 24 reaction pathways and 23 individual species. Although additional reaction processes and species are important, the set of reactions in table 4 captures the essence of the redox and acid-base dynamics of early diagenesis in marine sediments. The baseline sediment model thus serves to illustrate the potential use of reaction transport modeling as a diagnostic tool for interpreting pore water pH profiles. Chemical species that participate in the equilibrium reactions are represented in the reaction formulas of the kinetically-controlled processes with their variable stoichiometric coefficients, s_{keq}^i. The (fixed) stoichiometric coefficients describing production of T_C, T_S and T_A by the kinetic

reactions are listed in table 5. The rate laws for the kinetic reactions and the equilibrium conditions for the homogeneous acid-base reactions are given in table 6.

At the upper boundary (SWI), fixed concentrations are assigned to the solute species, while deposition fluxes are specified for the solid species (table 7). The lower boundary conditions are defined at a sufficiently great depth, such that all concentration gradients vanish as reaction rates approach zero. The molecular diffusion coefficients listed in table 7 are adjusted for the viscosity and temperature of the bottom water (for details, see Van Cappellen and Wang, 1995, and Boudreau, 1997). Tables 8 and 9 provide all the physical and reaction model parameters, plus the domain definition. Equilibrium constants are corrected for the pressure, temperature, and salinity conditions at the seafloor (Pilson, 1998; Millero and Sohn, 1992; Wang and Van Cappellen, 1996).

Table 4

The reaction network.

Primary Redox Reactions

R^1. oxic respiration
$$(CH_2O)(NH_3)_y(H_3PO_4)_z + O_2 \rightarrow \sum_{keq} s^1_{keq} C_{keq} + yNH_4^+ + zHPO_4^{2-}$$

R^2. Denitrification
$$(CH_2O)(NH_3)_y(H_3PO_4)_z + [(4+3y)/5]NO_3^- \rightarrow \sum_{keq} s^2_{keq} C_{keq} + [(2+4y)/5]N_2 + zHPO_4^{2-}$$

R^3. Mn(IV) reduction
$$(CH_2O)(NH_3)_y(H_3PO_4)_z + 2MnO_2 \rightarrow \sum_{keq} s^3_{keq} C_{keq} + 2Mn^{2+} + yNH_4^+ + zHPO_4^{2-}$$

R^4. Fe(III) reduction
$$(CH_2O)(NH_3)_y(H_3PO_4)_z + 4Fe(OH)_3 \rightarrow \sum_{keq} s^4_{keq} C_{keq} + 4Fe2^+ + yNH_4^+ + zHPO_4^{2-}$$

R^5. sulfate reduction
$$(CH_2O)(NH_3)_y(H_3PO_4)_z + (1/2)SO_4^{2-} \rightarrow \sum_{keq} s^5_{keq} C_{keq} + yNH_4^+ + zHPO_4^{2-}$$

R^6. methanogenesis
$$(CH_2O)(NH_3)_y(H_3PO_4)_z \rightarrow \sum_{keq} s^6_{keq} C_{keq} + yNH_4^+ + zHPO_4^{2-} + (1/2)CH_4$$

Table 4
(continued)

Secondary Redox Reactions

R^7. nitrification

$$NH_4^+ + 2O_2 \rightarrow \sum_{keq} s_{keq}^7 C_{keq} + NO_3^-$$

R^8. Mn^{2+} re-oxidation by O_2

$$Mn^{2+} + (\tfrac{1}{2})O_2 \rightarrow \sum_{keq} s_{keq}^8 C_{keq} + MnO_2$$

R^9. Fe^{2+} re-oxidation by O_2

$$Fe^{2+} + (1/4)O_2 \rightarrow \sum_{keq} s_{keq}^9 C_{keq} + Fe(OH)_3$$

R^{10}. Fe^{2+} re-oxidation by MnO_2

$$2Fe^{2+} + MnO_2 \rightarrow \sum_{keq} s_{keq}^{10} C_{keq} + 2Fe(OH)_3 + Mn^{2+}$$

R^{11}. sulfide re-oxidation by O_2

$$2O_2 \rightarrow \sum_{keq} s_{keq}^{11} C_{keq} + SO_4^{2-}$$

R^{12}. sulfide re-oxidation by MnO_2

$$MnO_2 \rightarrow \sum_{keq} s_{keq}^{12} C_{keq} + Mn^{2+} + S^0$$

R^{13}. sulfide re-oxidation by $Fe(OH)_3$

$$2Fe(OH)_3 \rightarrow \sum_{keq} s_{keq}^{13} C_{keq} + 2Fe^{2+} + S^0$$

R^{14}. methane re-oxidation by O_2

$$CH_4 + 2O_2 \rightarrow \sum_{keq} s_{keq}^{14} C_{keq}$$

R^{15}. methane re-oxidation by SO_4^{2-}

$$CH_4 + SO_4^{2-} \rightarrow \sum_{keq} s_{keq}^{15} C_{keq}$$

R^{16}. FeS re-oxidation by O_2

$$FeS + 2O_2 \rightarrow Fe^{2+} + SO_4^{2-}$$

Table 4
(continued)

Mineral Precipitation / Dissolution

R^{17}. CaCO$_3$ dissolution
$$CaCO_3 \rightarrow \sum_{keq} s^{17}_{keq} C_{keq} + Ca^{2+}$$

R^{18}. FeS precipitation
$$Fe^{2+} \rightarrow \sum_{keq} s^{18}_{keq} C_{keq} + FeS$$

R^{19}. MnCO$_3$ precipitation
$$Mn^{2+} \rightarrow \sum_{keq} s^{19}_{keq} C_{keq} + MnCO_3$$

R^{20}. FeCO$_3$ precipitation
$$Fe^{2+} \rightarrow \sum_{keq} s^{20}_{keq} C_{keq} + FeCO_3$$

Equilibrium Conditions

Eq1. carbonic acid dissociation
$H_2O + CO_2 \leftrightarrow HCO_3^- + H^+$

Eq2. bicarbonate dissociation
$HCO_3^- \leftrightarrow CO_3^{2-} + H^+$

Eq3. sulfide dissociation
$H_2S \leftrightarrow HS^- + H^+$

Eq4. boric acid dissociation
$B(OH)_3 + H_2O \leftrightarrow B(OH)_4^- + H^+$

For each kinetic reaction, *i*, the sum of species involved in the equilibrium conditions are expressed as:

$$\sum_{keq} s^i_{keq} C_{keq} = s^i_{co2}[CO_2] + s^i_{hco3}\left[HCO_3^-\right] + s^i_{co3}\left[CO_3^{2-}\right] + s^i_{h2s}[H_2S] + s^i_{hs}\left[HS^-\right] +$$

$$s^i_{boh3}[B(OH)_3] + s^i_{boh4}\left[B(OH)_4^-\right] + s^i_h\left[H^+\right] + s^i_{oh}\left[OH^-\right] \quad ,$$

where the stoichiometric coefficients of total components:

$$t^i_c = s^i_{co2} + s^i_{hco3} + s^i_{co3}$$

$$t^i_a = s^i_{hco3} + 2s^i_{co3} + s^i_{hs} + s^i_{boh4} + s^i_{oh} - s^i_h$$

$$t^i_s = s^i_{h2s} + s^i_{hs}$$

are given in table 5; y and z denote the nitrogen to carbon ratio (N:C) and the phosphorus to carbon ratio (P:C) of the degrading organic matter, respectively.

The simulated depth distributions of concentrations of chemical species and components are presented in figures 2 to 4. On the basis of the model results, three chemical redox zones can be delineated; the oxic (0 – 1.5 cm), suboxic (1.5 – 3.2 cm) and anoxic (> 3.2 cm) zone. The oxic/suboxic interface is defined here as the depth at which the aerobic respiration and denitrification rates are equal (not shown). Similarly, the suboxic/anoxic interface is defined as the depth at which the dissimilatory Fe(III) reduction and sulfate reduction rates are equal (not shown). Figure 4 shows that the depth profiles of pH and the concentrations of dissolved carbonate and borate species exhibit marked changes at these interfaces, hence illustrating the close coupling of redox and acid-base chemistry in the reaction transport system. The apparent activity coefficient of protons (f_{H+} in table 9) is used to display pH on the NBS scale.
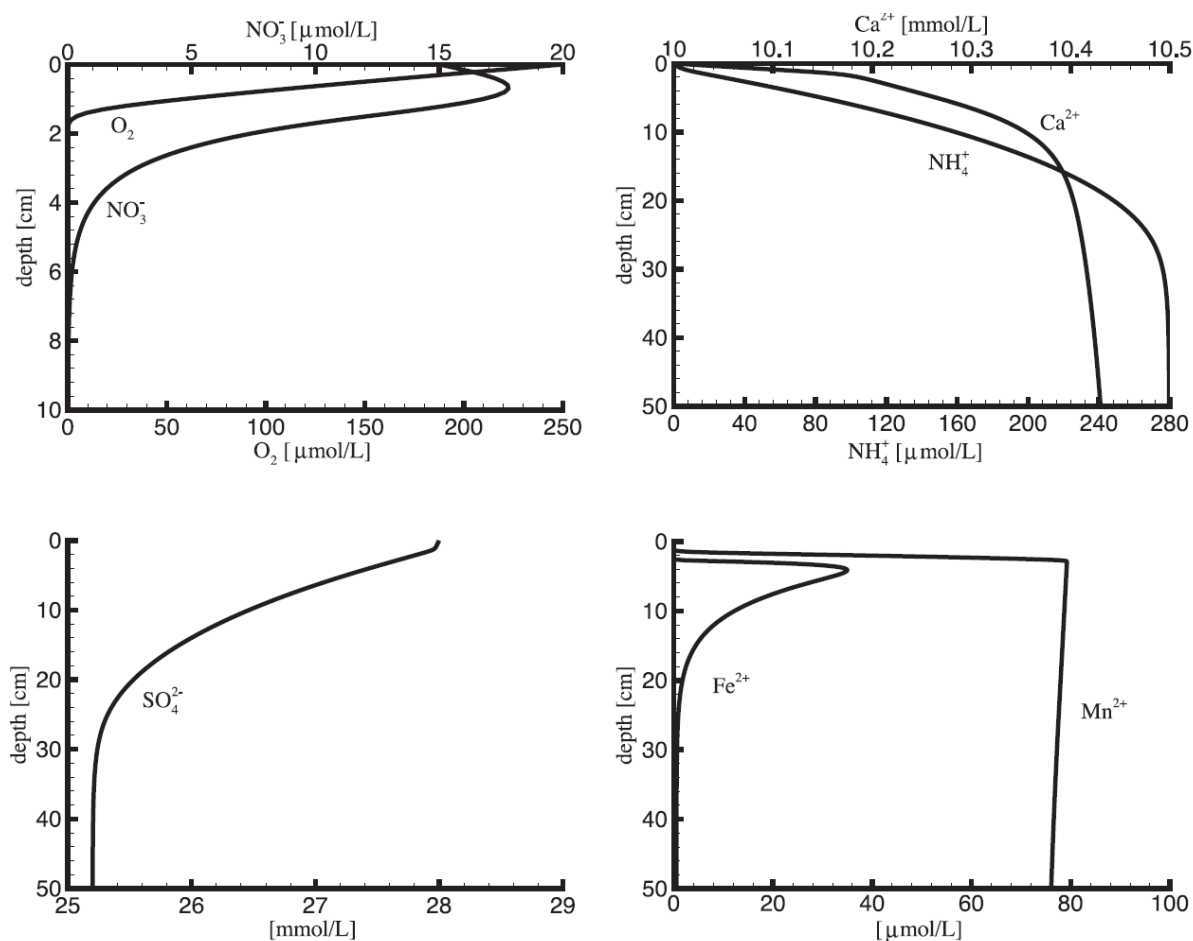
Fig. 2: Distributions of the non-protolytic solute species in the baseline simulation. Sulfate approaches a finite constant value at depth, when all of the reactive organic matter is degraded (fig. 3). Aqueous Fe and Mn concentrations build up in the suboxic layer and decrease in the anoxic zone by mineral precipitation reactions (see text).
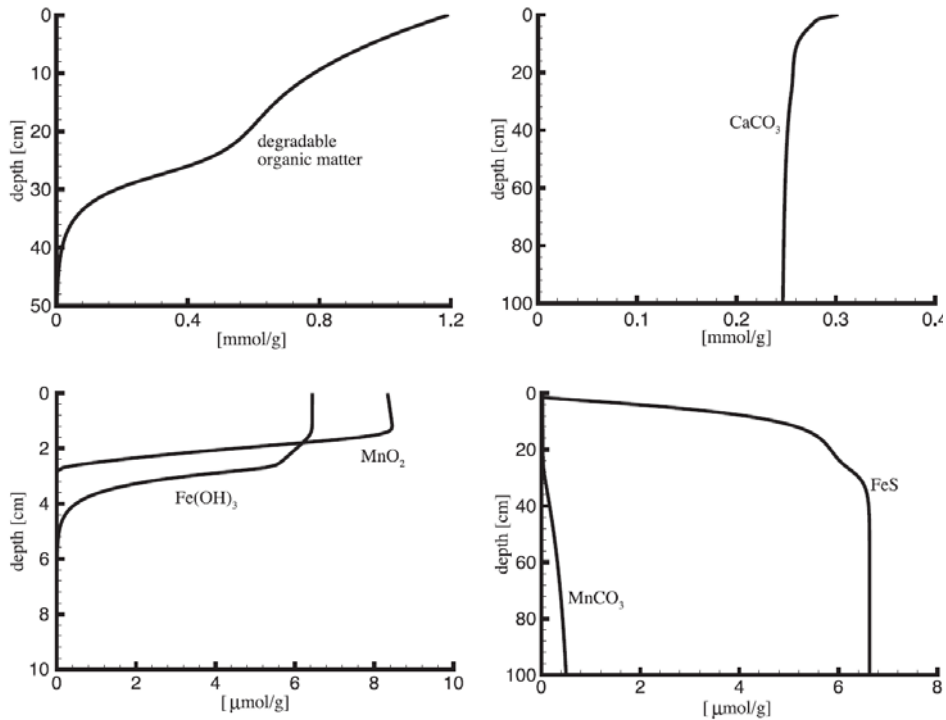
Fig. 3: Distributions of the solid species in the baseline simulation. Nearly all reactive organic carbon is degraded in the top 50 cm of the sediment, while 75% of calcite reaching the sediment dissolves in the top 15 cm. Precipitation of carbonate and sulfide minerals act as permanent sinks of reactive Fe and Mn (see text).
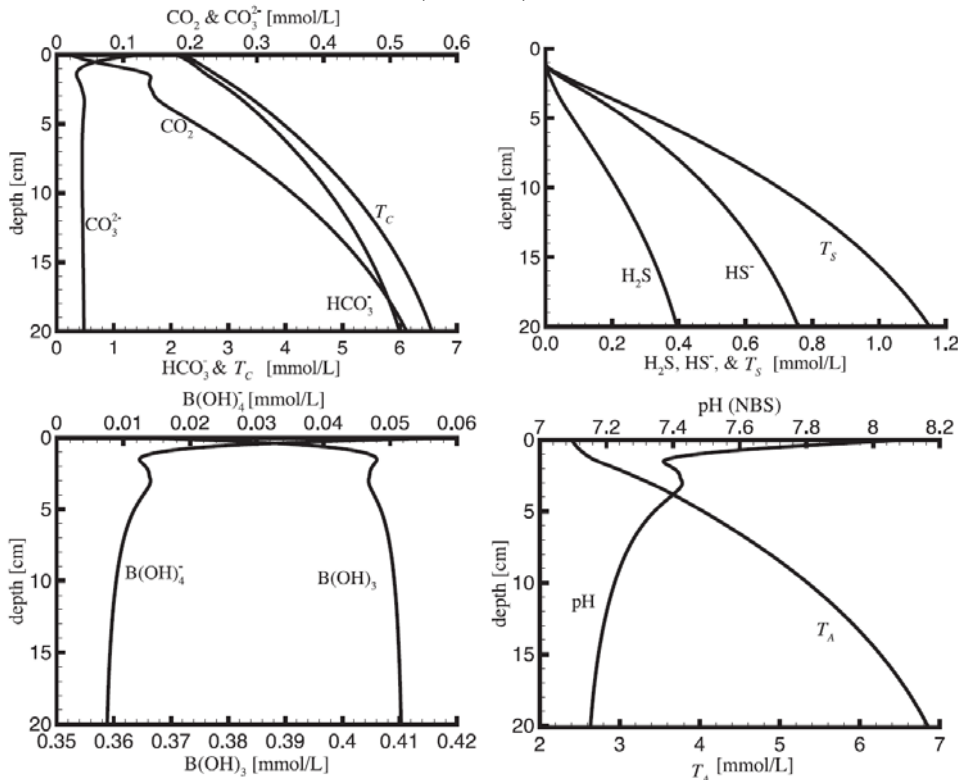
Fig. 4: Pore water distributions of protolytic species, total dissolved inorganic carbon (T_C), total alkalinity (T_A), total sulfides (T_S), and pH in the baseline scenario. The pH profile exhibits a local minimum at the oxic/suboxic interface (1.5 cm) and a local maximum at 3.0 cm near the suboxic/anoxic interface (3.2 cm).
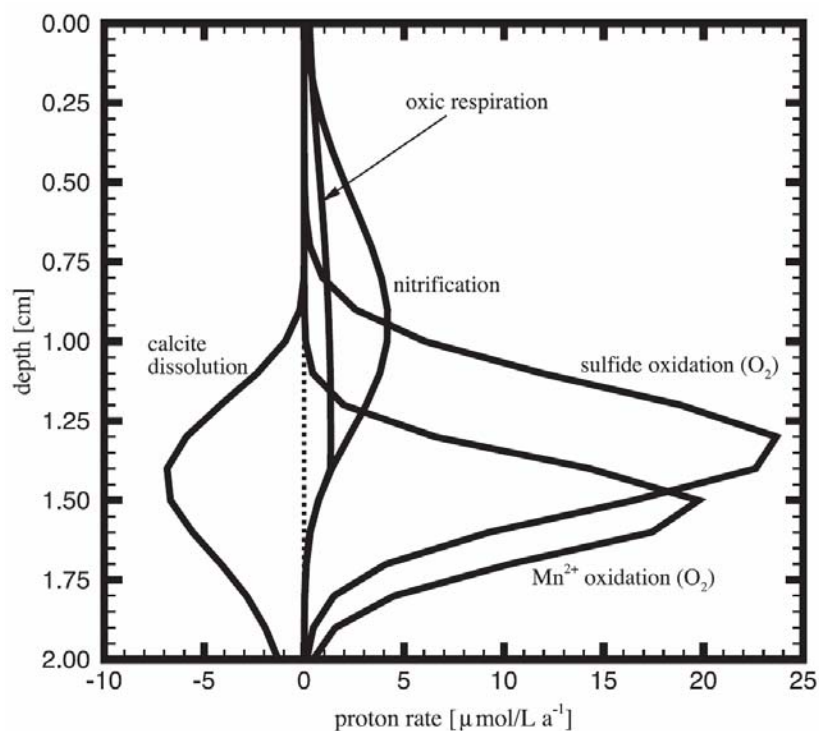
Fig. 5: Proton rates in the oxic zone: results of the baseline simulation.

Table 5

Stoichiometric coefficients of the components for each reaction i: the components refer to total dissolved inorganic carbon (t_c^i), total alkalinity (t_a^i), and total sulfides (t_s^i).

Reaction i	t_c^i	t_a^i	t_s^i
R^1	1	(y-2z)	0
R^2	1	(4+3y-10z)/5	0
R^3	1	(4+y-2z)	0
R^4	1	(8+y-2z)	0
R^5	1	(1+y-2z)	1/2
R^6	1/2	(y-2z)	0
R^7	0	-2	0
R^8	0	-2	0
R^9	0	-2	0
R^{10}	0	-2	0
R^{11}	0	-2	-1
R^{12}	0	2	-1
R^{13}	0	4	-1
R^{14}	1	0	0
R^{15}	1	2	1
R^{16}	0	0	0
R^{17}	*1*	2	0
R^{18}	0	-2	-1
R^{19}	-1	-2	0
R^{20}	-1	-2	0

While a direct comparison of model predicted pH profiles with measured profiles is beyond the scope of this paper, it is worth noting that the major features of the pH profile of our baseline simulation are consistent with published pore water pH data sets. In particular, the reader is referred to the studies of Cai and Reimers (1993), Cai and others (1995, 2000), Hensen and others (1997), Luff and others (2000), Adler and others (2001), Wenzhöfer and others (2001), Wijsman and others (2002), and Forja and others (2004). These studies show that a sharp drop in pH near the SWI followed by a local minimum in pH deeper in the sediment is commonly seen in marine sediments overlain by oxygenated waters, from coastal to deep-sea environments.

All the degradable organic carbon in the baseline scenario is oxidized in the top 50 cm of the sediment (fig. 3), at which point a high dissolved sulfate concentration remains (fig. 2). Thus, in this particular early diagenetic scenario, methanogenesis is inhibited and no methane is produced. Oxic degradation and secondary redox reactions with NH_4^+, Fe^{2+} and Mn^{2+} deplete oxygen in the first few centimeters of the sediment (fig. 2). The interplay between denitrification and nitrification reactions results in the occurrence of a peak in the nitrate profile near the sediment water interface, while NH_4^+ released from the degradation of organic carbon builds up with depth into the sediment (fig. 2). Calcite dissolution increases the pore water calcium ion concentrations by about 4% relative to the overlying seawater (fig. 2).

A significant fraction of the deposited calcite dissolves, most of it in the upper 15 cm (fig. 3). That is, pore water pH buffering by $CaCO_3$ dissolution extends well below the oxic zone of the sediment. In the anoxic zone, iron sulfide precipitation causes the near complete removal of dissolved Fe^{2+} from the pore waters (figs. 2 and 3). In contrast, dissolved Mn^{2+} builds up to high levels, because of less efficient removal by $MnCO_3$ precipitation. As a result, most dissolved Mn^{2+} returns to the oxic zone where it oxidatively precipitates. This explains why the concentrations of reactive Mn oxide exceed those of reactive Fe oxide (fig. 3), despite the lower deposition flux of reactive Mn oxide (table 7).

Table 6

Kinetic reaction rate laws and equilibrium mass action laws for the baseline simulation

Kinetic Rate Laws

$$R^1 = f_{O_2} k_c \left[CH_2O\right] (1-\phi)\rho_s, \text{ where } \begin{cases} f_{O_2} = 1 \text{ for } [O_2] > K_{O2} \\ f_{O_2} = \dfrac{[O_2]}{K_{O2}} \text{ for } [O_2] \leq K_{O2} \end{cases}$$

$$R^2 = f_{NO_3^-} k_c \left[CH_2O\right] (1-\phi)\rho_s, \text{ where } \begin{cases} f_{NO_3^-} = 0 \text{ for } f_{O_2} = 1 \\ f_{NO_3^-} = \left(1 - f_{O_2}\right) \text{ for } f_{O_2} < 1 \text{ and } \left[NO_3^-\right] > K_{NO3} \\ f_{NO_3^-} = \left(1 - f_{O_2}\right)\dfrac{\left[NO_3^-\right]}{K_{NO3}} \text{ for } f_{O_2} < 1 \text{ and } \left[NO_3^-\right] \leq K_{NO3} \end{cases}$$

$$R^3 = f_{MnO_2} k_c \left[CH_2O\right] (1-\phi)\rho_s, \text{ where } \begin{cases} f_{MnO_2} = 0 \text{ for } f_3 \equiv f_{O_2} + f_{NO_3^-} = 1 \\ f_{MnO_2} = \left(1 - f_3\right) \text{ for } f_3 < 1 \text{ and } \left[MnO_2\right] > K_{MnO2} \\ f_{MnO_2} = \left(1 - f_3\right)\dfrac{\left[MnO_2\right]}{K_{MnO2}} \text{ for } f_3 < 1 \text{ and } \left[MnO_2\right] \leq K_{MnO2} \end{cases}$$

$$R^4 = f_{Fe(OH)_3} k_c \left[CH_2O\right] (1-\phi)\rho_s, \text{ where } \begin{cases} f_{Fe(OH)_3} = 0 \text{ for } f_4 \equiv f_{O_2} + f_{NO_3^-} + f_{MnO_2} = 1 \\ f_{Fe(OH)_3} = \left(1 - f_4\right) \text{ for } f_4 < 1 \text{ and } \left[Fe(OH)_3\right] > K_{FeOH3} \\ f_{Fe(OH)_3} = \left(1 - f_4\right)\dfrac{\left[Fe(OH)_3\right]}{K_{FeOH3}} \text{ for } f_4 < 1 \text{ and } \left[Fe(OH)_3\right] \leq K_{FeOH3} \end{cases}$$

$$R^5 = f_{SO_4^{2-}} k_c \left[CH_2O\right] (1-\phi)\rho_s, \text{ where } \begin{cases} f_{SO_4^{2-}} = 0 \text{ for } f_5 \equiv f_{O_2} + f_{NO_3^-} + f_{MnO_2} + f_{Fe(OH)_3} = 1 \\ f_{SO_4^{2-}} = \left(1 - f_5\right) \text{ for } f_5 < 1 \text{ and } \left[SO_4^{2-}\right] > K_{SO4} \\ f_{SO_4^{2-}} = \left(1 - f_5\right)\dfrac{\left[SO_4^{2-}\right]}{K_{SO4}} \text{ for } f_5 < 1 \text{ and } \left[SO_4^{2-}\right] \leq K_{SO4} \end{cases}$$

$$R^6 = \left(1 - f_{O_2} - f_{NO_3^-} - f_{MnO_2} - f_{Fe(OH)_3} - f_{SO_4^{2-}}\right) k_c \left[CH_2O\right] (1-\phi)\rho_s$$

$$R^7 = k_7 \left[NH_4^+\right] \left[O_2\right] \phi\left(\frac{1L}{10^3 cm^3}\right)$$

$$R^8 = k_8 \left[Mn^{2+}\right] \left[O_2\right] \phi\left(\frac{1L}{10^3 cm^3}\right)$$

$$R^9 = k_9 \left[Fe^{2+}\right] \left[O_2\right] \phi\left(\frac{1L}{10^3 cm^3}\right)$$

$$R^{10} = k_{10} \left[Fe^{2+}\right] \left[MnO_2\right] (1-\phi)\rho_s$$

$$R^{11} = k_{11} \left[O_2\right] \left(\left[H_2S\right] + \left[HS^-\right]\right) \phi\left(\frac{1L}{10^3 cm^3}\right)$$

$$R^{12} = k_{12} \left[MnO_2\right] \left(\left[H_2S\right] + \left[HS^-\right]\right) (1-\phi)\rho_s$$

$$R^{13} = k_{13} \left[Fe(OH)_3\right] \left(\left[H_2S\right] + \left[HS^-\right]\right) (1-\phi)\rho_s$$

$$R^{14} = k_{14} \left[CH_4\right] \left[O_2\right] \phi\left(\frac{1L}{10^3 cm^3}\right)$$

$$R^{15} = k_{15} \left[CH_4\right] \left[SO_4^{2-}\right] \phi\left(\frac{1L}{10^3 cm^3}\right)$$

Table 6

(continued)

$$R^{16} = k_{16}\left[FeS\right]\left[O_2\right](1-\phi)\rho_s$$

$$R^{17} = \begin{cases} 0 \text{ for } \Omega_{17} \equiv \dfrac{\left[Ca^{2+}\right]\left[CO_3^{2-}\right]}{K_{s17}} > 1 \\ k_{17}\left[CaCO_3\right]\left(1-\Omega_{17}\right)^n(1-\phi)\rho_s \text{ for } \Omega_{17} \leq 1 \end{cases}$$

$$R^{18} = \begin{cases} 0 \text{ for } \Omega_{18} \equiv \dfrac{\left[Fe^{2+}\right]\left[HS^-\right]}{\left[H^+\right]K_{s18}} \leq 1 \\ k_{18}\left(\Omega_{18}-1\right)\phi\left(\dfrac{1L}{10^3 cm^3}\right) \text{ for } \Omega_{18} > 1 \end{cases}$$

$$R^{19} = \begin{cases} 0 \text{ for } \Omega_{19} \equiv \dfrac{\left[Mn^{2+}\right]\left[CO_3^{2-}\right]}{K_{s19}} \leq 1 \\ k_{19}\left(\Omega_{19}-1\right)\phi\left(\dfrac{1L}{10^3 cm^3}\right) \text{ for } \Omega_{19} > 1 \end{cases}$$

$$R^{20} = \begin{cases} 0 \text{ for } \Omega_{20} \equiv \dfrac{\left[Fe^{2+}\right]\left[CO_3^{2-}\right]}{K_{s20}} \leq 1 \\ k_{20}\left(\Omega_{20}-1\right)\phi\left(\dfrac{1L}{10^3 cm^3}\right) \text{ for } \Omega_{20} > 1 \end{cases}$$

Mass Action Laws

$$Eq1: K_1^* = \frac{\left[H^+\right]\left[HCO_3^-\right]}{\left[CO_2\right]}$$

$$Eq2: K_2^* = \frac{\left[H^+\right]\left[CO_3^{2-}\right]}{\left[HCO_3^-\right]}$$

$$Eq3: K_4^* = \frac{\left[H^+\right]\left[HS^-\right]}{\left[H_2S\right]}$$

$$Eq4: K_5^* = \frac{\left[H^+\right]\left[B(OH)_4^-\right]}{\left[B(OH)_3\right]}$$

Formulations taken from Van Cappellen and Wang (1995) with the exception of R^{17} for calcite dissolution, which is adapted from Keir (1980). All parameter values are specified in table 9. The species concentrations are defined in units of moles per gram of solid sediment and moles per liter of pore water volume for the solids and solutes, respectively. For simplicity, the concentration of $(CH_2O)(NH_3)_y(H_3PO_4)_z$ is denoted by $[CH_2O]$.
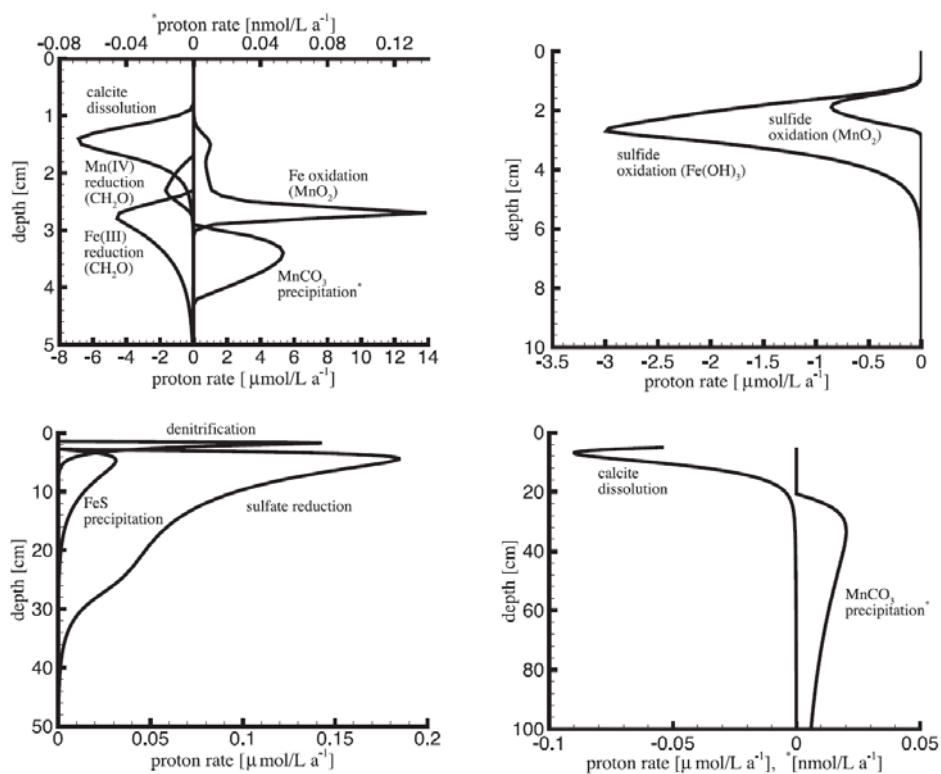
Fig. 6: Proton rates in the suboxic and anoxic zones: results of the baseline simulation. Note that variable scales are used for the depth and rates in order to highlight the main features of the profiles.
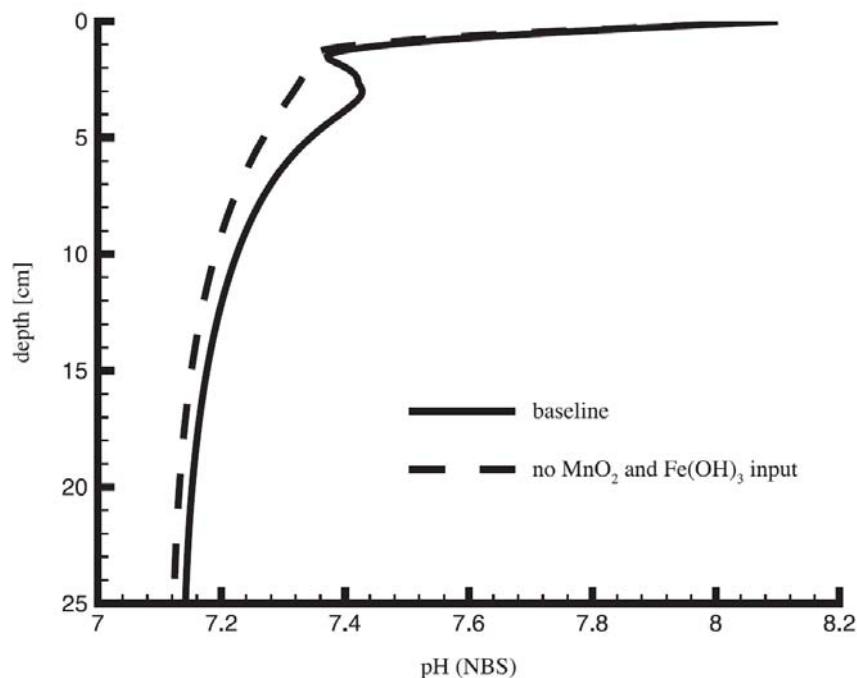

Fig. 7: pH profiles in the baseline simulation (solid line) and in the absence of deposition of reactive Fe and Mn (hydr)oxides (broken line).

Table 7

Species, boundary conditions, and molecular diffusion coefficients used in the baseline simulation

Species	Upper Boundary Condition	Molecular Diffusion [$cm^2 \, a^{-1}$]
O_2	250	459
NO_3^-	15	411
HCO_3^-	2088	243
CO_3^{2-}	126	195
CO_2	21	386
H^+	$(10^{-8.1})/f_{H+}$	-
CH_2O	80 (F)	0
Ca^{2+}	10^4	165
$CaCO_3$	20 (F)	0
NH_4^+	0	421
SO_4^{2-}	28×10^3	190
Mn^{2+}	0	140
MnO_2	1.2×10^{-2} (F)	0
Fe^{2+}	0	148
$Fe(OH)_3$	10^{-1} (F)	0
H_2S	0	400
HS^-	0	388
FeS	0 (F)	0
$FeCO_3$	0 (F)	0
$MnCO_3$	0 (F)	0
CH_4	0	303
$B(OH)_3$	60	123
$B(OH)_4^-$	365	108

The boundary condition is specified as fixed concentration in units of μmoles $L^{-1}_{porewater}$ for solute species, and as flux (F) for all solid species in units of μmoles $cm^{-2} \, a^{-1}$. The boundary conditions are taken from Van Cappellen and Wang (1995) except for the flux of calcite and the concentration of total borates; Flux of calcite is taken from Tsunogoi & Noriki (1991) for a water depth of 130 m; Total borates is calculated as a function of salinity according to Millero and Sohn (1992). See table 9 for the activity coefficient of protons, f_{H+}. The molecular diffusion coefficients are adapted from Li and Gregory (1974), Lerman (1979), Boudreau and Canfield (1993), and Iverson and Jørgensen (1993). The temperature, salinity, porosity, and pressure corrections were carried out according to Boudreau (1997).

Table 8

Physical parameters used in the baseline simulation

Burial (ω)	0.04	cm a^{-1}
Bioturbation coefficient at SWI (D_{b0})*	3	cm^2 a^{-1}
Porosity (ϕ)	0.85	
Temperature (T)	10	$^{\circ}$C
Pressure (P)	13	bar
Salinity (S)	35	‰
Number of nodes (N_x)	251	
Max depth	165	cm
Solid density (ρ_s)	2.5	g cm^{-3}
Fluid density (ρ_f)	1027.5	kg m^{-3}
α_k	0	cm a^{-1}

The bioturbation coefficient, D_b is a function of depth, *x* in cm:

$$D_b(x) = \frac{D_{b0}}{2} \, \text{erfc}\left(\frac{(x-20)}{4}\right),$$ where erfc is the complementary error function. A variable grid spacing that ranges from 0.1 cm at SWI to 2.0 cm at depth is used here. Burial rate, porosity, temperature, and solid density are taken from Van Cappellen and Wang (1995). The pressure is calculated from UNESCO web site, assuming a seafloor depth of 130 m as representative of shelf sediments (Millero and Sohn 1992). Fluid density for the given temperature, pressure, and salinity taken from UNESCO equation of state (Chester, 2000).

Table 9

Parameters for the reaction network and stoichiometric coefficients

Parameter Name	Parameter Value	Units	Reaction(s)
k_c	10^{-2}	a^{-1}	1-6
K_{O2}	8×10^{-6}	mol/L	1-6
K_{NO3}	10^{-5}	mol L	2-6
K_{MnO2}	2×10^{-6}	mol/g	3-6
K_{FeOH3}	5×10^{-6}	mol/g	4-6
K_{SO4}	10^{-3}	mol/L	5-6
y (N:C)	21/200		1-6
z (P:C)	1/200		1-6
k_7	1.5×10^7	L mol^{-1} a^{-1}	7
k_8	2×10^9	L mol^{-1} a^{-1}	8
k_9	2×10^9	L mol^{-1} a^{-1}	9
k_{10}	2×10^8	L mol^{-1} a^{-1}	10
k_{11}	6×10^8	L mol^{-1} a^{-1}	11
k_{12}	10^4	L mol^{-1} a^{-1}	12
k_{13}	10^4	L mol^{-1} a^{-1}	13
k_{14}	10^{10}	L mol^{-1} a^{-1}	14
k_{15}	10^{10}	L mol^{-1} a^{-1}	15
k_{16}	2.2×10^7	L mol^{-1} a^{-1}	16
K_{s17}	4.42×10^{-7}	mol^2 kg^{-2}	17
k_{17}	18.3	a^{-1}	17
n	4.5		17
k_{18}	5×10^{-6}	mol L^{-1} a^{-1}	18
k_{19}	10^{-5}	mol L^{-1} a^{-1}	19
k_{20}	10^{-6}	mol L^{-1} a^{-1}	20
K_{s18}	$(6.3 \times 10^{-3}) f_{H+}$	mol/L	18
K_{s19}	3.2×10^{-9}	mol^2 L^{-2}	19
K_{s20}	4×10^{-9}	mol^2 L^{-2}	20
f_{H+}	0.77		
K_1^*	$(8.05 \times 10^{-7})/f_{H+}$	mol/L	Eq1

Table 9
(continued)

K_2^*	$(4.8 \times 10^{-10})/f_{H+}$	mol/L	Eq2
K_4^*	$(1.35 \times 10^{-7})/f_{H+}$	mol/L	Eq4
K_5^*	$(1.3 \times 10^{-9})/f_{H+}$	mol/L	Eq5

See text for rate constant of calcite dissolution and rate order, n. The apparent equilibrium constants ($K_1^*, K_2^*, K_3^*, K_4^*$, and K_5^*) are calculated for the given temperature, salinity and pressure based on the total hydrogen ion (seawater) scale (Stumm and Morgan, 1996; Pilson, 1998). The apparent activity coefficient of hydrated proton or hydrogen ion, $f_{H+,}$ is calculated for the given salinity and temperature according to Pilson, 1998.

3.2. Proton Production and Consumption Rates

In what follows, the model-predicted pH profile (fig. 4) is interpreted in terms of the rates of production and consumption of H^+ by the various biogeochemical reactions taking place in the sediment (eq 12). Figures 5 and 6 present the depth profiles of the dominant proton rates in the oxic and suboxic plus anoxic zones, respectively. Note that variable depth and rate scales are used in order to highlight the important features of the profiles.

As systematically found in marine sediments deposited under oxygenated bottom waters, the model-derived pH profile exhibits a sharp decrease just below the SWI (see, for example, Cai and others, 1995; Hales and others, 1997a; Cai and others, 2000; Wenzhöfer and others, 2001; Wijsman and others, 2002; Forja and others, 2004). This pH drop is usually attributed to carbonic acid production by oxic respiration. However, in the model sediment considered, secondary oxygenation reactions play an even greater role than aerobic respiration of organic matter in generating H^+ (fig. 5). This is particularly true at the bottom of the oxic zone, where sulfide and Mn^{2+} oxidation by O_2 are the main sources of H^+. At these depths (~ 1 cm), the pore waters become undersaturated with respect to calcite, and $CaCO_3$ dissolution partly buffers the drop in pH (see *section 3.4*). Overall, net production of H^+ in the oxic zone causes the pH to reach a local minimum near the depth where pore water O_2 disappears.

In the suboxic zone, intense calcite dissolution in the 1-2 cm depth interval offsets H^+ production by denitrification and Fe^{2+} oxidation in the same depth interval (fig. 6). Sulfide oxidation coupled to reduction of Fe and Mn oxides, and dissimilatory Fe(III) and Mn(IV) reduction further consume protons within the suboxic zone, while Fe^{2+} oxidation coupled to Mn oxide reduction is the principal proton producing process in this zone. Precipitation of authigenic $MnCO_3$ is a minor source of H^+.

The suboxic zone is characterized by a pH minimum (fig. 4). The appearance of a reversal in the pH versus depth trend in the suboxic zone can be attributed to the reductive dissolution of iron and manganese (hydr)oxides coupled to organic matter and sulfide oxidation. This is shown in figure 7, where the pH distribution of the baseline scenario is compared to that of a simulation with no input of Fe and Mn (hydr)oxides at the sediment-water interface. In the latter case, no reversal of the pH trend below the oxic zone is observed. As also proposed by Van Cappellen and Wang (1996), the presence of a pronounced pH minimum below the oxic zone is a diagnostic feature of intense redox cycling of Fe and Mn.

Within the anoxic zone, the pH decreases with depth as a result of sulfate reduction and, to a lesser extent, iron sulfide precipitation (fig. 6). As a consequence, the pH profile shows a characteristic subsurface maximum in the suboxic zone. The pH continues to decrease until a depth of around 50 cm (not shown), where all degradable organic matter is consumed. In the anoxic zone, the pore waters remain undersaturated with respect to $FeCO_3$, near saturation with respect to $MnCO_3$, and slightly undersaturated with respect to calcite (fig. 8). Slow dissolution of calcite at depths > 50 cm causes a slight rise in pH with depth (not shown).
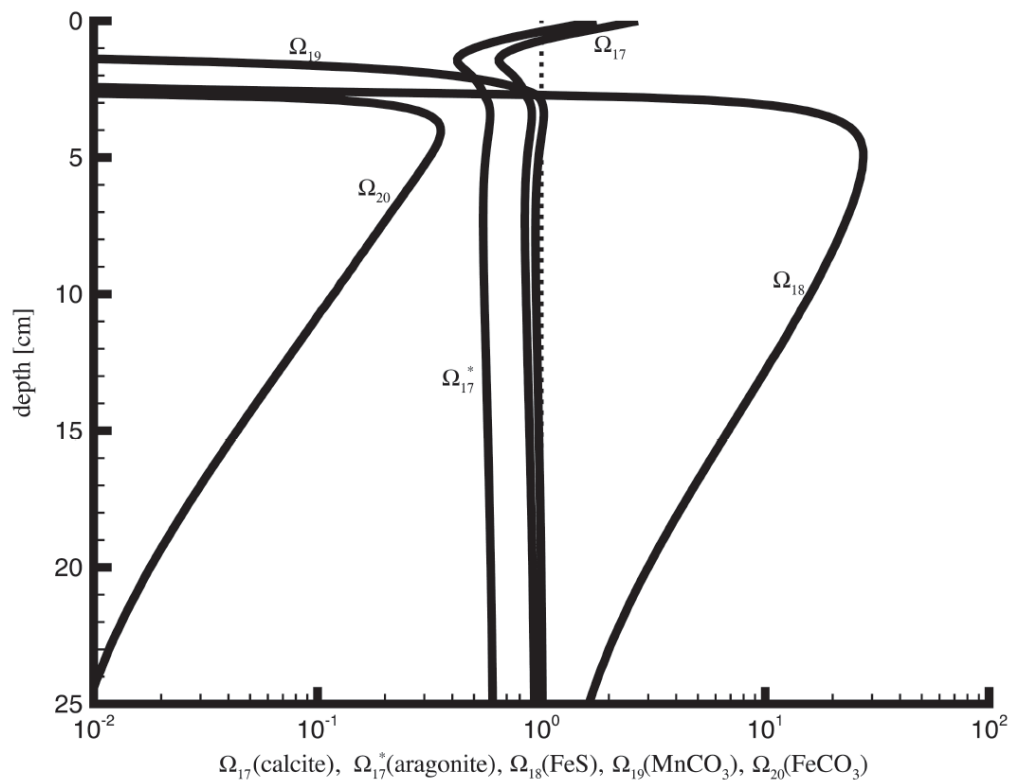

Fig. 8: Pore water saturation states with respect to $CaCO_3$, FeS, $MnCO_3$, and $FeCO_3$: results of the baseline simulation.

By combining the proton rates of the various biogeochemical processes, the net rate of proton production/consumption can be calculated as a function of depth below the SWI. In figure 9, the resulting net rate profile is broken down in a number of depth intervals. Note that the solid lines correspond to the baseline scenario. Comparison of the rate scales for the different depth intervals clearly shows that the most intense H^+ production and consumption is concentrated in the uppermost 5 centimeters of the sediment. In this depth interval, the net rate profile shows a close succession of zones of net production and consumption of H^+. At greater depths, net proton rates are orders of magnitude slower.
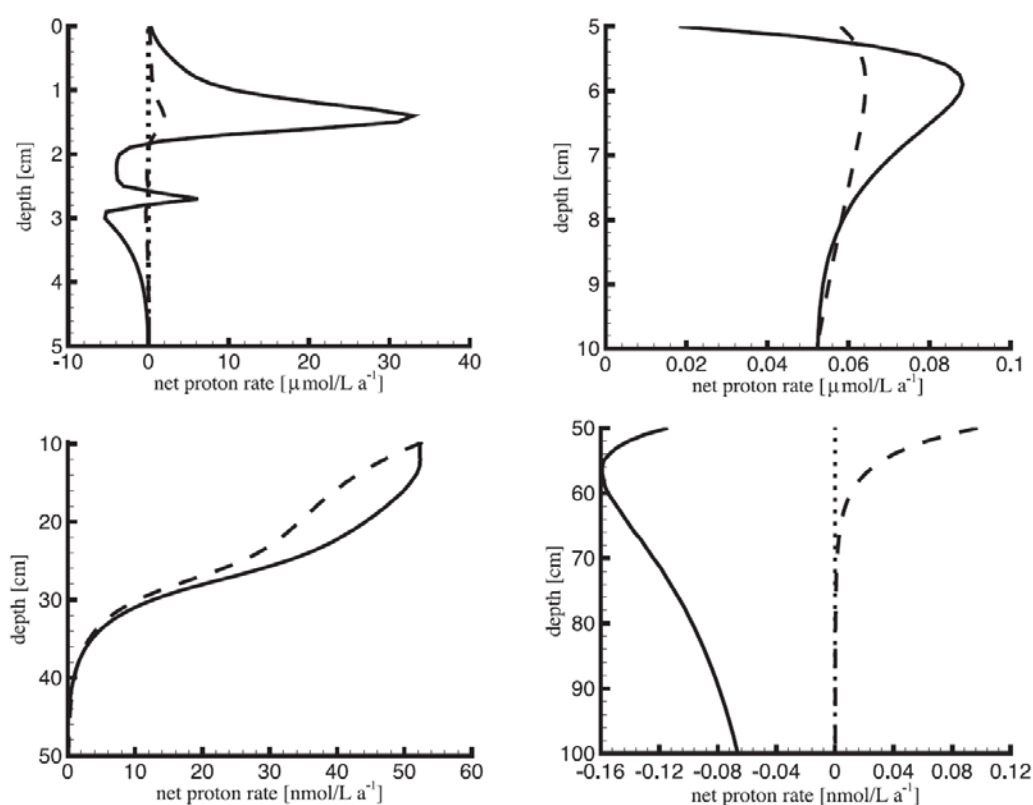

Fig. 9: Net rate of proton production (positive) and consumption (negative) in the baseline simulation (solid lines) and in a simulation assuming equilibrium with calcite (broken line). A thin dotted line indicates zero net rate. See text for complete discussion.

The overall contribution of any given biogeochemical process to the production or consumption of protons can be ranked by integrating the corresponding proton rate with depth (table 10). The dominant proton producing process in the sediment is sulfide oxidation by O_2, in line with the observations of Boudreau (1991) and Luff and Wallmann (2003). The results further imply that proton production mainly results from secondary redox reactions. The primary redox reactions sulfate reduction and aerobic respiration are only the 5th and 6th most important processes in terms of integrated proton production. The major

biogeochemical reactions responsible for proton consumption are calcite dissolution and the reduction of ferric (hydr)oxides by sulfide, followed by dissimilatory Fe(III) and Mn(IV) reduction.

Table 10

Integrated proton production (positive) and consumption (negative) rates for reaction processes in the baseline simulation, in order of decreasing magnitude

Kinetic Rate Description	Integrated Rate [nmol cm^{-2} a^{-1}]
1. Sulfide oxidation by O_2 (R^{11})	10.31
2. Mn^{2+} oxidation by O_2 (R^8)	6.84
3. Calcite dissolution (R^{17})	-4.34
4. Sulfide oxidation by $Fe(OH)_3$ (R^{13})	-4.19
5. Fe^{2+} oxidation by MnO_2 (R^{10})	3.90
6. $Fe(OH)_3$ reduction (R^4)	-3.44
7. Nitrification (R^7)	3.03
8. Sulfate reduction (R^5)	1.70
9. Oxic respiration (R^1)	1.29
10. MnO_2 reduction (R^3)	-0.90
11. Sulfide oxidation by MnO_2 (R^{12})	-0.74
12. FeS precipitation (R^{18})	0.20
13. Denitrification (R^2)	0.13
14. Fe^{2+} oxidation by O_2 (R^9)	0.01
15. $MnCO_3$ precipitation (R^{19})	0.001
16. Methanogenesis (R^6)	0.00
17. CH_4 oxidation by O_2 (R^{14})	0.00
18. CH_4 oxidation by SO_4^{2-} (R^{15})	0.00
19. FeS oxidation by O_2 (R^{16})	0.00
20. $FeCO_3$ precipitation (R^{20})	0.00

3.3. Sulfur Cycling

The effect of some reaction pathways on pH during early diagenesis is straightforward. For example, aerobic respiration decreases pore water pH and calcite dissolution increases pore water pH. Other processes of particular importance in marine sediments, such as sulfate reduction, may have a more complex influence on pH. Depending on the local pH, the

production of alkalinity by sulfate reduction, coupled to the increase in total dissolved sulfide (T_S), can result in either a production or consumption of protons (Ben-Yaakov, 1973; Mackenzie and others, 1995).

In the baseline simulation, sulfate reduction produces protons (fig. 6). At the pH conditions of the pore waters, the increase in T_S is accompanied by dissociation of H_2S and, hence, the release of protons (fig. 4). As Ben-Yaakov (1973) showed theoretically, the pH can increase if all sulfide produced is removed from solution, either by transport or mineral precipitation. In fact, in a closed system with no other reactions occurring concurrently, the reduced aqueous sulfur system would rapidly buffer the pore waters to a pH close to 6.9 (Wollast and Vanderborght, 1994; Mackenzie and others, 1995).

It has been argued that the production of carbonate alkalinity by sulfate reduction may increase the saturation state with respect to calcite and lead to $CaCO_3$ precipitation, despite concomitant proton production (Middelburg and others, 1990; Wollast and Vanderborght, 1994; Forja and others, 2004; Mucci and others, 2000). The opposing effects of alkalinity and proton production on calcite saturation can be described mathematically by computing the instantaneous rate of CO_3^{2-} production. Using equations (8), (9) and (16), the latter is expressed as

$$\left.\frac{d\left[CO_3^{2-}\right]}{dt}\right|_i = t_c^i \chi_2 R^i + T_C \frac{\partial \chi_2}{\partial\left[H^+\right]} \left.\frac{d\left[H^+\right]}{dt}\right|_i,$$ (24)

for any given kinetically-controlled reaction i. The second term on the RHS of equation (24) accounts for the dependence of CO_3^{2-} ion production on the local pH value and the rate of proton production by reaction i.

For sulfate reduction, the first term on the RHS of equation (24) is always positive and, therefore, favors $CaCO_3$ precipitation by increasing the degree of saturation of the pore waters. Because $\dfrac{\partial \chi_2}{\partial\left[H^+\right]} < 0$, the second term on the RHS of equation (24) translates the production of protons by sulfate reduction into a consumption of CO_3^{2-} ions. The overall effect of sulfate reduction on $CaCO_3$ saturation thus depends on the relative magnitudes of the two terms on the RHS of equation (24).

As shown in figure 10, for the baseline simulation, the rate of CO_3^{2-} production by sulfate reduction is negative throughout the model domain. This means that the second term on the RHS of equation (24) has a larger absolute value than the first term at all depths. Thus, as far as calcite saturation is concerned, proton production by sulfate reduction outweighs alkalinity

production.   While these results are specific to the particular environmental setting considered, they indicate that sulfate reduction may not necessarily create conditions favorable to $CaCO_3$ precipitation.

In the baseline simulation, the decrease in sulfate concentration with depth is fairly small (11 %) and can thus be assumed to have a negligible effect on the apparent equilibrium constants and the calculated proton rates. However, in organic rich environments, such as coastal sediments, the complete depletion of sulfate from the pore waters with depth represents a major change in the relative ionic composition of the aqueous medium, which may significantly affect the proton balance and calculated saturation states of the minerals (Gaillard and others, 1989). The full treatment of such systems then requires taking into account the contribution of the changes in the apparent equilibrium constants on the proton rates of the various reaction processes (eq 11 and Appendix I).

The oxidation of sulfide may also significantly affect the saturation state of pore waters with respect to $CaCO_3$ (see figs. 5 and 6). For example, at a 790 m water depth site on Hydrate Ridge, sulfide oxidation by oxygen appears to be the main driving force for shallow subsurface carbonate dissolution (Luff and others, 2003). In contrast, high pore water pH in sediments from the Baltic Sea has been attributed to sulfide oxidation coupled to reduction of Mn and Fe oxides (Carman and Rahm, 1997). As shown in this paper, the explicit computation of the rates of proton (eq 12) and carbonate ion (eq 24) production allows for a rigorous analysis of the relative contributions of various reaction pathways to the variations in pH and $CaCO_3$ saturation state of sediment pore waters.

A great advantage of the Biogeochemical Reaction Network Simulator (BRNS) is that it allows the user to easily add or remove reaction pathways. This is illustrated here by expanding the sulfur reaction network of the baseline simulation, by addition of pyritization, oxidation of pyrite by oxygen, and sulfur disproportionation. The reactions and their corresponding kinetic rate formulations, which are adopted from Berg and others, 2003, are given in table 11. Note that pyrite, FeS_2, is added as a new species, and the concentration of elemental sulfur, S^0, is now explicitly computed. Pyritization and sulfur disproportionation represent sinks for S^0, which in the original baseline reaction network was only produced via oxidation of sulfide by MnO_2 and $Fe(OH)_3$ (reactions 12 and 13).
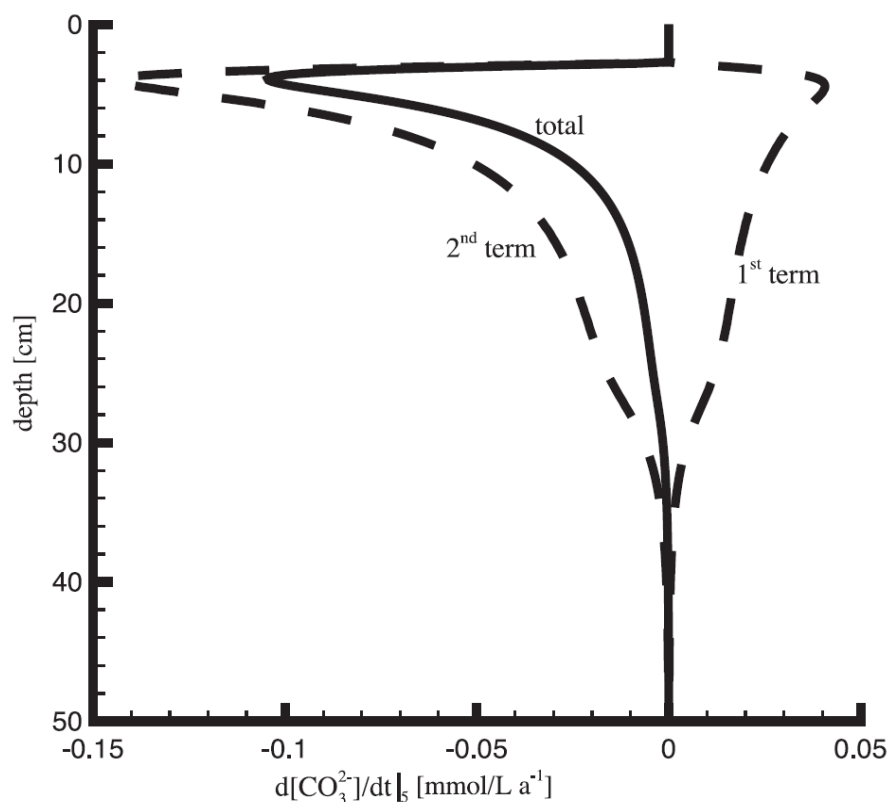
Fig. 10: Rate of change of the saturation state with respect to calcite, Ω_{17}, due to sulfate reduction (see equation 30, *section 3.3*).

The predicted pH and $CaCO_3$ distributions are compared to the baseline simulation in figure 11. Pore water pH values are slightly lower due to the FeS_2 oxygenation and S^0 disproportionation reactions. Despite the minor effect on pH, there is a noticeable decrease of the $CaCO_3$ concentrations in the sediment. The enhanced $CaCO_3$ dissolution compensates for the additional proton production by FeS_2 oxygenation and S^0 disproportionation. In terms of depth-integrated rates of proton production, S^0 disproportionation and oxidation of pyrite rank only 14th and 15th, repectively. Compared to the baseline simulation, a major change among the sulfur bearing solids is that hardly any FeS remains (not shown). That is, reduced sulfur is now buried mainly as FeS_2 and S^0.

Table 11

Reaction pathways, kinetic rate formulations, and related parameter values for the extended sulfur cycle (see section 3.3)

R^{21}. pyritization

$FeS + S^0 \rightarrow FeS_2$

R^{22}. oxidative dissolution of pyrite

$$2FeS_2 + 7O_2 \rightarrow \sum_{keq} s^{22}_{keq} C_{keq} + 2Fe^{2+} + 4SO_4^{2-}$$

R^{23}. sulfur disproportionation

$$4S^0 \rightarrow \sum_{keq} s^{23}_{keq} C_{keq} + SO_4^{2-}$$
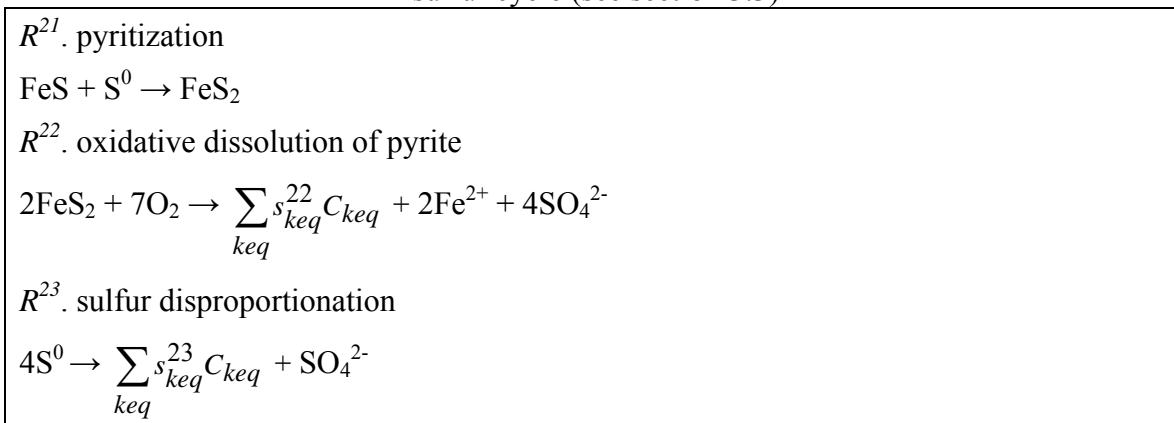
Reaction i	t_c^i	t_a^i	t_s^i
R^{21}	0	0	0
R^{22}	0	-4	0
R^{23}	0	-2	3

$$R^{21} = k_{21}\left[FeS\right]\left[S^0\right](1-\phi)\rho_s$$

$$R^{22} = k_{22}\left[O_2\right]\left[FeS_2\right](1-\phi)\rho_s$$

$$R^{23} = \begin{cases} 0 & \text{for } \Omega_{S^0} \equiv \left[H_2S\right]+\left[HS^-\right] \geq S_{stop} \\ k_{23}\left[S^0\right]\left(1-\dfrac{\Omega_{S^0}}{S_{stop}}\right)(1-\phi)\rho_s & \text{for } \Omega_{S^0} < S_{stop} \end{cases}$$

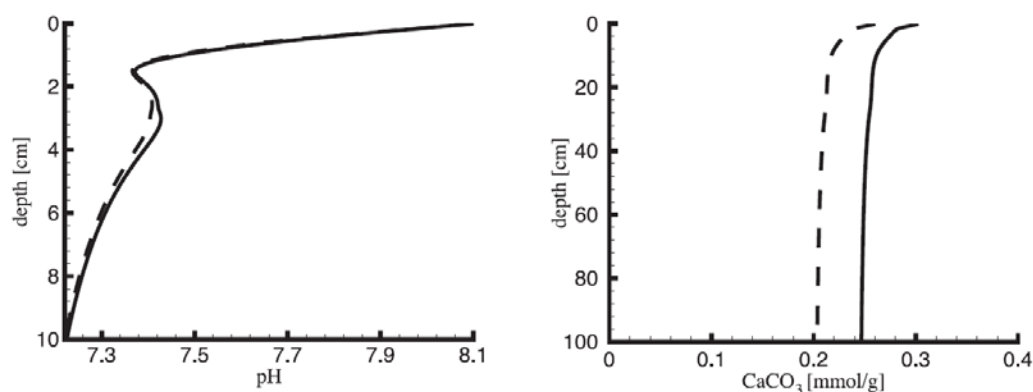| Parameter Name	Parameter Value	Units	Reaction(s)
k_{21}	2.36 x 10^6	g mol^{-1} a^{-1}	21
k_{22}	1.51 x 10^4	L mol^{-1} a^{-1}	22
k_{23}	3.15 x 10^{-3}	a^{-1}	23
S_{stop}	10^{-5}	mol L^{-1}	23

Fig. 11: Effect of sulfur cycling on pore water pH and $CaCO_3$ distributions. The solid line indicates the results of the baseline scenario, while the broken lines correspond to the additional simulation with the extended sulfur reaction network. See text for full details.

3.4. Calcite Dissolution

In the baseline simulation, calcite dissolution is the main sink of protons in the sediment (table 10). To further evaluate the significance of calcite dissolution, the baseline pH profile may be compared to the pH profile when calcite dissolution is completely inhibited (fig. 12). The latter is obtained by setting the calcite deposition flux, or the calcite dissolution rate constant, equal to zero. As can be seen, the absence of calcite dissolution shifts the pH profile to lower values (fig. 12, top left). The general shape of the pH profile, however, remains the same. The local pH minimum at the base of the oxygenated zone is approximately 0.2 pH units lower when no calcite dissolution takes place, relative to the baseline scenario.

Rate expressions for calcite dissolution are generally assumed to be proportional to the degree of undersaturation raised to a power n (reaction rate order) (Wollast, 1990). The constant of proportionality (k_{17} in table 9), however, is not well constrained (Jansen and others, 2002; Hales, 2003). Laboratory studies of calcite dissolution report reaction rate orders (n) ranging from 1.5 (Gledhill and Morse, 2004) to 4.5 (Keir, 1980), while n values ranging from 1 to 5 have been used in early diagenetic models of calcite dissolution (Cai and others, 1995; Hales and Emerson, 1997b; Jahnke and others, 1997). Rate constants determined for specific sites through parameter fitting range from 0.2% day^{-1} to 1000% day^{-1} for n = 4.5, and from 4x10^{-4} % day^{-1} to 0.01 % day^{-1} for n = 1. To test the response of the pH profile to calcite dissolution kinetics, we considered two additional scenarios: one with n = 4.5 and k_{17} = 1000 % day^{-1}, and the other with n = 1 and k_{17} = 0.01 % day^{-1}.

Over the entire depth interval considered (0-25 cm), the pore waters are in disequilibrium with respect to calcite, with supersaturation prevailing in the uppermost centimeter and undersaturation below (fig. 8). Changes in the rate constant of calcite dissolution or the

reaction order, while affecting the absolute pH values, do not modify the general features of the pH profiles (fig. 12). Thus, the shape of the pH profile primarily reflects the depth distributions of the main redox reactions that consume or produce protons. The value of the local pH minimum at the base of the oxic zone, however, is quite sensitive to the dissolution kinetics of calcite. Similarly, the preservation of $CaCO_3$ in the sediment depends on the rate expression and rate constant describing calcite dissolution. Whereas 18% of the input flux of calcite is buried in the baseline simulation, this value increases to 39% for n = 1 and k_{17} = 0.01 % day^{-1}, and nearly all calcite is dissolved for n = 4.5 and k_{17} = 1000 % day^{-1}.

A very different shape of the pH profile is obtained when the pore waters are assumed to remain at equilibrium with respect to calcite, at all depths (fig. 12, bottom right). (The implementation of the calcite-pore solution equilibrium condition in the mixed kinetic-equilibrium reaction system is detailed in Appendix III). The most pronounced difference with the kinetic dissolution formulations is the disappearance of the local minimum and maximum in the pH profile (fig. 12, bottom right). The large effect of the equilibrium assumption can also be seen in the significant attenuation of the net proton production and consumption rate (fig. 9, broken lines). The pore water calcium profile is also affected (not shown), as $CaCO_3$ is now allowed to precipitate in the supersaturated upper 0.2cm of the sediment.

The precipitation of other carbonate and sulfide minerals ($MnCO_3$, $FeCO_3$, and FeS) is also affected by the increased pH buffering effect of calcite in the equilibrium scenario (not shown). The zone of $MnCO_3$ precipitation extends to the SWI, but results in only 1.1% greater burial of this mineral, and a 3.3% decrease in the pore water Mn^{2+} concentrations at depth. The effect on the Fe cycle is far less significant as the burial of iron sulfide remains unchanged and the pore waters remain undersaturated with respect to $FeCO_3$.
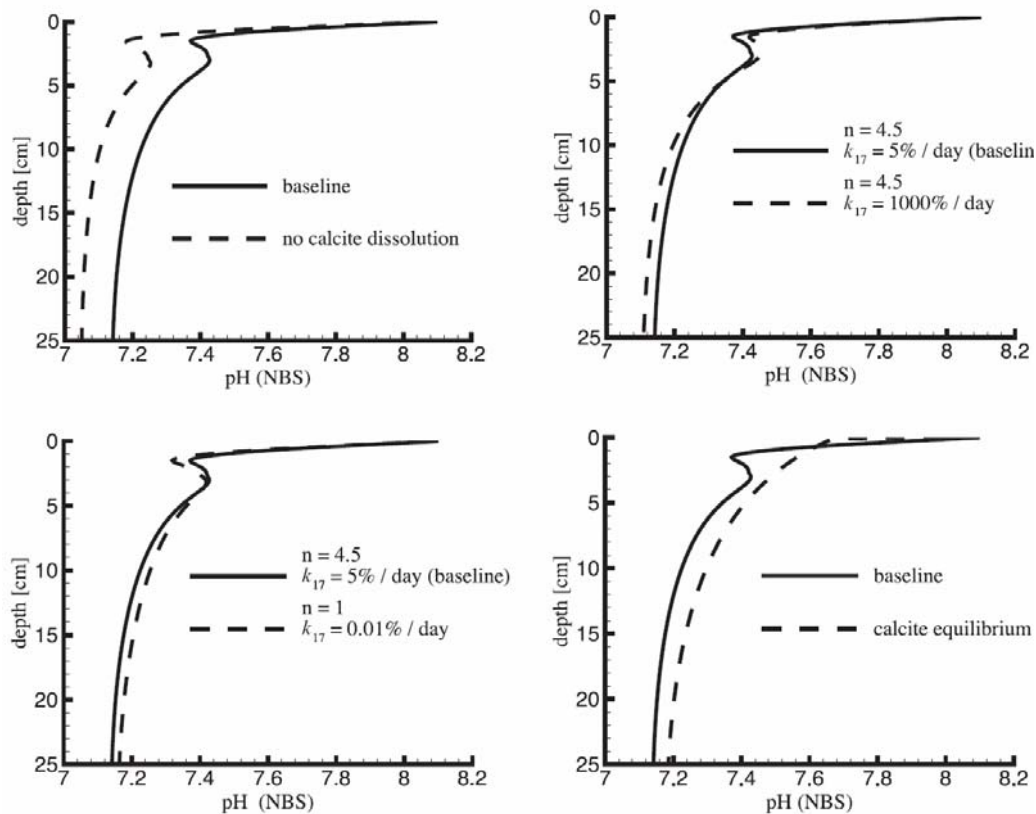
Fig. 12: Effect of calcite dissolution on pore water pH distributions. The solid line indicates the baseline scenario in all figures, while the broken lines are used for the additional simulations: no calcite dissolution (top left); increased rate constant (top right); first order reaction rate (bottom left); and calcite equilibrium (bottom right).

3.5. Irrigation

The pore water chemistry and reaction dynamics of marine sediments deposited under oxygenated bottom waters are strongly affected by the activity of benthic macrofauna (for comprehensive reviews, see, Berner, 1980; Van Cappellen and Gaillard, 1996; Boudreau, 1997; Aller, 2001). In particular, pore water irrigation by burrowing organisms increases the fluxes of dissolved oxidants into the sediment, thereby modifying the relative importance and depth distribution of the various redox reaction pathways. Given the crucial importance of redox reactions for the production and consumption of protons, irrigation is expected to have a major influence on the pore water pH distribution.

A number of simple irrigation scenarios are investigated (fig. 13). First, we consider a 30 cm deep uniformly irrigated layer, overlying non-irrigated sediment. That is, the imposed irrigation coefficient distribution ($\alpha_k = \alpha(x)$ for all dissolved species k in equation 1) is a step function, characterized by a constant value, α_0, in depth interval 0-30 cm. The values of α_0 tested (2.5, 5 and 7.5 a^{-1}) are typical for mid-shelf depositional environments (Meile and Van

Cappellen, 2003). The resulting oxygen penetration depths are 1.5, 3.4, 4.7 and 6.2 cm, for α_0 = 0, 2.5, 5 and 7.5 a^{-1}, respectively.

As in the baseline simulation, the pH profiles in the irrigated scenarios display a pH minimum, although it is less pronounced than in the absence of irrigation. The pH minimum depth increases with increasing irrigation intensity, which reflects the increasingly deeper penetration of oxygen below the SWI. Thus, despite significant differences in solute transport regime among the different scenarios, the computed pH profiles all record the marked change in net proton production across the oxic-anoxic transition.

Irrigation greatly reduces the overall variation of pH with depth. In fact, the pH at the bottom of the irrigated zone is nearly the same in the presence of irrigation regardless of the irrigation intensity, yet it is ~0.36 pH units higher than in the absence of irrigation. The higher pH values in the irrigated scenarios also coincide with lower concentrations of reduced pore water species: for example, the concentrations of free sulfides, Mn^{2+}, Fe^{2+}, and NH_4^+ are lower by one to two orders of magnitude for the case of $\alpha_0 = 5$ a^{-1}, relative to the baseline scenario.

To illustrate the potential effect of the functional dependence of the depth distribution of the irrigation coefficient, we also consider an exponentially decreasing $\alpha(x)$ profile (fig. 13). The depth attenuation constant is chosen such that at 30 cm depth α drops to 5 % of its value at the SWI, which is set to 5 a^{-1}. The resulting pH profile is similar to that obtained using the step function depth dependence with $\alpha_0 = 2.5$ a^{-1}. The depth integrated irrigation intensity in this case (75 cm a^{-1}) most closely matches that of the exponentially decreasing $\alpha(x)$ profile (50 cm a^{-1}). This may indicate that the pH profile is more sensitive to the integrated irrigation intensity than to the exact functional depth dependence of the irrigation coefficient.

In the simulations with irrigation, it is assumed that the same irrigation coefficient $\alpha(x)$ applies to all solute species. Recent theoretical work, however, does not support this assumption but rather implies that solute-specific irrigation coefficient distributions should be assigned in reactive transport calculations (Meile and others, 2005). While this adds another level of complexity, it points to the need for early diagenetic modeling approaches that account for the individual transport properties of the various reactive species.
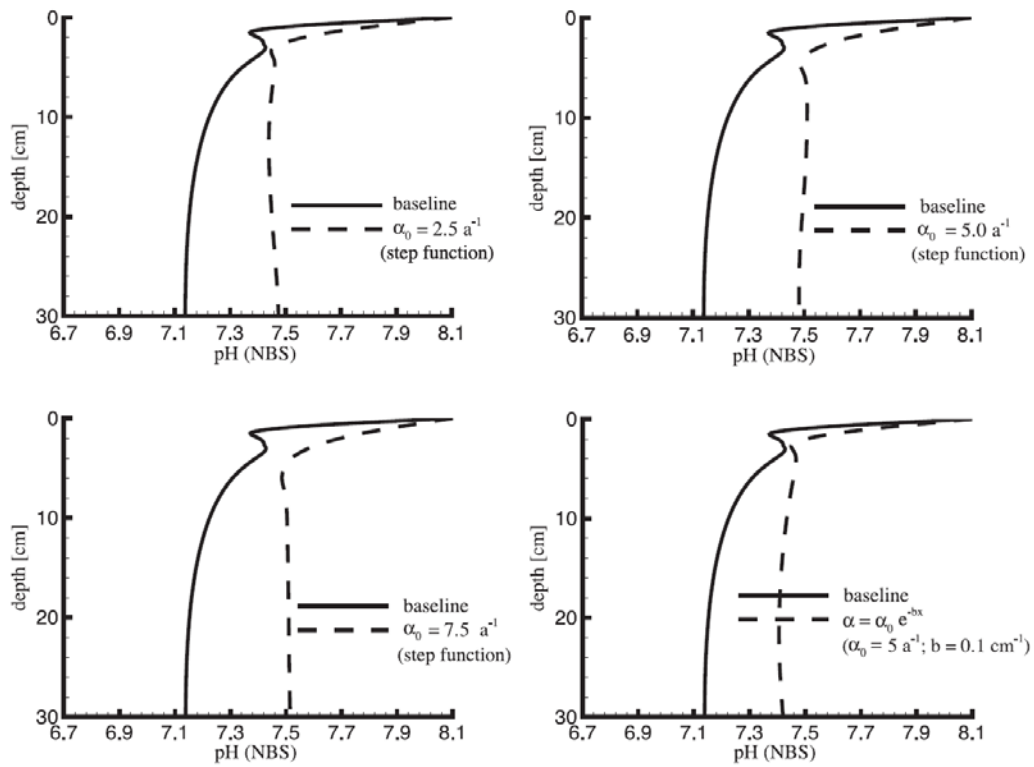
Fig. 13: Response of the pH distribution to irrigation. In the baseline scenario, there is no irrigation. In the step functions, α is set to α_0 to a depth of 30 cm and zero below.

4. Conclusions

The distribution of pore water pH in aquatic sediments is controlled by a complex network of biogeochemical reaction processes. The quantitative prediction of pH profiles, therefore, requires a rigorous mathematical treatment of the coupling of acid-base equilibria, irreversible kinetic reactions and transport processes. We have addressed the specific challenges of the treatment of mixed kinetic-equilibrium reaction systems in a transport environment with solute-specific molecular diffusion coefficients. In the proposed approach the chemical species participating in equilibrium reactions appear explicitly in the kinetic reaction stoichiometries. As the stoichiometric coefficients of these species are treated as unknowns in the model, the kinetic reaction stoichiometries are allowed to vary with time and depth in the sediment.

We illustrate the general theory for deriving the stoichiometric coefficients in an example seawater, taking into account the acid-base equilibria of the dissolved inorganic carbon, sulfide, and borate systems. The variable stoichiometric coefficients are expressed in terms of the stoichiometric coefficient of the proton, for which an explicit expression is derived. This method, which can be generalized to include other equilibrium reactions, yields the proton production and consumption rates due to each kinetic reaction process.

Calculation of the reaction-specific proton production and consumption rates allows us to quantitatively interpret pH distributions in aquatic sediments. The model is applied by using simulations of early diagenetic processes in a sediment representative of the continental shelf. The computed pH profiles exhibit features commonly observed in measured profiles. In particular, the occurrence of a pH minimum and maximum is explained in terms of the depth distributions of proton production and consumption by the various biogeochemical reactions. The proposed approach also provides a means to interpret the saturation state of pore waters with respect to mineral phases (carbonates, sulfides, oxides), since they are intimately linked to variations in pH. In this respect, the role of sulfate reduction in controlling the calcite saturation state is investigated, by explicitly computing the rate at which carbonate ions are produced or consumed by sulfate reduction. Model simulations are also used to determine the response of pH to variations in calcite dissolution kinetics and irrigation intensity.

The applications of the model in this study are limited to steady state simulations and they assume a constant ionic composition of the pore water. However, the proposed model approach can handle transient simulations, and account for changes in the ionic strength and relative composition of the pore water. Furthermore, the set of reaction processes considered

in this study may be expanded to include additional kinetic and equilibrium reactions. The approach presented here provides a framework for the quantification of proton production and consumption rates in biogeochemical reaction-transport systems, and will hopefully enhance the utilization of the diagnostic capabilities of pH distribution in early diagenesis.

APPENDIX I: EQUILIBRIUM CONSTANTS

The coefficients, η_m in equation (11) are themselves functions of the equilibrium species concentrations and are defined as,

$$\eta_m = T_C \frac{\partial(\chi_1 + 2\chi_2)}{\partial K_m^*} + T_S \frac{\partial \sigma_1}{\partial K_m^*} + T_B \frac{\partial \beta_1}{\partial K_m^*} + \frac{\partial\left(K_3^* / [H^+]\right)}{\partial K_m^*}.$$ (I-1)

Each apparent constant, K_m^* is a function of the activity coefficients, γ_k^* (activity coefficient of species k), which in turn depend on the total ionic strength of the solution, as well as specific interactions that may be estimated with ion pairing or Pitzer models. Expansion of the rate of change of the apparent equilibrium constants yields

$$\left.\frac{dK_m^*}{dt}\right|_i = \sum_{k=1}^{N_s}\left(\frac{\partial K_m^*}{\partial \gamma_k} \sum_{\ell=1}^{N_s} \frac{\partial \gamma_k^*}{\partial C_\ell} \left.\frac{dC_\ell}{dt}\right|_i\right),$$ (I-2)

where N_s is the number of species and

$$\frac{\partial K_m^*}{\partial \gamma_k} = K_m \frac{\partial}{\partial \gamma_k}\left(\prod_{\ell=1}^{N_s} \gamma_\ell^{-\nu_m^\ell}\right) = \frac{-\nu_m^k K_m^*}{\gamma_k},$$ (I-3)

in which ν_m^k represents the stoichiometric coefficient of species k in the 'fast' reversible reaction, m.

The functional form of the dependence of γ_k^* on the chemical composition, that is, $\frac{\partial \gamma_k}{\partial C_\ell}$, depends on the specific ion interaction model used (see for example, Millero and Schreiber, 1982, and He and Morse, 1993). The rate of change of each species concentration can be expressed more explicitly as

$$\left.\frac{dC_\ell}{dt}\right|_i = \lambda R^i + \Lambda_0 \left.\frac{d[H^+]}{dt}\right|_i + \sum_{p=1}^{N_{eq}} \Lambda_p \left.\frac{dK_p^*}{dt}\right|_i,$$ (I-4)

where λ is a function of the proton concentration and the apparent equilibrium constants, and the Λ terms (Λ_0 to $\Lambda_{N_{eq}}$) are each a function of the species concentrations and apparent dissociation constants. Collectively, equations (11) and (I-2) constitute a set of coupled $N_{eq} +$ 1 equations that can be solved numerically using an iterative scheme for the instantaneous rates of change of the protons and apparent dissociation constants for a given composition of the solution (that is, for known species concentrations).

APPENDIX II: TAYLOR EXPANSION AND TEMPORAL DISCRETIZATION

Taylor expansion of the total rate (sources and sinks) defined in equation (16) gives

$$\left. R_k^j \right|_{new} \cong \left. R_k^j \right|_{old} + \sum_{\ell=1}^{N_s} \left. \frac{\partial R_k^j}{\partial C_\ell^j} \right|_{old} \left(\left. C_\ell^j \right|_{new} - \left. C_\ell^j \right|_{old} \right), \tag{II-1}$$

where the labels *old* and *new* correspond to successive iterations. The partial differentials of total rates with respect to species concentrations are commonly represented by a Jacobian matrix. Thus, we define, at each node j, a matrix of size N_s by N_s, $\boldsymbol{J}^j$, with elements

$$\boldsymbol{J}^j(k,\ell) \equiv \frac{\partial R_k^j}{\partial C_\ell^j}. \tag{II-2}$$

The Taylor expansion allows us to linearize the set of coupled reaction-transport equations (15). At the same time, the terms involving the elements of the Jacobian matrix (eq II-1), couple the equations of all the species, and thereby require a global (or otherwise referred to as one-step) solution. Therefore, we define the vectors, $\vec{C}$ and $\vec{R}$, representing the concentrations and total rates affecting the species concentrations, for all species, k, and at all nodes, j:

$$\vec{C} = \left[C_{k=1}^{j=1}, C_{k=2}^{j=1}, \cdots, C_{k=N_S}^{j=1}, C_{k=1}^{j=2}, \cdots, C_{k=N_S}^{j=2}, \cdots, C_{k=1}^{j=N_x} \cdots C_{k=N_S}^{j=N_x} \right]^{\mathsf{T}}$$
$$\vec{R} = \left[R_{k=1}^{j=1}, R_{k=2}^{j=1}, \cdots, R_{k=N_S}^{j=1}, R_{k=1}^{j=2}, \cdots, R_{k=N_S}^{j=2}, \cdots, R_{k=1}^{j=N_x} \cdots R_{k=N_S}^{j=N_x} \right]^{\mathsf{T}} \tag{II-3}$$

Equation (15) can then be solved numerically by the temporal discretization at time step $m+1$ ($t = t_{m+1}$), given the solution at time step m ($t = t_m$), and expansion of the reaction term:

$$\frac{\partial(\xi \vec{C})}{\partial t} \approx \frac{\xi \left(\left. \vec{C} \right|_{new}^{t_{m+1}} - \left. \vec{C} \right|^{t_m} \right)}{\Delta t} = \boldsymbol{T} \left. \vec{C} \right|_{new}^{t_{m+1}} + \left. \vec{R} \right|_{old}^{t_{m+1}} + \left. \boldsymbol{J} \right|_{old}^{t_{m+1}} \left(\left. \vec{C} \right|_{new}^{t_{m+1}} - \left. \vec{C} \right|_{old}^{t_{m+1}} \right), \tag{II-4}$$

where the matrices $\boldsymbol{T}$, ξ, and $\boldsymbol{J}$ are each of dimension N by N, $N = N_s N_x$, and $\Delta t = t_{m+1} - t_m$. Matrix $\boldsymbol{T}$ is a block tridiagonal matrix,

$$\boldsymbol{T} = \begin{bmatrix} [\cdot\cdot] & [\cdot\cdot] & & & \\ [\cdot\cdot] & [\cdot\cdot] & \ddots & & \\ & \ddots & \ddots & \ddots & \\ & & \ddots & [\cdot\cdot] & [\cdot\cdot] \\ & & & [\cdot\cdot] & [\cdot\cdot] \end{bmatrix}, \tag{II-5}$$

where each block is a diagonal matrix of dimension N_s by N_s. Matrix $\boldsymbol{J}$ is a block diagonal matrix,

$$
\boldsymbol{J} = \begin{bmatrix} \left[\boldsymbol{J}^1\right] & & & & \\ & \left[\boldsymbol{J}^2\right] & & & \\ & & \ddots & & \\ & & & \left[\boldsymbol{J}^{N_x-1}\right] & \\ & & & & \left[\boldsymbol{J}^{N_x}\right] \end{bmatrix}, \tag{II-6}
$$

where the elements of the individual N_s by N_s blocks are given by equation (II-2). Matrix ξ is a diagonal matrix whose entries are the volume fractions in which the concentrations of the various species are defined at each node. The diagonal elements assume the same order as that of concentration and rate vectors (eq II-3).

<div align="center">APPENDIX III: CALCITE EQUILIBRIUM</div>

Equilibrium between pore water and calcite is represented by the heterogeneous equilibrium reaction

$$CaCO_{3(s)} \leftrightarrow Ca^{2+}_{(aq)} + CO^{2-}_{3(aq)}, \qquad \text{(III-1)}$$

with its corresponding mass action law

$$K_{s17} = \left[Ca^{2+}\right]\left[CO_3^{2-}\right], \qquad \text{(III-2)}$$

where K_{s17} represents the apparent solubility constant of $CaCO_3$. The total dissolved inorganic carbon (T_C) and total alkalinity (T_A) are affected by the degree of advancement of this equilibrium reaction. Using the change in the concentration of Ca^{2+} as a measure of this advancement, the contributions to T_A and T_C are

$$\left. \frac{d(T_C)}{dt}\right|_i = t_c^i R^i + \left.\frac{d\left[Ca^{2+}\right]}{dt}\right|_i$$

$$\left. \frac{d(T_A)}{dt}\right|_i = t_a^i R^i + 2\left.\frac{d\left[Ca^{2+}\right]}{dt}\right|_i , \qquad \text{(III-3)}$$

which are extensions of equations (6).

The instantaneous rate of production or consumption of Ca^{2+}, $\left.\dfrac{d\left[Ca^{2+}\right]}{dt}\right|_i$, due to reaction R^i can be expressed in terms of the rates of proton production and T_C using the mass action law (eq III-2) and the fractions defined in equations (7) and (8)

$$\left. \frac{d\left[Ca^{2+}\right]}{dt}\right|_i = \left.\frac{d}{dt}\left(\frac{K_{s17}}{\left[CO_3^{2-}\right]}\right)\right|_i = \frac{-K_{s17}}{\left[CO_3^{2-}\right]^2}\left.\frac{d\left[CO_3^{2-}\right]}{dt}\right|_i$$

$$\left. \frac{d\left[Ca^{2+}\right]}{dt}\right|_i = \frac{-K_{s17}}{\left[CO_3^{2-}\right]^2}\left(\chi_2 \left.\frac{dT_C}{dt}\right|_i + T_C \frac{\partial \chi_2}{\partial\left[H^+\right]}\left.\frac{d\left[H^+\right]}{dt}\right|_i\right). \qquad \text{(III-4)}$$

Substituting the instantaneous rate of T_C (III-3) into (III-4) yields an expression for the instantaneous rate of protons production/consumption in terms of the rate of change in Ca^{2+}

$$\left. \frac{d\left[Ca^{2+}\right]}{dt}\right|_i = \frac{-K_s}{\left[CO_3^{2-}\right]^2}\left(\chi_2\left(t_c^i R^i + \left.\frac{d\left[Ca^{2+}\right]}{dt}\right|_i\right) + T_C \frac{\partial \chi_2}{\partial\left[H^+\right]}\left.\frac{d\left[H^+\right]}{dt}\right|_i\right),$$

$$\left. \frac{d\left[H^+\right]}{dt}\right|_i = \frac{P_1}{P_2}\left.\frac{d\left[Ca^{2+}\right]}{dt}\right|_i - \frac{P_3 R_i}{P_2} \qquad \text{(III-5)}$$

where P_1, P_2, and P_3 are defined as

$$P_1 \equiv 1 + \frac{K_{s17}\chi_2}{\left[CO_3^{2-}\right]^2}$$

$$P_2 \equiv \frac{-K_{s17}}{\left[CO_3^{2-}\right]^2} \frac{\partial \chi_2}{\partial \left[H^+\right]} T_C \; .$$

$$P_3 \equiv \frac{-K_{s17}}{\left[CO_3^{2-}\right]^2} t_c^i \chi_2$$

(III-6)

Expanding the total alkalinity equation and its instantaneous rate of production (eqs 9 and 10), neglecting changes of apparent equilibrium constants, yields

$$\left. \frac{dT_A}{dt} \right|_i = \left. \frac{dT_C}{dt} \right|_i (\chi_1 + 2\chi_2) + T_C \frac{\partial(\chi_1 + 2\chi_2)}{\partial\left[H^+\right]} \left. \frac{d\left[H^+\right]}{dt} \right|_i + \left. \frac{dT_S}{dt} \right|_i \sigma_1 + T_S \frac{\partial\sigma_1}{\partial\left[H^+\right]} \left. \frac{d\left[H^+\right]}{dt} \right|_i$$
$$+ \left. \frac{dT_B}{dt} \right|_i \beta_1 + T_B \frac{\partial\beta_1}{\partial\left[H^+\right]} \left. \frac{d\left[H^+\right]}{dt} \right|_i - \frac{K_3^*}{\left[H^+\right]^2} \left. \frac{d\left[H^+\right]}{dt} \right|_i - \left. \frac{d\left[H^+\right]}{dt} \right|_i$$

(III-7)

Similarly, substituting the instantaneous rates of both T_A and T_C (eqs III-3) into equation (III-7) yields

$$t_a^i R^i + 2 \left. \frac{d\left[Ca^{2+}\right]}{dt} \right|_i = \left(t_c^i R^i + \left. \frac{d\left[Ca^{2+}\right]}{dt} \right|_i \right)(\chi_1 + 2\chi_2) + t_s^i \sigma_1 R^i + P_4 \left. \frac{d\left[H^+\right]}{dt} \right|_i ,$$

(III-8)

where P_4 is defined as

$$P_4 \equiv T_C \frac{\partial\chi_1}{\partial\left[H^+\right]} + 2T_C \frac{\partial\chi_2}{\partial\left[H^+\right]} + T_S \frac{\partial\sigma_1}{\partial\left[H^+\right]} + T_B \frac{\partial\beta_1}{\partial\left[H^+\right]} - \frac{K_w}{\left[H^+\right]^2} - 1.$$

(III-9)

Subsitituting the proton rate (eq III-5) into equation (III-8) and solving for the calcium ion rate, we obtain

$$\left. \frac{d\left[Ca^{2+}\right]}{dt} \right|_i = \frac{\left(t_c^i(\chi_1 + 2\chi_2) + t_s^i \sigma_1 - t_a^i \right)P_2 - P_3 P_4}{(2 - \chi_1 - 2\chi_2)P_2 - P_1 P_4} R^i \; .$$

(III-10)

The above expression provides us with the stoichiometric coefficient for Ca^{2+} for each reaction i and can be substituted back into equation (III-5) for the proton rate.

References

Adler, M., Hensen, C., Wenzhöfer, F., Pfeifer, K., and Schulz, H. D., 2001, Modeling of calcite dissolution by oxic respiration in supralysoclinal deep-sea sediments: Marine Geology, v. 177, p. 167-189.

Aguilera, D. R., Jourabchi, P., Spiteri, C., and Regnier, P., 2005, A knowledge-based reactive transport approach for the simulation of biogeochemical dynamics in Earth systems: Geochemistry, Geophysics Geosystems, v. 6, doi:10.1029/2004GC000899.

Aller, R. C., 2001, Transport and reactions in the bioirrigated zone, *in* Boudreau, B. P., and Jorgensen, B. B., editors, The Benthic Boundary Layer: Transport processes and biogeochemistry: Oxford Press, Oxford, p. 269-301.

Archer, D., Emerson, S., and Reimers, C., 1989, Dissolution of calcite in deep-sea sediments: pH and O_2 microelectrode results: Geochimica et Cosmochimica Acta, v. 53, p. 2831-2845.

Archer, D. E., Morford, J. L., and Emerson, S. R., 2002, A model of suboxic sedimentary diagenesis suitable for automatic tuning and gridded global domains: Global Biogeochemical Cycles, v. 16, doi:10.1029/2000GB1288.

Ben-Yaakov, S., 1973, pH buffering of pore water of recent anoxic marine sedimnets: Limnology and Oceanography, v. 18, p. 86-94.

Berg, P., Rysgaard, S., and Thamdrup, B., 2003, Dynamic modeling of early diagenesis and nutrient cycling. A case study in an Arctic marine sediment: American Journal of Science, v. 303, p. 905-955.

Berner, R. A., 1980, Early diagenesis: a theoretical approach: Princeton, Princeton University Press, 256 p.

Boudreau, B. P., 1986, Mathematics of tracer mixing in sediments: I. spatially-dependent, diffusive mixing: American Journal of Science, v. 286, p. 161-198.

Boudreau, B. P., and Canfield, D.E., 1988, A provisional diagenetic model for pH in anoxic porewaters: Application to the FOAM site: Journal of Marine Research, v. 46, p. 429-455.

Boudreau, B. P., 1991, Modelling the sulfide-oxygen reaction and associated pH gradients in porewaters: Geochimica et Cosmochimica Acta, v. 55, p. 145-159.

Boudreau, B. P., and Canfield, D. E., 1993, A comparison of closed- and open-system models for porewater pH and calcite-saturation state: Geochimica et Cosmochimica Acta, v. 57, p. 317-334.

Boudreau, B. P., 1996, A method-of-lines code for carbon and nutrient diagenesis in aquatic sediments: Computers and Geosciences, v. 22, p. 479-496.

Boudreau, B. P., 1997, Diagenetic models and their implementation: Modelling transport and reactions in aquatic sediments: Berlin, Springer-Verlag, 414 p.

Cai, W. -J., and Reimers, C. E., 1993, The development of pH and P_{CO2} microelectrodes for studying the carbonate chemistry of pore waters near the sediment-water interface: Limnology and Oceanography, v. 38, p. 1762-1773.

Cai, W. -J., Reimers, C. E., and Shaw, T., 1995, Microelectrode studies of organic carbon degradation and calcite dissolution at a California Continental rise site: Geochimica et Cosmochimica Acta, v. 59, p. 497-511.

Cai, W. -J., Zhao, P., and Wang, Y., 2000, pH and pCO_2 microelectrode measurements and the diffusive behavior of carbon dioxide species in coastal marine sediments: Marine Chemistry, v. 70, p. 133-148.

Carman, R., and Rahm L., 1997, Early diagenesis and chemical characteristics of interstitial water sediments in the deep deposition bottoms of the Baltic proper: Journal of Sea Research, v. 37, p. 25-47.

Chester, R., 2000, Marine Geochemistry: Oxford, Blackwell Science, 506 p.

Cussler, E. L., 1984, Diffusion: Mass transfer in fluid systems: New York, Cambridge University Press, 525 p.

Fisher, J. B., and Matisoff, G., 1981, High resolution vertical profiles of pH in recent sediments: Hydrobiologia, v. 79, p. 277-284.

Forja, J. M., Ortega, T., DelValls, T. A., and Gómez-Parra, A., 2004, Benthic fluxes of inorganic carbon in shallow coastal ecosystems of the Iberian Peninsula: Marine Chemistry, v. 85, p. 141-156.

Gaillard, J.-F., Pauwels, H., and Michard, G., 1989, Chemical diagenesis in coastal marine sediments: Oceanologica Acta, v. 12, p. 175-187.

Gledhill, D. K., and Morse, J. W., 2004, Dissolution kinetics of calcite in $NaCl$-$CaCl_2$-$MgCl_2$ brines at 25 °C and 1 bar pCO_2: Aquatic Geochemistry, v. 10, p. 171-190.

Hales, B., Emerson, S., and Archer, D., 1994, Respiration and dissolution in the sediments of the western North Atlantic: Estimates from models of in situ microelectrode measurements of porewater oxygen and pH: Deep-Sea Research II, v. 41, p. 695-719.

Hales, B., and Emerson, S., 1996, Calcite dissolution in sediments of the Ontong-Java Plateau: in situ measurements of pore water O_2 and pH: Global Biogeochemical Cycles, v. 10, p. 527-541.

Hales, B., and Emerson, S., 1997a, Calcite dissolution in sediments of the Ceara Rise: In situ measurements of porewater O_2, pH, and $CO_{2(aq)}$: Geochimica et Cosmochimica Acta, v. 61, p. 501-514.

Hales, B., and Emerson, S., 1997b, Evidence in support of first-order dissolution kinetics of calcite in seawater: Earth and Planetary Science Letters, v. 148, p. 317-327.

Hales, B., 2003, Respiration, dissolution, and the lysocline: Paleooceanography, v. 18, doi:10.1029/2003PA000915.

He, S. L., and Morse, J. W., 1993, The carbonic-acid system and calcite solubility in aqueous Na-K-Ca-Mg-Cl-SO_4 solutions from 0 to 90 °C: Geochimica et Cosmochimica Acta, v. 57, p. 3533-3554.

Hensen, C., Landenberger, H., Zabel, M., Gundersen, J. K., Glud, R. N., and Schulz, H. D., 1997, Simulation of early diagenetic processes in continental slope sediments off southwest Africa: The computer model CoTAM tested: Marine Geology, v. 144, p. 191-210.

Iversen, N., and Jørgensen, B. B., 1993, Diffusion coefficients of sulfate and methane in marine sediments: Influence of porosity: Geochimica et Cosmochimica Acta, v. 57, p. 571-578.

Jahnke, R. A., Craven, D. B., McCorkle, D. C., and Reimers, C. E., 1997, CaCO$_3$ dissolution in California continental margin sediments: The influence of organic matter remineralization: Geochimica et Cosmochimica Acta, v. 61, p. 3587-3604.

Jansen, H., Wolf-Gladrow, D. A., Zeebe, R. E., 2002, Modeling the dissolution of settling CaCO$_3$ in the ocean: Global Biogeochemical Cycles, v. 16, doi:10.1029/2000GB001279.

Keir, R. S., 1980, The dissolution kinetics of biogenic calcium carbonates in seawater: Geochimica et Cosmochimica Acta, v. 44, p. 241-252.

Komada, T., Reimers, C. E., and Boehme, S. E., 1998, Dissolved inorganic carbon profiles and fluxes determined using pH and P$_{co2}$ microelectrodes: Limnology and Oceanography: v. 43, p. 769-781.

Kulik, D. A., Kersten, M., Heiser, U., and Neumann, T., 2000, Application of Gibbs energy minimization to model early-diagenetic solid-solution aqueous-solution equilibria involving authigenic rhodochrosites in anoxic Baltic Sea sediments: Aquatic Geochemistry, v. 6, p. 147-199.

Lerman, A., 1979, Geochemical processes: Water and sediment environments: New York, John Wiley and Sons, 481 p.

Li, Y.-H., and Gregory, S., 1974, Diffusion of ions in sea water and in deep-sea sediments: Geochimica et Cosmochimica Acta, v. 38, p. 703-714.

Luff, R., Walmann, K., Grandel, S., and Schlüter, M., 2000, Numerical modeling of benthic processes in the deep Arabian Sea: Deep-Sea Research II, v. 47, p. 3039-3072.

Luff, R., Haeckel, M., and Wallmann, K., 2001, Robust and fast FORTRAN and MATLAB$^{®}$ libraries to calculate pH distributions in marine systems: Computers & Geosciences, v. 27, p. 157-169.

Luff, R., and Wallmann, K., 2003, Fluid flow, methane fluxes, carbonate precipitation and biogeochemical turnover in gas hydrate-bearing sediments at Hydrate Ridge, Cascadia Margin: Numerical modeling and mass balance: Geochimica et Cosmochimica Acta, v. 67, p. 3403-3421.

Marzal, P., Seco, A., Ferrer, J., and Gabaldón, C., 1994, Modeling multiple reactive solute transport with adsorption under equilibrium and nonequilibrium conditions: Advances in Water Resources, v. 17, p. 363-374.

Mackenzie, F. T., Vink, S., Wollast, R., and Chou, L., 1995, Comparative geochemistry of marine saline lakes, *in* Lerman, A., Imboden, D., and Gat, J., editors, Physics and Chemistry of Lakes: Berlin, New York, Springer-Verlag, Berlin, p. 265-278.

Meile, C., and Van Cappellen, P., 2003, Global estimates of enhanced solute transport in marine sediments: Limnology and Oceanography, v. 48, p. 777-786.

Meile, C., Berg, P., Van Cappellen, P., and Tuncay, K., 2005, Solute-specific pore water irrigation: Implications for chemical cycling in early diagenesis: Journal of Marine Research, v. 63, p. 601-621.

Meysman, F. J. R., Middelburg, J. J., Herman, P. M. J., and Heip, C. H. R., 2003, Reactive transport in surface sediments. I. Model complexity and software quality: Computers and Geosciences, v. 29, p. 291-300.

Middelburg, J. J., de Lange G. J., and Kreulen, R., 1990, Dolomite formation in anoxic sediments of Kau Bay, Indonesia: Geology, v. 18, p. 399-402.

Millero, F. J., and Schreiber, D. R., 1982, Use of the ion pairing model to estimate the activity coefficients of the ionic components of natural waters: American Journal of Science, v. 282, p. 1508-1540.

Millero, F. J., and Sohn, M. L., 1992, Chemical Oceanography: Boca Raton, CRC Press, 531 p.

Morel, F. M. M., and Hering, J. G., 1993, Principles and applications of aquatic chemistry: New York, Wiley, 588 p.

Mucci, A., Sundby, B., Gehlen, M., Arakaki, T., Zhong, S., and Silverberg, N., 2000, The fate of carbon in coninental shelf sediments of eastern Canada: a case study: Deep-Sea Research II, v. 47, p. 733-760.

Müller, B., Wang, Y., Dittrich, M., and Wehrli, B., 2003, Influence of organic carbon decomposition on calcite dissolution in surficial sediments of a freshwater lake: Water Research, v. 37, p. 4524-4532.

Mulsow, S., Boudreau, B. P., and Smith, J. N., 1998, Bioturbation and porosity gradients: Limnology and Oceanography, v. 43, p. 1-9.

Pilson, M. E. Q., 1998, An introduction to the chemistry of the sea: Upper Saddle River, Prentice-Hall, 431 p.

Regnier, P., O'Kane, J. P., Steefel, C. I., and Vanderborght, J. P., 2002, Modelling complex multi-component reactive-transport systems: Towards a simulation environment based on the concept of a Knowledge Base: Applied Mathematical Modelling, v. 26, p. 913-927.

Reimers, C. E., Ruttenberg, K. C., Canfield, D. E., and Christiansen, M. B., 1996, Porewater pH and authigenic phases formed in the uppermost sediments of the Santa Barbara Basin: Geochimica et Cosmochimica Acta, v. 60, p. 4037-4057.

Stumm, W., and Morgan, J. J., 1996, Aquatic chemistry: Chemical equilibria and rates in natural waters: New York, Wiley Interscience, 1022 p.

Thamdrup, B., Rossello-Mora, R., and Amann, R., 2000, Microbial manganese and sulfate reduction in Black Sea shelf sediments: Applied and Environmental Microbiology, v. 66, p. 2888-2897.

Tsunogai, S., and Noriki, S., 1991, Particulate fluxes of carbonate and organic carbon in the ocean. Is the marine biological activity working as a sink of the atmospheric carbon?: Tellus, v. 43B, p. 256-266.

Van Cappellen, P., and Gaillard, J.-F., 1996, Biogeochemical dynamics in aquatic sediments, *in* Lichtner, E. A., Steefel, C. I., and Oelkers, E., editors, Reactive transport in porous media: Mineralogical Society of America Reviews in Mineralogy, v. 34, p. 335-376.

Van Cappellen, P., and Wang, Y., 1995, Metal cycling in surface sediments: Modeling the interplay of transport and reaction, *in* Allen, H. E., editor, Metal contaminated sediments, Chelsea, Ann Arbor Press, p. 21-62.

Van Cappellen, P., and Wang, Y., 1996, Cycling of iron and manganese in surface sediments: A general theory for the coupled transport and reaction of carbon, oxygen, nitrogen, sulfur, iron, and manganese: American Journal of Science, v. 296, p. 197-243.

Wang, Y., and Van Cappellen, 1996, A multicomponent reactive transport model of early diagenesis: Application to redox cycling in coastal marine sediments: Geochimica et Cosmochimica Acta, v. 60, p. 2993-3014.

Wenzhöfer, F., Adler, M., Kohls, O., Hensen, C., Strotmann, B., Boehme, S., and Schulz, H. D., 2001, Calcite dissolution driven by benthic mineralization in the deep-sea: In situ measurements of Ca^{2+}, pH, pCO_2, and O_2: Geochimica et Cosmochimica Acta, v. 65, p. 2677-2690.

Wijsman, J. W. M., Herman, P. M. J., Middelburg, J. J., and Soetaert, K., 2002, A model for early diagenetic processes in sediments of the continental shelf of the Black Sea: Estuarine, Coastal and Shelf Science, v. 54, p. 403-421.

Wollast, R., 1990, Rate and mechanism of dissolution of carbonates in the system $CaCO_3$-$MgCO_3$, *in* Stumm, W., editor, Aquatic chemical kinetics: reaction rates of processes in natural waters: New York, Wiley, p. 431-445.

Wollast, R., and Vanderborght, J. P., 1994, Aquatic carbonate systems: chemical processes in natural waters and global cycles, *in* Bidoglio, G., and Stumm, W., editors, Chemistry of Aquatic Systems: Local and Global Perspectives: Chemical and Environmental Sciences, v. 5, p. 47-71.

Chapter 4

Quantitative interpretation of pore water O_2 and pH
distributions in deep-sea sediments

P. Jourabchi, C. Meile, L. R. Pasion, and P. Van Cappellen
submitted

Abstract

A reaction-transport model is used to interpret 13 data sets of in situ O$_2$ and pH microelectrode profiles measured in deep-sea sediments from 5 oceanic regions. The model includes a mechanistic description of the major early diagenetic redox transformations, as well as solid and solute transport processes, pore water acid-base equilibria, and calcite dissolution. Four different dependencies of the calcite dissolution rate on the degree of pore water saturation are considered. The results of the systematic and data-driven approach indicate that consideration of two pools of reactive organic carbon is sufficient to reproduce the oxygen data; that the more reactive pool dominates the organic carbon deposition flux; and that suboxic degradation pathways play a non-negligible role at the majority of sites. Estimation of the calcite related parameters, however, yields only 9 successful simulations of the pH profiles. The dissolution rate expressions with the higher rate orders tested (2 and 4.5) are generally more successful in reproducing the in situ pH profiles. While the pore water pH profiles cannot constrain the calcite deposition flux, robust estimates of the depth-integrated calcite dissolution rates can be obtained. These correlate positively with the benthic oxygen uptake fluxes, although sites overlain with undersaturated and supersaturated bottom waters exhibit separate trends.

1. Introduction

Marine sediments are characterized by biogeochemical conditions that vary significantly over short (mm - dm), predominantly vertical, distances with the most intense microbial activity concentrated close to the sediment-water interface (SWI). Because of the decomposition of biogenic constituents, sediments represent a source of inorganic nutrients to the overlying water (e.g. Hinga et al., 1979; Rabouille and Gaillard, 1991). From a geological perspective, the uppermost portions of marine sediments constitute the gateway to long-term burial, in which alteration of proxies may interfere with the reconstruction of past environmental conditions. Hence, early diagenetic processes have important implications on both short and long timescales.

Sediment pore water profiles are commonly used to identify the predominant reactions taking place in aquatic sediments. Amongst the chemical parameters that are measured routinely, the O_2 concentration and pH are particularly instructive. Oxygen penetration provides a measure for the flux of reduced reactive substances arriving at the seafloor, in particular organic matter (e.g. Reimers 1987), while the pH profile records the interplay between all major chemical and microbially mediated reactions (Boudreau and Canfield 1993; Jourabchi et al. 2005). The combination of O_2 and pH data have helped elucidate the role of calcite dissolution in sediments overlain by waters with contrasting saturation states (e.g. Cai and Reimers 1993; Wenzhöfer et al. 2001).

Mathematical reactive transport modeling is a powerful tool for interpreting pore water chemical profiles (Berner 1980). The introduction of numerical models that couple transport processes to comprehensive reaction networks (Van Cappellen and Wang 1995; Boudreau 1996; Soetaert et al. 1996) was a significant development. These initial formulations in the mid 90s represent the foundation of most current model developments. Early diagenetic models have been used primarily to analyze detailed data sets collected at individual study sites (e.g. Haeckel et al., 2001; Berg et al., 2003). Increasingly, however, efforts are made to incorporate vertically resolved sediment descriptions in the assessment of the role of sediments in ocean biogeochemistry, from regional to global scales (e.g. Archer et al. 2002; Luff and Moll 2004). Application of early diagenetic models to large-scale assessment of benthic-pelagic coupling requires a rigorous parameterization and calibration across a wide range of sedimentary environments.

In this study, we simulate and interpret published O_2 and pH microprofiles from deep-sea sediments deposited in oxygenated bottom waters at water depths greater than 2000 m. In our

data-driven approach, a general reaction-transport model is fitted to the measured profiles in order to quantify organic matter loading and reactivity, as well as the role of calcite dissolution on pore water pH. The key objective is to maximize the extraction of information on early diagenetic reaction dynamics from measured O_2 and pH microprofiles.

2. Sites

Only deep-sea sites (water depths > 2000 m) for which high-resolution microprofiles of both O_2 and pH are available are considered (Table 1). Furthermore, because of pressure artifacts on measurements performed ex situ (Glud et al., 1994; Cai and Reimers, 1993), we restrict ourselves to sites where the microprofiles were determined in situ from benthic landers. Of the 13 suitable sites, 10 are from lower to mid latitudes in the Atlantic ocean, while the other 3 sites are located in the Pacific ocean. Porosity profiles are derived from resistivity data available for 12 of the 13 sites and reported as formation factors (F). Porosity (ϕ) is estimated using the modified Archie's relation, $\phi = F^{\left(-1/b\right)}$, with the values for the exponent b reported in the respective studies. For site 120 (Table 1), the porosities are obtained from weight measurements (F. Wenzhöfer, personal communication). The location, water depth, average $CaCO_3$ content of the sediments, and relevant characteristics of the overlying bottom water, including the degree of saturation with respect to calcite (Ω_c), are summarized in Table 1.

Table 1: Summary of deep-sea sites with available in situ O_2 and pH microelectrode data. Ω_c is the degree of saturation with respect to calcite. Data from Hales et al., 1994 (sites 2,48-50); Archer et al., 1989 (sites 19-20); Hales and Emerson, 1996 (sites 39-41); Hales and Emerson, 1997a (sites 57-59); Wenzhöfer et al., 2001 (site 120).

Site	Longitude	Latitude	Depth [m]	Ω_c	Temperature [ºC]	O_2 [µM]	pH	Average [$CaCO_3$] weight %
2	-70.35°	34.33°	5210	0.87	2.2	266	8.015	22
19	-23.02°	-2.1°	4950	0.65	0.74	216	7.91	10
20	-23°	-5°	5075	0.63	0.73	211	7.902	10
39	159.5°	0°	2322	0.87	1.9	130	7.82	90
40	159.5°	0°	2335	0.87	1.9	131	7.825	90
41	160.5°	0°	2966	0.72	1.7	145	7.78	87
48	-69.67°	39.62°	2159	1.68	3.7	268	8.112	21
49	-71.52°	36.27°	4236	1.06	2.3	271	8.048	26
50	-71.58°	34.55°	4501	1.01	2.3	268	8.042	31
57	-44.15°	5.27°	3279	1.23	2.55	262	8.054	66
58	-43.57°	5.28°	3990	1.02	2.19	270	8.016	64
59	-42.88°	6.17°	4675	0.78	1.49	242	7.94	43
120	6.73°	2.68°	2185	1.31	3.5	233	7.97	3.2

3. Model Setup

We use a general early diagenetic model combined with a parameter estimation approach to constrain the most sensitive parameters shaping the measured pore water oxygen and pH profiles. In this section, we summarize the reaction and transport processes included in the model, followed by a brief description of the numerical model, its implementation and the boundary conditions.

3.1. Reactions

The reaction network is a slightly modified version of that presented in Jourabchi et al. (2005). It accounts for all the major pathways of organic matter degradation (primary redox reactions), in contrast to many existing models simulating O_2 distributions in deep-sea sediments, which only consider oxic respiration (Archer et al., 1989; Hales et al., 1994; Hales and Emerson, 1996 & 1997a). The primary redox reactions are assumed to proceed in the order of decreasing free energy yield, and are implemented following the approach of Van Cappellen and Wang (1995). Additionally, they produce reduced chemical species (e.g., NH_4^+, Mn^{2+}, Fe^{2+}, and HS^-), which participate in a set of secondary redox reactions, coupling early diagenetic cycling of redox-sensitive elements such as N, S, Fe and Mn.

The model includes a total of 20 reaction pathways and 20 individual chemical species. The major differences with our earlier model (Jourabchi et al., 2005) are as follows. Two rather than one pool of organic matter with differing reactivities and C:N:P ratios are considered (see Model Parameter Estimation for further details). This is necessary to capture the features of the oxygen microprofiles. Next, because pore waters in well-oxygenated deep-sea settings generally remain undersaturated with respect to mineral phases of reduced iron and manganese (e.g., $MnCO_3$, FeS, FeS_2), these minerals, and all corresponding production and consumption reactions, are excluded. For similar reasons, oxidation of methane is not included. Although additional reaction processes and chemical species may be important, the set of reactions considered here captures the essence of the redox and acid-base dynamics of early diagenesis in deep-sea sediments.

Oxygen is directly involved in the oxic respiration of organic matter and the oxidation of NH_4^+, Mn^{2+}, Fe^{2+}, and sulfide. In turn, the oxygen distribution is indirectly affected by the production and transport of reduced species in the system. All the reactions affecting O_2 either have a direct influence on pH, because they alter the proton balance, or they indirectly modify pH by altering the distribution of the chemical species influencing the reaction rates.

However, no explicit pH dependencies of the redox reaction rates are considered, which is partly justified by the relatively small variations in pore water pH (see below).

While, strictly speaking, the dissolution (and precipitation) of $CaCO_3$ is not redox-dependent, variations in the saturation state of pore waters with respect to calcite are intimately linked to the network of primary and secondary redox reactions through their effects on total alkalinity and dissolved inorganic carbon (DIC) (Hales, 2003). Calcite dissolution is represented by a rate equation that depends on the degree of pore water undersaturation (see section 4.2). Other significant processes that depend on and buffer the pH in marine pore waters are the fast and reversible acid-base equilibria of the DIC, sulfide, and boric acid systems.

3.2. Transport

The mixing of sediment by faunal activity is modeled as a diffusive process by assigning a bioturbation coefficient (D_b) to both solids and solutes. At the selected deep-sea sites, bioirrigation is assumed to be negligible and molecular and ionic diffusion are the dominant transport processes for the solute species (Meile and Van Cappellen, 2003). Diffusion coefficients used in the calculations are corrected for temperature, salinity and tortuosity using standard procedures (Boudreau, 1997).

We systematically impose values of the sedimentation rate (ω) and bioturbation coefficient (D_b) obtained from global relationships between ω and D_b, and water depth (Middelburg et al., 1997), because there are no independent estimates for many of the sites considered. The effects of compaction on the advective transport of solids and solutes are accounted for through the mass balances of total solids and total solutes (Berner, 1980), given an exponentially decaying porosity depth profile. The bioturbation coefficient is assumed to decay with depth below the SWI, following a complementary error function whose value falls to 50% at a depth of 20cm. Table 2 summarizes the sedimentation rates, bioturbation coefficients and porosities at the SWI for the different sites.

Table 2: Sedimentation rate ω, bioturbation coefficient D_b,
and porosity ϕ_0 at the SWI. The porosity profile is defined as a
function of depth x, as $\phi(x) = \phi_\infty + (\phi_0 - \phi_\infty)e^{\alpha x}$.

Site	ω	D_b	ϕ_0	ϕ_∞	α
	[cm/a]	[cm^2/a]			[cm^{-1}]
2	0.002	0.3	0.91	0.65	-2.20
19	0.003	0.3	0.99	0.90	-0.96
20	0.003	0.3	0.97	0.92	-0.64
39	0.04	3.6	0.99	0.72	-0.89
40	0.04	3.6	0.97	0.71	-1.86
41	0.02	2.0	0.95	0.72	-2.59
48	0.05	4.2	0.93	0.74	-1.44
49	0.006	0.6	0.95	0.73	-0.64
50	0.005	0.5	0.94	0.73	-1.10
57	0.02	1.5	0.92	0.62	-1.10
58	0.008	0.8	0.95	0.68	-1.60
59	0.004	0.4	0.96	0.71	-0.99
120	0.05	4.0	0.90	0.75	-0.084

3.3. Model Parameterization and Numerical Solution

The reaction network is implemented in a modified version of the Biogeochemical Reaction Network Simulator (BRNS) (Aguilera and others, 2005), which solves systems of mixed kinetic and equilibrium reactions, coupled to one-dimensional transport processes. For a detailed description of the mathematical and numerical aspects, the reader is referred to Jourabchi et al. (2005). The rate laws and corresponding parameter values for deep-sea conditions are taken mostly from Van Cappellen and Wang (1995). The decay rates of organic matter and the rate of calcite dissolution are allowed to vary (see section 4). We assume a power law relationship for calcite dissolution with respect to the degree of pore water undersaturation (see section 4.2). The apparent solubility of calcite (K_{sp}^{*}) and dissociation constants for CO_2(aq) (the sum of H_2CO_3 and CO_2), bicarbonate, borates and sulfides are calculated using the site-specific temperature, salinity, and pressure based on the total hydrogen ion (seawater) scale (Stumm and Morgan, 1996; Pilson, 1998).

At the upper boundary (i.e., at the SWI), fixed concentrations are assigned to the solute species and deposition fluxes are imposed for the solids (Table 3). The assigned values are derived from available measurements (M), inferred from global relationships (I, G), or estimated from the literature (L). The lower boundary conditions are defined at a sufficiently great depth (82 cm), such that all concentration gradients vanish as reaction rates approach zero. The spatial resolution of the finite difference solution varies with depth from 0.01 cm at the SWI to 2 cm at the lower boundary.

Table 3: Fixed concentrations (in μM) of solute species and pH at the SWI. The imposed deposition fluxes of MnO_2 and $Fe(OH)_3$ are 10^{-4} and 5×10^{-4} μmoles/cm²/a, respectively, at all sites[1]. The deposition fluxes of the two pools of organic carbon and calcite are allowed to vary (see text). A zero-gradient is specified for all solid and solute species at the lower boundary. M = measured field data; I = inferred from pH, alkalinity, and / or calcite saturation state; G = calculated from global relationship; L = literature (Van Cappellen and Wang, 1995; typical deep-sea conditions).

Site	O_2	NO_3^-	HCO_3^-	CO_3^{2-}	CO_2	pH	Ca^{2+}	NH_4^+	SO_4^{2-}	Mn^{2+}	Fe^{2+}	H_2S	HS^-	$B(OH)_3$	$B(OH)_4^-$
2	266	21	2156	117	17.5	8.015	10^4	0	28×10^3	0	0	0	0	351	73.6
19	216	28.8	2139	84.6	23.4	7.910	10^4	0	28×10^3	0	0	0	0	367	56.8
20	211	29.5	2141	83.9	23.5	7.902	10^4	0	28×10^3	0	0	0	0	368	56.6
39	130	38.1	2332	64.7	40.8	7.820	10^4	0	28×10^3	0	0	0	0	388	35.9
40	131	38.1	2330	65.4	40.2	7.825	10^4	0	28×10^3	0	0	0	0	388	36.4
41	145	36.9	2353	61.9	42.2	7.780	10^4	0	28×10^3	0	0	0	0	389	35.4
48	268	20.3	2099	120	18.4	8.112	10^4	0	28×10^3	0	0	0	0	358	66.4
49	271	19.8	2140	117	17.8	8.048	10^4	0	28×10^3	0	0	0	0	353	71.0
50	268	20.3	2142	118	17.6	8.042	10^4	0	28×10^3	0	0	0	0	352	72.1
57	262	20.9	2140	112	19.4	8.054	10^4	0	28×10^3	0	0	0	0	359	65.2
58	270	19.9	2159	107	20.0	8.016	10^4	0	28×10^3	0	0	0	0	359	64.8
59	242	19.9	2159	107	20.0	7.940	10^4	0	28×10^3	0	0	0	0	359	64.8
120	233	26.3	2292	94.3	27.9	7.970	10^4	0	28×10^3	0	0	0	0	374	49.9
Type	M	G[2]	I	I	I	M	L	L	L	L	L	L	L	I[3]	I[3]

1. based on a clay rain rate of 5μg/cm²/a with %Fe = 2.7 and %Mn = 0.3 (Ronov and Yaroshevski, 1969) and 50% bioavailability for Mn and 30% for Fe (Archer et al., 2002).
2. based on O_2 concentrations in the overlying water (Archer et al., 2002).
3. Total borate is calculated as a function of salinity according to Millero and Sohn (1992).

The deposition fluxes of reactive organic carbon and calcite, and the parameters related to the degradation of organic carbon and the dissolution of calcite, are estimated by minimizing a least squares measure of the difference between predicted O_2 and pH profiles and the measured microprofiles. The following section defines the parameters to be estimated and our approach to determining them from the available data.

4. Model Parameter Estimation

In deep-sea sediments, only a subset of processes in the reaction network of the model affect O_2, while they all affect pH. In particular, the depth profile of O_2 is independent of the dissolution of calcite and the acid-base equilibria of the carbonate, borate and sulfide systems. By excluding formation (and dissolution) of reduced and authigenic Mn(II) and Fe(II) mineral phases, the pH dependent sinks of the reduced metals such as carbonate or sulfide phases that could potentially react with O_2 are removed. The parameter estimation is thus performed in two steps. First, the parameter values related to organic carbon deposition and degradation are obtained from the best fit of the O_2 profile. Then, the organic carbon related parameters are held constant, and the pH profile is fitted by adjusting the parameters describing the deposition and dissolution of calcite. This sequential parameter estimation approach would not be possible for shallow water sediments, where reduced Mn and Fe minerals play a major role in early diagenetic redox cycling. Under these circumstances, the fits to the two depth profiles must be estimated simultaneously.

Parameter estimation is performed using MATLAB's 'fminsearch', based on the simplex algorithm (Lagarias et al., 1998). The parameter estimation minimizes the L2-norm (least-squares norm) of the residual vector, defined as the difference between measured and calculated values, divided by the reported uncertainty in the data.

4.1. Organic Carbon Related Parameters

Most early diagenetic models of O_2 in deep-sea sediments represent organic matter by a limited number of fractions of different reactivity (multi-G approach; Westrich and Berner, 1984), ranging from highly labile to refractory organic carbon. Typically, two to three fractions are sufficient to simulate measured O_2 profiles (Hammond et al., 1996; Luff et al., 2000; König et al., 2001; Rabouille et al., 2001). As we aim for the simplest model, we assume maximally two fractions of reactive organic matter: one highly degradable fraction exhibiting the Redfield stoichiometry of fresh plankton (C:N:P = 106:16:1); and another more refractory fraction with lower N and P contents (C:N:P = 200:21:1; Van Cappellen and Wang 1995; Soetaert et al., 1996).

The two fractions of organic carbon require four parameters, namely their respective input fluxes and degradation rate constants. However, different combinations of the fluxes and rate constants can produce similar results, that is, the parameters covary and the solution is non-unique. Therefore, we use prior information and constitutive relations to constrain or reduce the number of parameters involved, thereby narrowing the solution space.

We know a priori that there is a close relationship between the sediment oxygen demand (F_{O2}) and the total flux of reactive organic carbon reaching the sediment (F_{orgC}) (e.g. Glud et al. 1994). Without making any claims regarding the exact nature of this relationship, we assume that the vertical gradient of pore water oxygen at the SWI provides a measure of F_{orgC}, independent of the degradation rate constants and relative importance of the two pools of organic carbon. Results of the parameter estimation are later used to test this assumption. In order to estimate F_{orgC} from the concentration gradient of O_2 near the SWI, we first assign average values to the other three parameters, k_f (rate constant of the fast degrading organic carbon pool), k_s (rate constant of the slow degrading organic carbon pool), and f (fraction of the more reactive organic carbon to the total reactive organic carbon flux reaching the sediment). The initial parameter values are: $f = 0.9$ (0.7-0.9, Hammond et al. 1996; 0.96-0.98, Haeckel et al., 2001; 0.85, König et al., 2001; 0.84, Rabouille et al., 2001), $k_f = 0.1$ a^{-1} and $k_s = 0.001$ a^{-1}. The two orders of magnitude difference between the rate constants is based on the work of Soetaert et al. (1996). Using these parameter values, we adjust F_{orgC} to match the gradient of O_2 near the SWI.

Once a first estimate of F_{orgC} is obtained, the number of unknown parameters is reduced using the constitutive relationship between the degradation rate constant k_s of the less reactive organic carbon and the total flux of degradable organic carbon proposed by Boudreau (1997):

$$k_s \,(\mathrm{a}^{-1}) = 2.2 \times 10^{-5} F_{orgC}^{2.1},$$

where the flux of organic carbon F_{orgC} is given in units of μmoles cm^{-2} a^{-1}. Given F_{orgC} and k_s, the fraction f and degradation rate constant k_f are estimated. If this unconstrained parameter estimation yields a value of f exceeding 1, we impose $f = 1$. This is the case for sites 19 and 48. Similarly, when the estimated value of k_f exceeds 10 a^{-1}, which is considered an upper limit for marine sediments (Boudreau, 1997), we fix k_f at 10 a^{-1}, and only estimate the corresponding fraction f. This is the case for sites 20, 41 and 58.

To test the assumption that the oxygen gradient is essentially independent from f, k_f, and k_s, we calculate a new value of F_{orgC} from the estimated parameter values of f and k_f, and the constitutive relationship given above. We then compute the corresponding benthic O_2 uptake flux. In nearly all cases, the a posteriori calculated O_2 uptake flux differs by less than 2% from the original estimate, thereby supporting the assumption that the oxygen gradient mainly depends on the total flux of degradable organic carbon.

4.2. Calcite Related Parameters

The calcite related parameters are estimated by fitting the measured pH profile, given the fluxes and degradation rate constants of the two organic carbon fractions derived from the optimization of the oxygen profiles. We assume that the dissolution rate of calcite (R) depends on the degree of undersaturation ($1-\Omega_c$) of the pore water, such that

$$R = k_d[CaCO_3](1-\Omega_c)^n \text{ with } \Omega_c \equiv \frac{[CO_3^{2-}][Ca^{2+}]}{K_{sp}^*},$$

where k_d is the dissolution rate constant, expressed in percent solid phase dissolved per time, [$CaCO_3$] the concentration of calcite, and n the reaction rate order.

Laboratory studies suggest that nonlinear rate laws, with $n > 1$, apply to calcite dissolution in sea water (Keir, 1980; Gehlen et al., 2005). In several modeling studies, however, a linear rate law ($n = 1$) results in less variability in the dissolution rate constant, k_d, when comparing pore water data from multiple locations characterized by variable saturation states of the bottom water (Gehlen et al., 1999; Hales and Emerson, 1997b; Mekik et al, 2002). The majority of previous modeling studies have used a rate order of either 1 or 4.5 with the latter being most dominant (Table 4), whereas Adler et al. (2001) tested a range of values from 1 to 4.5. In two comprehensive reviews of calcite dissolution kinetics, Morse and Arvidson (2002) and Morse et al. (2007) discuss in detail the debate on the calcite dissolution rate order. In this study, we consider four values of rate order, $n = 0.5, 1.0, 2.0,$ and 4.5.

Two parameter estimation procedures are considered. In the first approach, the rate constant, k_d, plus the deposition flux of calcite, F_{cal}, are estimated simultaneously. The depth distribution of [$CaCO_3$] is therefore an explicit outcome of fitting the pH profile. In the second approach, the calcite concentration in the sediment is held constant at the average value measured at the site (Table 1). In this case, the modeled pH distribution is independent of the flux of calcite reaching the sediments and only the value of the rate constant k_d is estimated.

Table 4: Summary of calcite dissolution rate orders and constants determined in experimental studies[*], or used in modeling studies.

| Study	Rate order	Rate constant (%/day)
Keir, 1980[*]	4.5	30 - 1300
Berelson et al., 1990	4.5	5 - 130
Archer, 1991	4.5	10 - 1000
Berelson et al., 1994	4.5	5 - 100
Hales et al., 1994	4.5	3 – 30
Jahnke et al., 1994	4.5	0.2
Cai et al., 1995	3 / 4.5	1 – 3 / 5 - 10
Martin & Sayles, 1996	4.5	0.7 - 40
Hales & Emerson, 1997a	4.5	0.014 - 126
Hales & Emerson, 1997b	1	0.0004 - 0.01
Jahnke et al., 1997	4.5	5 - 1000
Luff et al., 2000	4.5	0.3
Adler et al., 2001	1, 2, 3, 4.5	0.04 - 18 (n= 4.5) 0.005 - 0.01 (n=1)
Wenzhöfer et al., 2001	4.5	95
Archer et al., 2002	1	?
Mekik et al., 2002	1	0.01
Pfeifer et al., 2002	4.5	0.01 – 0.5
Luff et al., 2004	1	0.14
Gehlen et al., 2005[*]	1.4 - 2.8	0.09 - 0.53 meq/m^2/day
Martin & Sayles, 2006	1	0.01, 0.001

5. Model Results & Discussion

5.1. Oxygen

The parameter estimation procedure yields excellent fits to the measured O$_2$ profiles at all 13 sites (Figure 1). The corresponding estimates of the deposition flux of degradable organic carbon, the most reactive fraction and its degradation rate constant are listed in Table 5. For comparison, the best fits obtained when assuming the existence of only one fraction of degradable organic carbon are shown as broken lines in Figure 1. In only 2 out of the 13 cases (sites 19 and 48, Table 5) is a one-G model able to reproduce the O$_2$ data. For the other 11 sites, a two-G model is necessary and sufficient to account for the pore water O$_2$ distributions. This result is consistent with the double exponential decay functions that are often successful in fitting O$_2$ profiles in deep-sea sediments (e.g., Martin and Sayles, 2006).
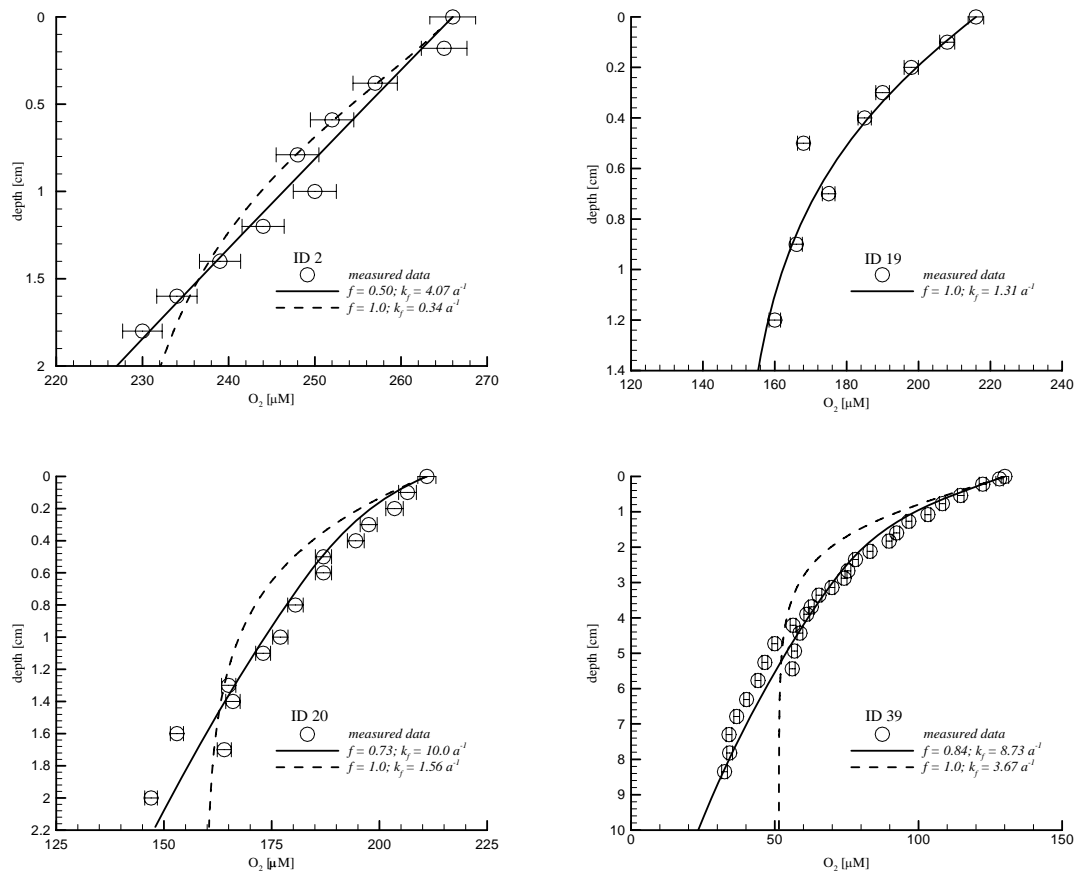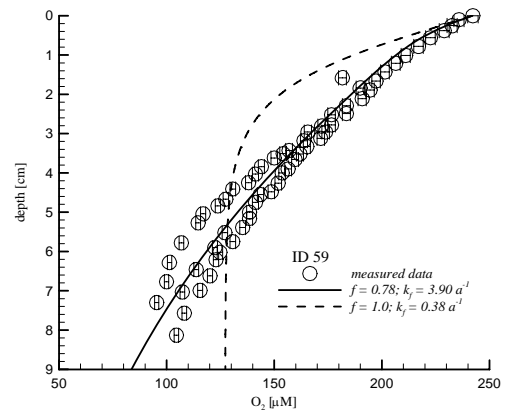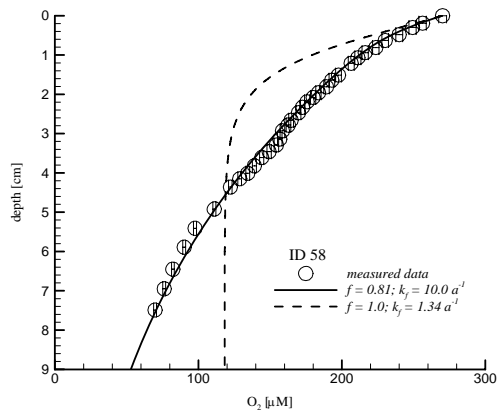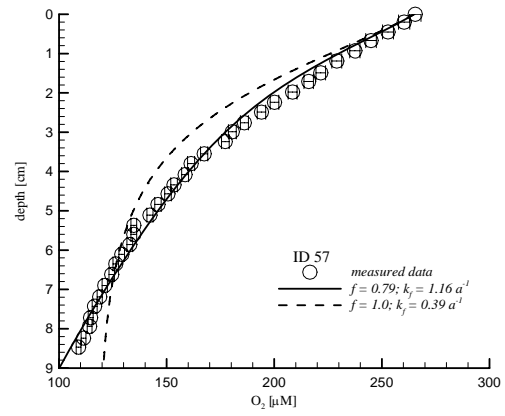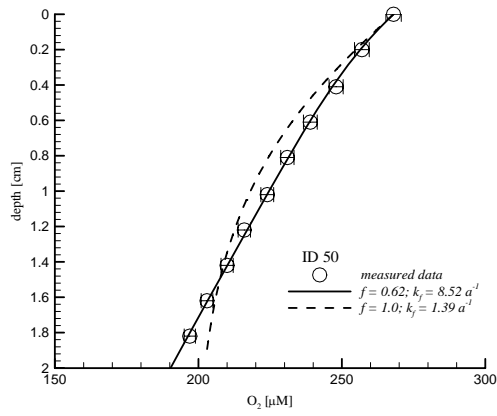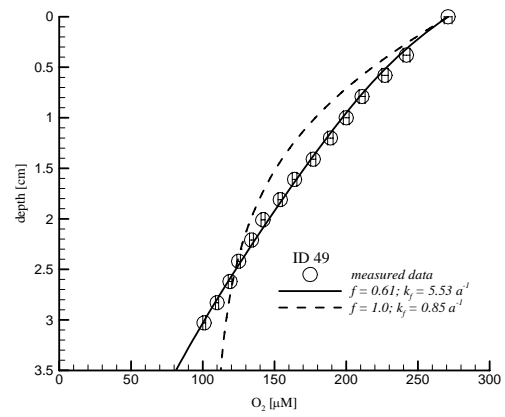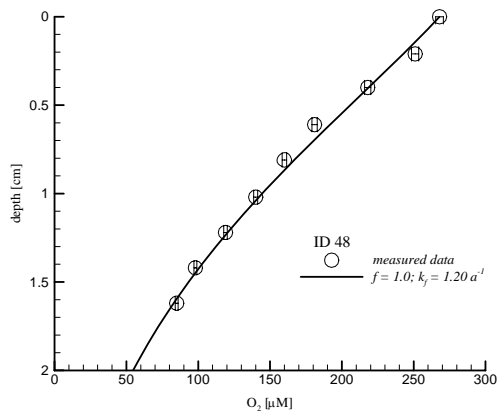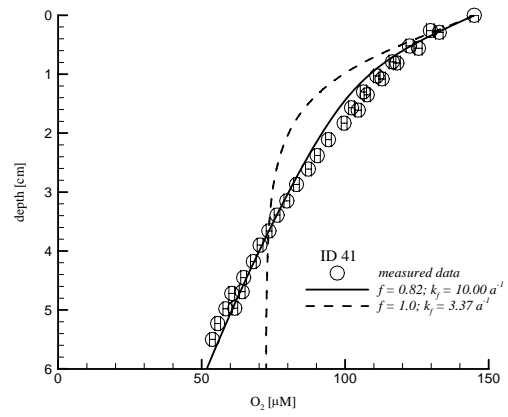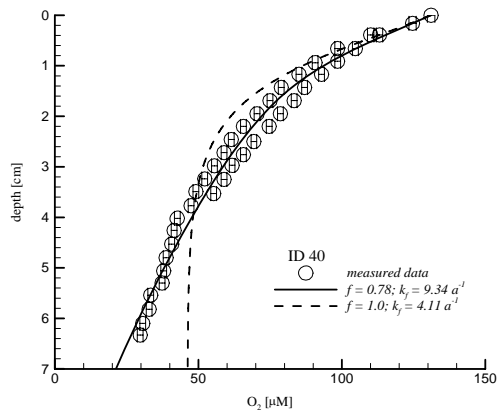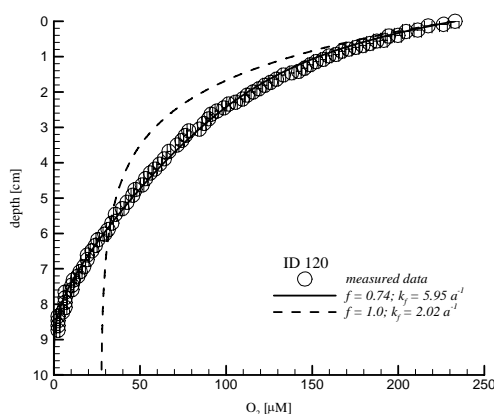
Figure 1: Model fits to O_2 data. The thick black lines show the best fit to the data. The broken lines are the results of assuming a single fraction of reactive organic carbon ($f = 1$).

Table 5: Deposition flux of total degradable organic carbon in μmol/cm^2/a, F_{orgC}, fraction of the more reactive organic carbon flux, f, and its degradation rate constant, k_f (a^{-1}), that best fit the oxygen data. The two rightmost columns are the relative χ^2 misfits between the optimized model results and the data (φ_m) assuming two-G and one-G organic carbon pools.

Site	F_{orgC}	f	k_f	φ_m (two-G)	φ_m (one-G)
2	4.3	0.50	4.07	0.59	1.3
19	22	1.00	1.31	7.1	7.1
20	22	0.73	10.00	5.0	20
39	9.3	0.84	8.73	13	120
40	10	0.78	9.34	12	87
41	10.5	0.82	10.00	9.2	130
48	32	1.00	1.20	8.3	8.3
49	28	0.61	5.53	2.0	73
50	16.4	0.62	8.52	0.06	4.6
57	7	0.79	1.16	5.1	48
58	22	0.81	10.00	5.2	480
59	13	0.78	3.90	32	210
120	29	0.74	5.95	6.5	310

At two of the sites, sediment trap data constrain the total deposition flux of organic carbon: 6 μmolC cm^{-2} a^{-1} at site 2 (Deuser, 1986) and 18-40 μmolC cm^{-2} a^{-1} at site 48 (Rowe and Gardner, 1979; Biscay et al., 1988). These values compare favorably with the estimated values of the flux F_{orgC} at the same sites: 4.3 μmolC cm^{-2} a^{-1} at site 2 and 32 μmol cm^{-2} a^{-1} at site 48. Note that F_{orgC} does not include organic carbon that is completely refractory to degradation on early diagenetic time scales. However, given the very low preservation efficiencies of deposited organic carbon in deep-sea sediments (<10%, Jahnke et al., 1994;

Tromp et al., 1995), F_{orgC} values should approach the total deposition fluxes of organic carbon.

The range of k_f for the deep-sea sites considered here coincides with the range of 1-10 a^{-1} reported by Boudreau (1997). The average value of k_f is 6.1±3.5 a^{-1}. In three cases, k_f is assigned the maximum allowable value of 10 a^{-1} (sites 20, 41 and 58, Table 5). For these sites, additional simulations show that the fits to the measured O_2 concentrations are no longer sensitive to k_f when the latter exceeds 10 a^{-1} (results not shown). The high k_f values confirm that sediment metabolism in the deep-sea is fueled by the deposition of relatively fresh organic matter (Sayles et al., 1994; Hammond et al., 1996; Martin and Sayles, 2006). At all the sites, the fraction of high reactivity organic matter exceeds 50%, with an average value of f on the order of 0.8. Previously reported values put f in the range 0.7-0.98 (Hammond et al., 1996; Haeckel et al., 2001).

In our study, the three sites that exhibit fractions f below 0.7 (sites 2, 49, and 50) are situated in the western North Atlantic and at water depths greater than 4000 m. A reduced supply of more reactive organic matter at these sites agrees with the benthic oxygen uptake fluxes measured by Hinga et al. (1979) in the North Atlantic. These authors reported that the benthic oxygen consumption at 5000 m water depth is an order-of-magnitude lower, compared to the shallow sea floor. They attributed this decrease to both the greater sinking distance of particulate material through the water column, and the lower primary productivity of the pelagic waters.

The model derived benthic O_2 fluxes are within the range expected for deep-sea sediments (Table 6). The relatively low O_2 fluxes are consistent with the omission of bioirrigation in the analysis of pore water profiles (Meile and Van Cappellen, 2003). Sediment O_2 uptake rates were measured with benthic chambers at four of the sites. Observed and modeled O_2 fluxes are in good agreement at three of the four sites. For the Ceara Rise site (site 57), the model estimated O_2 flux is lower than the benthic chamber flux. Although this result may be related to the lateral heterogeneity of the sediments, Hales and Emerson (1997a) reported that only one of the two O_2 profiles measured at site 57 yields a diffusive flux approaching the benthic chamber flux, suggesting that bioirrigation is non-negligible at this site.

Table 6: Oxygen flux across the sediment water interface: data and model results. Benthic chamber data from Jahnke et al., 1994 for site 41, and Hales and Emerson, 1997a for sites 57-59. The rightmost column shows the % of total O_2 consumed by oxic respiration.

Site	Benthic chamber [μmol/cm^2/a]	Model results [μmol/cm^2/a]	% O_2 used in oxic respiration
2		5.1	83
19		26.8	82
20		24.8	89
39		11.3	77
40		11.5	75
41	18+/-8	12.15	80
48		37.10	69
49		31.9	76
50		18.6	81
57	18+/-7	8.7	80
58	24+/-9	25.9	84
59	17+/-6	15.5	84
120		32.8	75

Although oxic respiration is the main organic carbon degradation pathway, the model results indicate that other pathways may contribute, especially to the degradation of the less reactive organic matter (Table 7). Denitrification is predicted to be significant at 11 of the 13 sites, while non-negligible contributions of dissimilatory Mn and Fe reduction, as well as sulfate reduction, are only expected at the shallowest water depths (sites 39, 40, 41, 48, 120). The release of ammonium during organic matter degradation, and the production of reduced species by the anaerobic degradation pathways, also mean that a fraction of O_2 is utilized in secondary oxygenation reactions. According to the model calculations, this fraction ranges from 11% at site 20, where oxic respiration is the only organic matter degradation pathway, to 31% at site 48, where suboxic and anoxic degradation pathways play a role. The main secondary oxygenation pathway is nitrification.

Table 7: Relative contributions (in %) of the various degradation pathways for the two fractions of organic carbon with high / low reactivity. *Total of percentages deviates from 100% due to round-off errors.

Site	Oxic respiration	Denitrification	Mn reduction	Fe reduction	Sulfate reduction
2	100 / 97.4	0 / 2.6	0 / 0	0 / 0	0 / 0
19	100 / 0	0 / 0	0 / 0	0 / 0	0 / 0
20	100 / 100	0 / 0	0 / 0	0 / 0	0 / 0
39	100 / 56.7	0 / 26.2	0 / 17.1	0 / 0	0 / 0
40*	100 / 36.6	0 / 25.8	0 / 0.2	0 / 25.8	0 / 11.5
41	100 / 57.9	0 / 22.1	0 / 19.9	0 / 0	0 / 0.1
48*	79.7 / 0	7.7 / 0	0.6 / 0	1.4 / 0	10.7 / 0
49	100 / 66.6	0 / 9.6	0 / 23.8	0 / 0	0 / 0
50	100 / 77.9	0 / 8.3	0 / 13.8	0 / 0	0 / 0
57	100 / 94.9	0 / 5.1	0 / 0	0 / 0	0 / 0
58	100 / 96.6	0 / 3.4	0 / 0	0 / 0	0 / 0
59	100 / 100	0 / 0	0 / 0	0 / 0	0 / 0
120*	100 / 41.6	0 / 16.8	0 / 0.5	0 / 1.4	0 / 39.6

5.2. pH

The fitted pH profiles obtained by simultaneously estimating the deposition flux (F_{cal}) and dissolution rate constant (k_d) of calcite are shown in Figure 2. (Note: a detailed discussion of the processes shaping the model-derived pH profiles can be found in Jourabchi et al. (2005).) Also shown are the simulated pH profiles when calcite dissolution is ignored. Except for site 120, the latter profiles largely underestimate the observed pore water pH values, clearly illustrating the necessity of including buffering by calcite dissolution. Of the 52 potential sets of results (one for each site and value of n considered (Table 8)), only those with a positive dissolution rate constant and a deposition flux of calcite below the allowable maximum (as determined from the sedimentation rate assuming 100% calcite) are accepted. These two criteria lead to the elimination of 9 sets of results, of which only one does not satisfy the first criterion (site 120 for $n = 4.5$), and 8 fail the second criterion (site 49 for all values of n; site 50 for $n = 0.5$; site 57 for all n except 0.5). The second criterion is most likely a conservative measure as the sediment accumulation rate at many deep-sea sites may have increased in the recent past. Because no meaningful fits to the pH profile are obtained at site 49, it is not considered further.
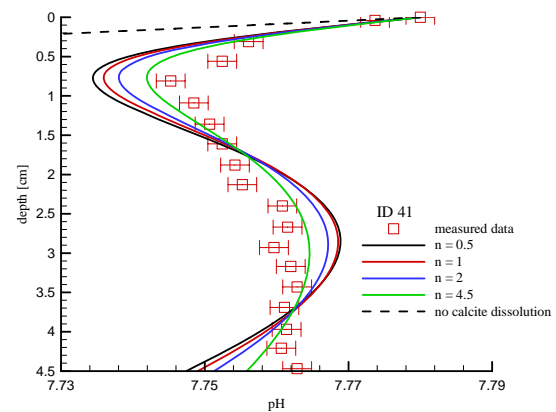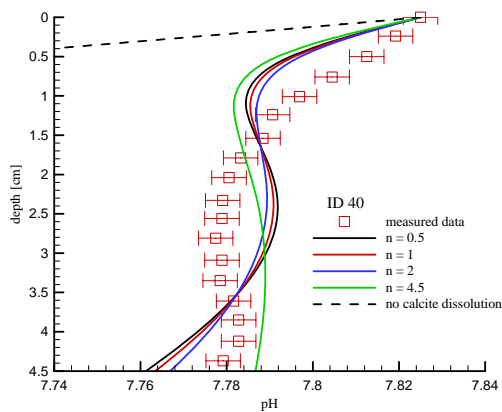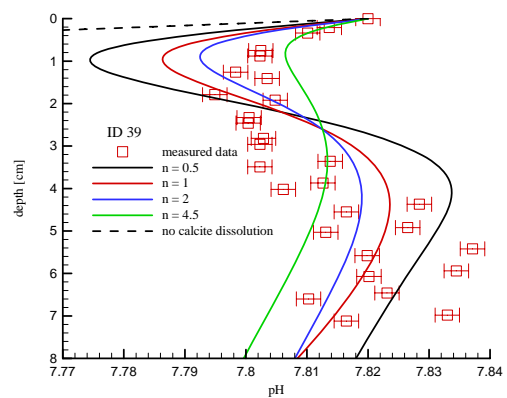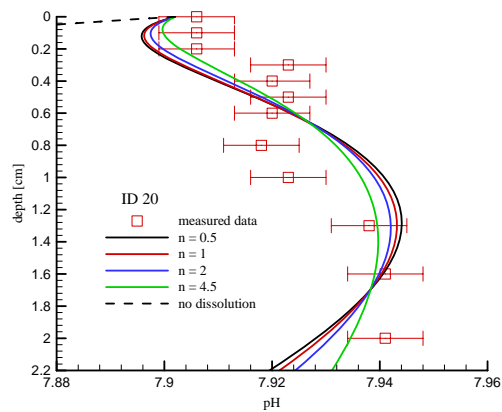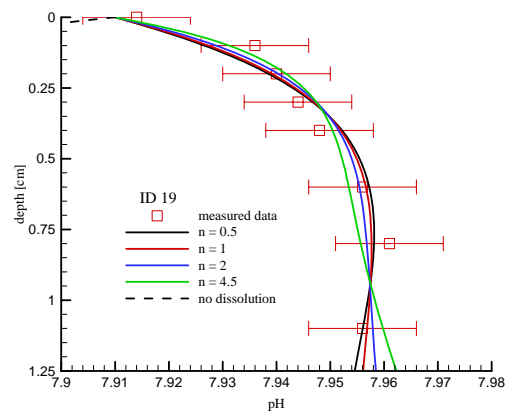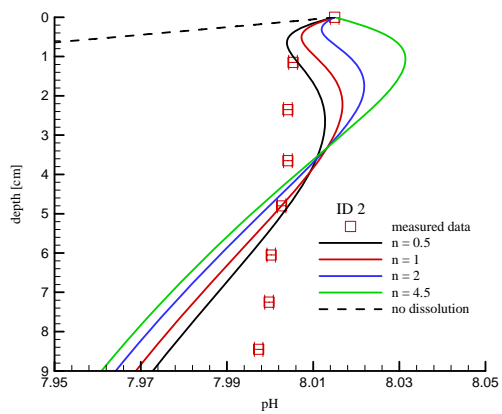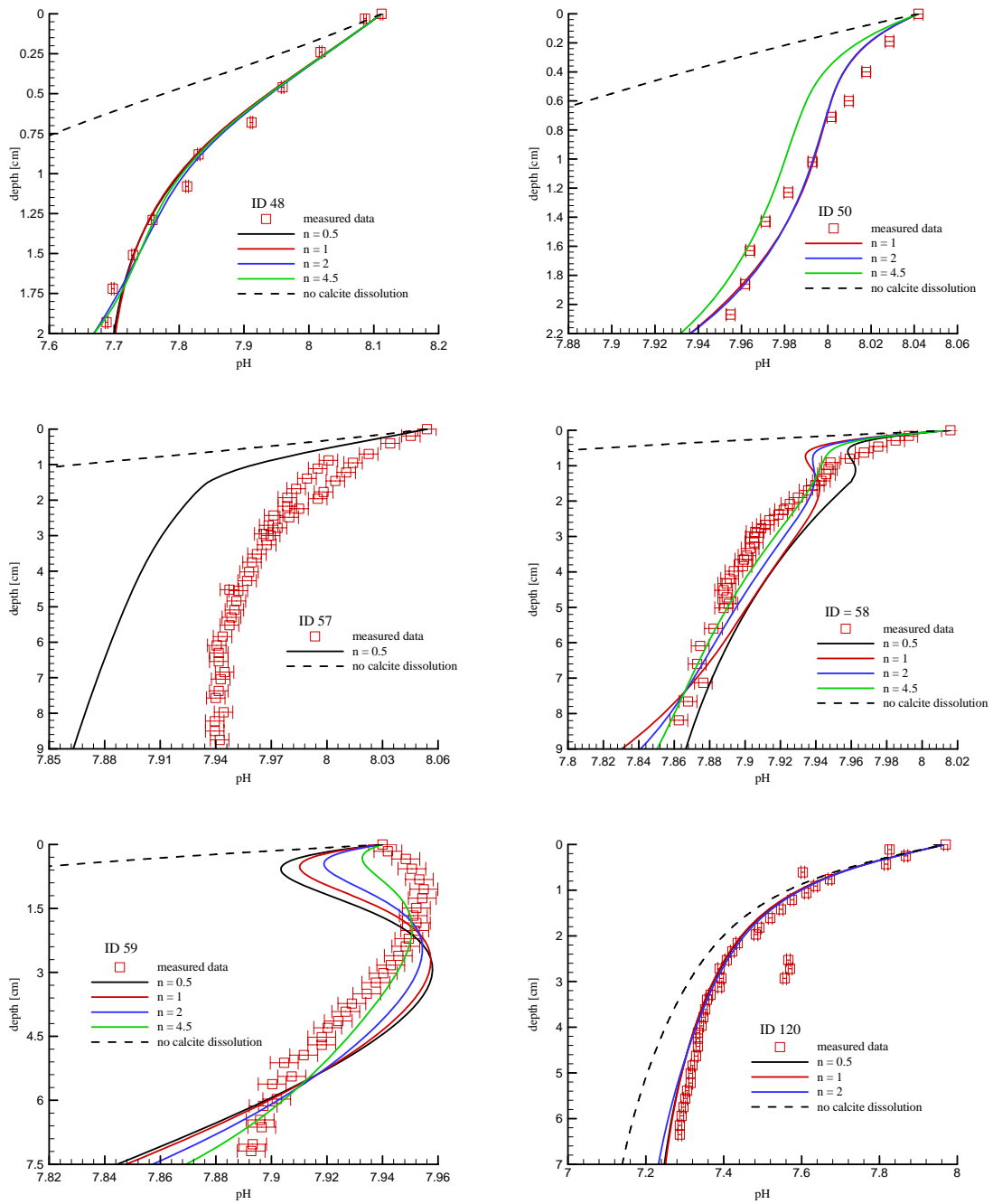
Figure 2: Model fits to pH data for *n* values of 0.5, 1, 2, and 4.5.

Table 8: Deposition flux of calcite, F_{cal} and dissolution rate order, k_d that best fit the pH profiles for rate orders, $n = 0.5$, 1.0, 2.0, and 4.5. When no values are given, convergence was not achieved. Bold font indicates the best-fit results for n. Relative chi-square misfits less than 1 indicate over-fitting of the data and values greater than 1 indicate the degree of under-fitting.

| n = 0.5 | Initial values: | | |
| | $F_{cal} = F_{orgC}$ & $k_d = 0.005$ % / day | | |
Site	F_{cal} [μmol/cm^2/a]	k_d [% / day]	relative χ^2 misfit
2	**4.8**	**7.5e-5**	**94.09**
19	33.4	9.0e-1	0.18
20	17.2	1.5e-1	2.61
39	5.5	5.4e-3	64.91
40	6.4	9.7e-1	7.23
41	5.5	2.5e-1	14.35
48	24.7	5.5e-3	56.92
49	-	-	-
50	-	-	-
57	**7.6**	**4.8e-3**	**134.39**
58	14.3	6.2e-3	12.70
59	7.2	4.5e-2	20.64
120	1.5	5.9e-3	99.00

| n = 1.0 | Initial values: | | |
| | $F_{cal} = F_{orgC}$ & $k_d = 0.01$ % / day | | |
Site	F_{cal} [μmol/cm^2/a]	k_d [% / day]	relative χ^2 misfit
2	7.0	1.8e-4	152.29
19	34.0	1.7e0	0.16
20	17.4	2.6e-1	2.38
39	6.1	1.5e0	28.49
40	6.4	2.5e0	6.15
41	5.6	4.7e-1	11.89
48	29.3	1.1e-2	63.61
49	-	-	-
50	9.0	1.9e0	12.42
57	-	-	-
58	9.6	7.0e-1	12.66
59	7.9	1.3e-1	15.43
120	1.5	1.6e-3	99.42

Table 8 (continued)

n = 2.0	Initial values: $F_{cal} = F_{orgC}$ & k_d = 1 % / day		
Site	F_{cal} [μmol/cm^2/a]	k_d [% / day]	relative χ^2 misfit
2	5.6	7.6e-3	246.40
19	35.4	6.5e0	0.14
20	18.1	8.0e-1	1.98
39	**6.5**	**6.9e0**	**24.87**
40	**6.6**	**1.7e1**	**4.66**
41	5.7	1.6e0	8.18
48	**14.8**	**1.9e2**	**39.64**
49	-	-	-
50	**8.9**	**5.4e1**	**12.41**
57	-	-	-
58	9.9	1.0e1	7.10
59	9.0	9.0e-1	8.96
120	**1.7**	**2.0e-1**	**97.92**

n = 4.5	Initial values: $F_{cal} = F_{orgC}$ & k_d = 100 %/day		
Site	F_{cal} [μmol/cm^2/a]	k_d [% / day]	relative χ^2 misfit
2	10.1	9.6e0	372.08
19	**38.3**	**1.5e2**	**0.14**
20	**19.6**	**1.4e1**	**1.31**
39	13.9	4.6e0	41.41
40	7.6	5.9e0	6.95
41	**6.0**	**3.3e1**	**3.14**
48	14.6	5.2e4	48.62
49	-	-	
50	7.6	1.1e4	37.96
57	-	-	
58	**10.5**	**1.2e4**	**3.38**
59	**11.5**	**1.1e2**	**2.80**
120	-	-	

At 9 of the sites, the best-fit pH profiles capture the general features of the measured microprofiles (sites 19, 20, 39, 40, 41, 48, 50, 58, and 120, Figure 2). In particular, the ranges of the observed pH variations are reproduced within 10% by the model. At sites 2 and 57, the optimized model profiles exhibit more pronounced pH fluctuations than seen in the data, suggesting that additional processes may contribute to the buffering of pore water pH. These may include surface exchange reactions between the calcite mineral surface and dissolved carbonate species (Jahnke and Jahnke, 2004), as well as protonation and deprotonation of functional groups of other mineral surfaces and sediment organic matter. It is not clear,

however, why the optimized model pH profiles for site 59 predict gradients at the SWI that are opposite to the observed one.

Comparison of data and model misfit values indicate that rate orders $n = 2$ and $n = 4.5$ yield the best fits to the measured pH profiles at 5 sites each (Table 8). Only two sites are best simulated with $n = 0.5$ (sites 2 and 57), while $n = 1$ does not provide the best pH fit at any of the sites. Although it is not possible to conclusively identify a generally applicable rate order, we note that pH profiles at sites with overlying water near equilibrium or oversaturated with respect to calcite are better simulated with $n = 2$, while those at sites overlain with undersaturated waters are best described by $n = 4.5$ (compare saturation states in Table 1 with shaded areas indicating best-fit reaction order in Table 9). Thus, differences in saturation state of the overlying water may in part explain the variability in n values found among previous studies.

Table 9: Calculated burial fluxes of calcium carbonate (F_b) based on available $CaCO_3$ wt % reported by the respective studies, the sedimentation rates reported in Table 2, and an assumed solid density of 2.5 g/cm^3 (see text for details). Also shown are the model predicted percentages of deposited calcite that are dissolved. The model simulations that give the best pH fit are shaded.

Site	F_b [μmol/cm^2/a]	% calcite flux dissolved			
		$n = 0.5$	$n = 1$	$n = 2$	$n = 4.5$
2	1.4	69	47	70	65
19	0.75	100	100	100	100
20	0.6	100	100	99	100
39	250	98	100	100	58
40	260	100	100	100	80
41	120	100	100	100	100
48	36	61	51	100	100
49	12	-	-	-	-
50	11	-	100	100	100
57	130	42	-	-	-
58	42	87	100	100	100
59	15	100	100	100	100
120	9.4	100	100	100	-

Regardless of the imposed dissolution rate order n, the estimated deposition flux of calcite, F_{cal}, differs by a factor of about 20 between the highest values obtained for site 19 and the lowest for site 120 (Table 8). In contrast, for any given value of n, the dissolution rate constant, k_d, varies by several orders of magnitude among the sites, which is in line with previous studies (Table 4). In addition, at a given site, the estimated values of F_{cal} typically

vary by less than a factor of 2 for the different values of n. However, as expected, changing the value of n has a large impact on the estimated value of k_d.

With two exceptions (sites 2 and 57), the model simulations using the estimated F_{cal} and k_d values from the best-fit pH profiles predict complete dissolution of the deposited $CaCO_3$ (Table 9). The reason is that the pH profile only constrains the amount of calcite that is needed for the pore waters to reach equilibrium with respect to calcite. In other words, the pH profiles are insensitive to the input of calcite in excess to that required for equilibrium. As such, it is not possible to estimate the total deposition flux of $CaCO_3$ from the pH data, but only its minimum value. Because steady state is assumed, the *minimum* calcite deposition flux needed to reach thermodynamic equilibrium corresponds to the depth-integrated calcite dissolution rate. The parameter estimation procedure is thus a better predictor of the amount of $CaCO_3$ being dissolved in the sediment than the actual deposition flux.

To estimate the calcite deposition flux, additional information is needed. For the sites considered, the $CaCO_3$ burial flux, F_b, can be calculated from the calcium carbonate concentration measured in the deepest portions of the sediment cores, plus the sedimentation rate (Table 9). Assuming steady state, the deposition flux is then the sum of integrated dissolution rate and F_b. However, there are considerable uncertainties associated with the estimates of F_b listed in Table 9. In some cases, dissolution is predicted to continue below the deepest $CaCO_3$ concentration measured in the cores (e.g., sites 19 and 20). Added to this are the uncertainties associated with the sedimentation rates (section 3.2), plus possible changes in sediment deposition over time (e.g., Berelson et al., 1997).

Because the pH profiles cannot be used to constrain the calcite deposition flux, they are also fitted by optimizing for k_d only. Rather than calculating the calcite concentration profile using the flux boundary condition, we keep the calcite concentration constant in the dissolution rate expression, and equal to the average $CaCO_3$ content measured at the site (Table 1). Although the misfits to the data are in general greater with this one-parameter (k_d) fitting approach (not shown), the predicted depth-integrated dissolution rates follow the same trend as for the previous, two-parameter (F_{cal}, k_d) estimation (Figure 3). However, the use of the core-averaged $CaCO_3$ concentrations systematically underestimates the dissolution rates in the uppermost portions of the sediments and, therefore, yields depth-integrated dissolution rates that are 10-15% lower than the values obtained with the two-parameter estimation.

Calcite dissolution in sediments is driven by CO_2 production coupled to O_2 reduction, which increases the degree of undersaturation of the pore waters with respect to calcite (e.g., Emerson and Bender, 1981; Jahnke et al., 1994; Wenzhöfer et al., 2001; Burdige, 2006, and

references therein). The model-derived depth-integrated calcite dissolution rates and benthic O_2 fluxes are indeed positively correlated, although a clear separation exists between sites overlain by undersaturated and supersaturated bottom waters (Figure 4). On a molar basis, the integrated dissolution rate of calcite accounts for more than 50% of the oxygen uptake flux at sites with undersaturated bottom waters, and less than 50% at those with supersaturated bottom waters.

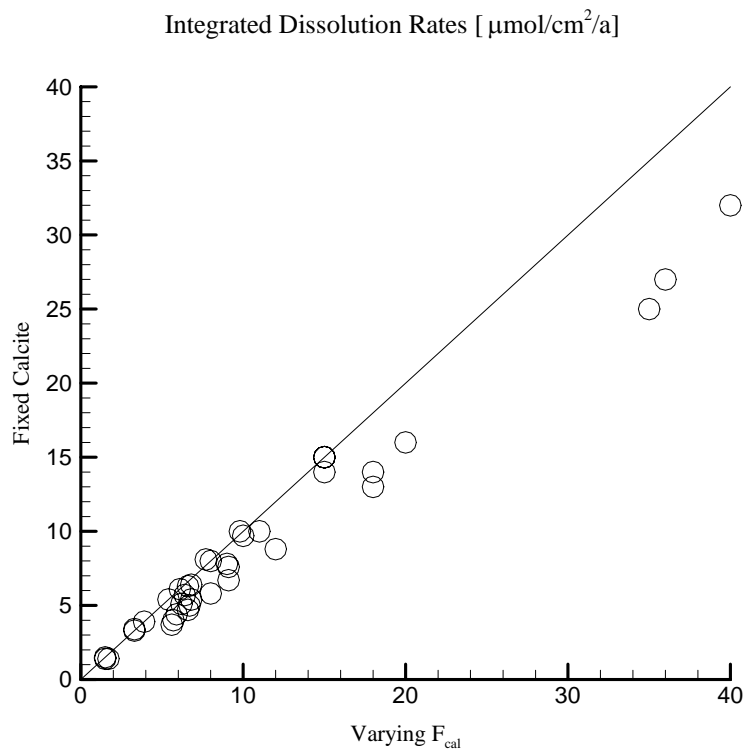Integrated Dissolution Rates [$\mu mol/cm^2/a$]

Figure 3: Comparison of depth-integrated calcite dissolution rates in the two pH optimization approaches. The line denotes the 1:1 relationship.
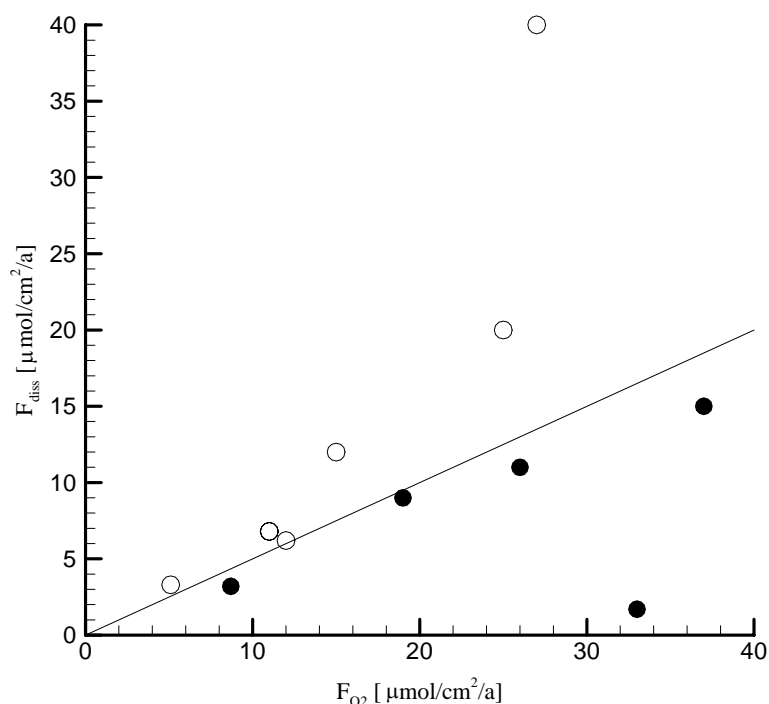
Figure 4: Depth-integrated calcite dissolution rate versus the oxygen uptake at the SWI. Model predictions are divided into sites with supersaturated (filled symbols) and undersaturated (open symbols) water overlying the sediment. A line with a slope of ½ delineates the two regions.

At Ceara Rise sites 57 and 58, benthic chamber measurements imply a flux of alkalinity into the sediment (Table 10), which is opposite to the model predicted benthic alkalinity fluxes. Among the reactions considered in the model, only five secondary redox reactions result in a consumption of alkalinity. The model results further indicate that, of these five reactions, only nitrification has a substantial influence on alkalinity at these two sites, but is not sufficient to overcome predicted alkalinity production due to calcite dissolution and organic carbon degradation. As noted by Jahnke and Jahnke (2004), this discrepancy shows that current diagenetic models based on redox reactions and calcite dissolution are insufficient in explaining benthic chamber measurements of alkalinity flux at sites where the sediments contain significant $CaCO_3$ and the overlying waters are supersaturated with respect to calcite. In these environments, precipitation of $CaCO_3$ in the topmost sediment may contribute to reversing the benthic alkalinity flux. This possibility deserves further investigation.

Table 10: Alkalinity Flux: benthic chamber data from Jahnke and Jahnke, 2004. All flux values are in $\mu mol/cm^2/a$. The model results correspond to the best-fit pH profiles for the three sites.

Site	Benthic chamber data	Model derived
57	3.4 +/- 2.5	-5.7
58	12.9 +/- 3.9	-20.8
59	-23.6 +/- 4.0	-22.8

6. Conclusions

The joint interpretation of pore water oxygen and pH microprofiles within a reactive transport modeling framework yields important quantitative constraints on organic matter degradation and $CaCO_3$ dissolution in deep-sea depositional settings. The statistical analysis of the model simulation results shows that two sedimentary pools of organic matter with distinct reactivities are necessary to reproduce the oxygen profiles at the majority of the sites considered (11 out of 13). Estimation of only three parameters (the input fluxes of the two organic matter fractions, plus the degradation rate constant of the more reactive pool) is sufficient to successfully simulate the observed oxygen profiles at all the sites. The model results further indicate that, although oxic respiration is the dominant pathway of degradation of organic matter, suboxic degradation plays a non-negligible role in most of the deep-sea sediments.

In contrast to oxygen, the successful simulation of the pore water pH profiles is less straightforward, due to the larger number of processes that affect the proton balance, as well as the uncertainties associated with the calcite dissolution kinetics. Hence, only 9 out of the 13 pH microprofiles are satisfactorily reproduced. In addition, while fitting the O_2 pore water concentrations yields estimates of the deposition flux of degradable organic matter, it is not possible to constrain the deposition flux of $CaCO_3$ from the pH data. This is because organic matter is unstable in early diagenetic environments, while pore waters reach equilibrium with respect to calcite. As a consequence, the depth-integrated calcite dissolution rate, rather than the corresponding deposition flux, is obtained from the best-fit pH profiles.

The model results highlight the major role of calcite dissolution in buffering pore water pH in marine sediments. Furthermore, dissolution rate expressions including nonlinear dependencies on the degree of undersaturation yield the best agreement between modeled and measured pH profiles. Nonetheless, the model-derived profiles overpredict the amplitude of pH variations observed at a number of the sites, even when $CaCO_3$ dissolution is included. We speculate that additional proton exchange processes, involving functional groups of mineral surfaces and sedimentary organic matter, may also contribute to pore water buffering.

The rigorous combination of pore water data with reactive transport modeling extends our understanding of early diagenetic processes and benthic-pelagic coupling beyond the temporal and spatial scales accessible to direct measurements. This understanding is necessary when embedding benthic exchanges into regional or global ocean models, in particular in the context of climate simulations that extend back over glacial-interglacial

timescales. Our approach not only illustrates the success in quantifying benthic O$_2$ dynamics, but also identifies remaining limitations in representing pore water acid-base chemistry and early diagenetic CaCO$_3$ dynamics. The latter has significant implications for the long-term interpretation of paleo-proxies linked to calcite composition and preservation, and highlights the need for further quantitative studies.

References

Adler M., Hensen C., Wenzhöfer F., Pfeifer K., and Schulz H. D. (2001) Modeling of calcite dissolution by oxic respiration in supralysoclinal deep-sea sediments. *Marine Geology* **177**, 167-189.

Aguilera D. R., Jourabchi P., Spiteri C., and Regnier P. (2005) A knowledge-based reactive transport approach for the simulation of biogeochemical dynamics in Earth systems. *Geochemistry Geophysics Geosystems* **6**, doi:10.1029/2004GC000899.

Archer D., Emerson S., and Reimers C. (1989) Dissolution of calcite in deep-sea sediments: pH and O_2 microelectrode results. *Geochimica et Cosmochimica Acta* **53**, 2831-2845.

Archer D. (1991) Modeling the calcite lysocline. *Journal of Geophysical Research* **96**, 17037-17050.

Archer D. E., Morford J. L., and Emerson S. R. (2002) A model of suboxic sedimentary diagenesis suitable for automatic tuning and gridded global domains. *Global Biogeochemical Cycles* **16** doi: 10.1029/2000GB001288.

Berelson W. M., Hammond D. E., and Cutter G. A. (1990) In situ measurements of calcium carbonate dissolution rates in deep-sea sediments. *Geochimica et Cosmochimica Acta* **54**, 3013-3020.

Berelson W. M., Hammond D. E., McManus J., and Kilgore T. E. (1994) Dissolution kinetics of calcium carbonate in equatorial Pacific sediments. *Global Biogeochemical Cycles* **8**, 219-235.

Berelson W. M., Anderson R. F., Dymond J., Demaster D., Hammond D. E., Collier R., Honjo S., Leinen M., McManus J., Pope R., Smith C., and Stephens M. (1997) Biogenic budgets of particle rain, benthic remineralization and sediment accumulation in the equatorial Pacific. *Deep-Sea Research II* **44**, 2251-2282.

Berg P., Rysgaard S., and Thamdrup B. (2003) Dynamic modeling of early diagenesis and nutrient cycling. A case study in an Arctic marine sediment. *American Journal of Science* **303**, 905-955.

Berner R. A. (1980) *Early diagenesis: a theoretical approach*. Princeton University Press, Princeton.

Biscaye P. E., Anderson R. F., and Deck B. L. (1988) Fluxes of particles and constituents to the eastern United States continental slope and rise: SEEP-I. *Continental Shelf Research* **8**, 855-904.

Boudreau B. P. and Canfield D. E. (1993) A comparison of closed- and open-system models for porewater pH and calcite-saturation state. *Geochimica et Cosmochimica Acta* **57**, 317-334.

Boudreau B. P. (1996) A method-of-lines code for carbon and nutrient diagenesis in aquatic sediments. *Computers and Geosciences* **22**, 479-496.

Boudreau B. P. (1997) *Diagenetic models and their implementation: modelling transport and reactions in aquatic sediments*. Springer-Verlag, Berlin.

Burdige D. J. (2006) *Geochemistry of marine sediments*. Princeton University Press, Princeton.

Cai W.-J. and Reimers C. E. (1993) The development of pH and P$_{CO2}$ microelectrodes for studying the carbonate chemistry of pore waters near the sediment-water interface. *Limnology and Oceanography* **38**, 1762-1773.

Cai W.-J., Reimers C. E., and Shaw T. (1995) Microelectrode studies of organic carbon degradation and calcite dissolution at a California Continental rise site. *Geochimica et Cosmochimica Acta* **59**, 497-511.

Deuser W. G. (1986) Seasonal and interannual variations in deep-water particle fluxes in the Sargasso Sea and their relation to surface hydrography. *Deep-Sea Research* **33**, 225-246.

Emerson S. and Bender M. (1981) Carbon fluxes at the sediment-water interface of the deep-sea: calcium carbonate preservation. *Journal of Marine Research* **39**, 139-162.

Gehlen M., Mucci A., and Boudreau B. (1999) Modeling the distribution of stable carbon isotopes in porewaters of deep-sea sediments. *Geochimica et Cosmochimica Acta* **63**, 2763-2773.

Gehlen M., Bassinot F. C., Chou L., and McCorkle D. (2005) Reassessing the dissolution of marine carbonates: II. Reaction kinetics. *Deep-Sea Research I* **52**, 1461-1476.

Glud R. N., Gundersen J. K., Jørgensen B. B., Revsbech N. P., and Schulz H. D. (1994) Diffusive and total oxygen uptake of deep-sea sediments in the eastern South Atlantic Ocean: in situ and laboratory measurements. *Deep-Sea Research I* **41**, 1767-1788.

Haeckel M., König I., Riech V., Weber M. E., and Suess E. (2001) Pore water profiles and numerical modelling of biogeochemical processes in Peru Basin deep-sea sediments. *Deep-Sea Research II* **48**, 3713-3736.

Hales B., Emerson S., and Archer D. (1994) Respiration and dissolution in the sediments of the western North Atlantic: estimates from models of in situ microelectrode measurements of porewater oxygen and pH. *Deep-Sea Research II* **41**, 695-719.

Hales B. and Emerson S. (1996) Calcite dissolution in sediments of the Ontong-Java Plateau: in situ measurements of pore water O$_2$ and *p*H. *Global Biogeochemical Cycles* **10**, 527-541.

Hales B. and Emerson S. (1997a) Calcite dissolution in sediments of the Ceara Rise: In situ measurements of porewater O$_2$, pH, and CO$_{2(aq)}$. *Geochimica et Cosmochimica Acta* **61**, 501-514.

Hales B. and Emerson S. (1997b) Evidence in support of first-order dissolution kinetics of calcite in seawater. *Earth and Planetary Science Letters* **148**, 317-327.

Hales B. (2003) Respiration, dissolution, and the lysocline. *Paleooceanography* **18**, doi:10.1029/2003PA000915.

Hammond D. E., McManus J., Berelson W. M., Kilgore T. E., and Pope R. H. (1996) Early diagenesis of organic material in equatorial Pacific sediments: stoichiometry and kinetics. *Deep-Sea Research II* **43**, 1365-1412.

Hinga K. R., Sieburth J. M., and Heath G. R. (1979) The supply and use of organic material at the deep-sea floor. *Journal of Marine Research* **37**, 557-579.

Jahnke R. A., Craven D. B., and Gaillard J.-F. (1994) The influence of organic matter diagenesis on CaCO$_3$ dissolution at the deep-sea floor. *Geochimica et Cosmochimica Acta* **58**, 2799-2809.

Jahnke R. A., Craven D. B., McCorkle D. C., and Reimers C. E. (1997) $CaCO_3$ dissolution in California continental margin sediments: The influence of organic matter remineralization. *Geochimica et Cosmochimica Acta* **61**, 3587-3604.

Jahnke R. A. and Jahnke D. B. (2004) Calcium carbonate dissolution in deep sea sediments: Reconciling microelectrode, pore water and benthic flux chamber results. *Geochimica et Cosmochimica Acta* **68**, 47-59.

Jourabchi P., Van Cappellen P., and Regnier P. (2005) Quantitative interpretation of pH distributions in aquatic sediments: a reaction-transport modeling approach. *American Journal of Science* **305**, 919-956.

Keir R. S. (1980) The dissolution kinetics of biogenic calcium carbonates in seawater. *Geochimica et Cosmochimica Acta* **44**, 241-252.

König I., Haeckel M., Lougear A., Suess E., and Trautwein A. X. (2001) A geochemical model of the Peru Basin deep-sea floor—and the response of the system to technical impacts. *Deep-Sea Research II* **48**, 3737-3756.

Lagarias J. C., Reeds J. A., Wright M. H., and Wright P. E. (1998) Convergence properties of the Nelder-Mead Simplex Method in Low Dimensions. *SIAM Journal of Optimization* **9**, 112-147.

Luff R., Wallmann K., Grandel S., and Schlüter M. (2000) Numerical Modeling of benthic processes in the deep Arabian Sea. *Deep-Sea Research II* **47**, 3039-3072.

Luff R. and Moll A. (2004) Seasonal dynamics of the North Sea sediments using a three-dimensional coupled sediment-water model system. *Continental Shelf Research* **24**, 1099-1127.

Luff R., Wallmann K., and Aloisi G. (2004) Numerical modeling of carbonate crust formation at cold vent sites: significance for fluid and methane budgets and chemosynthetic biological communities. *Earth and Planetary Science Letters* **221**, 337-353.

Martin W. R. and Sayles F. L. (1996) $CaCO_3$ dissolution in sediments of the Ceara Rise, western equatorial Atlantic. *Geochimica et Cosmochimica Acta* **60**, 243-263.

Martin W. R. and Sayles F. L. (2006) Organic matter oxidation in deep-sea sediments: distribution in the sediment column and implications for calcite dissolution. *Deep-Sea Research II* **53**, 771-792.

Meile C. and Van Cappellen P. (2003) Global estimates of enhanced solute transport in marine sediments. *Limnology and Oceanography* **48**, 777-786.

Mekik F. A., Loubere P. W., and Archer D. E. (2002) Organic carbon flux and organic carbon to calcite flux ratio recorded in deep-sea carbonates: Demonstration and a new proxy. *Global Biogeochemical Cycles* **16**, 1052.

Middelburg J. J., Soetaert K., and Herman P. M. J. (1997) Empirical relationships for use in global diagenetic models. *Deep-Sea Research I* **44**, 327-344.

Millero F. J. and Sohn M. L. (1992) *Chemical Oceanography*. CRC Press, Boca Raton.

Morse J. W. and Arvidson R. S. (2002) The dissolution kinetics of major sedimentary carbonate minerals. *Earth-Science Reviews* **58**, 51-84.

Morse J. W., Arvidson R. S., and Lüttge A. (2007) Calcium carbonate formation and dissolution. *Chemical Reviews* **107**, 342-381.

Pfeifer k., Hensen C., Adler M., Wenzhöfer F., Weber B., and Schulz H. D. (2002) Modeling of subsurface calcite dissolution, including the respiration and reoxidation processes of marine sediments in the region of equatorial upwelling off Gabon. *Geochimica et Cosmochimica Acta* **66**, 4247-4259.

Pilson M. E. Q. (1998) *An Introduction to the Chemistry of the Sea*. Prentice-Hall, Upper Saddle River.

Rabouille C. and Gaillard J.-F. (1991) A coupled model representing the deep-sea organic carbon mineralization and oxygen consumption in surficial sediments. *Journal of Geophysical Research* **96**, 2761-2776.

Rabouille C., Witbaard R., and Duineveld G. C. A. (2001) Annual and interannual variability of sedimentary recycling studied with a non-steady-state model: application to the North Atlantic Ocean (BENGAL site). *Progress in Oceanography* **50**, 147-170.

Reimers C. E. (1987) An *in situ* microprofiling instrument for measuring interfacial pore water gradients: methods and oxygen profiles from the North Pacific Ocean. *Deep-Sea Research* **34** , 2019-2035.

Ronov A. B. and Yaroshevski A. A. (1969) Chemical composition of earth's crust and upper mantle. In *The Earth's Crust and Upper Mantle* (ed. P. J. Hart). American Geophysical Union, Washington. pp. 37-57.

Rowe G. T. and Gardner W. D. (1979) Sedimentation rates in the slope water of the northwest Atlantic Ocean measured directly with sediment traps. *Journal of Marine Research* **37**, 581-600.

Sayles F. L., Martin W. R., and Deuser W. G. (1994) Response of benthic oxygen demand to particulate organic carbon supply in the deep sea near Bermuda. *Nature* **371**, 686-689.

Soetaert K., Herman P. M. J., and Middelburg J. J. (1996) A model of early diagenetic processes from the shelf to abyssal depths. *Geochimica et Cosmochimica Acta* **60**, 1019-1040.

Stumm W. and Morgan J. J. (1996) *Aquatic Chemistry: Chemical Equilibria and Rates in Natural Waters*. Wiley Interscience, New York.

Tromp T. K., Van Cappellen P., and Key R. M. (1995) A global model for the early diagenesis of organic carbon and organic phosphorus in marine sediments. *Geochimica et Cosmochimica Acta* **59**, 1259-1284.

Van Cappellen P. and Wang Y. (1995) Metal cycling in surface sediments: modelling the interplay of transport and reaction. In *Metal Contaminated Sediments* (ed. H. E. Allen). Ann Arbor Press, Chelsea. pp. 21-62.

Wenzhöfer F., Adler M., Kohls O., Hensen C., Strotmann B., Boehme S., and Schulz H. D. (2001) Calcite dissolution driven by benthic mineralization in the deep-sea: In situ measurements of Ca^{2+}, pH, pCO$_2$, and O$_2$. *Geochimica et Cosmochimica Acta* **65**, 2677-2690.

Westrich J. T. and Berner R. A. (1984) The role of sedimentary organic matter in bacterial sulfate reduction: The *G* model tested. *Limnology and Oceanography* **29**, 236-249.

Chapter 5

Steady state compaction in deep-sea sediments:
compression versus mineral dissolution

P. Jourabchi, I. L'Heureux, C. Meile, and P. Van Cappellen
in preparation

Abstract

Marine sediments typically exhibit large porosity gradients in their uppermost centimeters. Although the decrease in porosity with depth below the sediment-water interface is primarily due to compression arising from the accumulation of overlying sediment, early diagenetic mineral dissolution and precipitation reactions may also affect the porosity gradients in surface sediments. Here, we present a steady state compaction model, based on the mass and momentum conservation of total fluid and solid phases, in order to quantify the relative contributions of mineral reactions and physical compaction on porosity changes. The compaction model is applied to estimate hydraulic conductivity and elastic response coefficients of deep-sea sediments from measured porosity depth profiles. The results suggest an inverse relation between the elastic response coefficient and the lithogenic content of marine sediments. For deep-sea sediments exhibiting high rates of dissolution of calcareous or siliceous shell fragments, the compaction model overestimates the hydraulic conductivity and elastic response coefficients, when dissolution of the biogenic minerals is neglected. In contrast to non-compacting porous media, the net effect of mineral dissolution in surficial sediments can lead to lower porosity (chemical compaction). Model results further indicate that porosity data from a deep-sea sediment in the equatorial Atlantic are better fitted by nonlinear, rather than a linear, rate laws for calcite dissolution.

1. Introduction

A major objective of current research on the fate of carbon in marine sediments is to develop accurate representations of calcite diagenesis in surficial sediments (Metz et al., 2005; Kleypas et al., 2006). At the same time, the reconstruction of past oceanic conditions from sediment records requires the separation of early diagenetic processes from surface ocean processes. In this context, reaction-transport models (RTMs) allow one to quantify the complex interplay of biogeochemical processes, including mineral dissolution and precipitation, taking place at the seafloor (e.g., Berelson et al., 1987; Jahnke et al., 1994; Pfeifer et al., 2002; Archer et al., 2002, Martin and Sayles, 2006).

The significance of calcite dissolution in pelagic sediments and its potential effect on sediment compaction have been discussed by Berner (1980). Yet, most early diagenetic models do not explicitly account for the effects of physical compaction and mineral dissolution and precipitation reactions on porosity profiles. In existing early diagenetic RTMs the porosity depth profile is imposed. Typically, an exponentially decaying function is used to account for sediment compaction (e.g., Soetaert et al., 1996; Berg et al., 2005). In the broader field of reaction-transport in porous media, a number of studies explicitly account for time-dependent changes in porosity, and hence permeability, due to mineral dissolution and precipitation reactions. These studies, however, have so far only considered non-compacting systems (e.g., Steefel and Lasaga, 1994; Mayer et al., 2002). Luff et al. (2004) adopted the same approach to investigate carbonate crust formation at methane vents.

Although porosity decrease with depth in sediments is a common observation, porosity itself is not included as a state variable in the mass conservation equations used to construct early diagenetic models (Boudreau and Bennett, 1999). Porosity decrease is not restricted to surficial sediments. In sedimentary basin research, continuum mechanics is used to model gravitational compaction and to explicitly compute porosity (or void ratio), while the effects of chemical transformations are ignored (e.g., Audet, 1995; Deudé et al., 2004; L'Heureux and Fowler, 2000). Therefore, diagenetic and early diagenetic models tend to complement each other in their treatment of physical and geochemical processes, respectively.

Here we present a model of physical and chemical compaction, which is used to compute the porosity and the advection velocities of solids and solutes in one dimension. Although a time-dependant formulation is possible, as a first step we restrict ourselves here to steady state conditions. First, we investigate the constitutive equations that relate hydraulic conductivity and differential elastic response to porosity. The compaction model is applied to

a set of porosity data from deep-sea sediments and an inverse model approach is used to estimate the corresponding physical parameters. We consider only deep-sea sediments, where the complicating processes of bioirrigation and bioturbation are of lesser importance (Middelburg et al., 1997; Meile and Van Cappellen, 2003).

Initially, we ignore mineral dissolution reactions and investigate the effect of sediment composition on the hydraulic conductivity and elastic response coefficients. Next, available mineral reaction rates at two sites in the Southern Ocean (silica dissolution rate profiles) and at one site in the equatorial Atlantic (calcite dissolution rate profile) are taken as input to the compaction model in order to compute porosities and derive model parameters. Finally, we couple the compaction model to a reaction-transport model through an iterative approach. The coupled model is then applied to the equatorial Atlantic site to quantify the elastic response and hydraulic conductivity coefficients, and to assess alternative forms of the calcite dissolution rate law, by considering the resulting fits to the porosity and pH depth profiles.

2. Model Development

2.1. Mass and momentum conservation

Berner (1980) describes the evolution of porosity (ϕ) in aquatic sediments through the mass conservation equations for the total solids and the fluid phases. In this way, the advection velocities of solids and pore fluid can be derived for steady state compaction, given an empirically imposed porosity profile and in the absence of mineral dissolution or precipitation reactions. Berner (1980) also discusses models of calcite diagenesis in deep-sea sediments in which porosity is assumed to be unaffected by calcite dissolution (e.g., Schink and Guinasso, 1977).

Here, we add the effect of dissolution and precipitation reactions of mineral constituents in the sediment. This is mathematically described by the last term in Equation 1, where R_m is the net rate of precipitation of mineral m expressed in moles per sediment volume per unit time, and V_m is its molar volume. (Note: when the mineral dissolves, the rate R_m is negative.) Assuming a two-phase sediment system (fully saturated), mass balance for total fluids can be represented by

$$\frac{\partial(\phi\rho_f)}{\partial t} = -\vec{\nabla}\cdot\left(\rho_f\phi\vec{v}\right) - \rho_f\sum_m V_m R_m, \tag{1}$$

where t is time, and ρ_f and $\vec{v}$ are the fluid density and velocity, respectively. Similarly, mass balance for total solids can be represented by

$$\frac{\partial((1-\phi)\rho_s)}{\partial t} = -\vec{\nabla}\cdot\left(\rho_s(1-\phi)\vec{\omega}\right) + \rho_s\sum_m V_m R_m, \tag{2}$$

where ρ_s and $\vec{\omega}$ are the solid density and velocity, respectively.

The mass balance equations for total solids and fluids presented here assume that bioturbation causes intraphase mixing only. In that case, bioturbation has a negligible effect on reducing porosity gradients. Early diagenetic models commonly consider either intraphase or interphase mixing modes (Boudreau, 1986) in the mathematical description of bioturbation. However, Meysman et al. (2005) suggest that both forms of mixing may need to be considered, which would result in modified velocity terms (see equation 62 in Meysman et al., 2005). As the intensity of bioturbation is greatly reduced in deep-sea sediments (Tromp et al., 1995; Middelburg et al., 1997), we restrict ourselves to these depositional settings and neglect interphase mixing for simplicity.

Assuming constant densities for the pore fluid and the solids, the mass balance equations can be re-written in one dimension as

$$\frac{\partial \phi}{\partial t} = -\frac{\partial(\phi v)}{\partial z} - \sum_m V_m R_m \tag{3}$$

and

$$\frac{\partial \phi}{\partial t} = \frac{\partial \omega}{\partial z} - \frac{\partial(\phi \omega)}{\partial z} - \sum_m V_m R_m, \tag{4}$$

where z is depth into the sediment, and $z=0$ corresponds to the sediment-water interface (SWI). Given the mineral dissolution or precipitation rates and the advective velocities, the mass balance equations can be solved for porosity.

To determine the advective velocities, we use Darcy's law to account for the conservation of momentum of the fluid phase,

$$\phi(v - \omega) = K\left(1 - \frac{1}{\rho_f g}\frac{\partial p}{\partial z}\right), \tag{5}$$

which introduces the pore fluid pressure p, the sediment hydraulic conductivity K and the acceleration of gravity g. The conservation of solid phase momentum can be used to close the system of equations. The mechanical response of the system assuming no inertial terms (no sound waves) is described by the equilibrium relation: stress = external force/area. This can be accomplished by defining the total overburden stress (S) as the sum of the effective stress, σ and fluid pressure p as proposed by K. Terzaghi (Bear, 1988). Thus, the spatial gradient of fluid pressure can be replaced by

$$\frac{\partial p}{\partial z} = \frac{\partial S}{\partial z} - \frac{\partial \sigma}{\partial z}, \tag{6}$$

where

$$\frac{\partial S}{\partial z} = g\left(\phi \rho_f + (1-\phi)\rho_s\right) \tag{7}$$

Instead of solving the full elasticity problem, we assume that the mechanical response (the porosity) is uniquely defined by some function F of the effective stress (Hubbert and Rubey, 1959):

$$\phi = F(\sigma). \tag{8}$$

After inversion, the differential form of this relation can be written as:

$$d\sigma = H(\phi)d\phi, \tag{9}$$

where H is called the differential response function, whose negative inverse (-1/H) is referred to as the pore space compressibility by Mello et al. (1994). Thus

$$\frac{\partial \sigma}{\partial z} = H \frac{\partial \phi}{\partial z}. \tag{10}$$

At steady state, Equations 4 becomes

$$\frac{d(\omega(1-\phi))}{dz} = \sum_m V_m R_m, \tag{11}$$

while subtracting Equation 4 from Equation 3 yields, at steady state,

$$\frac{d}{dz}(\phi v + (1-\phi)\omega) = 0, \tag{12}$$

which can be combined with Equations 5-7, 10 to give

$$\phi(v - \omega) = K\left((1-\phi)\left(1 - \frac{\rho_s}{\rho_f}\right) \frac{H}{\rho_f g} \frac{d\phi}{dz} \right) \tag{13}$$

Solving the above system of equations (Equations 11 - 13) for ϕ, v, and ω requires three boundary conditions that we specify as follows.

1. Known porosity at the upper boundary ($z=0$),

$$\phi(0) = \phi_0 \tag{14}$$

2. Known sedimentation rate, ω_0 at the upper boundary ($z=0$),

$$\omega(0) = \omega_0 \tag{15}$$

3. Mixed condition at the lower boundary ($z=L$), for a known Darcy flow rate,

$$Q = \phi(v - \omega)\big|_{z=L} \tag{16}$$

We integrate Equation 11 and use the first two boundary conditions to calculate the constant of integration, A

$$\omega = \frac{A}{(1-\phi)} + \frac{1}{(1-\phi)} \int_0^z \sum_m V_m R_m \, dz \tag{17}$$

$$A = (1-\phi_0)\omega_0 \tag{18}$$

Likewise, integrating Equation 12 combined with the third boundary condition yields the constant of integration (B)

$$B = \phi v + (1-\phi)\omega \tag{19}$$

$$B = Q + \omega\big|_{z=L} = Q + \frac{A}{(1-\phi_L)} + \frac{1}{(1-\phi_L)} \int_0^L \sum_m V_m R_m \, dz, \tag{20}$$

where ϕ_L is the porosity evaluated at $z=L$.

Substituting Equations 17 and 19 into Equation 13 and solving for $d\phi/dz$ gives a single first order differential equation in terms of ϕ

$$\frac{d\phi}{dz} = \frac{\rho_f g}{HK}\left(B - \frac{A}{(1-\phi)} - \frac{1}{(1-\phi)}\int_0^z \sum_m V_m R_m \, dz + K(1-\phi)\left(\frac{\rho_s}{\rho_f} - 1\right)\right) \tag{21}$$

provided that there are constitutive relationships to express the hydraulic conductivity (K) and the differential response function (H) in terms of ϕ. The yet unknown parameter ϕ_L that appears in Equation 20 must be determined self-consistently from the solution of Equation 21.

2.2. Constitutive Equations

2.2.1. Hydraulic Conductivity

The most common expression relating hydraulic conductivity to porosity is the Carman-Kozeny equation (Kozeny, 1927; Carman, 1937; Boudreau, 1997),

$$K = \frac{d_p^2 \rho_f g}{180\eta}\frac{\phi^3}{(1-\phi)^2} \tag{22}$$

with d_p the mean particle diameter and η the dynamic fluid viscosity. Putting all constants into the parameter, β, such that

$$K = \beta\frac{\phi^3}{(1-\phi)^2} \tag{23}$$

gives an expression that can be used in the compaction model (Equation 21). According to Boudreau (1997), however, the applicability of Equation 23 is not well established for sediments with porosities >80%, that is, most muddy surficial sediments. For such settings, another permeability equation, based on the work of Hsu and Cheng (1991), is

$$\lim_{\phi \to 1} K = 10\beta\frac{\phi^2}{(1-\phi)}, \tag{24}$$

These authors also suggest using Equation 23 in the limit that $\phi \to 0.4$, which represents a sand-like limit. Combining these two limits, Hsu and Cheng (1991) propose multiplying Carman-Kozeny's permeability equation by a factor, $f(\phi)$

$$f(\phi) = 1 - e^{-10\frac{(1-\phi)}{\phi}}. \tag{25}$$

resulting in a hydraulic conductivity equation,

$$K = \beta\frac{\phi^3}{(1-\phi)^2}\left(1 - e^{-10\frac{(1-\phi)}{\phi}}\right), \tag{26}$$

that can potentially apply to a medium of variable porosity ranging from 0.4 to 1.0. The effect of the choice of the expression for $K(\phi)$ (Equations 23 versus 26) is evaluated below (section 3.1.2).

2.2.2. Elastic Response

In the compaction model, we assume a basic mechanical response to variations in porosity described by the differential response function H (Equation 9),

$$H(\phi) = \frac{d\sigma}{d\phi}. \tag{27}$$

We further use an empirical relationship that relates the effective stress to porosity through an exponential function (Rubey and Hubbert, 1959; Keith and Rimstidt, 1985; Shi and Wang, 1986; Boudreau and Bennett, 1999):

$$\phi = \phi_\infty + (\phi_0 - \phi_\infty)e^{-b\sigma}, \tag{28}$$

where ϕ_0 and ϕ_∞ represent porosities at the SWI and at large depth below the SWI, respectively, and parameter, b is the elastic response coefficient. The elastic response coefficient has also been described as the compaction coefficient (Hart et al., 1995), or sediment compressibility (Gordon and Flemings, 1998). The differential response function associated with the relation $\phi(\sigma)$ of Equation 28 is:

$$H = -\frac{1}{b(\phi - \phi_\infty)}. \tag{29}$$

In the absence of mineral precipitation or dissolution reactions, and for zero advection velocities (and , thus, $B = A = 0$), the porosity profile can formally be derived by integrating Equation 21. Using Equation 29, the result is consistent with Equation 23 in Boudreau and Bennett (1999):

$$\phi = 1 - \frac{(1-\phi_0)(1-\phi_\infty)}{1 - \phi_0 + (\phi_0 - \phi_\infty)\exp[-gb(\rho_s - \rho_f)z]}. \tag{30}$$

The above non-trivial porosity profile is consistent with the condition of hydrostatic equilibrium ($dp/dz = \rho_f g$) and with the continuity equations only when there is no advection ($v = \omega = 0$). In general, however, there is no obvious reason to neglect the velocity terms (that is, the terms proportional to B and A) in Equation 21.

The elastic response coefficient can in principle be estimated for sediments for which both porosity and effective stress measurements are available. Five such data sets are presented by Bennett et al. (1999) and Boudreau and Bennett (1999): Figure 1 shows nonlinear regression fits of Equation 28 to these data. In the regression analysis, we solve for b, ϕ_0, and ϕ_∞ in Equation 28, taking into account the measurement errors in both variables ϕ and σ. The following objective function is minimized

$$f_o = \sum_i \left(\left(\frac{\phi_i^d - \phi_i^m}{\Delta_i^\phi} \right)^2 + \left(\frac{\sigma_i^d - \sigma_i^m}{\Delta_i^\sigma} \right)^2 \right), \tag{31}$$

which considers the sum of the least squared residuals between data (d) and model (m) results at every measurement depth i for porosity and effective stress, weighted by the measurement uncertainties, $\varDelta^{\phi}$ and $\varDelta^{\sigma}$, in these two variables. The best-fit values of the parameters are listed in Table 1.

It should be noted that the data for effective stress shown in Figure 1 are derived from density and porosity measurements based on the assumption of hydrostatic equilibrium (Bennett et al., 1999), and are representative for shallow continental shelf environments. A profile that decays exponentially with depth (modified Athy's law) is often successful in describing measured porosity profiles:

$$\phi = \phi_{\infty} + (\phi_0 - \phi_{\infty})e^{-cz}, \tag{32}$$

where c is a depth attenuation coefficient. As an alternate approximation, we can thus search the appropriate ϕ and σ relationship that, under the assumption of steady state hydrostatic equilibrium ($dp/dz = g\rho_f$) and no advection, yields an exponentially decaying porosity as described by Equation 32. Under these assumptions,

$$H = \frac{d\sigma}{d\phi} = \frac{-g\Delta\rho(1-\phi)}{c(\phi - \phi_{\infty})}, \tag{33}$$

where $\Delta\rho$ is the difference in solid sediment and water densities. Integration of Equation 33 with the boundary condition $\sigma = 0$ at the SWI, yields

$$\sigma = \frac{-g\Delta\rho}{c}\left[(1-\phi_{\infty})ln\left(\frac{\phi - \phi_{\infty}}{\phi_0 - \phi_{\infty}}\right) + \phi_0 - \phi\right]. \tag{34}$$

Equation 34 is equivalent to Equation 24 in Boudreau and Bennett (1999), who favour defining a function of porosity in terms of effective stress and therefore do not consider the application of this equation any further. It is also consistent with equations 14 and 15 in L'Heureux and Fowler (2000), where in the limit of hydrostatic equilibrium both advection velocities go to zero.

Here, we also consider the applicability of Equation 34 to the same data set used for the exponential relationship (Equation 28), assuming a 5% measurement error for both porosity and effective stress. The resulting fits and parameter values are shown in Figure 1 and Table 2, respectively.

In general, the exponential relationship (Equation 28) gives a better fit to the data than the logarithmic relationship (Equation 34), particularly for low effective stress values ($\sigma < 0.1$ kPa). For four of the five sites, porosity depth profiles are provided in Bennett et al. (1999), which allows us to estimate ϕ_0 and ϕ_{∞}, independently (Table 3). Again, the parameter values

for ϕ_0 and ϕ_∞ are generally better estimated by the exponential relationship of Equation 28 (compare parameter values in Tables 1 to 3). Thus, in the compaction model, we opt for the differential elastic response given by Equation 29.
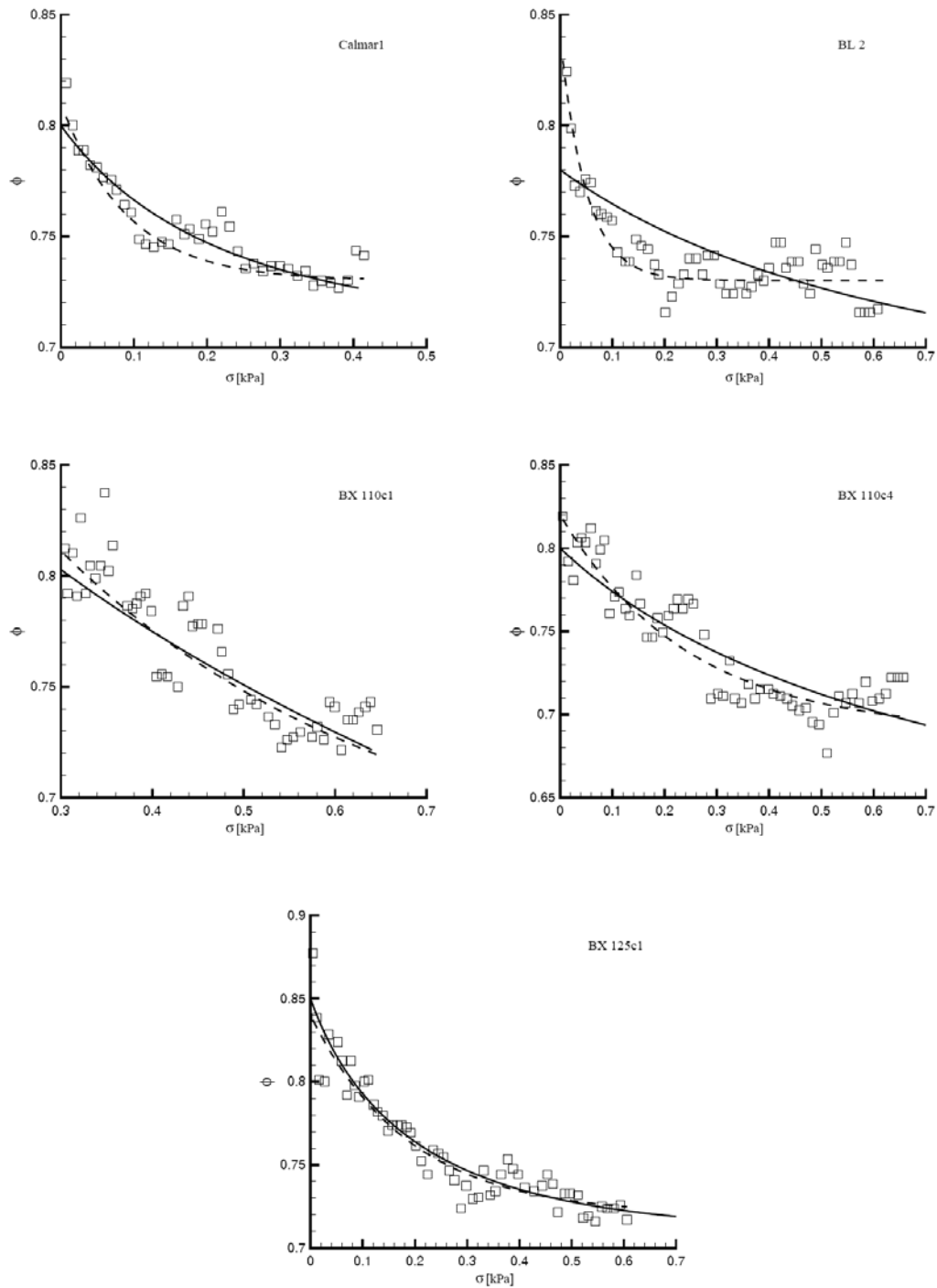

Figure 1: Porosity vs. effective stress: symbols indicate measured data points, broken line is the exponential fit (Equation 28) , and solid line is the logarithmic fit (Equation 34). See text for complete discussion.

163

Table 1: Regression results for the exponential model (Equation 28) fit to the data shown in Figure 1: best fit values of b, ϕ_0 and ϕ_∞ and the corresponding misfit.

Site	b [kPa^{-1}]	ϕ_0	ϕ_∞	χ^2 misfit
Calmar1	11	0.81	0.73	1.9
BL 2	20	0.84	0.73	4.6
BX 110c1	2.7	1.0	0.66	7.0
BX 110c4	4.1	0.82	0.69	9.1
BX 125c1	5.3	0.84	0.72	4.3

Table 2: Regression results for the logarithmic model (Equation 34) fit to the data shown in Figure 1: best fit values of c, ϕ_0 and ϕ_∞ and the corresponding misfit.

Site	c [cm^{-1}]	ϕ_0	ϕ_∞	χ^2 misfit
Calmar1	0.15	0.80	0.71	1.9
BL 2	0.056	0.78	0.68	12
BX 110c1	0.011	1.0	0.0	7.6
BX 110c4	0.049	0.80	0.62	11
BX 125c1	0.14	0.85	0.71	4.4

Table 3: Fits of Equation 32 to the porosity profiles at four of the five sites in Figure 1.

Site	c [cm^{-1}]	ϕ_0	ϕ_∞
BL 2	0.96	0.86	0.73
BX 110c1	0.055	0.83	0.64
BX 110c4	0.15	0.83	0.68
BX 125c1	0.18	0.85	0.71

2.3. Numerical Solution

Given the expressions for hydraulic conductivity (K) and differential elastic response (H) in terms of porosity, we use the shooting method for the solution of Equation 21. This method assumes an initial guess for porosity at the lower boundary (ϕ_L), and solves the differential equation for ϕ using a fourth order Runge-Kutta routine. If $\phi(z = L)$ is sufficiently close to ϕ_L (within an absolute tolerance of 10^{-4}), then the problem is considered solved. Otherwise, the value ϕ_L is changed and the procedure repeated, until convergence is obtained. We thus find the root of the function $\phi(z = L) - \phi_L = 0$. A bisection subroutine is used to drive the procedure.

3. Applications

3.1. Model Parameters

3.1.1. Basic set of parameters

The simulation of porosity profiles by the compaction model requires knowledge of a number of physical parameters, especially the hydraulic conductivity coefficient (β), the elastic response coefficient (b), and the sedimentation rate (ω_0). To obtain values for these three parameters, an inverse modeling approach is adopted, assuming that mineral dissolution or precipitation reactions have a negligible effect on changes in the pore volume. The PANGAEA database (http://www.pangaea.de) is searched for suitable data sets on deep-sea sediments, using the following criteria:

1. porosity and calcite content available for the surface sediment
2. deep-sea sites >1500m water depth
3. < 5% by weight variation in $CaCO_3$ content.

The last criterion selects against sediments that may experience significant dissolution of $CaCO_3$.

The search yields 13 data sets that match the above criteria. To this list, are added two data sets from the Ontong-Java Plateau and one set from Ceara Rise, for which resistivity data are available. Table 4 summarizes the location, depth, and sediment $CaCO_3$ content for these sites. In the absence of reported error measurements for porosity, we assumed an absolute error of 0.05.

To obtain initial guesses, each of the three parameters, β, b and ω_0, is first varied over a specified range ($\beta = 0.007\text{-}1000$ cm/a; $b = 0.1\text{-}100$ kPa^{-1}; $\omega_0 = 0 - 1.2$ cm/a) in forward model simulations. In these simulations, we assume a porosity profile that decreases from 0.85 at the SWI to 0.7 at depth, and apply Equations 23 and 29 for the hydraulic conductivity and differential response function, respectively.

The simulation results (not shown) indicate that the porosity profile is most sensitive to variations in b and least sensitive to variations in β. As the porosity profile is insensitive to values of β between 0.05 to 1000 cm/a, the initial guess for β is set at 0.1 cm/a. The initial guess for the elastic response coefficient, b is derived from the exponential fit (Athy, 1930; Equation 32) to the porosity profile, from which we derive $b = c/(g(\rho_s - \rho_f))$ (Shi and Wang, 1986). We assume $\rho_s = 2.5$ g/cm^3 and $\rho_f = 1.0$ g/cm^3 and no imposed flow at the lower boundary $z = L$ ($Q = 0$). Finally, the initial guess for sedimentation rate (ω_0) is estimated from

the water depth of the site, using the global relationship proposed by Middelburg et al. (1997).

Table 4: Site descriptions. 1. Freudenthal (2001) 2. Wenzhöfer et al. (2001) and pers. com. (F. Wenzhofer) 3. Sayles and Martin (2003a-c) 4. Birgisdottir and Thiede (2002a,b) 5. Weber (2000a,b) 6. Lowry (2004a,b) 7. Anderson (2005) 8. Hales and Emerson (1996) 9. Hales and Emerson (1997).

Description	Location	longitude	Latitude	Depth [m]	CaCO$_3$ content [weight %]
GeoB4301-1[1]	Eastern Atlantic (Canary islands)	-15.50°	29.15°	3614	56.81-59.65
GeoB4901[2]	Eastern Atlantic (river Niger)	2.68°	6.73°	2185	2.2-4.5
NBP98-02-09[3]	Southern Ocean (Ross Sea)	-170.17°	-56.88°	4945	0.16-0.39
NBP98-02-08[3]	Southern Ocean (Ross Sea)	-169.98°	-58.69°	4345	23.85-26.74
NBP98-02-06[3]	Southern Ocean (Ross Sea)	-169.97°	-61.88°	3300	4.01-7.79
PS1243-1[4]	Norwegian Sea	-6.55°	69.37°	2711	0-1.1
PS1244-2[4]	Greenland Sea	-8.66°	69.37°	2127	0-2.4
PS1599-3[5]	Halley Bay (Antarctica)	-27.69°	-74.07°	2487	0.27-1.77
PS1789-1[5]	Lyddan Island (Antarctica)	-27.30°	-74.24°	2411	0.16-1.28
BOFS11M-1[6]	NE Atlantic	-20.35°	55.19°	2080	79.49-84.29
BOFS14M-1[6]	NE Atlantic	-19.42°	58.65°	1756	9.63-10.37
A_EN179-BC7[7]	middle Atlantic bight	-73.82°	37.42°	1989	20.29-23.46
A_EN187-BC6[7]	middle Atlantic bight	-73.83°	37.40°	2000	23.24-27.66
station 2A[8]	Ontong-Java Plateau	159.5°	0°	2322	88.03-91.91
station 2B[8]	Ontong-Java Plateau	159.5°	0°	2335	88.03-91.91
station A[9]	Ceara Rise	-43.57°	5.28°	3990	61.29-65.95

Since we have some independent estimate for ω_0, and given the lack of sensitivity of the porosity profile towards β, the emphasis is on finding a value for *b*. We use a least squares minimization with Matlab's function 'fminsearch', based on the simplex algorithm (Lagarias et al., 1998). The objective function is the square of the difference between model and data, weighted by the standard deviation of the data. The following optimizations are carried out.

1. Varying only *b*: the other two parameters are set to their initial guess values. These results are summarized in Table 5.

Table 5: Inversion results when varying b only.

Site	initial b [kPa^{-1}]	best fit b [kPa^{-1}]	β [cm/a]	ω_0 [cm/a]
GeoB4301-1	3.5	20	0.1	0.01
GeoB4901	0.57	3.5	0.1	0.05
NBP98-02-09	0.82	8.7	0.1	0.003
NBP98-02-08	2.6	41	0.1	0.006
NBP98-02-06	3.0	42	0.1	0.02
PS1243-1	0.056	0.21	0.1	0.03
PS1244-2	0.088	0.37	0.1	0.05
PS1599-3	2.2	12	0.1	0.04
PS1789-1	0.41	1.5	0.1	0.04
BOFS11M-1	5.6	26	0.1	0.05
BOFS14M-1	1.7	9.2	0.1	0.08
A_EN179-BC7	1.0	5.0	0.1	0.06
A_EN187-BC6	0.21	0.95	0.1	0.06
station 2A	6.1	120	0.1	0.04
station 2B	13	150	0.1	0.04
Station A	11	91	0.1	0.008

2. Varying b and β: using as initial guesses for b the values from Table 5, we invert for both parameters while keeping ω_0 constant. These results are summarized in Table 6. As expected, the fits to the data are rather insensitive to variations in β. Therefore, there is either $\leq 10\%$ change in β, or its value tends to $+\infty$ (as indicated by large +ve) in the inversion results. In the latter case, there is negligible difference in the misfit between model and data for β greater than ~ 1.

3. Varying b and ω_0: The previous results (Table 6) are used as the initial guess values for b and fixed values for β, where the large +ve values are replaced by $\beta = 1.0$. The new inversion results are summarized in Table 7. In a number of cases, the inversion results in negative values for ω_0. Otherwise, there is almost no variation in b, with $\leq 20\%$ variation in the sedimentation rate.

4. Varying b, β, and ω_0: Combining all of the above results, where realistic (finite and positive) values for β and ω_0 are predicted, we invert the model to optimize for all three parameters. The initial guess values and inversion results are summarized in Table 8.

Table 6: Inversion results when varying b and β. Values approaching $+\infty$ are denoted by large +ve.

	initial values:		best fit values:		
Site	β [cm/a]	b [kPa^{-1}]	β [cm/a]	b [kPa^{-1}]	ω_0 [cm/a]
GeoB4301-1	0.1	20	large +ve	20	0.010
GeoB4901	0.1	3.5	large +ve	3.5	0.050
NBP98-02-09	0.1	8.7	0.11	8.7	0.003
NBP98-02-08	0.1	41	large +ve	41	0.006
NBP98-02-06	0.1	42	large +ve	42	0.020
PS1243-1	0.1	0.21	0.10	0.21	0.030
PS1244-2	0.1	0.37	0.10	0.36	0.050
PS1599-3	0.1	12	large +ve	12	0.040
PS1789-1	0.1	1.5	0.11	1.5	0.040
BOFS11M-1	0.1	26	large +ve	25	0.050
BOFS14M-1	0.1	9.2	large +ve	8.8	0.080
A_EN179-BC7	0.1	5.0	large +ve	4.8	0.060
A_EN187-BC6	0.1	0.95	0.10	0.95	0.060
station 2A	0.1	120	large +ve	120	0.040
station 2B	0.1	150	large +ve	150	0.040
station A	0.1	91	large +ve	90	0.008

Table 7: Inversion results when varying b and ω_0.

	initial values:		best fit values:		
Site	b [kPa^{-1}]	ω_0 [cm/a]	b [kPa^{-1}]	ω_0 [cm/a]	β [cm/a]
GeoB4301-1	20	0.01	12	<0	1.0
GeoB4901	3.5	0.05	3.5	0.052	1.0
NBP98-02-09	8.7	0.003	8.66	0.0024	0.11
NBP98-02-08	41	0.006	40	<0	1.0
NBP98-02-06	42	0.02	0.53	<0	1.0
PS1243-1	0.21	0.03	0.21	0.032	0.10
PS1244-2	0.36	0.05	0.37	0.051	0.10
PS1599-3	12	0.04	7.4	<0	1.0
PS1789-1	1.5	0.04	1.5	0.038	0.11
BOFS11M-1	26	0.05	2.02	<0	1.0
BOFS14M-1	9.2	0.08	1.9	<0	1.0
A_EN179-BC7	5.0	0.06	4.8	0.052	1.0
A_EN187-BC6	0.95	0.06	0.95	0.06	0.10
station 2A	120	0.04	2.1	<0	1.0
station 2B	150	0.04	1.8	<0	1.0
station A	91	0.008	8.6	<0	1.0

Table 8:   Inversion results when varying β, b, and ω_0. Values approaching $+\infty$ ($-\infty$) are denoted by large +ve (-ve).

site	Initial values:			best fit values:		
	β [cm/a]	b [kPa^{-1}]	ω_0 [cm/a]	β [cm/a]	b [kPa^{-1}]	ω_0 [cm/a]
GeoB4301-1	1.0	20	0.01	1.1	20	0.0099
GeoB4901	1.0	3.5	0.052	large +ve	3.4	large -ve
NBP98-02-09	0.11	8.7	0.0024	0.12	8.7	0.0022
NBP98-02-08	1.0	41	0.006	1.1	41	0.0059
NBP98-02-06	1.0	42	0.02	large +ve	29	large -ve
PS1243-1	0.10	0.21	0.032	0.10	0.21	0.034
PS1244-2	0.10	0.37	0.051	0.11	0.37	0.051
PS1599-3	1.0	12	0.04	1.0	12	0.042
PS1789-1	0.11	1.5	0.038	0.12	1.5	0.036
BOFS11M-1	1.0	26	0.05	large +ve	25	large -ve
BOFS14M-1	1.0	9.2	0.08	large +ve	7.7	large -ve
A_EN179-BC7	1.0	4.8	0.052	51	1.1	<0
A_EN187-BC6	0.10	0.95	0.06	0.10	0.95	0.060
station 2A	1.0	120	0.04	0.99	120	0.042
station 2B	1.0	150	0.04	large +ve	150	large -ve
station A	1.0	91	0.008	large +ve	90	large -ve

When we restrict ω_0 and β to be positive and finite, the inversion results for b are quite robust, and independent of the exact values of ω_0 and β. There are no reasons to believe any of the sites selected are undergoing erosion and, therefore, the sedimentation rates should all be positive. Table 9 shows the parameter values chosen to represent the best fit of the compaction model to the porosity data. The relative χ^2 misfits for this model are comparable to those of the exponential fit, although slightly higher for all sites except station 2A (Table 9). In fact, both the compaction model (Equation 21) and the exponential fit (Equation 32) are successful in representing the porosity data (Figure 2). The compaction model, however, offers a mechanistic description of the porosity profile, which can be naturally extended to include external Darcy flows and the effect of mineral dissolution and precipitation reactions.

Table 9: Overall best fit values for β, b, and ω_0 with their corresponding misfit between the compaction model and porosity data. Also shown are the misfit values associated with an exponential fit (Equation 32) to the porosity data.

Site	β [cm/a]	b [kPa^{-1}]	ω_0 [cm/a]	relative χ^2 misfit model	relative χ^2 misfit exponential
GeoB4301-1	1.0	20	0.01	0.028	0.022
GeoB4901	1.0	3.5	0.052	0.084	0.084
NBP98-02-09	0.12	8.7	0.0022	0.019	0.013
NBP98-02-08	1.0	41	0.0060	0.011	0.0073
NBP98-02-06	1.0	42	0.020	0.080	0.073
PS1243-1	0.10	0.21	0.034	0.80	0.80
PS1244-2	0.11	0.37	0.051	0.55	0.55
PS1599-3	1.0	12	0.042	0.078	0.076
PS1789-1	0.12	1.5	0.036	0.14	0.14
BOFS11M-1	1.0	26	0.050	0.080	0.070
BOFS14M-1	1.0	9.2	0.080	0.35	0.33
A_EN179-BC7	1.0	4.8	0.052	0.19	0.15
A_EN187-BC6	0.10	0.95	0.060	0.10	0.097
station 2A	0.99	120	0.042	3.2	5.8
station 2B	1.0	150	0.040	5.9	3.8
station A	1.0	91	0.0080	3.5	1.7

The major outcome of the inversion process are estimations of the elastic response coefficient (b). Reasonable estimates of the sedimentation rate can be obtained from the global relationship with water depth, without significantly affecting the predicted porosity profile.

The hydraulic conductivity coefficient remains fairly unconstrained by the optimizations (Table 6), possibly because of the very low pore fluid flow velocities. In the absence of further constraints, we suggest using values in the range 0.1 - 1 cm/a. The elastic response coefficient of the various deep-sea sediments ranges from 0.21 to 150 kPa^{-1} (Table 9). These values can be compared to those obtained for continental shelf sediments presented earlier (2.7-20 kPa^{-1}, Table 1), and with the value reported for clay rich deep-sea sediments (0.65 kPa^{-1}; Bahr et al., 2001) and that much lower for a low permeability shale of about 40% porosity (3.68 10^{-5} kPa^{-1}; Hart et al., 1995).
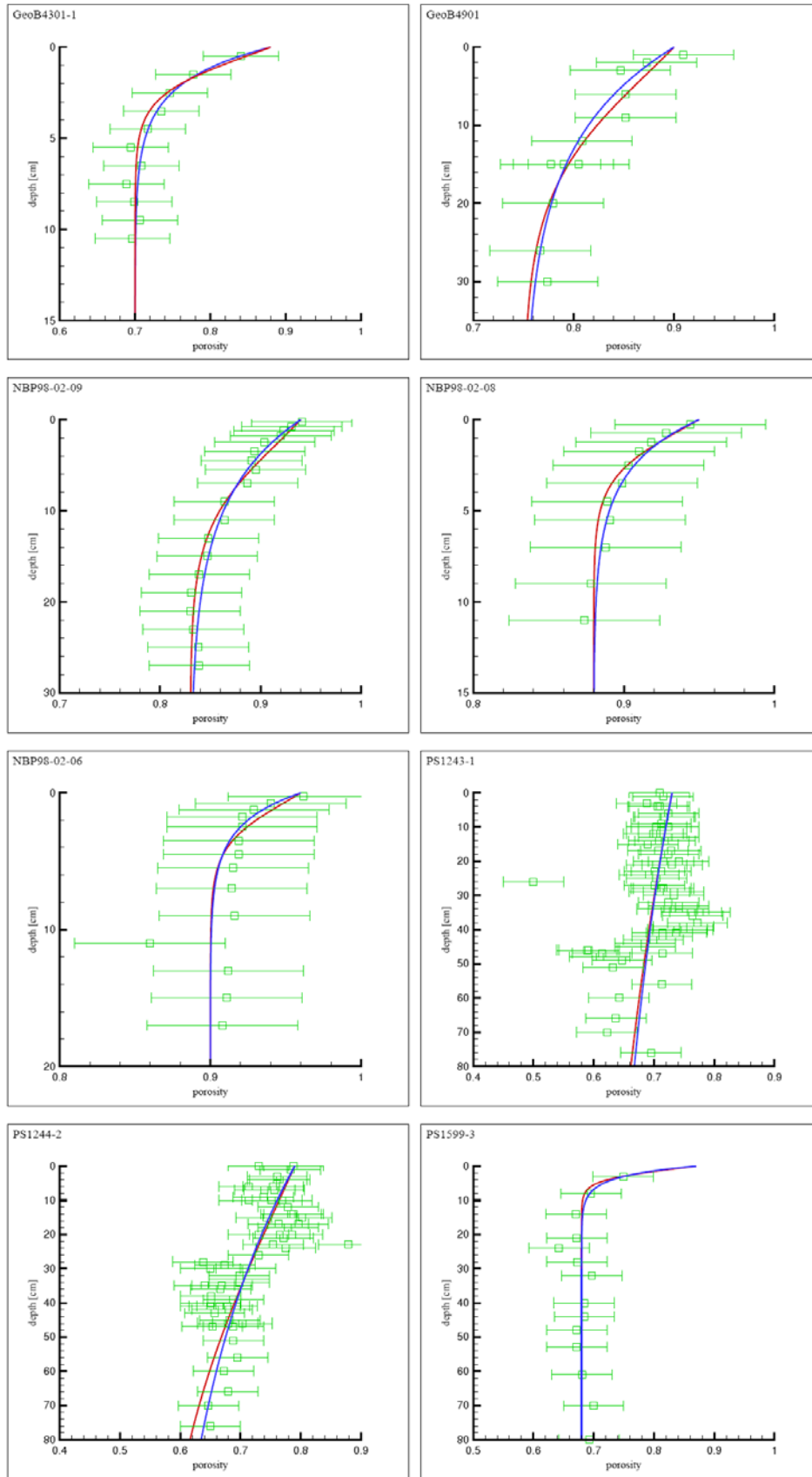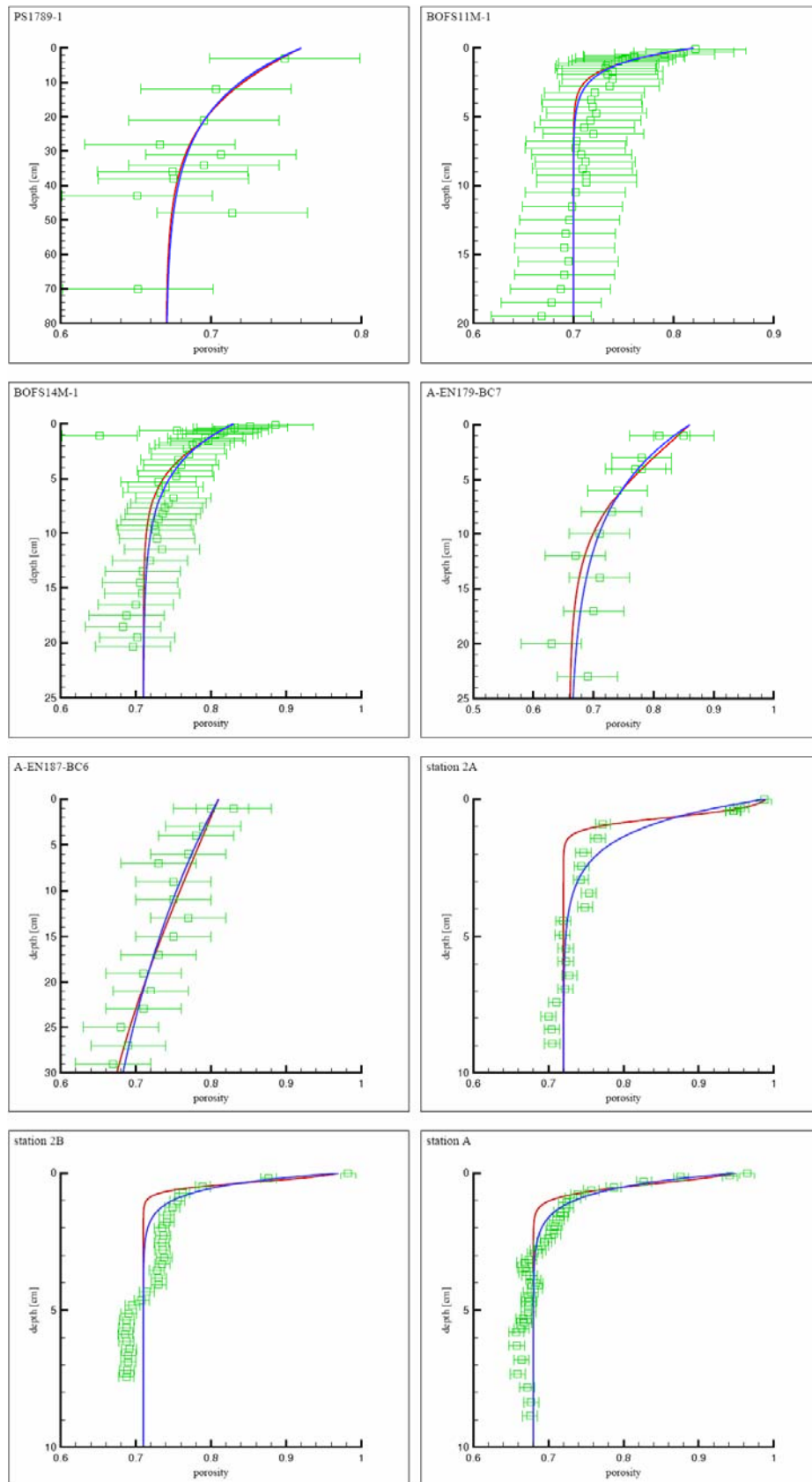
Figure 2: Porosity profiles: symbols indicate measured data points, blue line is the exponential fit (Equation 32), and red line is the best fit by the compaction model (Equation 21).

3.1.2. Hydraulic conductivity expression

The results in the previous section are based on the Carman-Kozeny equation for relating porosity to hydraulic conductivity (Equation 23). In this section, we apply the alternative Equation 26, which has been proposed to be more realistic for high porosity sediments. In particular, Equation 26 predicts lower permeabilities than the Carman-Kozeny equation in the porosity range 0.7-1.0. We wish to assess the effect of the hydraulic conductivity expression (K) on the parameters: β, b, and ω_0.

The inversion results based on Equation 26 are summarized in Table 10. The exact same procedure was used to derive the best-fit parameter values as for the values in Table 9. In comparison with the results using the Carman-Kozeny equation shown in Table 9, the new results fit the data equally well in terms of the relative χ^2 misfit.

Table 10: Overall best fit values for β, b, and ω_0 with their corresponding misfit between the compaction model and porosity data, when using Equation 26 to relate the hydraulic conductivity to the porosity.

site	β [cm/a]	b [kPa^{-1}]	ω_0 [cm/a]	Relative χ^2 misfit
GeoB4301-1	1.1	20	0.0099	0.028
GeoB4901	0.12	3.5	0.050	0.084
NBP98-02-09	1.0	8.7	0.0029	0.019
NBP98-02-08	1.0	41	0.0060	0.011
NBP98-02-06	1.0	42	0.020	0.080
PS1243-1	0.10	0.21	0.034	0.80
PS1244-2	0.12	0.36	0.052	0.55
PS1599-3	1.0	12	0.044	0.078
PS1789-1	0.11	1.5	0.038	0.14
BOFS11M-1	1.0	26	0.050	0.080
BOFS14M-1	1.0	9.3	0.080	0.35
A_EN179-BC7	1.0	5.0	0.060	0.19
A_EN187-BC6	0.11	0.95	0.063	0.10
station 2A	0.012	130	0.043	3.2
station 2B	1.0	150	0.040	5.9
station A	1.0	91	0.0080	3.5

The greatest difference is in the estimated values of the hydraulic conductivity coefficient, β. In three cases (GeoB4901, NBP-98-02-09, and station 2A), the values differ by one to two orders of magnitude. While for two of them, they remain within the range of 0.1-1 cm/a previously estimated, the value at station 2A decreases to 0.012 cm/a. Station 2A is the site exhibiting the highest porosity values. However, station 2B, station A, and NBP-98-02-

06 also have high porosities >96%. At these sites, the hydraulic conductivity expression used has no effect on the inversion results.

The estimated elastic response coefficients *b* differ by less than 10% between the old and new inversion results. Similarly, the hydraulic conductivity expression has little effect on the optimized sedimentation rates. Thus, for the selected settings, fitting of the compaction model to porosity profiles yields robust values of the elastic response coefficients, with little interference from uncertainties related to the hydraulic conductivity or sedimentation rate. Note that the lack of sensitivity to the hydraulic conductivity coefficient and sedimentation rate may no longer be true when considering sites with higher sediment accumulation rates, or sediments experiencing significant imposed pore fluid flow. Given the above results, we continue using the Carman-Kozeny relationship in what follows.

3.1.3. *Impact of sediment composition*

In this section, we relax the third criterion used in selecting the sites (< 5% by weight variation in $CaCO_3$ content, see section 3.1.1). This results in an additional 15 porosity profiles (Table 11). The inversion steps for estimating the model parameters, β, b and ω_0 remain exactly the same as before, i.e. do not consider the effect of mineral dissolution or precipitation reactions. Based on the combined results of the inversions for the 31 deep-sea sites, we then examine the relation between the elastic response coefficient and sediment composition.

The fits to the additional porosity profiles are shown in Figure 3; the corresponding parameter values for the compaction model are listed in Table 12. Except for two sites, the best-fit estimates for the hydraulic conductivity coefficient vary from ~0.1 to ~1.0 cm/a. The two exceptions, GeoB1602-7 and BOFS15M-1, exhibit much lower conductivity coefficients (0.0026 and 0.0045 cm/a) and correspond to the sites with the highest weight % change in $CaCO_3$ content (35% and 46%). The elastic response coefficients vary from 0.49 to 83 kPa^{-1}, and thus fall within the range obtained for the previous set of deep-sea sediments (0.21-150 kPa^{-1}). The sedimentation rates remain close to the initial values estimated from sea-floor depth.

Table 11: Site descriptions. 1. Müller (1999) 2. Budziak (2004a,b) 3. Leng and Kuhn (1999) 4. Kuhn (2003) 5. Lowry (2004c-h) 6. Sayles and Martin (2003d-f).

Description	Location	longitude	latitude	Depth [m]	CaCO$_3$ content [weight %]
GeoB1602-7[1]	Eastern Atlantic (off Cape Blanc)	-20.71°	21.18°	4098	39-74
GeoB3003-5[2]	Western Arabian Sea	50.30°	13.49°	2013	45-55
GeoB3004-4[2]	Western Arabian Sea	52.92°	14.61°	1801	54-66
PS2513-3[3]	Scotia Sea	-43.01°	-53.71°	2515	0.37-27
PS2674-1[4]	Southeast Pacific	-91.83°	-57.98°	4780	0-51
BOFS1M-1[5]	NE Atlantic	-22.49°	47.15°	3945	80-87
BOFS5M-1[5]	NE Atlantic	-21.86°	50.68°	3560	72-83
BOFS5M-2[5]	NE Atlantic	-21.86°	-50.68°	3560	70-83
BOFS11M-2[5]	NE Atlantic	-20.35°	-55.19°	2080	71-80
BOFS15M-1[5]	NE Atlantic	-20.12°	59.10°	2790	31-77
BOFS15M-2[5]	NE Atlantic	-20.12°	59.10°	2790	43-74
NBP98-02-05[6]	Southern Ocean (Ross Sea)	-169.85°	-63.17°	2860	6.3-12
NBP98-02-03[6]	Southern Ocean (Ross Sea)	-169.63°	-66.14°	3136	12-28
NBP98-02-04[6]	Southern Ocean (Ross Sea)	-170.08°	-64.20°	2740	2.8-11
NBP98-02-07[6]	Southern Ocean (Ross Sea)	-170.19°	-60.24°	3900	25-38

Table 12:   Overall best fit values for β, b, and ω_0 with their corresponding misfit between the compaction model (Equation 21) and porosity data. Also shown are the misfit values associated with an exponential fit (Equation 32) to the porosity data.

| site	β [cm/a]	b [kPa^{-1}]	ω_0 [cm/a]	relative χ^2 misfit	
				Model	Exponential
GeoB1602-7	0.0026	12	0.0069	0.087	0.090
GeoB3003-5	1.0	5.9	0.047	0.041	0.011
GeoB3004-4	1.0	9.9	0.070	0.038	0.019
PS2513-3	0.091	0.49	0.046	0.22	0.25
PS2674-1	1.0	83	0.0040	0.010	0.010
BOFS1M-1	1.0	28	0.0080	0.089	0.060
BOFS5M-1	1.0	9.6	0.0088	0.11	0.087
BOFS5M-2	0.11	4.1	0.0080	0.25	0.15
BOFS11M-2	0.10	1.9	0.055	0.12	0.12
BOFS15M-1	0.0045	5.8	0.030	0.14	0.20
BOFS15M-2	0.10	2.0	0.030	0.083	0.084
NBP98-02-05	1.0	64	0.030	0.013	0.013
NBP98-02-03	1.0	14	0.020	0.045	0.023
NBP98-02-04	1.0	80	0.030	0.015	0.0088
NBP98-02-07	1.0	62	0.0090	0.0090	0.0079
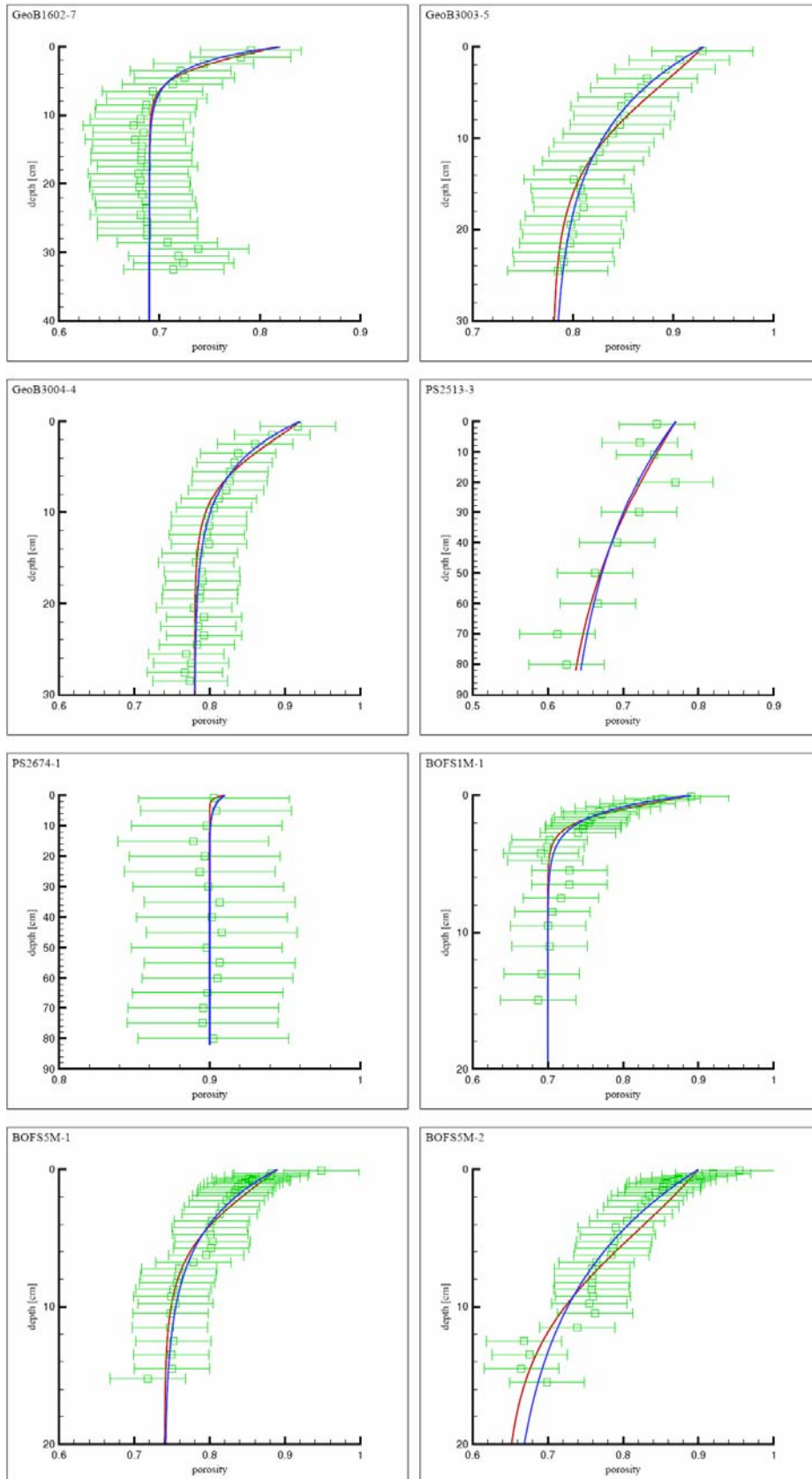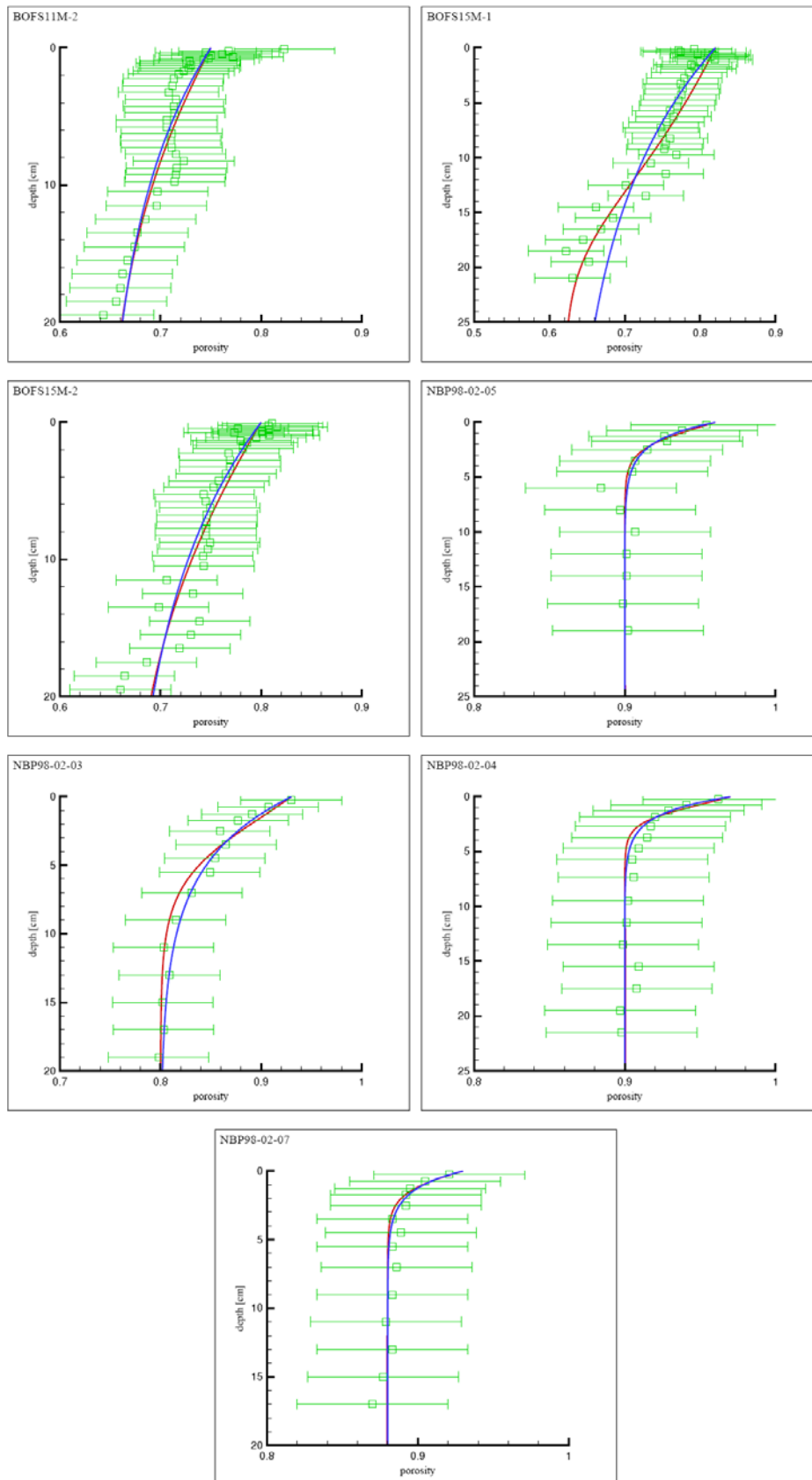
Figure 3: Porosity profiles of additional sites (see Table 11): symbols indicate measured data points, blue line is the exponential fit (Equation 32), and red line is the best fit by the compaction model (Equation 21).

For a number of the sites considered, the available information allows us to constrain the contributions of the main biogenic constituents, organic matter plus calcareous and biosiliceous shell fragments, to the total solid sediment composition (Table 13). The results suggest a relationship between the elastic properties of the sediment and its non-biogenic content, also referred to as the lithogenic fraction. The latter is estimated from the mid-range of values of the biogenic fractions reported in Table 13 except for the Ross Sea sites (NBP-98-02-xx). At these sites, Sayles et al. (2001) estimate the lithogenic fractions from the measured concentration of [232]Th, assuming that lithogenic sediments have an average thorium content of 10ppm.

Table 13: Sediment composition. The %lithogenic is calculated as 100% minus the sum of % biogenic silica, calcite, and 2.8 times weight %organic carbon (OC), where these data are available. The factor 2.8 is used to convert from g organic carbon to g organic matter (Sayles et al., 2001).

Site	%lithogenic	% OC	% CaCO$_3$	% Silica
GeoB4301-1	?	0.41-0.60	57-60	?
GeoB4901	?	0.83-1.9	2.2-4.5	?
NBP98-02-09	66-74	0.34-0.61	0.16-0.39	25-32
NBP98-02-08	27-33	0.25-0.48	24-27	42-46
NBP98-02-06	0-16	0.23-0.69	4.0-7.8	79-100
PS1243-1	?	0-50	0-1.1	?
PS1244-2	?	3.1-65	0.20-0.80	?
PS1599-3	65-98	0.27-0.67	0.27-0.99	0.14-33
PS1789-1	64-94	0.24-0.58	0.16-0.78	4.8-35
BOFS11M-1	?	0.16-0.57	79-84	?
BOFS14M-1	?	0.13-0.45	9.6-10	?
A_EN179-BC7	?	0.93-1.2	20-23	?
A_EN187-BC6	?	0.98-1.3	23-28	?
station 2A	?	0.14-0.28	88-92	?
station 2B	?	0.14-0.28	88-92	?
station A	?	0.44-0.59	61-66	?
GeoB1602-7	25-58	0.19-0.35	39-74	0.63-2.0
GeoB3003-5	?	1.9-2.3	45-55	?
GeoB3004-4	?	1.3-2.2	54-66	?
PS2513-3	71-90	0.24-0.45	0.85-5	7.9-25
PS2674-1	?	0.15-0.34	0-6	?
BOFS1M-1	?	0.064-0.78	80-87	?
BOFS5M-1	?	0.21-0.64	72-83	?
BOFS5M-2	?	0.32-0.83	70-83	?
BOFS11M-2	?	0.29-0.59	71-80	?
BOFS15M-1	?	0.14-0.70	31-77	?
BOFS15M-2	?	0-0.79	43-74	?
NBP98-02-05	0-4.0	0.21-0.61	6.3-12	82-100
NBP98-02-03	47-55	0.17-0.59	12-28	20-38
NBP98-02-04	0-11	0.37-0.69	2.8-11	50-92
NBP98-02-07	0.050-10	0.19-0.37	25-38	52-73

There is a negative correlation between the elastic response coefficient and the amount of lithogenic material in the sediments (Figure 4). This suggests that sediments with higher lithogenic contents tend to compress less easily. Comparison of the elastic response coefficient to other physical characteristics, such as grain size, where this data is available, could be more fruitful. Aplin et al. (1995) relate the clay fraction, defined as <2μm sized particles, to the sediment's compression coefficient. Obviously, further information on grain size and clay mineralogy is needed to fully assess the significance of the relationship in Figure 4.

$$b = -0.76*(\% \text{ lithogenic}) + 63$$

$$R^2 = 0.80$$
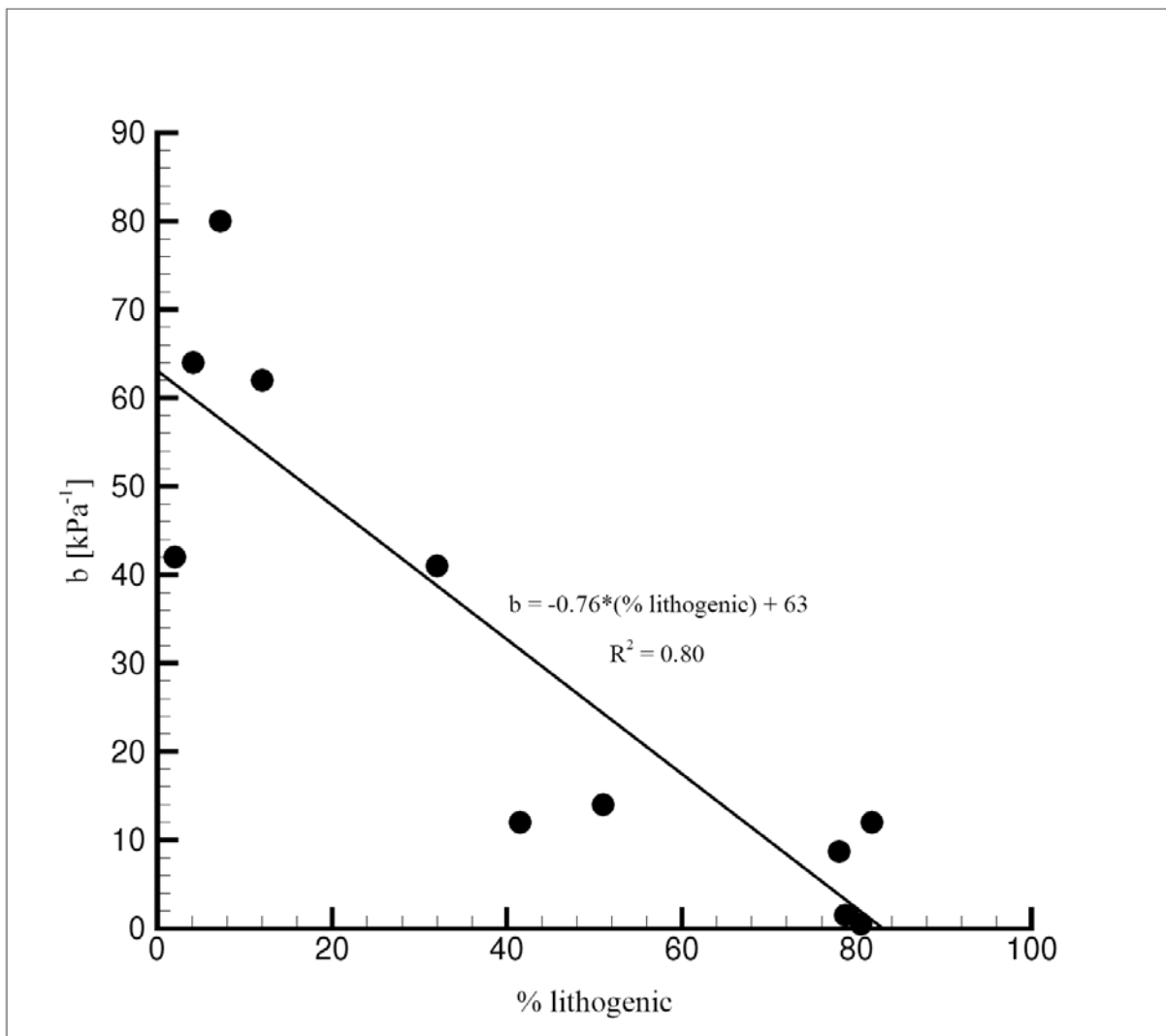
Figure 4: Elastic response coefficient versus the lithogenic fraction of deep-sea sediments.

3.2. Mineral Reactions

While the above results point to lower elastic response and conductivity coefficients for sites with greater change in $CaCO_3$ content (Tables 9 and 12), including its dissolution rate may also affect these parameter values. The effect of mineral reactions on porosity can be evaluated through the compaction model in two ways. Known mineral dissolution and precipitation rates can either serve directly as input to the model (via the R_m terms in Equation 21), or a reaction-transport model capable of estimating the rates can be coupled to the compaction model.

3.2.1. Biogenic silica dissolution

One example where mineral dissolution rate distributions have been constrained are the siliceous sediments sampled during the Antares I cruise in the Indian Ocean sector of the Southern Ocean (Rabouille et al., 1997). Detailed experimental studies on the solubility and dissolution kinetics of biogenic silica in these sediments (Van Cappellen and Qiu, 1997a and 1997b) have been combined with reactive transport modeling to simulate early diagenetic silica cycling (Rabouille et al., 1997). The modeling results show that, at all the sites studied, large fractions (>50%) of the biogenic silica reaching the seafloor dissolve and are recycled to the overlying water as silicic acid.

Here, we focus on the two southernmost Antares I sites (KTB05 and KTB06), which also exhibit the highest biogenic silica contents (65-81 weight %). Together with the high post-depositional silica regeneration efficiencies (76 and 84% at KTB05 and KTB06, respectively), this means that large fractions of the solid sediment matrix dissolve away at the sites. Most of the dissolution is restricted to the upper two centimeters, as shown by the rate profiles in Figure 5 (rate profiles courtesy of Christophe Rabouille). Unfortunately, the raw porosity data are no longer available, only the exponential fits to the porosity depth profiles are available (Christophe Rabouille, personal communication).

In what follows, the exponential fits to the porosity are treated as data in the model optimizations. The compaction model is optimized by varying b and β. The sedimentation rate, ω_0, is kept constant at 0.01 cm/a, the value estimated for the two sites by Rabouille et al. (1997). The inversion results are shown in Table 14, considering two scenarios: 1) the silica dissolution rates are directly incorporated into the compaction model (+SR), and 2) zero rates of silica dissolution are imposed in the compaction model (-SR). The corresponding porosity profiles are shown by the solid and broken red lines in Figure 5, respectively.
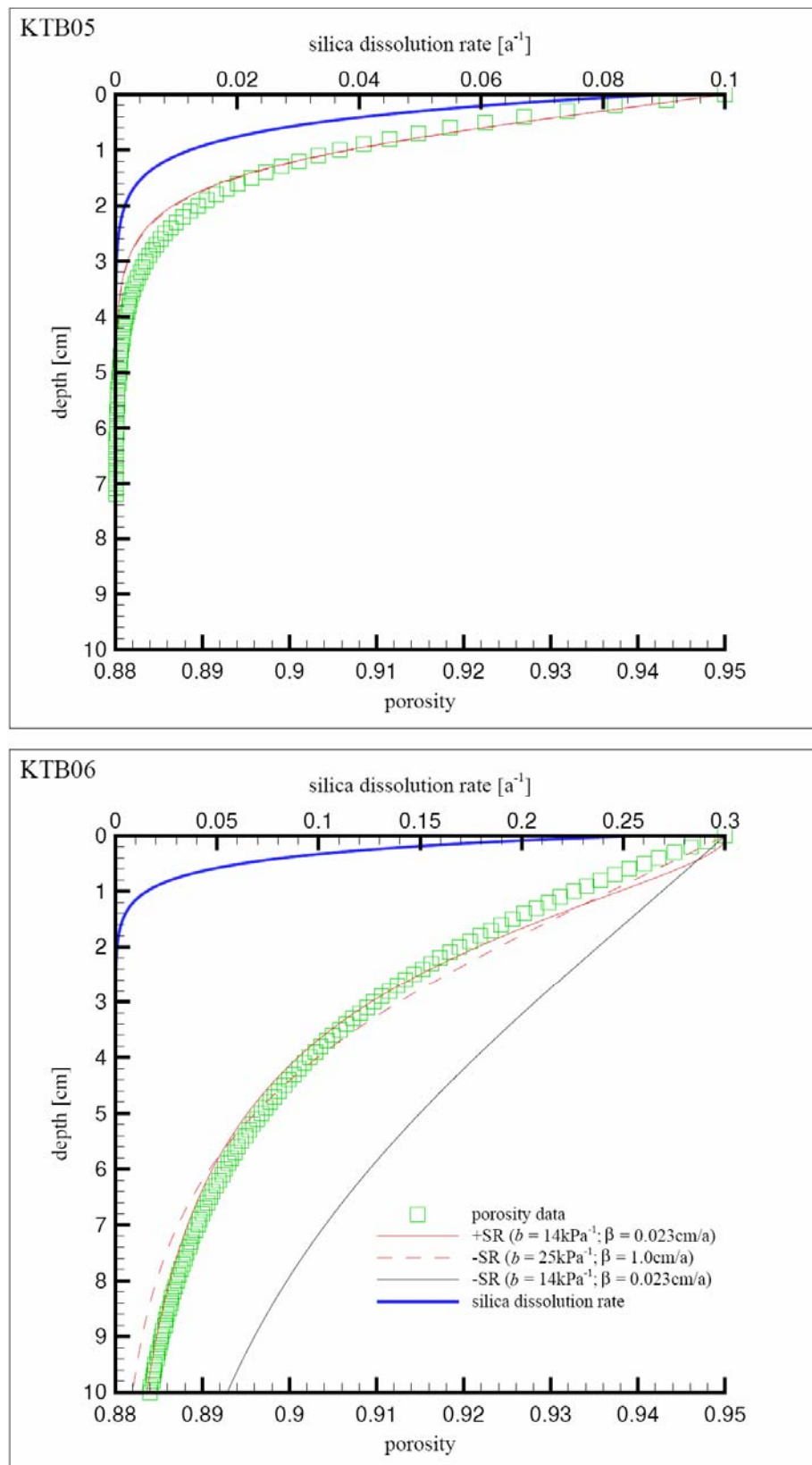
Figure 5: Modelled porosity profiles with (+SR) and without (-SR) silica dissolution, using optimized best-fit parameters. The silica dissolution rates, which serve as input to the compaction model in the +SR simulations, are from Rabouille et al. (1997).

Table 14: Best fit values for β and b with their corresponding misfit between the compaction model and porosity data with (+SR) and without (-SR) silica dissolution.

site	β [cm/a]	b [kPa^{-1}]	relative χ^2 misfit
+SR:			
KTB05	1.0	90	0.012
KTB06	0.023	14	0.024
-SR:			
KTB05	1.0	90	0.011
KTB06	1.0	25	0.040

For site KTB05, inclusion or not of silica dissolution has no noticeable effect on the best-fit values of the hydraulic conductivity and elastic response coefficients, despite significant dissolution of the solid sediment matrix. For site KTB06, lower values of β and b are obtained when dissolution is included. The difference between the two sites is explained by the fact that KTB06 is characterized by a factor of 3 higher dissolution rates than KTB05 (Figure5, Rabouille et al., 1997). To illustrate the effect of dissolution at KTB06, the resulting porosity profile using best-fit parameter values from the +SR (with dissolution) optimization is shown after setting the dissolution rate to zero (solid black line in Figure 5). The difference between the latter porosity profile and that from the +SR optimization can be regarded as the chemical compaction effect. Thus, the net effect of dissolution is actually to lower the porosity. This is opposite to a non-compacting porous medium where dissolution increases the porosity.

As indicated by the results, a significant impact of dissolution (or precipitation) reactions on the model-derived physical parameters b and β requires high rates of removal (or addition) of total solid sediment mass within the depth range over which the porosity profile is fitted. At site KTB06, over 50% of the total solid sediment mass dissolves in the uppermost centimeters, according to the reactive transport calculations of Rabouille et al. (1997). Thus, in many cases, neglecting mineral dissolution or precipitation when applying the compaction model may be justified.

3.2.2. Calcite dissolution

A number of studies have estimated rate profiles of calcite dissolution in deep-sea sediments using early diagenetic models. Model fits to pore water oxygen and pH data are most commonly used to estimate parameter values describing calcite dissolution kinetics (e.g., Archer et al., 1989; Hales and Emerson, 1997; Wenzhöfer et al., 2001). Based on the

previous results on biogenic silica dissolution, we select a site where the dissolution rate of calcite is of the same order of magnitude to that of silica at site KTB06.

The intensity of dissolution can be compared based on the maximum rate in units of volume fraction per year, as well as the depth-integrated dissolution rate in units of $\mu moles/cm^2/a$. The maximum rate of silica dissolution at site KTB06, is 2.6×10^{-1} a^{-1}, while the depth-integrated rate equals 190 $\mu moles/cm^2/a$. One non-siliceous site with a comparable calcite dissolution intensity is Station 13 situated in the equatorial Atlantic at a water depth of 4950 m (Archer et al., 1989).

At this site, application of a reaction-transport model (Aguilera et al., 2005; Jourabchi et al., 2005) to the O_2 and pH data, yields a maximum rate and an integrated dissolution rate of 4.1×10^{-1} a^{-1} and 40 $\mu moles/cm^2/a$, respectively. The model-predicted rate distribution indicates that most dissolution takes place in the upper 0.5 centimeters below the SWI (Figure 6). Note that an exponential fit to the porosity data (solid blue line on Figure 6) is used as input to the reaction-transport model (RTM). The resulting dissolution rate profile of calcite, in turn, serves as input to the compaction model when computing porosity profiles. The sedimentation rate is set to 0.003 cm/a in both models.

The best fits of the compaction model (CM) to the porosity data when including the RTM-derived calcite dissolution rate (CM + diss) and when setting the dissolution rate to zero (CM) are compared in Figure 6. The parameter values of b and β obtained with and without considering the dissolution rate are quite different (values given on Figure 6). Including dissolution yields lower values b and β, as was also observed for silica dissolution at site KTB06.

Especially the elastic response coefficient seems to be more realistic with ($b = 0.16$ kPa^{-1}) than without dissolution ($b = 200$ kPa^{-1}). The latter value exceeds any value obtained so far for deep-sea sediments (Tables 9 and 12). In addition, the sediment at Station 13 is likely to be dominated by lithogenic material. The $CaCO_3$ content is estimated at about 10% (Archer et al., 1989), while the organic matter and silica contents tend to be low in sediments of the equatorial Atlantic (e.g., Archer, 1999; Heinze et al., 2003; Gehlen et al., 2006). According to the relationship in Figure 4, we would then expect a relatively low value (≤ 1 kPa^{-1}) for the elastic response coefficient. Thus, at sites with high $CaCO_3$ dissolution rates, neglecting their effect on porosity gradients below the SWI may cause the value of b (and that of β) to be overestimated by the compaction model.
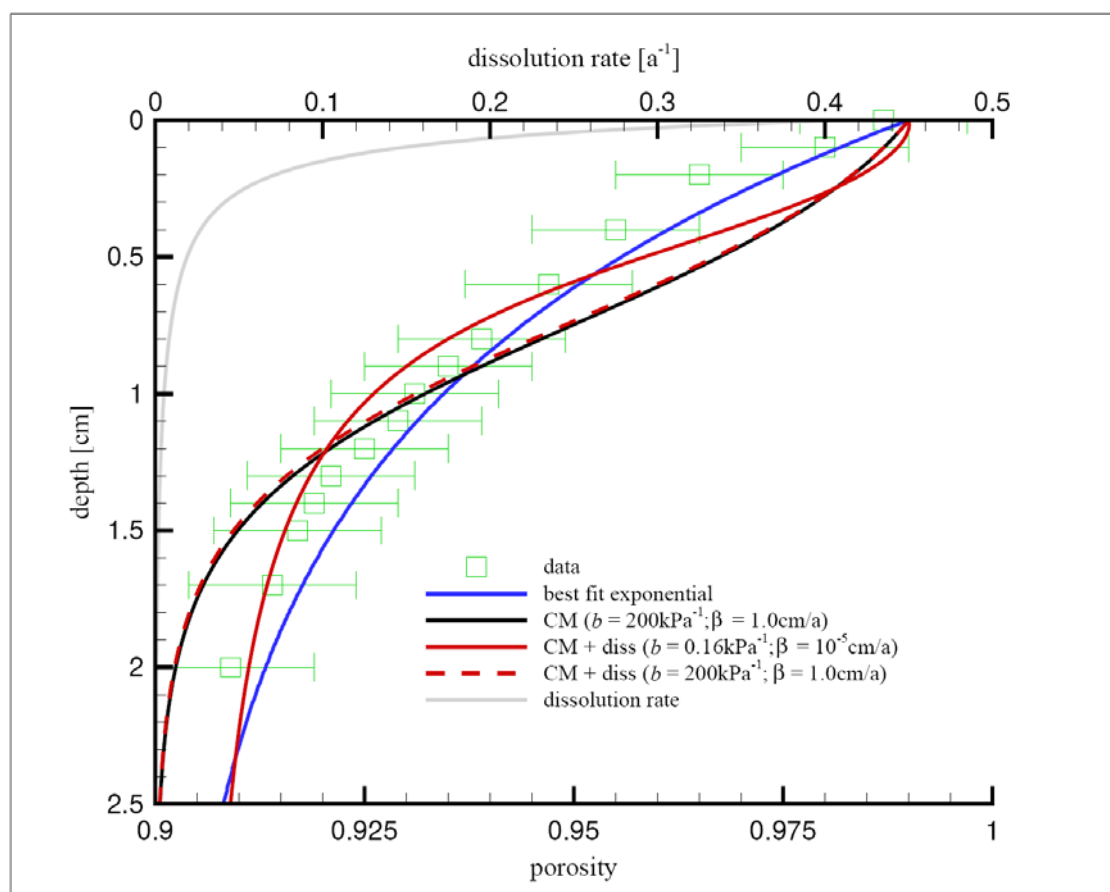
Figure 6: Porosity fits for the compaction model (CM, Equation 21) with (+ diss) and without calcite dissolution included. The porosity data and dissolution rate profile are for Station 13 in the equatorial Atlantic.

3.2.3. Coupling reaction transport and compaction models

In the previous section, the porosity profile imposed in the reaction-transport model (RTM) calculations differs from that derived by the compaction model (CM). A logical next step is therefore to iteratively couple the RTM and CM, whereby the modified porosity profile from the CM is fed back into the RTM, in order to obtain a new calcite dissolution rate profile, which is returned to the CM and so on. The procedure is then repeated until all chemical species concentrations in the RTM and the porosity profile in the CM become invariant within specified tolerance limits. With this approach, it becomes possible to examine the effect of optimizing the porosity profile on the dissolution rate profile itself.

Calcite dissolution rate laws assume that the rate is proportional to the degree of undersaturation of the pore waters raised to a reaction rate order, n (Keir, 1980; Gehlen et al., 2005). For the rate profile in Figure 6, the rate order is set equal to 4.5, the value most often used in early diagenetic RTMs (Keir, 1980; Jourabchi et al., submitted). To test the effect of n on the porosity profile by the CM, we vary the rate order ($n = 4.5$, 2 or 1) and input the resulting calcite dissolution rates (as determined by fitting to the pH profiles) to the CM. We

then invert the CM to determine the best-fit values of β and b corresponding to each reaction order (Table 15).

Lower porosities are obtained with the coupled reaction-transport and compaction model (RT&CM), regardless of the reaction rate order considered (Figure 7). Thus, as for silica early diagenesis, $CaCO_3$ dissolution leads to a chemical compaction effect. The nonlinear dissolution rate laws, however, provide better fits to the porosity profile than the linear rate law (Table 15). Furthermore, for $n = 4.5$ and $n = 2$ (nonlinear rate laws), the elastic response coefficient falls within the range of values determined in sections 3.1.1 and 3.1.2 (Tables 9 and 12), while for $n = 1$ (linear rate law), b is an order of magnitude lower than any value obtained so far. Thus, overall, the porosity data appear to be more consistent with nonlinear rate expressions for calcite dissolution. Note, however, that the optimized porosity profiles for the three rate orders result in hydraulic conductivity coefficients that are order-of-magnitude lower than previously determined values. The reason for these very low values of β is not entirely clear.

Table 15: Best fit values for β and b with their corresponding misfit between the compaction model and porosity data. Calcite dissolution rates with rate orders (n), are input to CM.

n	β [cm/a]	b [kPa^{-1}]	relative χ^2 misfit
4.5	10^{-5}	0.16	0.52
2	$2.5\ 10^{-5}$	0.52	0.60
1	$6.4\ 10^{-7}$	0.016	0.66
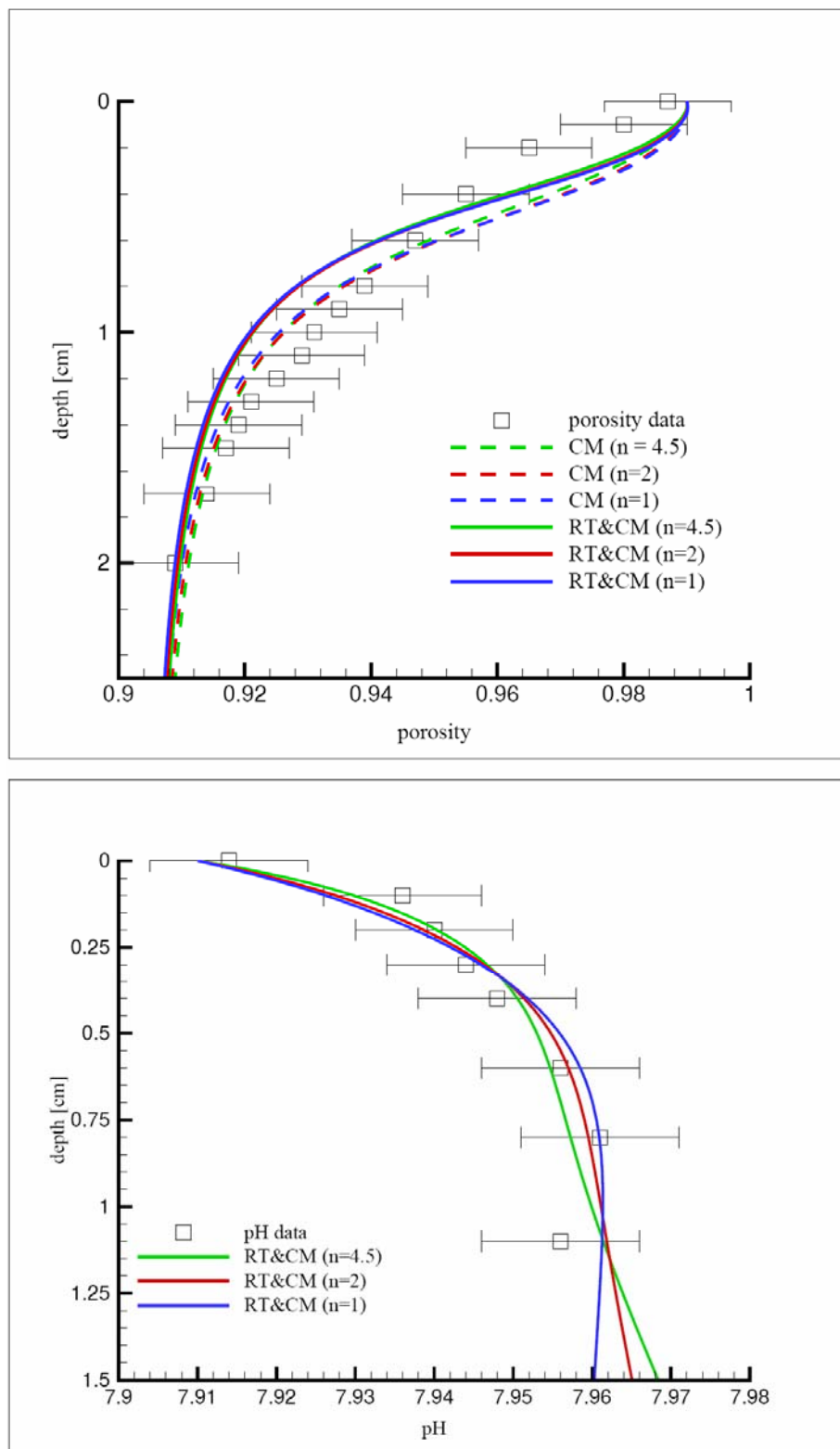
Figure 7: Porosity and pH data, CM results (Equation 21) and coupled reaction-transport and compaction model (RT&CM) results for *n* = 4.5, 2, and 1.

5. Conclusions

Porosity distributions in marine sediments can be interpreted within the framework of general continuum theory, which considers both conservation of mass and momentum. By including mineral dissolution and precipitation reactions, the compaction model presented here can be used to separate the effects of mechanical compression from those of mineral reactions on steady state porosity depth profiles.

Analysis of porosity profiles of 31 deep-sea sediments illustrates that robust estimates of the elastic response coefficient (b) can be obtained, when mineral dissolution or precipitation can be assumed to have a negligible effect on porosity. The values of b range over several orders of magnitude (0.2-150 kPa^{-1}). Part of the variability in b can be assigned to variations in sediment composition: sediments with high lithogenic contents exhibit lower values of b than sediments dominated by biogenically-derived matter. Hydraulic conductivity coefficients (β) are less well constrained by the porosity profiles, presumably because of the very low rates of fluid flow within the settings considered. The most probable range for β in deep-sea sediments is 0.1-1 cm/a.

Application of the compaction model to sediments, for which the rates of biogenic silica or calcite dissolution can be estimated independently, indicates that very high mineral dissolution rates can significantly modify porosity profiles in the uppermost centimeters. In fact, mineral dissolution causes the porosity to decrease more rapidly with depth. This chemical compaction effect in surface sediments is opposite to that in non-compacting porous media, where dissolution increases porosity. Given the very high rates of mineral dissolution needed to significantly affect the porosity profiles (> 0.1 a^{-1}), mechanical compaction is likely the main process controlling porosity profiles in most deep-sea sediments. It cannot be excluded, however, that some of the observed variability in the elastic response coefficient is due to unaccounted effects of mineral reactions.

In a final application, the compaction model is coupled to reactive transport calculations. Results for a sediment from the equatorial Atlantic show that use of a nonlinear rate law for calcite dissolution provides a better fit to the measured porosity profile than a linear rate law. Although the generality of this conclusion remains to be verified, the application illustrates the potential of a unified, mechanistic analysis of the physical and chemical properties of marine sediments.

References

Aguilera D. R., Jourabchi P., Spiteri C., and Regnier P. (2005) A knowledge-based reactive transport approach for the simulation of biogeochemical dynamics in Earth systems. Geochemistry Geophysics Geosystems 6, doi:10.1029/2004GC000899.

Anderson, Robert F (2005): TOC, CaCO$_3$, porosity, Lead 210 of Sites A_EN179, A_EN187, PANGAEA, doi:10.1594/PANGAEA.53382.

Aplin A. C., Yang Y., and Hansen S. (1995) Assessment of β, the compression coefficient of mudstones and its relationhip with detailed lithology. Marine and Petroleum Geology 12, 955-963.

Archer D., Emerson S., and Reimers C. (1989) Dissolution of calcite in deep-sea sediments: pH and O$_2$ microelectrode results. Geochimica et Cosmochimica Acta 53, 2831-2845.

Archer, David (1999): Opal, quartz and calcium carbonate content in surface sediments of the ocean floor, PANGAEA, doi:10.1594/PANGAEA.56017.

Archer D. E., Morford J. L., and Emerson S. R. (2002) A model of suboxic sedimentary diagenesis suitable for automatic tuning and gridded global domains. Global Biogeochemical Cycles 16, doi:10.1029/2000GB001288.

Athy L. F. (1930) Density, porosity and compaction of sedimentary rocks. American Association of Petroleum Geology Bulletin 14, 1-24.

Audet D. M. (1995) Modelling of porosity evolution and mechanical compaction of calcareous sediments. Sedimentology 42, 355-373.

Bahr D. B., Hutton E. W. H., Syvitski J. P. M., and Pratson L. F. (2001) Exponential approximations to compacted sediment porosity profiles. Computers & Geosciences 27, 691-700.

Bear J. (1988) Dynamics of fluids in porous media, 764 pp., Dover Publications, inc., New York.

Bennett R. H., Ransom B., Kastner M., Baerwald R. J., Hulbert M. H., Sawyer W. B., Olsen H., and Lambert M. W. (1999) Early diagenesis: impact of organic matter on mass physical properties and processes, California continental margin. Marine Geology 159, 7-34.

Berelson W. M., Hammond S. D., and Johnson K. S. (1987) Benthic fluxes and the cycling of biogenic silica and carbon in two southern California borderland basins. Geochimica et Cosmochimica Acta 51, 1345-1363.

Berg P., Rysgaard S., and Thamdrup B. (2005) Dynamic modeling of early diagenesis and nutrient cycling. A case study in an arctic marine sediment. American Journal of Science 303, 905-955.

Berner R. A. (1980) Early diagenesis: a theoretical approach, 250 pp., Princeton University Press, Princeton.

Birgisdottir, L; Thiede, Jrn (2002a): Carbon and density analysis of sediment core PS1243-1, PANGAEA, doi:10.1594/PANGAEA.87536.

Birgisdottir, L; Thiede, Jrn (2002b): Carbon and density analysis of sediment core PS1244-2, PANGAEA, doi:10.1594/PANGAEA.87427.

Boudreau B. P. (1986) Mathematics of tracer mixing in sediments: I. spatially-dependent, diffusive mixing. American Journal of Science 286, 161-198.

Boudreau B. P. (1997) Diagenetic models and their implementation: modelling transport and reactions in aquatic sediments, 414 pp., Springer-Verlag, New York.

Boudreau B. P. and Bennett R. (1999) New rheological and porosity equations for steady-state compaction. American Journal of Science 299, 517-528.

Budziak, Dörte (2004a): Alkenones of sediment core GeoB3003-5, PANGAEA, doi:10.1594/PANGAEA.227298.

Budziak, Dörte (2004b): Alkenones of sediment core GeoB3004-4, PANGAEA, doi:10.1594/PANGAEA.227299.

Carman P. C. (1937) Fluid flow through granular beds. Transactions of the Institution of Chemical Engineers 15, 150-166.

Deudé V., Dormieux L., Maghous S., Barthélémy J. F., and Bernaud D. (2004) Compaction process in sedimentary basins: the role of stiffness increase and hardening induced by large plastic strains. International Journal for Numerical and Analytical Methods in Geomechanics 28, 1279-1303.

Freudenthal, Tim (2001): Organic material and carbon analysis with accumulation rates from multicorer sediment profile GeoB4301-1, PANGAEA, doi:10.1594/PANGAEA.57866.

Gehlen M., Bassinot F. C., Chou L., and McCorkle D. (2005) Reassessing the dissolution of marine carbonates: II. Reaction kinetics. Deep-Sea Research I 52, 1461-1476.

Gehlen M., Bopp L., Emprin N., Aumont O., Heinze C., and Ragueneau O. (2006) Reconciling surface ocean productivity, export fluxes and sediment composition in a global biogeochemical ocean model. Biogeosciences 3, 521-537.

Gordon D. S. and Flemings P. B. (1998) Generation of overpressure and compaction-driven fluid flow in a Plio-Pleistocene growth-faulted basin, Eugene Island 330, offshore Louisiana. Basin Research 10, 177-196.

Hales B. and Emerson S. (1996) Calcite dissolution in sediments of the Ontong-Java Plateau: in situ measurements of pore water O_2 and pH. Global Biogeochemical Cycles 10, 527-541.

Hales B. and Emerson S. (1997) Calcite dissolution in sediments of the Ceara Rise: In situ measurements of porewater O_2, pH, and $CO_{2(aq)}$. Geochimica et Cosmochimica Acta 61, 501-514.

Hart B. S., Flemings P. B., and Deshpande A. (1995) Porosity and pressure: Role of compaction disequilibrium in the development of geopressures in a Gulf Coast Pleistocene basin. Geology 23, 45-48.

Heinze C., Hupe A., Maier-Reimer E., Dittert N., and Ragueneau O. (2003) Sensitivity of the marine biospheric Si cycle for biogeochemical parameter variations. Global Biogeochemical Cycles 17, 1086, doi:10.1029/2002GB001943.

Hsu C. T. and Cheng P. (1991) A singular perturbation solution for Couette flow over a semi-infinite porous bed. Journal of fluids engineering 113, 137-142.

Hubbert M. K. and Rubey W. W. (1959) Role of fluid pressure in mechanics of overthrust faulting I. Mechanics of fluid-filled porous solids and its application to overthrust faulting. Bulletin of the Geological Society of America 70, 115-166.

Jahnke R. A., Craven D. B., and Gaillard J.-F. (1994) The influence of organic matter diagenesis on $CaCO_3$ dissolution at the deep-sea floor. Geochimica et Cosmochimica Acta 58, 2799-2809.

Jourabchi P., Van Cappellen P., and Regnier P. (2005) Quantitative interpretation of pH distributions in aquatic sediments: a reaction-transport modeling approach. American Journal of Science 305, 919-956.

Jourabchi P., Meile C., Pasion L. R., and Van Cappellen P.(submitted) Quantitative interpretation of pore water O_2 and pH distributions in deep-sea sediments. Geochimica et Cosmochimica Acta.

Keir R. S. (1980) The dissolution kinetics of biogenic calcium carbonates in seawater. Geochimica et Cosmochimica Acta 44, 241-252.

Keith L. A. and Rimsidt J. D. (1985) A numerical compaction model of overpressuring in shales. Mathematical Geology 17, 115-135.

Kleypas J. A., Feely R. A., Fabry V. J., Langdon C., Sabine C. L., and Robbins L. L. (2006) Impacts of ocean acidification on coral reefs and other marine calcifiers: A guide for future research. In report of a workshop held 18-20 April 2005, 88 pp., NSF, NOAA, and the U. S. Geological Survey.

Kozeny J. (1927) ber kapillare leitung des wassers im boden. Sitzungsber Akademie Wissenschaften 136, 271-306 (Translated by Striedieck WF, Davis CM, published by the Petroleum Branch of AIME).

Kuhn, Gerhard (2003): Bulk sedimentology of core PS2674-1, Alfred Wegener Institute for Polar and Marine Research, Bremerhaven, PANGAEA, doi:10.1594/PANGAEA.131712.

L'Heureux I. and Fowler A. D. (2000) A simple model of flow patterns in over pressured sedimentary basins with heat transport and fracturing. Journal of Geophysical Research - Solid Earth 105, 23741-23752.

Lagarias J. C., Reeds J. A., Wright M. H., and Wright P. E. (1998) Convergence properties of the Nelder-Mead Simplex Method in Low Dimensions. SIAM Journal of Optimization 9, 112-147.

Leng, C; Kuhn, Gerhard (1999): Sedimentology of core PS2513-3, PANGAEA, doi:10.1594/PANGAEA.55728.

Lowry, Roy K; BODC (2004a): Carbon and nitrogen of sediment core BOFS11M-1, PANGAEA, doi:10.1594/PANGAEA.199855.

Lowry, Roy K; BODC (2004b): Carbon and nitrogen of sediment core BOFS14M-1, PANGAEA, doi:10.1594/PANGAEA.199861.

Lowry, Roy K; BODC (2004c): Carbon and nitrogen of sediment core BOFS1M-1, PANGAEA, doi:10.1594/PANGAEA.199867.

Lowry, Roy K; BODC (2004d): Carbon and nitrogen of sediment core BOFS5M-1, PANGAEA, doi:10.1594/PANGAEA.199895.

Lowry, Roy K; BODC (2004e): Carbon and nitrogen of sediment core BOFS5M-2, PANGAEA, doi:10.1594/PANGAEA.199896.

Lowry, Roy K; BODC (2004f): Carbon and nitrogen of sediment core BOFS11M-2, PANGAEA, doi:10.1594/PANGAEA.199856.

Lowry, Roy K; BODC (2004g): Carbon and nitrogen of sediment core BOFS15M-1,

PANGAEA, doi:10.1594/PANGAEA.199864.

Lowry, Roy K; BODC (2004h): Carbon and nitrogen of sediment core BOFS15M-2, PANGAEA, doi:10.1594/PANGAEA.199865.

Luff R., Wallmann K., and Aloisi G. (2004) Numerical modeling of carbonate crust formation at cold vent sites: significance for fluid and methane budgets and chemosynthetic biological communities. Earth and Planetary Science Letters 221, 337-353.

Martin W. R. and Sayles F. L. (2006) Organic matter oxidation in deep-sea sediments: distribution in the sediment column and implications for calcite dissolution. Deep-Sea Research II 53, 771-792.

Mayer K. U., Frind E. O., and Blowes D. W. (2002) Multicomponent reactive transport modeling in variably saturated porous media using a generalized formulation for kinetically controlled reactions. Water Resources Research 38, doi:10.1029/2001WR000862.

Martin W. R. and Sayles F. L. (1996) $CaCO_3$ dissolution in sediments of the Ceara Rise, western equatorial Atlantic. Geochimica et Cosmochimica Acta 60, 243-263.

Meile C. and Van Cappellen P. (2003) Global estimates of enhanced solute transport in marine sediments. Limnology and Oceanography 48, 777-786.

Mello U. T., Karner G. D., and Anderson R. N. (1994) A physical explanation for the positioning of the depth to the top of overpressure in shale dominated sequences in the Gulf Coast basin, United States. Journal of Geophysical Research 99, 2775-2789.

Metz B., Davidson O., de Coninck H., Loos M., and Meyer L. (2005) IPCC special report on carbon dioxide capture and storage, 440 pp., Cambridge University Press, New York.

Meysman F. J. R., Boudreau B. P., and Middelburg J. J. (2005) Modeling reactive transport in sediments subject to bioturbation and compaction. Geochimica et Cosmochimica Acta 69, 3601-3617.

Middelburg J. J., Soetaert K., and Herman P. M. J. (1997) Empirical relationships for use in global diagenetic models. Deep-Sea Research I 44, 327-344.

Müller, Peter J (1999): Density, water content, carbon, nitrogen and opal data of sediment core GeoB1602-7, Department of Geosciences, Bremen University, PANGAEA, doi:10.1594/PANGAEA.54977.

Pfeifer k., Hensen C., Adler M., Wenzhöfer F., Weber B., and Schulz H. D. (2002) Modeling of subsurface calcite dissolution, including the respiration and reoxidation processes of marine sediments in the region of equatorial upwelling off Gabon. Geochimica et Cosmochimica Acta 66, 4247-4259.

Rabouille C., Gaillard J.-F., Trguer P., and Vincendeau M.-A. (1997) Biogenic silica recycling in surficial sediments across the Polar Front of the Southern Ocean (Indian Sector). Deep-Sea Research II 44, 1151-1176.

Rubey W. W. and Hubbert M. K. (1959) Role of fluid pressure in mechanics of overthrust faulting II. Overthrust belt in geosynclinal area of Western Wyoming in light of fluid-pressure hypothesis. Bulletin of the Geological Society of America 70, 167-206.

Sayles F. L., Martin W. R., Chase Z., and Anderson R. F. (2001) Benthic remineralization and burial of biogenic SiO_2, $CaCO_3$, organic carbon, and detrital material in the Southern Ocean along a transect at 170° West. Deep-Sea Research II 48, 4323-4383.

Sayles, Frederick L; Martin, William R (2003a): Composition of sediment core NBP98-02-09-10, PANGAEA, doi:10.1594/PANGAEA.132760.

Sayles, Frederick L; Martin, William R (2003b): Composition of sediment core NBP98-02-08-1, PANGAEA, doi:10.1594/PANGAEA.132759.

Sayles, Frederick L; Martin, William R (2003c): Composition of sediment core NBP98-02-06-3, PANGAEA, doi:10.1594/PANGAEA.132757.

Sayles, Frederick L; Martin, William R (2003d): Composition of sediment core NBP98-02-05-12, PANGAEA, doi:10.1594/PANGAEA.132756.

Sayles, Frederick L; Martin, William R (2003e): Composition of sediment core NBP98-02-03-17, PANGAEA, doi:10.1594/PANGAEA.132754.

Sayles, Frederick L; Martin, William R (2003f): Composition of sediment core NBP98-02-04-2, PANGAEA, doi:10.1594/PANGAEA.132755.

Schink D. R. and Guinasso N. L. (1977) Modelling the influence of bioturbation and other processes on calcium carbonate dissolution at the sea floor. In The fate of fossil fuel CO_2 in the ocean (ed. N. R. Andersen and A. Malahoff), pp. 375-400. Plenum Press.

Soetaert K., Herman P. M. J., and Middelburg J. J. (1996) A model of early diagenetic processes from the shelf to abyssal depths. Geochimica et Cosmochimica Acta 60, 1019-1040.

Steefel C. I. and Lasaga A. C. (1994) A coupled model for transport of multiple chemical species and kinetic precipitation/dissolution reactions with application to reactive flow in single phase hydrothermal systems. American Journal of Science 294, 529-592.

Tromp T. K., Van Cappellen P., and Key R. M. (1995) A global model for the early diagenesis of organic carbon and organic phosphorus in marine sediments. Geochimica et Cosmochimica Acta 59, 1259-1284.

Van Cappellen P. and Qiu L. (1997a) Biogenic silica dissolution in sediments of the Southern Ocean. I. Solubility. Deep-Sea Research II 44, 1109-1128.

Van Cappellen P. and Qiu L. (1997b) Biogenic silica dissolution in sediments of the Southern Ocean. II. Kinetics. Deep-Sea Research II 44, 1129-1149.

Weber, Michael E (2000a): Sedimentology of sediment core PS1599-3, PANGAEA, doi:10.1594/PANGAEA.57660.

Weber, Michael E (2000b): Sedimentology and sand fractions of sediment core PS1789-1, PANGAEA, doi:10.1594/PANGAEA.56841.

Wenzhöfer F., Adler M., Kohls O., Hensen C., Strotmann B., Boehme S., and Schulz H. D. (2001) Calcite dissolution driven by benthic mineralization in the deep-sea: In situ measurements of Ca^{2+}, pH, pCO_2, and O_2. Geochimica et Cosmochimica Acta 65, 2677-2690.

Acknowledgements

Thilo, Jacqueline, Steeve, Katja, and Vincent. I'd like to particularly acknowledge Mariette Wolthers, Yvonne van Lith, Gert-Jan Reichart, and Anke Dählmann. My sincere thanks go to Anniet Laverman for all her help, specially with the Dutch translation of the summary.

My stay in Utrecht and in the geochemistry department was made so much more pleasant by the company of Céline Pallud, Christelle Hyacinthe, Victoria Knowles, and Jeff Vinuesa. Christelle, thank you for all the good times and your positive encouragement both in W112 and Sweelinckstraat 23. Thank you Maisha, Viktor, Paddy, and Gert-Jan for the fun runs. My warm thanks also go to Hamid and Behrooz for the Iranian cultural activities as well as to Zohreh, Melika, and Marjan for their hospitality.

For their encouragement and giving me a place to complete my thesis work at UBC, I thank Doug Oldenburg and Roman Shekhtman and the GIF members. I'm specially grateful for the talks with Megan Sheffer and the collaboration with Len Pasion on inverse modelling.

I have been very fortunate to meet Nasrin Vaziri and her wonderful family in the Netherlands - thank you for your encouraging support and warm hospitality. Shideh, Nahid, and Andras, thanks for your interest in my research and for keeping in touch though I was far away for long periods of time. Gwenn, thank you so much for all the academic advice and for taking the time to listen to my concerns.

For their loving support I am always grateful to Maryam, Mohsen and Ali. I also acknowledge Fandogh for all the welcome home greetings! Finally, I thank my dear Arash for the kind and loving encouragement and our sweetheart who prompted the completion of this thesis.

Curriculum Vitae

Parisa Jourabchi was born on September 2nd 1972 in Tehran, Iran. In 1995 she received a Bachelor of Applied Science in Engineering Physics from the University of British Columbia (UBC) in Vancouver, Canada. During her study she specialized in Electrical Engineering and developed a device for measuring the uniformity of paper, for which she won the Roy Nodwell award for the best project of her graduating year. After graduation, she continued on this work on contract with MacMillan Bloedel pulp and paper company before joining the control group at Automed Corporation, where she worked for two years. During this time, Parisa maintained and develped software for real time machine control of clinical laboratory equipment. In 1998 she joined the Rock Physics group in the Earth and Ocean Sciences Department at UBC as a research assistant and began her masters studies in 1999. After completion of her Master of Science degree in 2001, she joined the Geochemistry Department of Utrecht University and began work on this thesis in January, 2002.